Bound exciton-assisted spin-to-charge conversion of donors in silicon

Marc Philipp Ross

A thesis submitted for the degree of

Doctor of Philosophy

University College London

Physics & Astronomy

London, 19th July 2017

I, Marc Philipp Ross, confirm that the work presented in this thesis is my own. Where information has been derived from other sources, I confirm that this has been indicated in the thesis.

London, 19th July 2017 Marc Philipp Ross

Bound exciton-assisted spin-to-charge conversion of donors in silicon

Marc Philipp Ross

Abstract

Donor spins in silicon are promising candidates for quantum information applications. The information storage time in donor qubits greatly exceeds the single operation time-scale and hence promises fast and accurate quantum computation, as well as highly sensitive magnetometers. Yet, the spin-readout of single donors and small donor ensembles remains non-trivial. One potential spin-to-charge conversion method is provided by the bound exciton, which is a long-lived, excited state of the donor that can be created optically in a spin-selective manner. It decays via an Auger process, whereby the donor is ionized while the electron is promoted to the conduction band, resulting in a spin-dependent change of sample conductivity. The main subject of this thesis is to understand the physical processes surrounding the photoconductivity of the bound exciton transition and to take first steps towards the spin-measurement of small donor ensembles in devices.

To this end, first, fundamental properties of the bound exciton transition are studied. Expressions for the transition energy-dependence to strain and magnetic fields are derived and experimentally validated. Furthermore, a proper treatment of the competing processes of direct, spin-independent donor ionisation is introduced, which significantly impacts the achievable read-out fidelity and spin polarisation.

Secondly, experiments utilizing the bound exciton transition for spin resonance experiments on bulk samples are presented. After a development of a circuit-model for the capacitive measurement technique, coherence time measurement of the phosphorus electron spin in highly purified ^{28}Si samples are presented and a novel, electrical method for state tomography of donor ensembles is developed.

Lastly, usage of the bound exciton transition in silicon devices is demonstrated with spin resonance measurements showing the potential for device-based magnetometry. Thereafter, a multitude of transport processes for n-type silicon at 4 K and under illumination are found and explained using current-voltage measurements. Finally, the relatively small sensitivity of the bound exciton transition energy to electric fields is determined.

Acknowledgements

This work, which culminates three and a half years of my life, accompanied by all its joys and hardships, would not have been possible without the great people that surround and support me. In particular, I want to thank:

John Morton, for the unquestioned support and encouragement that I received. Thank you for the fruitful and valuable discussions, but also the freedom with which I could pursue those topics that seemed interesting. Thank you also for all the great times off work, be it at the various dinners and activities in London or the joyful experiences at conferences.

Cheuk Lo, who helped me unravel the mysteries of electron spin resonance and the bound exciton transition in his typical relaxed and ever-understanding manner.

Matias Urdampilleta, who, together with Cheuk, established the great social bond of the QSD group. Thank you for two years as a great flatmate!

Christoph Zollitsch, for all the late night discussions about life, physics, people, music and whatever else we could think of, and which we, hopefully, carry on until the retirement home.

Anasua Chatterjee & Sroyon Mukherjee for their inspirational curiosity ranging from beekeeping, over cooking, to gardening and many more diverse and interesting topics that broaden the horizon.

Salahuddin Nur, for his ability to strike the right balance between being very dedicated to your projects, but also taking yourself not too seriously while doing them.

Naitik Panjwani, for all the calm help with broken spectrometers, cooling water problems and other lab-related issues, but even more so for always being a person that you can rely on.

Gary Wolfowicz, for sharing a small piece of his vast ESR knowledge with me, sufficient to write this thesis. Thank you also for the board game nights and the enthusiastic discussions.

The rest of the QSD group, namely *John Mansir, Roberto LoNardo, Jarryd Pla,*

HeeJin Lim, Leonid Abdurakhimov, Pierandrea Conti, Simon Schaal, David Wise, James O'Sullivan & Gavin Dold for the light-hearted atmosphere that you guys created; it was a real pleasure to work with you! Thank you, for the group activities and the Friday pubs, which were always as interesting and joyful as you could hope for.

Simon Benjamin, Naomi Nickerson & Joe O'Gorman, for the great, to-the-point discussions and the help getting up to speed with the surface code, straight at the beginning of my supposed-to-be PhD in experimental physics.

Mike Thewalt & Kaymer Saeedi, for the supply of the ^{28}Si samples and the various discussions about bound excitons at conferences.

Steve Lyon, Brendon Rose & Alexei Tyryshkin, for the help with the noisy spectrometer, for sharing the coherence time data and for all discussions at various conferences.

Steve Etienne, Nicholas Constantino, Rohit Khanna, Lorella Rossi & Vijayalakshmi Krishnan, for the help in the cleanroom at various stages of the device fabrication process and for the prompt support with a variety of other problems in the lab.

All of my other *friends in London and Munich,* without whom life would have less pop than a skateboard left in the rain.

My family *Verena, Iris-Tamara & Werner Ross, and Klaus-Dieter Finke,* for the great, unconditional love and support that I have been blessed with all these years. I take none of the opportunities that life has offered me for granted and I attribute the luck, that I may experience, partially on my ability to take decisions based on my authentic free will. Thank you for putting me in a position that allows me to enjoy that ability! I'm so looking forward to being united with all of you again!

Lastly, and above all, thank you to my partner, *Franziska Horstmann.* It is amazing to have someone that so deeply understands me and sees the world with such similar eyes. Thank you for trying to make the UK your home, too, when I decided to move, and thank you, later on, for all of the hours spent in the air between Munich and London! Thank you for being the straight-forward, funny, and caring human being that you are. I treasure every minute spent with you on our journey. I love you dearly.

Contents

Chapter 1

Introduction

Silicon has been at the forefront of technological and electronic innovation over the last half century. This predominance started with the development of silicon MOSFET transistors in the early 1960s [1], roughly a decade after the realization of the first solid state transistor by John Bardeen, Walter Brattain, and William Shockley in 1947 at the Bell Laboratories. Since then, silicon-based computing has fuelled an astonishing 'Digital Revolution' with the development of home computers, mobile phones and the world wide web. The new technologies furthermore caused a shift towards a data-driven labour market and an information-hungry society, which coined the term 'Information Age' for the period from the late 1970's up to today.

Two aspects of the Information Age have especially highlighted the capabilities of silicon: First, the ever-increasing demand for computational power for data-processing and simulation led to the most-remarkable advances in transistor and processor design. A miniaturisation process took place that saw a doubling of transistor density every two years (Moore's law) over more than four decades.

It is evident that Moore's law can not proceed indefinitely. With the introduction of the 10 nm fabrication node in 2017 [2], device dimensions are rapidly approaching the dimensions of donor wavefunctions. It is expected that the classical laws may no-longer apply fully and that quantum mechanical effects will play an increasingly big role. Due to statistical aspects of donor placement, this is expected to lead to greater variation in transistor characteristics and a higher rate of defect transistors on a chip.

The second aspect, which is sometimes overshadowed by the stellar improvements in computation power, is the quest of the Information Age to gather accurate data, i.e. the increasing demand for sensing applications. Here, too, silicon plays an important role with a variety of sensors, which is partly due to advanced silicon fabrication methods such as micromachining, and largely due to the intrinsic compatibility of silicon sensing devices with integrated circuits to perform, e.g., on-chip

sensor calibration with respect to drift in the output signal or the ability to provide bus systems. This allows for highly integrated sensing chips, with sensors developed for mechanical applications (accelerometers, flow & pressure sensors), radiation detection (CCDs, avalanche diodes), thermal sensing as well as magnetic field (Hall) sensing [3, 4].

Quantum computation is often proposed as a possible solution to the dooming stagnation of computation power by the failure of Moore's law in the future. Instead of treating quantum mechanical effects as a source of error, quantum computers aim to develop systems that manipulate and entangle quantum mechanical two-level systems (qubits) in order to run new types of algorithms, which feature superior scaling of computational demand with problem size. Furthermore, quantum systems are increasingly proposed for sensing applications in a variety of fields. In the following, a brief introduction to both quantum computation and quantum sensing is given and the current state of the art and prospect for silicon based systems is discussed. The section ends with an outline of this thesis, which aims to contribute to the development of a laser-based measurement of silicon donor spin qubits, with potential applications both in quantum computation and quantum sensing.

1.1 Quantum information processing

There are several requirements for a quantum mechanical system in order for it to be used to build an operational quantum computer. These are called the DiVincenzo criteria [5] and several qubit systems are on the verge of fullfilling all criteria [6]. Today, arguably the most advanced qubit systems are ion-traps [7–9], linear quantum computers based on photons [10–12] and qubits made from superconducting circuts. As an example, for the latter, single qubit gate, two-qubit gate and measurement fidelities in excess of 99 % [13] enabled the demonstration of bit-flip surface code error correction on 9 qubits in a linear chain of "Xmon" qubits [14, 15]. Furthermore, the first steps towards commercialisation have started, with quantum annealing computers based on superconducting circuits being sold by *D-Wave* and IBM providing web-access to a 5-qubit superconducting quantum computation test bed.

1.1.1 Silicon qubits

Qubits fabricated in silicon have not yet reached such level of maturity. While many different arguments could be discussed as reasons for this, a widely accepted point

is the more advanced fabrication requirements for silicon qubits. Compared to the above mentioned qubit system whose inter-qubit distance and system dimensions are on the order of µm to mm, the high effective mass and electric constant of silicon leads to Bohr radii and quantum dot sizes on the nanometre length scale. Consequently, fabrication precision down to the nanometre is required, which renders tasks such as consistent single electron read-out or even multi-qubit entangling more difficult. Still, remarkable advances have been achieved over the last couple of years, and the hope is that, once the fabrication issues are solved, the qubit density achievable in silicon may be significantly above the rivalling qubit systems. This would reduce the size and cost of a potential silicon quantum computer, which may thus outperform in the long run the more mature qubit systems of today.

Typically two different types of silicon qubits are distinguished—donor spin qubits and gate defined quantum dot (spin) qubits. In both cases an attractive potential for one (or a small number of) electrons defines the qubits. Quantum dot qubits either use the charge or the spin state of the captured electron as the quantum mechanical two-level system, but are not further discussed in the course of this thesis. Instead, the remainder of the section discusses the current state of the art of donor spin qubits.

1.1.2 Donor spin qubit performance

Donor spin qubits are particularly attractive since their typical single electron spin qubit manipulation time ($\sim$10 ns) is up to eight order of magnitudes faster than the best measured quantum information storage time (a quantity known as coherence time), with values for an electron spin up to about one second [16, 17]. Furthermore, all group-V donor impurities carry a finite nuclear spin, which, due to its smaller magnetic moment, features an even longer coherence time of up to 3 h [18]. As such, the donor spin-system may provide both fast operations via the electron spin and an intrinisic long-term storage of quantum information in the nuclear spin [19], where the time-scale for an exchange of information between nuclear and electron spin state is on the order of 10 µs or shorter. In order to achieve the longest coherence times, the nuclear spin-carrying ^{29}Si isotope, which is found in natural silicon with an abundance of 4.7 % needs to be removed from the host lattice. Such isotopically purified ^{28}Si substrates have been realized, e.g. in the Avogadro project [20], which achieved ^{28}Si silicon crystals with ^{29}Si concentrations of $\lesssim$ 50 ppm. Still, today ^{28}Si silicon wafers are rare and can not currently be purchased commercially. In $^{\mathrm{nat}}$Si, electron coherence times are usually on the order of 1 ms, due to the higher

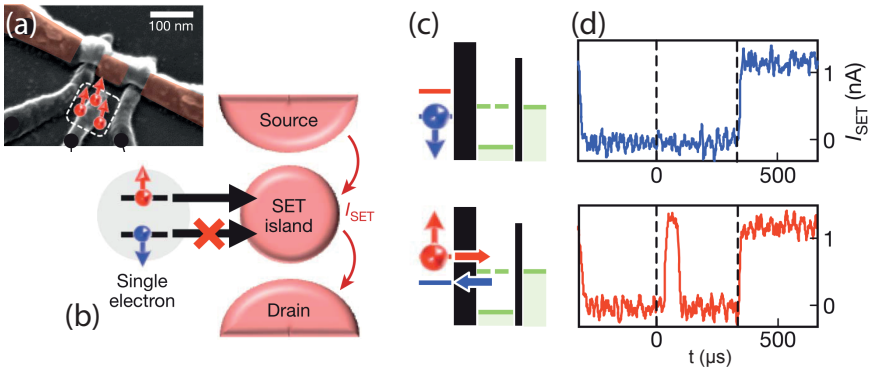

Figure 1.1: Spin-to-charge conversion of a donor electron using spin-dependent tunneling to a nearby single-electron-transistor (SET). (a,b) Scanning electron micrograph and function principle of the device. (c) Spin-dependent tunneling prinicple to the nearby reservoir (here the SET) which leads to the corresponding current traces of (d). Images reproduced from [23].

magnetic field noise from the ^{29}Si nuclear spin, except for operation of the donor spin system at magnetic field insensitive points, where coherence times $> 100\,\text{ms}$ could be reached ([17] & Ch. 3.4.4).

The mentioned coherence times are values for ensembles of donors in the bulk. While such ensemble spins may have applications as quantum memory in hybrid schemes with superconducting resonaters [21], quantum computation relies on the manipulation, entanglement and measurement of single electron spins. Due to the small magnetic moment, a direct magnetic measurement of the spin-state is extremely difficult and hence the single electron spin-measurement relies typically on the spin-dependent creation of a charge, which is known as spin-to-charge conversion. The first demonstration of this principle has been realized with spin-dependent tunneling in a GaAs quantum dot [22] and the same principle has later been adopted by Morello *et al.* for the measurement of a single donor electron spin [23] in silicon.

The principle is depicted in Fig. 1.1. At the time in the quantum algorithm at which the qubit readout is due, the Zeeman-split donor states $|\uparrow\rangle$ and $|\downarrow\rangle$ are tuned by an electric gate to align above and below the energy level of a nearby electron reservoir. Depending on the spin-state, the electron does ($|\uparrow\rangle$) or does not ($|\downarrow\rangle$) tunnel to the electron reservoir, thereby ionizing the donor depending on the spin-state. The ionized donor in turn changes the electrostatics of a nearby charge detector (here the same single electron tranistor (SET) and gives rise to a current spike through the charge detector until an electron tunnels back from the reservoir to the donor $|\downarrow\rangle$ state and neutralizes it. Optimisation of this read-out scheme over the past few years [24, 25] has pushed the measurement fidelity to values of 97 % for the electron spin and 99.995 % for the nuclear spin [26]. During

this optimisation process, microwave strip lines and a ^{28}Si substrate have been incorporated and it has been shown that the good qubit performance in the bulk could be maintained in nano-devices close to the interface and electric gates. Single qubit control fidelities of 99.95 % (99.99 %) could be achieved [27], with coherence times between 1 ms to 560 ms (20 ms to 35 s) depending on the exact dynamical decoupling sequence used for the electron (ionised nuclear) spin [26].

In order to ensure spin-selectivity of the tunnelling process, the Zeeman splitting needs to be significantly larger than the electron temperature of the reservoir. This restricts the scheme to $T \approx 100$ mK and high magnetic fields (> 1 T). As relaxation towards thermal equilibrium (characterized by T_1) becomes increasingly more efficient towards high magnetic fields ($T_1 \propto B^{-4}$), high magnetic fields have the potential to decrease the qubit performance (cf. Ch. 3.4.4.1). Furthermore, it is questionable if electron temperatures in the mK range can be maintained when scaling up the system to thousands and millions of qubits with each their own control electronics.

Another problem of the spin-dependent tunnelling readout scheme could arise from the exponential dependence of the tunnelling rate on the distance between donor and electron reservoir. In typical quantum computation schemes, the read-out time-scale has a relatively narrow window: On the one hand, if the tunnelling rate is too fast, the measurement fidelity decreases due to the electronic measurement bandwidth. On the other hand, if the tunnelling rate is to slow, the overhead per calculation cycle increases, i.e. the measurement would take significantly longer than the qubit operations, thus reducing the "clock frequency" of the quantum computer. Therefore, good control of the tunnelling rate is required which requires donor placement accuracy at the nanometre scale, maintained across a large number of single-donor devices. In summary, while very suitable for proof-of-principle in single qubit devices, a scale up of the spin-dependent tunnelling-based donor ionisation to larger qubit densities might prove challenging.

An alternative, optical spin-to-charge conversion may alleviate the fabrication and operational demands and is the main focus of this thesis: The donor bound exciton (D^0X) transition. Excitons are electron-hole pairs in a semiconductor and are often discussed in their free, unbound form. They may however bind to a donor electron, where, due to the absence of kinetic energy and due to the long lifetime of the D^0X state (272 ns [28]), a very clearly defined energy level is formed. The bound exciton transition linewidth is narrow enough to resolve the Zeeman splitting of the neutral donor electron spin and, in ^{28}Si, even the hyperfine splitting [18, 29–31]. The bound exciton decays via an Auger transition where electron and hole

recombine and transfer the D^0X energy onto the remaining electron of the neutral donor, thereby ionizing the donor [28]. The D^0X transition may thus be used to spin-selectively ionize a neutral donor.

The benefits include operation at any magnetic field strength and liquid-helium temperatures [32], thus significantly easing cooling power requirements. Furthermore, the hope is that the measurement time scale can be tuned simply with the laser intensity and thus would not depend on the fabrication precision. By pumping on the D^0X transition for a number of electron capture and ionisation cycles it is furthermore possible to initialize the donor spin state and polarization values of electron and nuclear spin of 90 % have been achieved [18, 33].

A somewhat disregarded aspect of the D^0X process are the competing mechanisms on donor and conduction band electrons upon illumination with D^0X photons, whose energy is close to the band-gap. One of the objectives of this thesis is to shed more light on spin-independent, off-resonant donor ionization processes and to thus better assess the potential of the D^0X transition as a spin-to-charge conversion method for qubit readout in silicon based quantum computation.

1.1.3 Silicon donor quantum computation architectures

A single, isolated qubit does not constitute a quantum computer and methods are required to entangle at least nearest-neighbour qubits. A couple of design proposals for fully scaled silicon quantum computers have been developed over the years and are summarized here.

The seminal work, igniting interest for silicon based qubits, is the Kane proposal [34]. The qubits are represented by the nuclear spin of phosphorus atoms which are placed with donor separations of $10 - 20\,\mathrm{nm}$. Single qubit rotations are envisioned by tuning individual nuclear spins into resonance with a globally applied radio frequency (rf) field using electrical fields from so-called "A-gates" placed above each donor. The application of an electric field modulates the wavefunction overlap of electron and nuclear spin and hence their mutual hyperfine interaction and transition frequency. In subsequent years, such Stark shifting has been demonstrated both for the nuclear [35, 36] and electron spin [37, 38]. Interactions and entanglement of nearby nuclear spins is provided using "J-gates", placed in-between donor sites, which attract the electron wavefunctions from the adjacent donors and mediate the interaction between the nuclear spins using the exchange interaction [39, 40].

The proposal raised significant challenges, some of which have since been addressed, while others remain unsolved. First, the fabricational demands are tough: The reliable positioning of three gates over the span of 10 nm is challenging even to the most advanced lithographic processes. Furthermore, although a lot of progress has been achieved regarding the placement of single donors with accuracies in the range of 0.5 nm, achievable now using scanning tunneling microscope lithography (STML) [41, 42], still a lot of progress is required until the reliable fabrication of full grids with this accuracy is achieved. Another point of criticism is the layout of the proposal, which effectively is a one dimensional chain. While error-correction on such linear, possibly segmented chains is possible (e.g. [43]), a stronger error-correcting code, known as surface code [44], can only be implemented on a 2D grid. There is no clear fabricational path forward to scale the Kane proposal to a two dimensional layout. Finally, and likely the most critical point of criticism is the fact that the exchange interaction strength varies both exponentially and oscillatory with donor separation, a trait due to the lattice periodicity of the the donor electron wavefunction. This results in largely differing two-qubit gate times from minuscule fabrication variations and renders the Kane proposal in its original form unfeasible.

In recent years a number of proposals tried to improve on the orginal Kane concept. Hollenberg [45] tries to ease the fabricational requirements by shuffling electrons between donor sites to localized A- and J-gates. Hill [46] proposes a design reminiscent of RAM multiplexing with shared control lines and tunneling from precission (STML-) fabricated single-electron quantum dots (acting as the measurement qubits in the surface code error-correction) to the donor qubits (acting as data qubits). Pica *et al.* [47] proposed a similar concept with bismuth donors as data qubits and gate-defined quantum dots on the Si/SiO_2 interface as measurement qubits, with one of the benefits being the operation close to a magnetic-field insensitve spot of the bismuth energy level-diagram, where magnetic noise does not affect the coherence time of the electron spin [17]. Finally, Morse *et al.* [48] suggest to provide long-distance entanglement between silicon qubits by exploiting the sub-bandgap optical transitions to excited states of deep (group-VI) silicon donors, while Tosi *et al.* [49] want to achieve two-qubit operations between hybrid donor-dot qubits for ranges up to 200 nm using the electrical dipole moment of the donor upon the application of an electric field.

In Ch.2 of this thesis, an alternative approach is investigated, which utilizes the dipolar coupling between two different spin species to provide the four qubit stabilizer measurement of the surface code. The proposed device features two separate

qubit grid stages that may be translated with respect to each other and has the main advantage that the device geometry and operation speed may be scaled according to the available fabrication precision.

1.2 Quantum sensing

The sensitivity of qubits to noise from the environment is the primary reason for qubit decoherence. Reversing roles, however, this sensitivity may be harnessed to detect and measure signals of the respective fields. This is the realm of quantum sensing which both describes the use of quantum mechanical systems for sensing application using e.g. coherent qubit states, but is also often used as a description for exploiting entanglement across multiple qubit to push the sensitivity closer to the Heisenberg-limit [50]. Here, we focus on the former definition, where a range of sensors exploiting coherent qubit states have been developed over the years [50], ranging from e.g. gravimeters [51] to electric field sensors [52, 53].

Due to the magnetic dipole moment, spins of donor can be used quite naturally as magnetic field sensors. The magnetic field determines the spin precession frequency and any changes of magnetic field hence establish themselves as phase shifts in the rotating frame. A large variety of magnetometers have already been established, which either show extraordinary sensitivity but require large ($\sim$ mm^3) sensing volumes (atomic vapor cell magnetometers [54, 55] & SQUID loops [56–58]), ease of operation, but limited sensitivity (Hall bars [59]) or limited ease of operation but exceptional sensitivity and mode volume (magnetic resonance force microscopy [60]).

A lot of attention has been given to the NV center defect of diamond lately. The NV center is a nitrogen impurity and adjacent vacancy defect of the diamond lattice, whose negative charge state forms an $S = 1$ spin system. One of the transitions $m_s \pm 1 \Leftrightarrow 0$ may be used as the qubit and the Larmor frequency of this qubit responds to changes of the applied magnetic field. The NV center spin can be measured optically and within its coherence time different ESR pulse sequences may be used to detect either static (DC) or periodically modulated (AC) magnetic fields [61–63]. The chemical inertness of diamond, combined with the high magnetic field sensitivity and the possible operation at room temperature make it ideally suitable for (in-vivo) bio-sensing applications [64, 65]. However, magnetometry applications reach beyond this with potentials in security, on-chip short-circuit detection, structural biology, condensed matter physics and the detection of brain and heart diseases [56, 57, 66, 67].

How does the spin of donors in silicon compare against the NV center in terms of performance? At low temperatures, the donor spins exhibit significantly longer coherence times (for a detailled spin-property comparision see Ch. 2.5.3), which should result in both higher magnetic field sensitivities and a larger bandwidth with AC

magnetic field detection possible down to the low frequency regime of ∼10 Hz. Furthermore, efficient fluorescence detection, i.e. efficient optical measurement of NV centers is difficult, leaving the performance of NV centers several orders of magnitude below their theoretical limit [50]. It is likely that charge detection in silicon may be accomplished more efficiently, as e.g. indicated by the performance of CCD arrays or avalanche diodes. Certainly, the requirement for cryogenic temperature is a drawback for silicon magnetometry, but the effects may not be as grave, since e.g. squid loops require similar temperatures and can still be used for medical purposes using special cryostat designs that allows for working distances on the order of 2 mm between cold sensor and room temperature specimen [56].

The main drawback for silicon donor magnetometry is currently the readout mechanism. Typical electron spin resonance (ESR) experiments acquire the signal inductively via either 3D cavities (standard ESR) or on-chip fabricated superconducting resonators [68, 69]. Both of these require structure sizes on the order of the microwave wavelength ∼3 cm, resulting in very large sensing volumes. Here, the spin-to-charge conversion of the D^0X transition may provide the required improved read-out of small, µm-sized donor ensembles patches. A chip may be envisioned with a CCD-like array of devices that produces an electric signal proportional to the amount of electrons ionized by the spin-selective D^0X ionization of donors. If this chip is confined within a 3D cavity that supplies the required microwave manipulation simultaneously to all ensemble patches, magnetometry spin resonance experiments could be conducted, while still retaining the spatial accuracy set by the device array.

It is one of the main tasks of this thesis to develop, test and discuss the relevant physics of a µm-sized silicon device that converts the spin polarization of a donor spin ensemble into an electrical (current) signal via the spin-dependent donor ionization of the D^0X transitions.

1.3 Thesis outline

This thesis is organized in the following way:

Chapter 2 discusses a novel silicon quantum computer proposal based on the surface code quantum error correction. The surface code is introduced, followed by a discussion of the device, operation principle and error threshold fidelities for a variety of error sources. At the end, the feasibility of fabricating the device in the future is assessed based on the performance of several state-of-the-art spin qubit systems.

Chapter 3 gives a brief introduction into a variety of fundamental aspects of donors in silicon. First the phononic and electronic band structure, including the dependence of the latter on magnetic field and strain are discussed, which is followed by the energy spectrum of the shallow donor impurity in silicon. Then, an introduction to spin resonance experiments and their underlying theory is given and a variety of decoherence mechanisms are compared. The chapter ends with a section on charge transport in silicon, including the effects of carrier freeze-out, electron mobility and magnetoresistance.

Chapter 4 introduces the samples used throughout the thesis including the fabrication process of the µm-scale D^0X devices used. Furthermore, those setup components common to all experiments of the thesis are explained.

Chapter 5 starts with a thorough theoretical review of the D^0X transition and the competing spin-independent photo-carrier generation mechanisms, which leads to an estimate for the best-achievable measurement fidelity of the donor electron spin using the D^0X spin-to-charge conversion. The chapter then discusses fundamental aspects of the D^0X transition with the aid of a few basic experiments: First, photo-Hall experiments separate the laser effects on photoconductivity, carrier density and carrier mobility, both on- and off-resonance with the D^0X transition. This is followed by a discussion of the magnetic field and strain related shifts of the D^0X transition energy. Finally, the build-up of spin polarisation during continuous pumping on the D^0X transition is measured using electron spin resonance experiments.

Chapter 6 includes experiments performed on bulk samples, whose spin-dependent photo-conductivity is measured capacitively in a parallel plate capacitor. A model is developed for the origin of the capacitive D^0X signal, followed by a D^0X measurement of the electron spin coherence time of phosphorus in a low-doped ^{28}Si sample. The chapter ends with a novel method to perform quantum state tomography which is based on absolute state-population measurements using the D^0X transition.

Chapter 7 deals with D^0X experiments performed on devices. First, a proof-of-principle experiment shows that typical spin resonance experiments are possible in ^{28}Si devices using direct electrical D^0X spin-readout. Thereafter, the complicated current-voltage characteristics of simple resistive n^+nn^+ resistors at 4 K are measured and modelled, both in the dark and under laser illumination. Furthermore, a scanning photocurrent microscopy experiment investigates the role of the contact area to the observed photo-conductivity. Finally, the last section investigates the shift of the D^0X transition energy due to electric fields, which—in disagreement with a recent tight-binding calculation—seems to be quite small and instead agrees with an older effective mass theory for excitons in silicon.

Chapter 8 includes a summary of the thesis and possible future research directions.

Chapter 2

A silicon architecture for surface code quantum computation

This chapter introduces a silicon donor-based architecture to perform universal quantum computation. Its two-dimensional layout is designed for the surface code approach to quantum error correction. A mobile stage hosts the probe qubit grid which is made to interact with the static data qubit below via dipolar spin-spin coupling. Motion of the platform modifies the interaction strength between probe and data-qubits and permits the four data qubit parity measurement central to the surface code algorithm.

This chapter is structured as follows: First, the difficulties of quantum error correction and the underlying idea of stabilizer measurements are discussed in Sec. 2.1. This is followed by a discussion of the main operating principles of the surface code in Sec. 2.2. The proposed architecture is introduced in Sec. 2.3, with its tolerance to qubit misplacements and other sources of error calculated in Sec. 2.4. Finally, Sec. 2.5 addresses how realistic the proposal is, addressing questions regarding the fabricational and mechanical feasibility, the qubit performance of candidate solid state spin qubit systems and the compatibility of the device operation with the refocussing pulses required for solid state spin qubits.

The results of this chapter are derived in collaboration with Prof. Simon Benjamin's group from the University of Oxford. Credit for the theoretical simulation of the device and the presented error tolerances go to Joe O'Gorman (University of Oxford) and Naomi Nickerson (Imperial College London). The results have been published in npj Quantum Information [70].

2.1 Introduction to quantum error correction

For classical information stored in bits, development of simple error correcting codes based on majority voting can be readily understood: Instead of storing the information in a single physical unit, the information is copied onto multiple redundant physical systems. In the event of bit-flip errors during the transmission via a noisy channel, the original information may still be retrieved using the majority vote, as long as the probability for error p is small. With k being the number of physical copies, the error rate of this majority-vote error correction scheme scales according to $p^{(k-1)}$ — the more copies, the better [71].

For quantum mechanical information stored in, e.g., the two-dimensional Hilbert space of a qubit, such simple protocols are not possible for several reasons. Firstly, the non-cloning theorem of quantum mechanics prevents the creation of additional qubit copies with the same quantum state as the original source qubit. Secondly, in contrast to classical bits, errors are not discrete for qubits. While in classical systems the only possible error is a complete flip from $0 \rightarrow 1$ or vice versa, for qubits, errors constitute rotations on the Bloch sphere of *any*, even the smallest degree. Hence, qubit errors are continuous and arbitrarily small, but still must be corrected for. Thirdly, and perhaps most importantly, any measurement of the qubit system leads to the destruction of its state due to the projective nature of quantum measurement. Hence, a measurement of the system itself would not allow the quantum state to be subsequently used in an algorithm. Instead, a protocol is required that detects the occurrence and kind of error on a qubit, but does not acquire any information about the qubit state itself, thus preventing its destruction.

As with the classical example, redundancy is key to achieving quantum error correction. The following section reviews the benefits of adding more physical qubits to the representation of one logical qubit, ending with a brief review of Shor's algorithm that protects a logical qubit from arbitrary qubit errors, by spreading its quantum state across 9 physical qubits.

The starting point is a single qubit with energy quantization axis along $\hat{Z}$ with eigenstates $|1\rangle$ with $\hat{Z}|1\rangle = +1|1\rangle$ and $|0\rangle$ with $\hat{Z}|0\rangle = -1|0\rangle$. Possible errors on this qubit system comprise bit-flip errors with operator $\hat{X}$, phase flip errors ($\hat{Z}$) or simultaneous bit-flip and phase flip errors ($\hat{Y} = \hat{X}\hat{Z}$). Only full phase or bit flip errors are considered here and the discussion of arbitrary small error-angles is deferred to later.

It is straightforward to see that a bit flip error can be detected by a repetitive measurement along Z. Similarly, phase flip errors can be detected by repetitive $\hat{X}$

measurements of the qubit projection to the X axis. Each measurement leads to a collapse of the wavefunction onto one of the eigenstates of the operator, destroying any qubit phase information for $\hat{Z}$ measurements and any energy information for an $\hat{X}$ measurement. The underlying mathematical principle is that $\hat{X}$ and $\hat{Z}$ do not commute $[\hat{X}, \hat{Z}] \neq 0$, therefore these two operators can not share the same eigenstates.

The situation changes slightly when two qubits and two-qubit operators are considered. The operators $\hat{X}_a\hat{X}_b$ and $\hat{Z}_a\hat{Z}_b$, operating on qubits a and b of state $|\psi\rangle = |ab\rangle$ do commute, and the four shared eigenstates of these two operators are:

$\hat{Z}_a\hat{Z}_b$	$\hat{X}_a\hat{X}_b$	$\|\psi\rangle$
$+1$	$+1$	$(\|11\rangle + \|00\rangle)/\sqrt{2}$
$+1$	-1	$(\|11\rangle - \|00\rangle)/\sqrt{2}$
-1	$+1$	$(\|01\rangle + \|10\rangle)/\sqrt{2}$
-1	-1	$(\|01\rangle - \|10\rangle)/\sqrt{2}$

Repetitive measurement of these two operators continuously projects the combined qubit state back into one of these four eigenstates. Once in this eigenstate, the repetitive measurement of $\hat{Z}_a\hat{Z}_b$ & $\hat{X}_a\hat{X}_b$ protects the quantum state, hence the term stabilizer measurement is coined for this kind of repetitive multi-operator measurement.

Now consider errors on the individual physical qubits: A bit flip of the first qubit takes, e.g., an initial $(|11\rangle + |00\rangle)/\sqrt{2}$ state to a $(|01\rangle + |10\rangle)/\sqrt{2}$, which is detected as a change of the measurement outcome of $\hat{Z}_a\hat{Z}_b$. In the same way, a phase flip error of an individual qubit can be detected as a change of $\hat{X}_a\hat{X}_b$. Thus it is possible to detect what kind of error occurred on the physical qubit by monitoring the stabilizer measurement outcome. Unfortunately, a logical qubit formed of two physical qubit is not useful as the location of the physical qubit error is unknown. An error on the first physical qubit changes the measurement observable in the same way as an error on the second physical qubit. Furthermore, the two-qubit logical qubit does not have any degrees of freedom under repetitive measurement of these two stabilizers, since any superposition of the four eigenstates would be immediately collapsed by the stabilizer measurement.

Next, consider a system of three physical qubits. The logical qubit $|\psi\rangle_{\mathrm{L}} = \alpha_1 |1\rangle + \alpha_2 |0\rangle$ is encoded by entangling the original qubit state with two more ancilla qubits, resulting in the Bell state $|\psi\rangle = \alpha_1 |111\rangle + \alpha_2 |000\rangle$.

Two (commuting) two qubit Z-projection operators are chosen for repetitive measurement, e.g., acting on the first two qubits ($\hat{Z}_a\hat{Z}_b$) and on the second two qubits ($\hat{Z}_b\hat{Z}_c$). Now consider a bit flip error on one of the physical qubits. The measurement outcomes following a bit flip error on no qubit, on the first, second or third qubit, respectively, are:

$\hat{Z}_a\hat{Z}_b$	$\hat{Z}_b\hat{Z}_c$	$\|\psi\rangle$
$+1$	$+1$	$\alpha_1\|111\rangle + \alpha_2\|000\rangle$
-1	$+1$	$\alpha_1\|011\rangle + \alpha_2\|100\rangle$
-1	-1	$\alpha_1\|101\rangle + \alpha_2\|010\rangle$
$+1$	-1	$\alpha_1\|110\rangle + \alpha_2\|001\rangle$

By combination of the measurement results of $\hat{Z}_a\hat{Z}_b$ and $\hat{Z}_b\hat{Z}_c$, it is possible to deduce the position of the bit-flip error. The sequence does not gain any information regarding the complex prefactors α_1 and α_2, it only gains information whether a bit flip occurred and on which qubit it happened. This means that the logical qubit state is not projected/destroyed by the stabilizer measurement and a flip of the erroneous physical qubit restores the original, complex, logical state $|\psi\rangle_{\mathrm{L}}$.

It should be noted that this encoding only corrects for bit flips on the physical qubits, while phase flip errors, which change α_1 and α_2 remain uncorrected for. In an analogous way, the logical qubit can be encoded as a Bell state of the eigenvectors of the $\hat{X}$ operator, $|\psi\rangle = \alpha_1|+++\rangle + \alpha_2|---\rangle$. Measurement of the combined $\hat{X}_a\hat{X}_b$ and $\hat{X}_b\hat{X}_c$ operators then allows for the detection and correction of phase flip errors, while bit flip errors are unaccounted for.

Finally, the Shor code combines the above 3-qubit bit-flip and phase-flip correction codes into a measurement sequence that stabilizes and detects the logical qubit against both error types [71–73], using three groups of three physical qubits each, i.e., 9 qubits in total. The logical qubits is encoded as a phase flip code with the ground and excited state being $|0_{\mathrm{S}}\rangle = \frac{1}{\sqrt{2}}|+++\rangle$ and $|1_{\mathrm{S}}\rangle = \frac{1}{\sqrt{2}}|---\rangle$, respectively. Now each of these three qubits is again comprised of three physical qubits as: $|+\rangle = \frac{1}{\sqrt{2}}(|000\rangle + |111\rangle)$. Hence the two eigenstates of the logical qubit state of the Shor code read:

$$|0\rangle_{\mathrm{S}} = \frac{(|000\rangle + |111\rangle) \otimes (|000\rangle + |111\rangle) \otimes (|000\rangle + |111\rangle)}{2\sqrt{2}} \tag{2.1}$$

$$|1\rangle_{\mathrm{S}} = \frac{(|000\rangle - |111\rangle) \otimes (|000\rangle - |111\rangle) \otimes (|000\rangle - |111\rangle)}{2\sqrt{2}} \tag{2.2}$$

In order to detect bit flip errors, the code operates within the three groups with the $\hat{Z}_a\hat{Z}_b$ and $\hat{Z}_b\hat{Z}_c$ operators. Phase flips of *single* qubits are characterized by $\alpha|0\rangle + \beta|1\rangle \rightarrow \alpha|0\rangle - \beta|1\rangle$. The behaviour of the *logical* $\hat{X}$ basis states is analogous under phase flips of single physical qubits: $\alpha|000\rangle + \beta|111\rangle \rightarrow \alpha|000\rangle - \beta|111\rangle$. In order to detect such phase flips of single physical qubits, after the correction for bit flips within the groups, the $\hat{X}_b\hat{X}_c$ operate on the reduced states of the three groups, comparing the phase of the first group to the phase of the other two groups. In this way, both phase and bit flips on individual qubits can be detected.

The code breaks down when two phase flips occur at the same time, thus it is preferable to spread the logical qubit over even a higher number of qubits. So far only full phase flip or bit flip errors have been considered. Indeed, this treatment is justified by the projective kind of a measurement. Suppose a phase error of only a small angle is occurring on a physical qubit. The act of the stabilizer measurement forces the qubit state into an eigenstate of the measurement, which will for small error angles be the original, error-free state with a high probability, or with a lower probability a phase flipped state, whose full phase flip is then detected and corrected for. Hence, arbitrarily small errors show up in the stabilizer measurement most of the time as no error and, if they occur, only as detectable full-flip errors.

It is relatively complex to scale the Shor code to larger numbers of logical qubits. Furthermore, single qubit gates or entangling gates are not straightforward to implement on the logcial qubit level. An elegant alternative to the Shor code is discussed in the next section—the surface code—which features quite a natural scaling of the code to larger qubit numbers, while still retaining a straightforward method to perform logical gates.

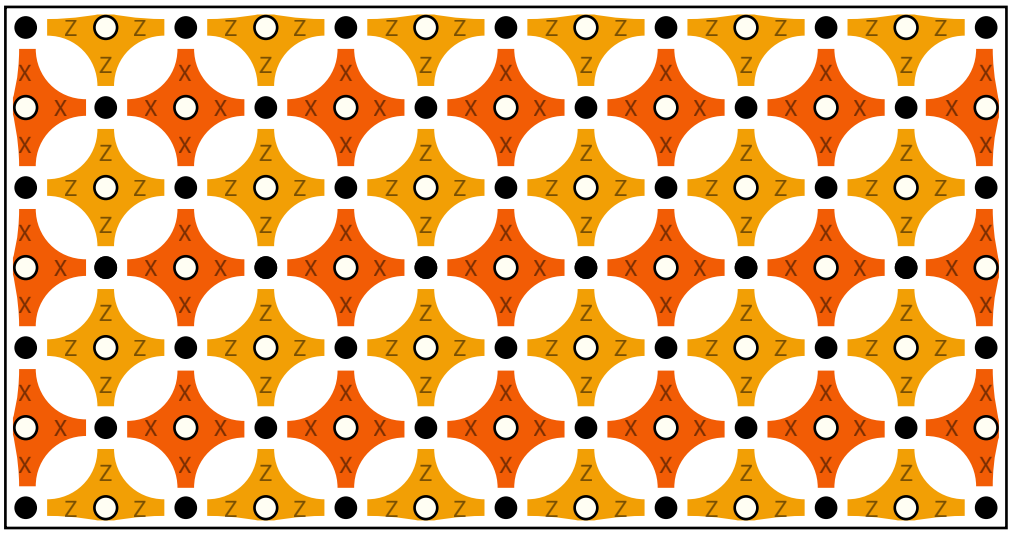

Figure 2.1: A small surface code grid. The measurement qubits (empty circles) measure the parity of their four surrounding data qubits (black dots) either in the $\hat{Z}$-basis (yellow) or in the $\hat{X}$-basis (orange). The black line represents the border of the surface code, where three qubit parity measurements are measured instead. With this selection of borders there is one extra data qubit than probe qubits in the surface code grid (here 46 to 45).

2.2 The surface code

A popular example of stabilizer error correction schemes is the surface code, which has a few advantages compared to other error correcting alogirthms. Firstly, the layout of the qubits is in a 2D grid, which can be arranged in a way to ensure sufficient space for the required electrostatic gates of solid state qubits. Furthermore, the third dimension could be used for the delivery of the required wiring. The second big advantage is that only nearest neighbour entanglement operations are required, which is especially interesting, if not a necessity for optically inactive solid state qubits, for which entanglement operations with distant qubits might prove challenging. The third reason why the surface code acquired a lot of interest is its high error tolerance: Reported thresholds for fault-tolerance, i.e. the error rate below which an increase in grid size leads to a stronger protection of the logical qubit are on the order of 1 % [44, 74, 75]. This means that if the average error during a surface code stabilizer cycle is kept below this threshold, the computer could in theory be made fault-tolerant by simply increasing the grid size drastically.

The layout of the surface code is depicted in Figure 2.1. The qubit grid is divided into data qubits (black dots), i.e. the qubits that actually carry the quantum state for computation, and measurement qubits[1] (empty circles), that are used to per-

[1] In the latter sections of this Chapter the measurement qubits are also labelled as probe qubits.

form the four qubit stabilizer measurement. The measurement qubits are divided into two kinds: 'Measure-Z' qubits (yellow), that measure the $\hat{Z}_a\hat{Z}_b\hat{Z}_c\hat{Z}_d$ operator of its four surrounding data qubits and 'measure-X' qubits (orange), running the $\hat{X}_a\hat{X}_b\hat{X}_c\hat{X}_d$ stabilizer on its neighbouring qubits. This operation is essentially a parity measurement of their neighbouring data qubits in the respective measurement axis. With the parity even, i.e. an even number of $|1\rangle$ data qubits in the $\hat{Z}$-basis, the measurement gives $\hat{Z}_a\hat{Z}_b\hat{Z}_c\hat{Z}_d\,|\psi\rangle = +1\,|\psi\rangle$, while an odd parity results in the negative measurement value. The corresponding is true for the measure-X stabilizer, with $\hat{X}_a\hat{X}_b\hat{X}_c\hat{X}_d\,|\psi\rangle = +1\,|\psi\rangle$ for an even number of data qubits with $+X$ projection, and $\hat{X}_a\hat{X}_b\hat{X}_c\hat{X}_d\,|\psi\rangle = -1\,|\psi\rangle$ for an odd number. On the edge of the surface code, the corresponding three data qubit parities are measured. It is important to note that due to the different grouping of data qubits for the $\hat{X}$ and $\hat{Z}$ stabilizer, $\hat{Z}_a\hat{Z}_b\hat{Z}_c\hat{Z}_d$ on one data qubit set and $\hat{X}_c\hat{X}_d\hat{X}_e\hat{X}_f$ on the neighbouring data set commute, allowing for a shared eigenstate.

The operation of the surface code consists of alternating measurement rounds of the X- and Z-stabilizers, respectively[2], which preserves one particular quantum state across the whole data qubit grid [44].

How does the surface code handle errors occurring on the physical qubits? Each of these errors shows up with a different signature, which allows for its correction: If a data qubit is subject to a bit flip error, the results of both neighbouring Z parity measurements change sign, signalling which kind of error (bit-flip, because the Z parity changed) has occurred and the error location (between the two measurement qubits affected by a sign change). Analogously, a phase flip error changes the eigenvalue of the two adjacent X parity measurements, while a $\hat{Y}$ error affects both the X and Z parity measurement. Hence, data qubit errors are characterized by sign changes of two neighbouring parity measurements. In the time-domain, bit- or phase-flip errors have a signature of a sudden change of two neighbouring parity measurements, with the new parity measurement outcome not changing in consecutive cycles (as long as the error is not negated). In contrast, errors during readout of the measurement qubit, such as a measurement result that signalizes even parity, although the real data qubit parity was odd, are characterized as isolated events—both spatially (only one measurement qubit triggers) and temporarily (the

[2]The operation $\hat{Z}_a\hat{Z}_b\hat{Z}_c\hat{Z}_d$ is carried out by the initialisation of the measure-Z qubit, followed by four CNOT gates of the four data qubits with the probe qubit and the measurement of the measurement qubit. The $\hat{X}$ measurement is done very similarly, except for two Hadamard gates on the measurement qubit before and after the CNOT gate. Both the X and Z stabilizer can thus be measured simultaneously. Chapter 2.3 introduces a different, maybe more intuitve way to conduct the stabilizer/parity measurement using four controlled phase gates of the measurement qubit with the data qubits.

measurement result is back to its original value after one round). The only way in which an error leads to an unrecoverable break down of the surface code is when simultaneous errors happen on a chain of data qubits that connects from one side of the grid to the other. In that case, each parity measurement contains two bit (phase)-flipped data qubits, therefore not changing the parity measurement result and hence the error remains undetected for a long chain of data qubit errors. The probability of simultaneous errors on all data qubits within a chain reduces with the number of data qubits within the chain. Hence, logical qubits are better protected in surface codes with larger grid sizes. It should be noted that while it is certainly possible to hardware-correct for detected errors by applying the corresponding bit or phase flips, the surface code actually offers a better solution: Mathematically equivalently, the errors can simply be detected and stored, and every subsequent measurement can later be adjusted for the error that had occurred using the control software. In this way, no additional errors are introduced by (non-ideal) 'repair' operations. Furthermore, certain errors tend to cancel each other during longer computations.

The question remains which degrees of freedom the surface code grid possesses and thus, what operations form the logical qubits. At first glance, it seems as if the X and Z parity measurements completely lock the quantum state of the data qubits into one particular eigenstate. This, however, is not true: When counting the number of data qubits and measurement qubits in the grid layout of Fig. 2.1, it is found that there is one more data qubit than measurement qubit. Every data qubits adds two degrees of freedom, while every measurement qubit reduces it by two. Hence, two degrees of freedom should remain in the grid, i.e., two operations should exist that can be used to encode a logical qubit. These operations have already been encountered: They are the only ones that the surface code does not gain any information about (hence are subject to possible errors): A chain of operations on the data qubits, spanning from one side of the grid to the other one. Figure 2.2(a) depicts the two operations $\hat{X}_{\mathrm{L}} = \hat{X}_8\hat{X}_7\hat{X}_3\hat{X}_6$ and $\hat{Z}_{\mathrm{L}} = \hat{Z}_1\hat{Z}_2\hat{Z}_3\hat{Z}_4$ that manipulate the Hilbert space of the logical qubit of the data qubit grid.

A single logical qubit is only useful as quantum memory. To construct a quantum computer, it is possible to introduce more logical qubits: Whenever a stabilizer is chosen not to be measured, another two degrees of freedom are added to the surface code grid, hence, another logical qubit is added. This is depicted in Figure 2.2(b), where a Z stabilizer is deactivated, leaving a hole in the grid. The two logical operations for a Z stabilizer hole are firstly $\hat{Z}$ operations on all data qubits surrounding the hole and secondly a chain of $\hat{X}$ operators from the Z stabilizer hole

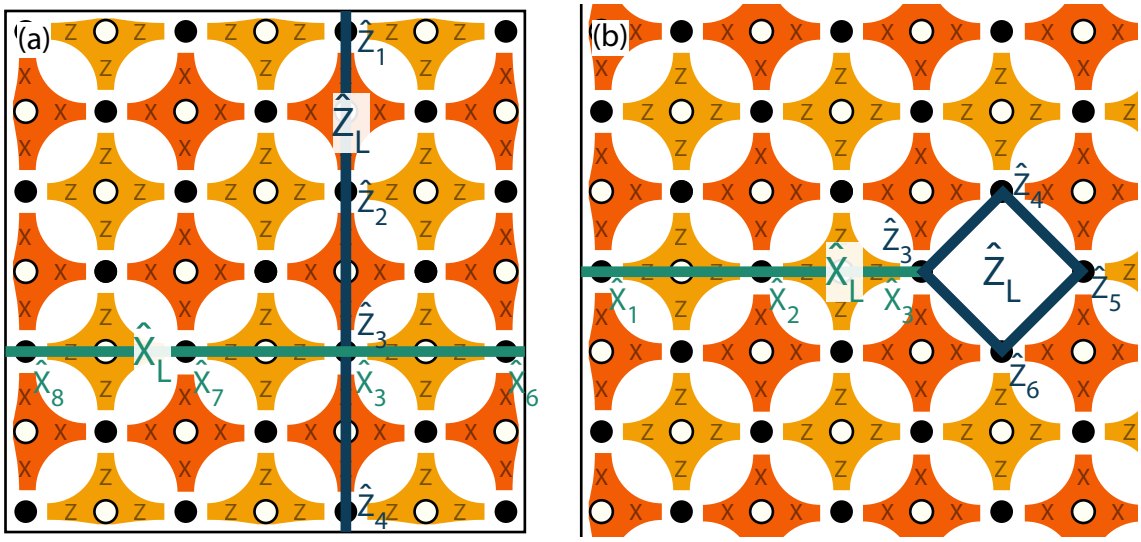

Figure 2.2: (a) The logical qubit operations of a hole-free surface code grid are simultaneous $\hat{X}$ or $\hat{Z}$ operations on all data qubits spanning from one side of the grid to the other one. It can be shown that every neighbouring chain of operators is physically equivalent to the ones highlighted. (b) shows the introduction of another logical qubit by introduction of a 'hole', i.e. the choice to not measure a Z-parity measurement qubit. The logical qubit for a Z-parity hole is a chain of $\hat{Z}$ operations around the hole and a chain of $\hat{X}$ operation to the nearest border or neighbouring hole and, as above, the choice of the exact $\hat{X}$ operation- and $\hat{Z}$ operation chain is irrelevant, as long as $\hat{Z}_{\mathrm{L}}$ circles the hole and $\hat{X}_{\mathrm{L}}$ leads to a border or another hole.

up to the edge of the surface code grid (or equivalently from the Z stabilizer hole to the nearest other logical qubit hole).

Now equipped with the ability to generate and protect logical qubits and also perform single qubit gates, the next step is to perform two qubit operations. The basic idea here is braiding, in which the hole of a logical qubit circulates another logical qubit hole, enabling logical qubit CNOT and Hadamard gates. The details of these operations are beyond the scope of this thesis and the reader is instead referred to reference [44] for further insights.

This concludes the introduction to the operation principles of the surface code. In the following section the proposal for a surface code implementation, based on solid state spin qubits is presented and its feasibility investigated.

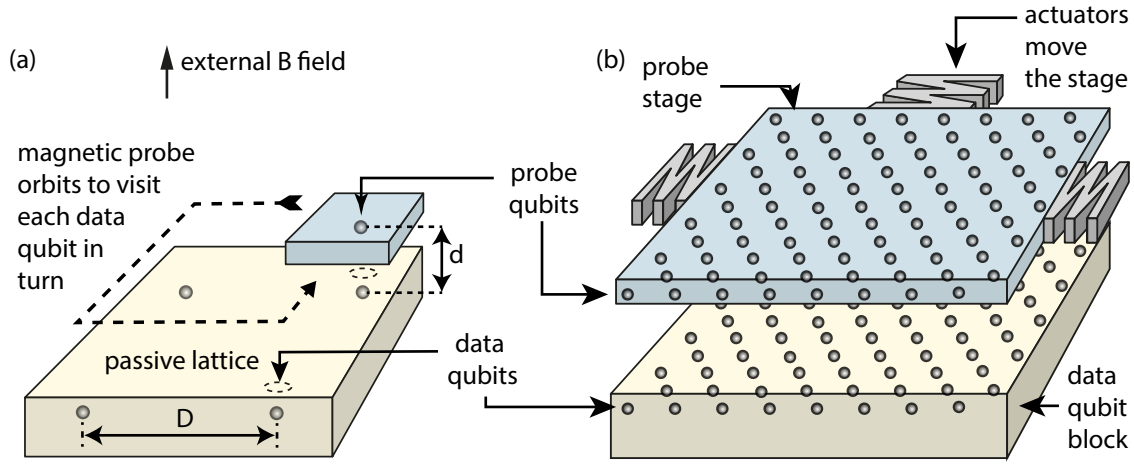

Figure 2.3: (a) The principle of the proposed stabilizer measurement via dipolar interaction. A probe spin interacts with four data qubits by orbital motion of the stage. (b) A simplified schematic of the proposed design with the probe stage motion supplied by actuating elements at the edges of the stage and the data qubit grid in a static element beneath. In fact, if advantageous, the data qubit grid may be placed on the mobile unit with the probes being static, since only their relative motion has significance.

2.3 Proposed architecture

Device design Figure 2.3 (b) shows the conceptual design of the device. The data qubit block, which carries the logical qubit state is comprised of solid state spin qubits in a grid alignment. The data qubits are required to have long coherence times, rendering donors in ^{28}Si a promising candidate for their realisation.

The second component of the device is the probe stage, whose purpose is the stabilizer parity measurement of the data qubits. To achieve this, this second grid of spin qubits is fabricated on the probe stage, which is able to modulate the dipolar interaction between the probe and data qubits by a lateral motion of the stage. In contrast to the data qubits, which only require global control, the probes need to be addressed individually, both for control and for readout. Deferring a discussion of suitable qubit system to later, it should be noted here that either NV centers in diamond or a second type of donor in silicon might be possible to form the probe stage. In order to avoid dipolar interactions between adjacent data qubits on the time scale of the stabilizer measurement it is necessary that the distance D between the data qubits is much larger than the separation d between the probe and data qubits (see Fig. 2.3(a)). A reasonable ratio D/d to avoid decoherence of the data qubits during the time scale of a parity measurement is $D/d = 7$ to 10.

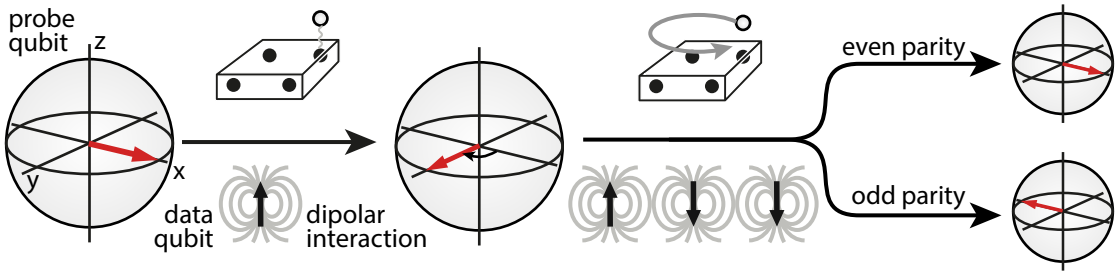

Figure 2.4: The details of the parity measurement. After probe initialisation in $|+X\rangle$, the dipolar interaction between the probe and data qubit results in a positive phase acquisition for a $|\uparrow\rangle$ data qubit, while a negative phase is acquired for a $|\downarrow\rangle$ data qubit. Timing of the interaction to allow for $\pi/2$ phase gates and subsequent interaction with all four data qubits reveals their parity: For even parity, the probe spin remains in $|+X\rangle$, while for odd parity it acquired a π-phase and is left in $|-X\rangle$.

The parity measurement With the described device, a parity measurement is carried out by a circular motion of the probe stage, bringing each probe qubit into proximity with its four surrounding data qubits (cf. Fig. 2.3(a)). The principle of the parity measurement is laid out in Figure 2.4: At the beginning of the stabilizer cycle the probe is prepared in a $|+X\rangle$ state by a locally controlled rotation, depending on the previous measurement outcome of each probe. Next, the probe qubits move into proximity with the first data qubits, where both qubits are subject to a Hamiltonian consisting of the two Zeeman terms and the dipolar interaction:

$$\mathcal{H} = \mu_{\mathrm{B}} B_z (g_1 S_z^{(1)} + g_2 S_z^{(2)}) + \frac{J}{r^3}\left(\boldsymbol{S}^{(1)} \cdot \boldsymbol{S}^{(2)} - 3(\hat{\boldsymbol{r}} \cdot \boldsymbol{S}^{(1)})(\hat{\boldsymbol{r}} \cdot \boldsymbol{S}^{(2)})\right) \tag{2.3}$$

Here, μ_{B} is the Bohr magneton, B_z is the magnitude of the magnetic field ($\mathbf{B} \parallel \hat{z}$), g_1, g_2 are g-factors of probe and data qubit, $\boldsymbol{S}$ the Pauli spin-matrices, $\hat{\boldsymbol{r}}$ and r are the unit vector connecting the two qubits and their distance and $J = \frac{\mu_0 g_e^2 \mu_B^2}{4\pi}$ is the dipolar interaction strength. For the case where the difference in Zeeman energy between the two spins is much larger than their dipolar interaction strength, flip-flops between probe and data qubits are suppressed and the Hamiltonian reduces to a very simple interaction in the rotating frame of the two spins:

$$S(\theta) = \begin{pmatrix} 1 & 0 & 0 & 0 \\ 0 & \exp(i\theta) & 0 & 0 \\ 0 & 0 & \exp(i\theta) & 0 \\ 0 & 0 & 0 & 1 \end{pmatrix} \tag{2.4}$$

$$= \left(\cos\frac{\theta}{2}\right)\mathbb{1} - i\left(\sin\frac{\theta}{2}\right) S_z^{(1)} S_z^{(2)} \tag{2.5}$$

with $\theta = \frac{J}{r^3}t$. $S(\theta)$ constitutes a two-qubit phase gate. For the probe spin prepared in $|+X\rangle$, the parity measurement is then realized as four consecutive $S(\frac{\pi}{2})$ gates, where the probe-data qubit interaction time is managed to allow for the $\theta = \frac{\pi}{2}$ phase acquisition. As shown in Fig. 2.4, $S(\frac{\pi}{2})$ leads to a positive phase acquisition on the first data qubit if the data qubit is $|\uparrow\rangle$, while it results in a negative $\pi/2$ phase acquisition for a $|\downarrow\rangle$ data qubit. Interaction with all 4 data qubits of the stabilizer thus leaves the probe spin in the $|-X\rangle$ state for odd parity, while even parity results in a $|X\rangle$ probe spin state. At the end, a projective microwave pulse and probe spin measurement reveals the four qubit parity of the data qubits along Z. The data qubits are also subject to a phase shift from the probe qubits during the interaction, but since the probe state is known, the data qubit phase shift can in fact be reversed by a global data qubit phase gate [70].

Two different kinds of stage motion are conceivable. In the first, described above, the stage moves to the first qubit, hovers over the qubit for the interaction time and then moves quickly with negligible transfer time to the next data qubit. This operation mode is the quickest, but also most likely difficult to realize mechanically. A second option is a cyclic motion, in which the stage moves slowly enough to pick up the required interaction phase during the probe transit with continuous velocity. This is a more natural operation mode for micro-mechanical systems—a simple two axis harmonic oscillation—but leads to a prolongation of the stabilizer cycle time on the order of D/d.

The surface code protocol requires the stabilizer to be measured both in the Z-basis (as described above) and in the X-basis. Fortunately, the X-stabilizer can be introduced in a very natural manner: A global Hadamard rotation of the data qubits prior to the stabilizer measurement projects the data qubit X coherence into a Z projection, where the stabilizer measurement described above reveals the parity of the initial X projection. A final global data qubit Hadamard gate restores the original data qubit projection after the X parity is revealed.

The data qubits for the X- and Z-stabilizer have to be grouped differently, as shown in Fig. 2.5. This allows for different choices of probe qubit grid layouts with their own advantages and challenges. Figure 2.5(a) describes a probe spin grid of the same density as the data qubit grid, where the same cyclic motion is performed twice. In the first cycle, only the Z-stabilizer probes are active, i.e. in the $|+X\rangle$ state, while the probe for the X stabilizer are left in, e.g. the $|\uparrow\rangle$ eigenstate. At the end of the cycle, the known phase shift caused by the inactive X-stabilizer probes can be reversed on the data qubits by a global phase shift. After this Z stabilizer, a Hadamard gate is performed on the data qubits and the X-stabilizer can be

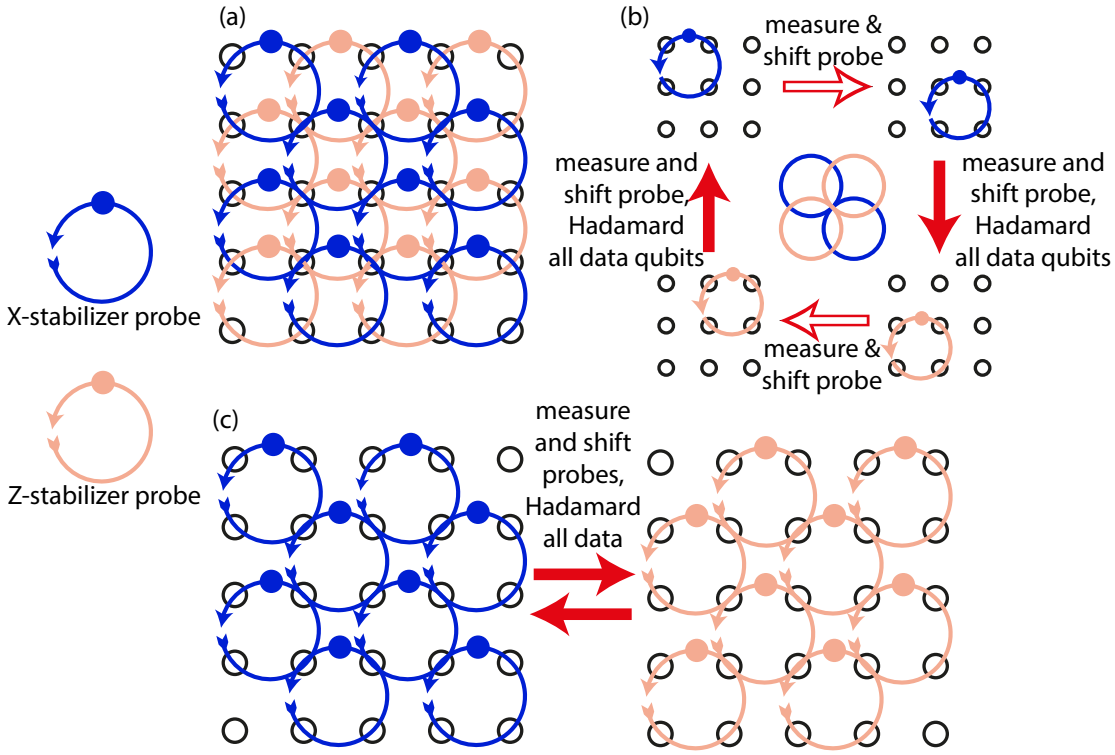

Figure 2.5: Concepts for different probe qubit grid layouts and the parity measurement operation. (a) A probe qubit grid with the same probe grid density as data qubit density is operated by a circular motion and respective deactivation of the X-parity or Z-parity probes. (b) A single probe qubit for four neighbouring parity cycles eases the fabricational demands, but adds mechanical difficulties (stage shifting motion) and increases stabilizer cycle time. (c) Compromise with the same stabilizer time as (a), but only half of the required probe qubits, which still relies on accurate stage shifts.

performed with the Z-stabilizer probe qubits now inactive. This scheme has the advantage of fast operation and simple mechanical motion, but has the disadvantage of a probe spin grid of high density with readout electronics that are redundant for half of the stabilizer cycle. In contrast Fig. 2.5(b) features only one probe spin for every four data qubits, easing the qubit density requirements. Here, the X and Z stabilizers are measured consecutively for the four neighbouring parity cycles, leading to a stabilizer cycle that is two times longer and the additional difficulty of mechanically shifting the probe stage accurately between stabilizer orbits. If this stage shifting motion is feasible, the approach of Fig. 2.5(c) with a probe spin grid density half as large as the data qubit density might offer an ideal combination of both stabilizer cycle speed and fabrication feasibility.

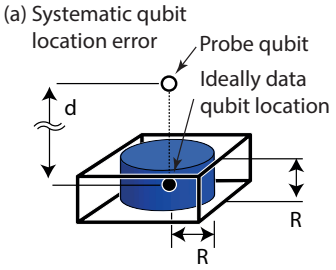

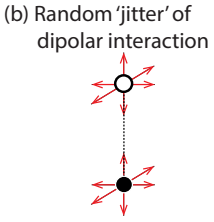

(c)

Sources of **error**	Error rate employed in simulations	Best reported experimental result in ^{28}Si
Probe preparation	1%	1% (i)
Probe measures 0	9%	4.6% (ii)
Probe measures 1	1%	1.2% (ii)
Probe rotations	0.1%	0.05% (iii)
Probe "jitter"	4.4%	–
Data qubit error	0.2%	0.05% + 0.07% (iii) (iv)

Figure 2.6: The different sources of error considered in the device simulation. (a) shows the error due to fabrication variation of the qubit location, with the example of a pill box distribution of the donor location. (b) shows the error due to random variations of the probe-data qubit interaction, for example due to imperfect stage orbits. (c) lists the qubit specific sources of errors, such as the initialisation, control and readout errors, as well as data qubit decoherence and error of the Hadamard gate during a cycle. The experimental comparision values are cited from sources (i) [24] , (ii) private communication with the author of [26], (iii) [27] and (iv) [16] .

2.4 Error threshold estimates

In order to gauge the feasibility of the proposed scheme, it is important to check the described operation of the ideal device against the various imperfections of the fabrication process, the mechanical motion, and the qubit operation. The errors considered comprise the initialisation, control and readout fidelity of the probe qubit as well as decoherence on both the data and probe qubit. Variations of the probe stage trajectories are included as variations of the probe-data qubit interaction strength between consecutive runs, an error labelled as 'probe jitter' in the following (see Fig 2.6(b)). The final error considered is the distribution of qubit locations due to errors in ion implantation (or other fabrication method). The location error leads to static imperfections of the dipolar interaction strength between probe and data qubit and thus to imperfect phase gates for every consecutive probe-data qubit interaction (cf. Fig 2.6(a)). This error type is the most specific to the proposed design and a primary objective of this discussion is to identify the tolerance of the proposed architecture against qubit placement imperfections.

A full simulation of the device, including the error sources stated above has been carried out by our collaborators Joe O'Gorman and Simon C. Benjamin from the University of Oxford and Naomi Nickerson from Imperial College London. Devices with different grid sizes are encoded with a single logical qubit and the probability of protecting the logical qubit is simulated as a function of error propability, or, more specifically, as a function of the width of the qubit location distribution. The remaining error probabilities of the simulations are chosen to be compatible with the best reported values of ^{28}Si, as listed in Fig. 2.6(c).

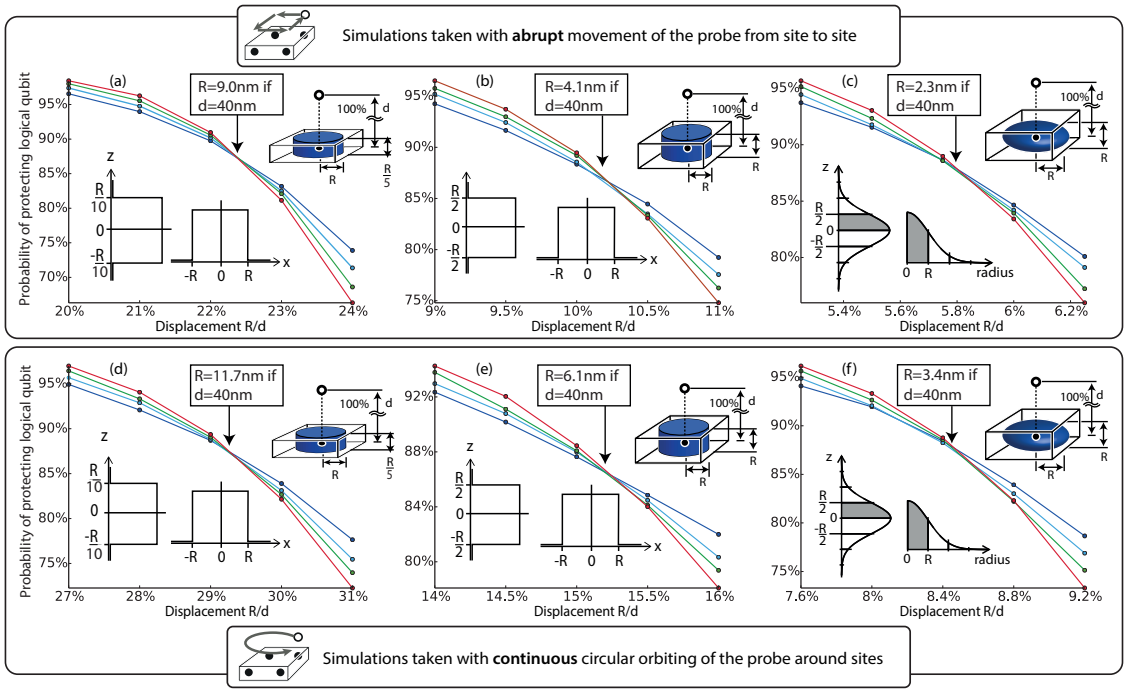

Figure 2.7: Results of the numerical device simulations regarding the threshold to fault-tolerance for the qubit distribution width. Abrupt stage motion (top row) and a continuous circular motion (bottom row) as well as three different donor distributions are considered. Flat pill-box distributions with radius R and height $R/5$ (a,d), a regular pill-box with both radius and height R and a Gaussian distribution with mean deviation of R laterally and $R/2$ vertically. The threshold values are normalized and scale linearly with the vertical probe-data qubit separation d.

2.4.1 Threshold results for the positioning

In the following the robustness of the device against qubit placement imperfections of the device fabrication are examined. For this purpose, the simulations were conducted for two types of pillbox distributions, one with the expected flat donor distribution from STML-patterned hydrogen mask lithographiy [41, 42] and the other assuming low energy implantation with a mask. Furthermore, a Gaussian distribution of donors is simulated, similar to the result of a focussed ion beam type of implantation. The results are depicted in Fig. 2.7, both for a continuous circular stage motion as wells as for an abrupt, hopping motion with negligible stage transfer times. Here, the variables R for the radius of distribution and d the vertical separation of probe and data qubits are introduced.

For surface codes, there exists a threshold in error probability, below which it is beneficial to increase the grid size, i.e., below which a larger grid results in a higher probability to protect the encoded logical qubit. This threshold point is marked by the crossing of the curves in Fig. 2.7.

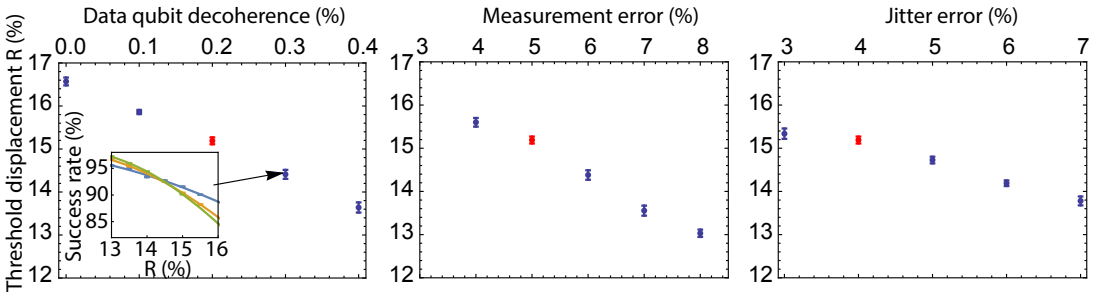

Figure 2.8: Sensitivity of the device to other sources of error. Plotted is the the displacement threshold R/d derived for the scenario of Fig. 2.7 (e) (pill-box distribution, continuous circular motion), against variations of the qubit error probabilities listed in the Table of Fig. 2.6(c).

For the donor displacement error, the most generous threshold is $R/d = 0.29$, which is found for the flat pill-box distribution and a continuous stage motion, which, as a general trend, is more lenient towards donor displacements. For the circular motion, only offsets perpendicular to the probe spin trajectory result in a faulty interaction strength, while a displacement along the path of the stage does not result in an error. For the hovering-probe qubit stage motion, displacements in all three dimensions are critical. The distribution with the greatest fabrication restriction is the Gaussian distribution, whose error threshold is as low as $R/d = 0.058$, where R is the standard deviation. For a probe to data qubit separation with sufficiently fast operation time, such as $d = 40\,\text{nm}$, the derived thresholds allow e.g. pill box distributions with diameters of 10 nm to 20 nm, compatible with fabrication methods currently being developed.

2.4.2 Sensitivity to other sources of error

The threshold accuracy of qubit placement depends of course on the other sources of error as well, i.e., the threshold value is in fact a 'team effort'. To investigate the importance of the other types of error, the threshold calculations are also carried out as a function of the data qubit decoherence, the probe qubit measurement error and the jitter error. The results are shown in Fig. 2.8. The measurement error is quite well tolerated, as is usually the case for surface codes, with even relatively high error values of $> 5\,\%$ not affecting the displacement error dramatically. The same is true for jitter error: Random fluctuations of interaction strength between data qubit and donors seem to have a relatively low impact on the threshold. This is encouraging because the accuracy of the stage motion is difficult to gauge without testing and a good tolerance to random errors in interaction strength is thus reassuring. The most crucial source of error, impacting the displacement threshold quite significantly even

at values $< 1\,\%$, is the data qubit decoherence. Fortunately, long coherence times are one of the strength of donors in ^{28}Si, with measured coherence times orders of magnitudes longer than the envisaged stabilizer cycle times of $\sim$1 ms.

2.5 Feasibility considerations

In this section, the feasibility of actually building the proposed device is considered. Questions to be answered concern whether the device operation is compatible with refocussing pulses, whether mechanical systems are conceivable to perform the probe stage motion with the required speed and accuracy and, if so, which physical qubit systems could be candidates for the probe and data qubit grids.

2.5.1 Compatibility of operation with refocussing sequences for donors

Due to the permanent nature of the donor displacement, any errors in the dipolar interaction strength between probe and data qubit are static errors. What that means is that on average, a Z stabilizer does not perfectly measure a Z parity. Crucially, a faulty Z parity measurement does lead to skewed, off-axis state projections and additional techniques have to be introduced to average out the skewed projections. The theoretical treatment of this effect is detailed in [70] and its results are summarized below. Thereafter, the compatibility of the derived parity measurements with refocussing sequences essential for the qubit operation of solid state spin qubits is discussed.

The ideal parity projector for the case of even parity is

$$\hat{P}_{\text{even}} = |0000\rangle\langle 0000| + |1100\rangle\langle 1100| + ... + |1111\rangle\langle 1111| . \tag{2.6}$$

With misaligned spins, and hence a permanently erroneous dipolar interaction, one finds that different terms in the projector acquire different weights, so that the even projector has the form,

$$\begin{aligned}\hat{P}'_{\text{even}} = A\big(\,|0000\rangle\langle 0000| \;+\; |1111\rangle\langle 1111|\,\big) + \\ B\big(\,|0011\rangle\langle 0011| \;+\; |1100\rangle\langle 1100|\,\big) + \\ C\big(\,|0110\rangle\langle 0110| \;+\; |1001\rangle\langle 1001|\,\big) + \\ D\big(\,|0101\rangle\langle 0101| \;+\; |1010\rangle\langle 1010|\,\big) + \hat{W}\end{aligned}$$

where $\hat{W}$ is a set of lower weighted projectors on odd parity states. With the constants A, B, C and D being unbalanced, each successive projection would enhance the projection into a faulty quantum state. In order to cope with this problem and effectively 'smooth out' the imbalance a 'twirling' protocol is used: By flipping

either no, two or all four data qubits randomly before and after the stabilizer cycle, the prefactors within the projection operators are interchanged, while the measurement outcome stays the same. For example, consider the twirling operator $\hat{X}\hat{X}\mathbb{1}\mathbb{1}$, applied before and after the stabilizer cycle to the data qubits. This would result in a projection measurement where now the initial states $|1100\rangle$ and $|0011\rangle$ would be associated with the A prefactor, instead of $|0000\rangle$ and $|1111\rangle$. In a similar way, other, parity-conserving unitary operations on the data qubits prior to the stabilizer cycle exchange the prefactors of other terms of the projection operator. By choosing a different twirling protocol prior to every stabalizer cycle, their prefactors are smoothened and an unbiased parity projection is ensured.

Due to this feature, the following parity measurement protocol is considered: A set of unitary single qubit flips is applied both before and after the $\hat{P}'_{\text{even}}$ projector, with the unitary operation chosen from the set $U_1 = \mathbb{1}\mathbb{1}\mathbb{1}\mathbb{1}$, $U_2 = \mathbb{1}\mathbb{1}\hat{X}\hat{X}$, $U_3 = \mathbb{1}\hat{X}\mathbb{1}\hat{X}$, $U_4 = \mathbb{1}\hat{X}\hat{X}\mathbb{1}$, resulting in the new parity projection $U_i\hat{P}'_{\text{even}}U_i$ where i is chosen at random. Instead of actually flipping data qubits, it is possible to achieve these different unitaries by flipping the probe qubit state prior to their interaction, since only the net orientation between probe and data qubits affects the CPhase gate of the parity measurement. Therefore, the protocol can be substituted with one in which the probe is subjected to a series of flips on its trajectory around its four data qubits, while the data qubits themselves are not subjected to any flips [70].

Compatibility with refocussing pulses Solid state spin qubit systems largely feature a distribution in transition frequencies that is inhomogeneously broadened. This results in a relatively short dephasing time T_2^* after which the phase coherence of an ensemble is lost. Fortunately, this transition frequency distribution is predominantely static and the coherence between the qubits can be recovered by a π-pulse, shifting the phase of the faster oscillating spins exactly by twice the phase acquired during the free evolution time up to the refocussing pulse (cf. Chapter 3.4.3). This leads to a recovery of the ensemble coherence, symmetrically around the refocussing pulse.

For donors in ^{28}Si, typical dephasing times are on the order of 10 µs, while the coherence times approach 1 s [16]. In order to benefit from the long coherence times, a pulse sequence must be found that combines both the refocussing pulses on probe and data qubits with the different twirling protocol described above. In fact, it is quite natural to combine these two, with one possible pulse sequence depicted in Fig. 2.9. By adding refocussing π pulses midway through the phase gates between

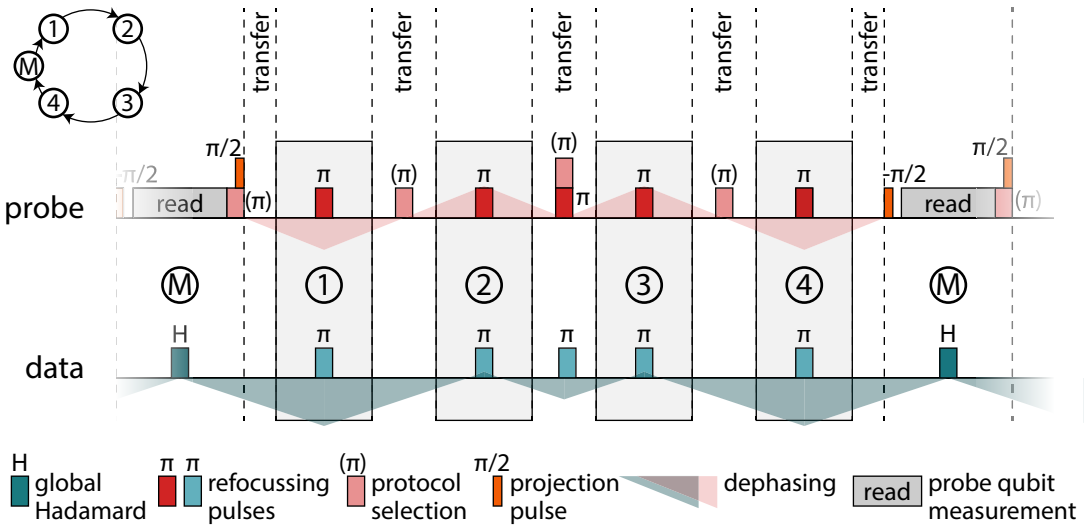

Figure 2.9: Proposed combination of the twirling protocol (π) pulses (light red) and the the refocussing pulses (dark red and blue) necessary to ensure phase coherence across all data and probe qubits at the moment of projective pulse application. The ensemble dephasing due to the transition frequency distribution is exemplified by the shaded area.

probe and data qubits it is possible to refocus the probe spin coherence for the moment of its readout. Simultaneously, it ensures that the data qubit coherence are refocussed to the point of their Hadamard gate. Since the time scale of the probe qubit measurement is likely to be significantly longer than data qubit Hadamard gate, it is furthermore necessary to add another refocussing pulse for both the probe and the data qubit, midway during the transfer from data qubit 2 to 3, to ensure the correct timing of the refocussed coherence. The twirling protocol is enacted on the probe qubits midway through transfer to the next qubit, where also the coherences match up to provide the required $\hat{X}$ operators.

The described pulse sequence is just one example and there might exist better sequences. If, for example, it is found that the error probability of the refocussing pulses is too high, then the number of refocussing pulses could be reduced by visiting all data qubits twice: During the first cycle with a phase pick-up of $S(\pi/4)$ no refocussing pulses are applied. Then at the start of the second run, both data and spin qubits are flipped, ensuring that the coherences realign after the second cycle of $S(\pi/4)$ gates, in time for the probe spin readout and data qubit Hadamard gate. This sequence would furthermore ensure that possible interactions between the probe qubits and defects on the surface of the data qubit stage are refocussed, which is true as long as the orbital path of consecutive cycles is relatively consistent.

The phase used for the refocussing pulses is a further matter to be determined. Without investigating this in detail, it could be beneficial to alterante the phase

of the refocussing pulses between X and Y, similar to the dynamical decoupling sequences XY-4 and XY-16 [76, 77]. Indeed, it might even be beneficial to replace the individual refocussing π-pulses by a whole dynamical decoupling pulse sequence, such as the aforementioned XY-4 and XY-16, acting simultaneously on the probe and data qubits. This would decouple the probe and data qubit from an even larger part of the of magnetic noise spectrum, while retaining their mutual dipolar interaction necessary for the CPhase gates.

2.5.2 Mechanical feasibility

The time required for the four $S(\pi/2)$ gates between the probe qubit and the four data qubits of the stabilizer cycle depends on the separation d as $t_{\text{int}} = 2\pi\frac{d^3}{J}$. The choice of d and D is a trade off between the smallest possible fabrication feature sizes, the achievable stage translation velocities and the decoherence time of the qubits. One 'sweet spot' for the probe-data qubit separation is $d = 40\,\text{nm}$ and $D = 400\,\text{nm}$, resulting in interaction times of $t_{\text{int}} \approx 1\,\text{kHz}$. Manufacturing precision on this length scale, although likely beyond today's capabilities, does not seem to be impossible, with e.g. hard disk manufacturers citing a read head to hard drive separation of 3 nm to 5 nm [78]. Notice also the cubic scaling of $t_{\text{int}} \propto d^3$, meaning that if, over time, the manufacturing precision increases to enable a size reduction by a factor of 2, this would allow for an eight-fold increase of operation frequency of the device.

How can the motion of the probe stage be realised in practice? The typical mechanical system that enables motions with sub-nanometer positional accuracy is the tip of an atomic force microscope cantilever. In principle, an array of tips on a single cantilever could incorporate the probe qubits and a cyclic motion of the cantilever would allow the four qubit phase gates. However, practical constraints such as height uniformity of the probe tips, might impose severe challenges to the scalability of this approach.

A more viable mechanical system could be a device similar to the x-y translation stages realised in the context of micro electromechanical systems (MEMS). These devices are often manufactured from silicon-on-insulator wafers and could exploit the uniformity of the oxide layer to achieve a high homogeneity of the probe – data qubit separation d across the grid. Various designs for MEMS x-y translation stages have been put forward with travel ranges in the 10 µm range or higher [79–81]—more than sufficient for the schemes discussed in Fig. 2.5. The standard deviation of $x-y$ positioning of these systems have been demonstrated to be in the nm regime

[82, 83], although such precision has so far only been demonstrated at low feedback loop bandwidths of 30 Hz. The motion speed of translation stages is limited by their eigenfrequency and designs with frequencies $> 10\,\mathrm{kHz}$ [84] would permit stabilizer cycle translation times on the order of $\sim 100\,\mu\mathrm{s}$. In summary, MEMS devices could be on track to enable the required fast and precise motion and individual device have already fulfilled the requirements partially. However, further work and improvements are needed to combine stages of high eigenfrequency (light weight, but stiff to avoid bending) with accurate positioning sensing and fast feedback loops.

An important question regards the electrical control of the probe qubits, which need to be individually addressed and measured. There are two basic strategies to bring the metallic leads to the stage: With the probe stage as the mobile top component, it is necessary to deliver the metallic wiring over the suspension beams at the side of the probe stage. A single large beam, at each side of the stage, runs into the problem that its spring constant scales with the cube of its width. With N probe qubits to be addressed and w as the width required for the electric leads of this qubit, the stiffness of the mobile stage against lateral translation would scale cubicly as $(Nw)^3$. In turn, to achieve the same deflection of the stage, the driving force, i.e. the voltages across the electric comb actuators would need to increase cubicly. To circumvent this scaling problem, it might be beneficial to use a multitude of thin beams. The spring constant of the multitude of beams for the in-plane motion is then simply Nw^3, scaling only linearly with N.

A different strategy might be to flip the role of the probe stage and data qubit stage, since only the relative motion between data and probe qubits is relevant. Indeed, realizing that the data qubits need to be controlled only globally, i.e. don't need any supply electronics, it seems more natural to move the data qubits to the mobile platform. However, there are also disadvantages: The fabrication of electric gates for the probe qubit control in-between the gap to the mobile stage could prove to be too difficult. A possibility to circumvent such problems could be to write the control electronics in the same process in which the probe spins themselves are placed—by relying on atomic-precise STML fabrication of phosphorous impurity SETs, gates and the probe qubit placement in a single step [42, 85].

2.5.3 Compatible solid state spin systems

The final section of the feasibility discussion addresses possible solid state qubit systems for the orbital probe architecture, namely donor impurities in silicon, NV centers in diamond and divacancy centers in silicon carbide.

For all systems, local control of the probe qubits has to be implemented. A convenient method to avoid individual microwave feedlines for each probe qubit utilizes the possiblity to Stark shift spin qubits into resonance with a globally applied background microwave field. This has been demonstrated both for donors in silicon [35, 37], for NV centers [52, 86] and for silicon carbide divacancy centers [87]. Alternatively, and maybe less elegantly, this could be achieved using magnetic field gradients, detuning the individual resonance frequencies of the probe qubit grid.

Most of the discussed systems exhibit hyperfine structure, resulting in a nuclear spin state dependence of the transition energy between the $|0\rangle$ and $|1\rangle$ state of the electron spin. This leads effectively to two or more possible 'species' of qubits, each of which must be manipulated by a microwave pulse of a different frequency. To perform the required qubit operations regardless of the nuclear spin state, it is proposed to use multi-tone microwave pulses composed of all resonance frequencies of the different species. With this it can be ensured that nuclear spin flips do not affect the proposed protocol, as long as they occur less frequently than the time for a stabilizer cycle.

In the following, the predicted performance of the different material systems is compared.

Donors in silicon Due to advanced fabrication processes and its excellent material properties, silicon is the predominant material for the realisation of high-quality MEMS devices and is a promising candidate to meet the mechanical requirements of the proposed device.

Furthermore, its qubit properties are excellent. With isotopic purification of the host lattice, the coherence times of donor electron spins in ^{28}Si approach 1 s (cf. Ch. 6.3 and [16]). This would enable very low data qubit memory error rates (sub 0.1%) over the timescale of a single parity measurement of 1.2 ms (cf. Fig. 2.6). If donors in silicon are employed as the probe qubits, then initialisation and read-out of the electron spin could be performed using spin-dependent tunnelling to a nearby reservoir and subsequent charge detection using SETs [23, 24, 26]. The average measurement fidelity has been reported as 97 % and the read-out timescale (which depends on the tunnel coupling between donor and SET and can vary dramatically) was on the order of milliseconds[3]. The single qubit control fidelity for an electron spin of a single P donor in ^{28}Si in these devices has been reported as 99.95 % [27],

[3] Although the device tolerates measurement errors quite well, it should be noted that the read-out fidelity can be further increased if, by the end of a stabilizer cycle, the electron spin state is transferred to the nuclear spin [19] from which it can then be measured with higher fidelity up to values of 99.99 % [26]. This advantage has to be traded against the cost of a longer

which could be improved even further by the use of composite microwave pulses, as done in [88]. Using dynamical decoupling sequences, a coherence time of 0.56 s has been measured for a single qubit in an electric device [26].

The footprint of the required electronic components to measure a single donor spin in silicon is typically on the order of $200 \times 200\,\mathrm{nm}^2$ [24] and is thus small enough to achieve probe qubit grid separations of $D = 400\,\mathrm{nm}$. If the required measurement temperatures on the order of 100 mK become difficult to maintain due to amount of electronic control lines and/or the actuation motion, then the alternative of bound-exciton assisted spin-to-charge conversion discussed in Ch. 5 may allow single spin detection at liquid helium temperatures where higher cooling powers are available [32].

As shown by the threshold calculations, a key figure for this scheme is the implantation accuracy achievable for the probe and data qubit arrays. Ion implantation methods with resolutions approaching 10 nm can be achieved using either e-beam lithography directly on the substrate [89, 90] or nanostencil masks drilled into AFM cantilevers [91]. For donors in silicon, these approaches can be combined with ion impact detection to ensure deterministic single qubit implantation [92]. Another technique for silicon is the STML patterning of a hydrogen mask and the subsequent exposure to phosphene gas, which enables atomically-precise ($\pm 3.8\,\text{Å}$) phosphorus donor incorporation in all three dimensions [41, 42]. This accuracy is more than an order of magnitude below thresholds of Fig. 2.7 and the challenge remaining is to maintain this precision over larger qubit arrays.

Diamond nitrogen-vacancy centers The electron spin qubit associated with the nitrogen-vacancy (NV) defect center of diamond features optically addressable spin states, which could be manipulated even at room temperature. By using resonant laser excitation and detection of luminescence photons, fast ($\sim$40 µs [93]) and reliable (measurement fidelity of 96.3 % [94]) read-out of single NV center spins could be employed for the probe spin measurement and initialisation[4]. The coherence times in isotopically purified diamond samples ($T_2 = 600\,\mathrm{ms}$ at 77 K using strong dynamical decoupling [96]) are long enough to allow millisecond long stabilizer cycles.

While the qubit operations in NV centers are advanced, so far very few micro-electromechanical devices have been realised using diamond as the main material.

measurement time: Reported times of order 100 ms are two orders of magnitude slower than discussed stabilizer cycle time.

[4]The nuclear spin of ^{14}N or of adjacent ^{13}C may again be exploited to enhance the measurement fidelity (99.6 % [95]).

Among the reported structures are resonators from single crystalline diamond-on-insulator wafers [97] and from nano-crystalline diamond [98]. In principle though, diamond possesses promising material properties for MEMS applications [99] and, given further research, could become an established material to build translation stages.

The implantation accuracy for the NV center is determined primarily by the ion beam techniques discussed above. The most accurate method uses a hole in an AFM cantilever and achieves lateral accuracies of $\sim 25\,\mathrm{nm}$ at implantation depths of $8 \pm 3\,\mathrm{nm}$ [100]. This precision is only slightly below the threshold of the proposed scheme and it is reasonable to hope that new implantation methods could meet the requirements in the near future. Furthermore, it should be noted that the proposed grid spacing of $D = 400\,\mathrm{nm}$ is well beyond the diffraction limit for optical read-out ($250\,\mathrm{nm}$ [101]).

Another critical factor for all NV centre fabrication methods is the low yield of active NV centres per implanted nitrogen atom, which is typically well below 30 % [102, 103]. Such a low yield would result in too great a number of 'dead pixels' to allow for the construction of a useful device.

While there are still significant challenges remaining to an integrated diamond MEMS probe array, it is encouraging that the basic requirement of the proposed scheme, i.e. the control of the dipolar interaction of two electron spins by means of changing their separation mechanically, has already been achieved. Grinolds *et al.* were able to sense the position and the dipolar field of a single NV centre by scanning a second NV centre in a diamond pillar attached to an AFM cantilever across it—at an NV centre separation of $50\,\mathrm{nm}$ [104].

Silicon carbide vacancy defects In addition to NV centres, divacancy defects of certain silicon carbide (SiC) polytypes exhibit optically addressable spin states suitable for qubit operation [105]. Furthermore, SiC micro electromechanical devices [106] and the required fabrication techniques have evolved in recent years, which could open up the possibility of a material with both optical qubit read-out and scalable fabrication techniques. Some important aspects of qubit operation, however, such as longer decoherence times ($1.2\,\mathrm{ms}$ [107]), improvements to the single shot qubit read-out [107]) and deterministic defect creation with high positional accuracy have yet to be demonstrated. As some of the optical transitions of SiC feature energies below the bandgap of silicon [105], SiC carbide is a good candidate for a hybrid device with both silicon qubits and optical active spins. In contrast, NV centre photo-luminescence requires lasers with energies above the bandgap of

silicon (1.7 eV to 2.5 eV [93]), which could significantly impact the silicon donor spin coherence time due to the presence of photo-carriers.

2.6 Conclusion

In summary, a concept for a universal quantum computer, based on solid state spin qubits has been proposed, relying on a four qubit parity measurement mediated by the dipolar interaction. Its device design comprises stages for data and probe qubits and its operation requires a lateral motion of the two with respect to each other. Detailed numerical simulation of the device operation using realistic qubit error rates reveal generous requirements for the qubit placement accuracy. Device-specific static errors due to qubit misplacement require the introduction of a 'twirling' mechanism, whose compatibility with the refocussing sequence has been confirmed. MEMS x-y translation stages show promising characteristics for a realisation of the concept and a review of the major solid-state qubit systems show error rates compatible with those that the simulation has been based on.

The encouraging threshold results obtained for the qubit error-rate and implantation accuracy of this novel proposal furthermore act as motivation to experimentally improve on the silicon qubit fidelity and in particular to gain a better understanding of the optical, D^0X-assisted spin-to-charge conversion in the remainder of this thesis.

Chapter 3

Fundamentals of silicon and its donors

This chapter reviews basic properties of silicon and donors in silicon. It starts with a brief discussion of the phononic band structure followed by a more detailed introduction to the electronic band structure and its properties under stress and in a magnetic field. This is followed by a discussion about donors in silicon, their energy levels and properties in a magnetic field. Thereafter, spin-resonance and the related experiments and phenomena are introduced. The last section of this chapter focusses on charge transport in silicon at low temperatures and in finite magnetic fields.

3.1 Silicon crystal structure and phonon spectrum

The crystal structure, i.e. the spatial arrangement and type of atoms in a pure solid determine fully the electronic, phononic and optical properties. For silicon, the crystal symmetry is diamond cubic with basis atoms located at $(0, 0, 0)$ and $(a_{\mathrm{Si}}/4, a_{\mathrm{Si}}/4, a_{\mathrm{Si}}/4)$, where $a_{\mathrm{Si}} = 0.543\,\mathrm{nm}$ is the lattice constant of silicon.

Physical displacements of atoms propagate through solids due to the electronic bonds between atom sides. In a quantum mechanical treatment, these displacements can be treated as particle-like excitations which are known as phonons. The bond strength and crystal structure determines the dispersion relationship between the wavelength of a phonon and its energy. Typically one observes 3 acoustical phonon branches and $(3p - 3)$ optical branches, where p is the number of atoms in the unit cell of the crystal [109]. The difference between acoustical and optical phonons lies in their phase relationship: For the acoustic branch, neighbouring atoms swing in-phase, while in the optical branch the atoms oscillate with a 180° phase shift. Each of the branches is again split into one longitudinal mode, for which the atom motion direction is parallel to the progagation direction of the wave, and two transverse modes for which the atom motion is perpendicular to the propagation direction.

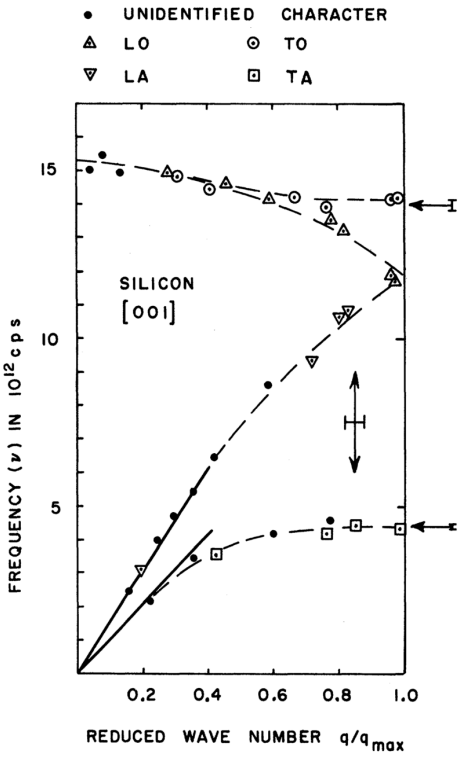

Figure 3.1: The phonon spectrum of silicon with two acoustic branches (*TA* & *LA*) with vanishing energy in the long wavelength limit ($q = 0$) and two optical branches (*TO* & *LO*) with a maximum energy at $q = 0$ of $\sim$60 meV. Figure reproduced from Brockhouse *et al.* [108].

For silicon, with $p = 2$ and diamond cubic crystal structure, both the transerse acoustic (*TA*) and transverse optical (*TO*) branch are doubly degenerate and the spectrum thus exhibits 4 branches. Figure 3.1 depicts the measured phonon spectrum of silicon. Of particular importance are the phonon values at a wavevector $q/q_{\max} \approx 0.85$, which corresponds to the momentum difference of the indirect electronic bandgap of silicon, as discussed in the next section. These values are given by $E_{\mathrm{TA}}(0.85q_{\max}) = 18\,\mathrm{meV}$, $E_{\mathrm{TO}}(0.85q_{\max}) = 58\,\mathrm{meV}$ [110] and $E_{\mathrm{LO}}(0.85q_{\max}) \approx 53\,\mathrm{meV}$, $E_{\mathrm{LA}}(0.85q_{\max}) \approx 45\,\mathrm{meV}$ [108].

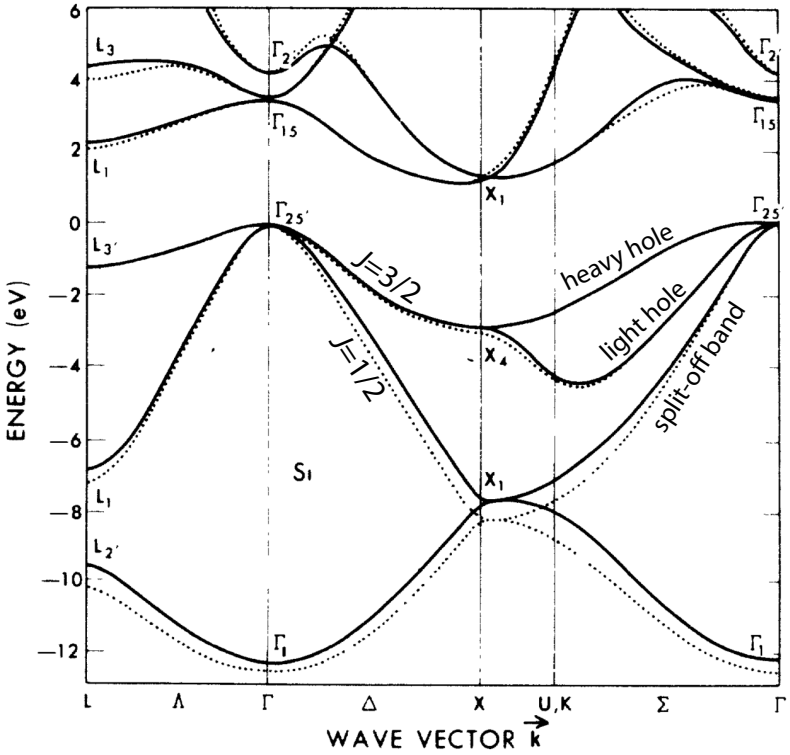

Figure 3.2: The electronic band structure of silicon. The energy scale is set to the valence band maximum and the conduction band minimium is located at $k \approx 0.85\frac{2\pi}{a_{\mathrm{Si}}}$, giving rise to an indirect bandgap of $E_{\mathrm{g}}(300\,\mathrm{K}) \approx 1.12\,\mathrm{eV}$. Heavy hole ($m_j = \pm 3/2$) and light hole ($m_j = \pm 1/2$) bands as well as the split-off band are indicated. Reproduced from Chelikowsky *et al.* [111].

3.2 Electronic band structure

The formation of energy bands, i.e. the occurrence of permitted and forbidden electron energy levels in a crystal may be explained rather intuitively. Starting at the limit where the inter-atomic spacing in the crystal is large, the permitted energy levels are simply the atomic levels of the host atoms. As the inter-atomic spacing is reduced the orbitals start to overlap and Fermi's exclusion principle forces the electrons to stay in different orbital energy levels. Bonding and anti-bonding states form. For a whole crystal with many electrons and therefore many overlapping orbitals this results in the formation of bands of allowed electron energies.

Figure 3.2 shows the silicon band structure as derived by local-pseudopotential theory[1]. The valence band maximum is located in the centre of the Brillouin zone (Γ-point) and is built from p-like states with orbital momentum $l = 1$. Due to the spin-orbit coupling of silicon, neither the spin $\mathbf{s}$ of the valence band electrons, nor

[1]The energy of the valence electrons states are calculated, while the full electron-electron and electron-core potential is replaced by a pseudo-potential of the core and the non-valence electrons

the state angular momentum $\mathbf{l}$ are good quantum numbers, but instead the valence band states are eigenfuctions of the the total angular momentum operator $\mathbf{j} = \mathbf{l} + \mathbf{s}$ [112]. Consequently, the valence band states with $J = 3/2$ are split from the $J = 1/2$ states, which are lower in energy by the spin-orbit splitting $\Delta_0 = 44\,\mathrm{meV}$ [113]. The separation of these two bands at the valence-band maximum is not visible on the scale of Fig. 3.2, but their different dispersions towards the X- and L-points are clear. In the absence of external stress, the higher energy $J = 3/2$ band is four-fold degenerate at the Γ-point and features two differently strong dispersion relations. The states with $m_j = \pm 3/2$ have a higher effective mass ($m^*_{\mathrm{hh}} \approx 0.50 m_{\mathrm{e}}$, [112]) and are called heavy-holes, while the states with $m_j = \pm 1/2$ have a smaller effective mass ($m^*_{\mathrm{lh}} \approx 0.15 m_{\mathrm{e}}$), thus called light-holes.

The conduction band minima are located along the six equivalent $\langle 100 \rangle$ directions of the crystal, close to the the X-point at the boundary of the Brillouin zone, rendering silicon an indirect semiconductor.

The bandgap of silicon, $E_{\mathrm{g}} = E_{\mathrm{CB}} - E_{\mathrm{VB}}$, is temperature-dependent. The reasons for this are firstly the smearing of the electronic potential due to electron-phonon coupling, which reduces towards lower temperatures and secondly, and to a lesser extent especially at low temperatures, thermal contraction of the lattice, reducing the lattice constant [114, 115]. At room temperature the bandgap is $E_{\mathrm{g}} \approx 1.12\,\mathrm{eV}$ and towards $0\,\mathrm{K}$ it approaches a value of $E_{\mathrm{g}} \approx 1.17\,\mathrm{eV}$ asymptotically [116]. At cryogenic temperatures the behaviour is well described by [115]:

$$E_{\mathrm{g}}(T) = E_{\mathrm{g0}} - AT^4 \tag{3.1}$$

with $E_{\mathrm{g0}} = 1.1701\,\mathrm{eV}$ and $A = 1.45 \times 10^{-9}\,\mathrm{eV/K^{-4}}$.

3.2.1 Strain induced shifts of the conduction and valence band

Application of stress to the silicon lattice results in a deformed crystal. The lower crystal symmetry has direct effects on the electronic structure and lifts the degeneracies of the six valleys in the conduction band as well as the heavy-hole, light-hole degeneracy of the valence band. In the following discussion of these effects, it is assumed that Hooke's relation between the stress and the strain tensor are known and hence the deformation, expressed as the 3×3 strain tensor ϵ is known. The diagonal components describe the principal strains along the crystallographic [100], [010] and [001] directions, while the off-diagonal components represent shear deformations.

Strained conduction band

The ground state of the unstrained conduction band can be written as a linear combination of the Bloch functions of the individual valleys:

$$\Psi(\mathbf{r}) = \sum_{i=1}^{6} \alpha^{(i)} \psi(\mathbf{k}^{(i)}, \mathbf{r}) \tag{3.2}$$

where $\alpha^{(i)}$ represents the population of the valley with wavevector $\mathbf{k}^{(i)}$.

The shift of energy of the six conduction band minima due to a strain ϵ has been investigated by Herring and Vogt [117] and can be expressed as a Hamiltonian of the form [118], acting on the six conduction band valleys:

$$H_{\epsilon\mathrm{CB}}(\epsilon) = \Xi_d \mathrm{Tr}(\epsilon) + \Xi_u \begin{pmatrix} \epsilon_{11} & 0 & 0 & 0 & 0 & 0 \\ 0 & \epsilon_{11} & 0 & 0 & 0 & 0 \\ 0 & 0 & \epsilon_{22} & 0 & 0 & 0 \\ 0 & 0 & 0 & \epsilon_{22} & 0 & 0 \\ 0 & 0 & 0 & 0 & \epsilon_{33} & 0 \\ 0 & 0 & 0 & 0 & 0 & \epsilon_{33} \end{pmatrix}. \tag{3.3}$$

Due to the symmetry of the silicon lattice, two deformation potentials Ξ_d and Ξ_u are sufficient to describe the strain-induced conduction band shifts. Literature values for Ξ_u range from 7.7 eV to 11.3 eV [118, 119], while $\Xi_d \ll \Xi_u$ is not well known [120]. Reference [119] gives a value for $\Xi_d - a \approx 1\,\mathrm{eV}$, where a is the hydrostatic deformation potential of the valence band (cf. Sec. 3.2.1).

As an example, consider a uniaxial compression of δ along [100]. Due to simultaneous expansion along the other two principle axis, the resulting strain has components $\epsilon_{11} = -\delta$, $\epsilon_{22} = \epsilon_{33} \approx 2\delta/7$ [118]. Solving Eq. 3.3 it is found that valleys in the direction of the stress, i.e. along [100] and $[\bar{1}00]$ are shifted to lower energy ($\Xi_u \gg \Xi_d$)

$$\Delta E^{(1)} = \Delta E^{(2)} \approx -\frac{3}{7}\delta\ \Xi_d - \delta\ \Xi_u\ , \tag{3.4}$$

while the valleys perpendicular to the stress direction are lifted to

$$\Delta E^{(3)} = \Delta E^{(4)} = \Delta E^{(5)} = \Delta E^{(6)} \approx -\frac{3}{7}\delta\ \Xi_d + \frac{2}{7}\delta\ \Xi_u \tag{3.5}$$

Both an absolute shift of the conduction band energy as well as a splitting of the six-fold degeneracy into a doublet and a four-fold degenerate band is found under uniaxial stress.

Strained valence band

Similarly, the valence band is subject to strain induced energy shifts. The hole-strain interaction Hamiltonian for the $J = 3/2$ valence band is described by the Pikus and Bir effective strain Hamiltonian [112, 120]

$$H_{\epsilon\mathrm{VB}} = a\mathrm{Tr}(\epsilon) + b\sum_{i=1}^{3}\left(J_i^2 - \frac{1}{3}J^2\right)\epsilon_{ii} + \frac{2d}{\sqrt{3}}\sum_{i\neq j}\left(\frac{1}{2}\left(J_iJ_j + J_jJ_i\right)\epsilon_{ij}\right) \tag{3.6}$$

a, b and d are the three valence band deformation potentials and J_i are the Pauli matrices for $J = 3/2$. Literature values for the deformation potentials are $b = -1.72\,\mathrm{eV}$, $d = -5.3\,\mathrm{eV}$ and $\Xi_d - a \approx 1\,\mathrm{eV}$ [119–122].

In the general case, $H_{\epsilon\mathrm{VB}}$ leads to a splitting between the heavy-hole and light-hole bands. The magnitude of the splitting and the energetic ordering of the bands depends respectively on the magnitude of the strain and its direction with respect to the crystallographic axes.

3.2.2 Zeeman splitting of the valence band

The valence band hole is subject to the Zeeman interaction, in the same way as any spin-carrying entity is influenced by an external magnetic field. However, for the valence band with $J = 3/2$, the Zeeman Hamiltonian is slightly more complex than for a single free electron. Due to the angular momentum dependence of the valence band the Zeeman Hamiltonian contains both isotropic and anisotropic contributions. Pikus and Bir derived the following expression based on the symmetry of the $J = 3/2$ band [123, 124]:

$$H_{\mathrm{Zeeman,VB}} = -g_1\mu_\mathrm{B}\mathbf{J}\cdot\mathbf{B} - g_2\mu_\mathrm{B}\sum_{i=1}^{3}J_i^3B_i \tag{3.7}$$

where $g_1 \approx 0.8$, is the isotropic contribution, and $g_2 \approx 0.2$, is the anisotropic contribution [123]. The g-factors of the heavy and light holes are thus different and may furthermore depend on magnetic field direction.

The full Hamiltonian for the $J = 3/2$ valence band under strain and in a magnetic field is given by:

$$H_\mathrm{VB}(\epsilon, \mathbf{B}) = H_{\epsilon\mathrm{VB}}(\epsilon) + H_{\mathrm{Zeeman,VB}}(\mathbf{B}) \tag{3.8}$$

3.3 Shallow donors in silicon

The group V elements (P, As, Sb & Bi) with the exception of nitrogen[2] act as substitutional donors in silicon, i.e. they replace a silicon atom in the lattice. The additional electron, unpaired in the lattice configuration, is loosely bound to the donor. The following section first reviews the calculation of the donor energy spectrum, then discusses the effects of stress on the donor energy and finally discusses the spin-related donor level splitting due to the electron and nuclear Zeeman interaction and the hyperfine interaction.

3.3.1 Donor binding energy and excited states

The available theoretical treatments for the ground and excited states of a donor can roughly be divided into three categories. The first category is a simplistic model with the Hamiltonian and energy levels similar to the hydrogen atom, but scaled for the dielectric constant of silicon and effective mass of the conduction band electron [112, 120]. A more involved model is the multi-valley effective mass theory (EMT) which takes into account the periodic potential of the conduction band and treats the donor as a screened Coulomb potential with a central cell correction to modify the potential in the vicinity of the core. These calculations permit a fairly intuitive picture of the physical principles and have proven succesful to fit many experimental results, such as ESR spectra under strain [126], the Stark parameter of shallow donors [35, 36] and recently also the wavefunctions of donors [127]. The third group of donor models are tight-binding calculation, i.e. ab-initio calculations based on the atomic orbitals of the involved valence electrons and possibly also a number of non-valence electrons. This approach is very computationally demanding and the underlying physical phenomena are thus at times difficult to extract. However, these calculations are able to deliver very accurate results and predictions, with a highlight being the astonishing match of calculated and measured phosphorous donor wavefunction [128].

For the purposes of this thesis, the simple effective mass approach first introduced by Kohn and Luttinger [129] is sufficient and the main results are reviewed here.

The starting point of effective mass theory is the decomposition of the donor state wave function $\Psi(\mathbf{r})$ into the fast oscillating contributions from the Bloch functions $\psi(\mathbf{k}^{(i)}, \mathbf{r}) = u^{(i)}(\mathbf{r}) \exp\left(i\mathbf{k}^{(i)}\mathbf{r}\right)$ of the six conduction band minima $i = 1..6$ and a

[2]Nitrogen is electrically inert in silicon and believed to either form Si_3N_4 or remain as N_2 at interstitial sites [125].

slowly varying envelope function $F^{(i)}(\mathbf{r})$, localizing the electron at the donor site:

$$\Psi^{(i)}(\mathbf{r}) = \sum_{i=1}^{6} \alpha^{(i)} F^{(i)}(\mathbf{r}) \psi(\mathbf{k}^{(i)}, \mathbf{r}) \tag{3.9}$$

It can be shown that the envelope function of each valley $F^{(i)}(\mathbf{r})$ must then satisfy an equation of the form [112, 129, 130]

$$\left[-\hbar^2 \left(\frac{2\nabla_{i,l}^2}{m_t} + \frac{\nabla_{i,l}^2}{m_l} \right) - eU(\mathbf{r}) \right] \alpha^{(i)} F^{(i)}(\mathbf{r}) = \varepsilon^{(i)} \alpha^{(i)} F^{(i)}(\mathbf{r}) \tag{3.10}$$

where $\varepsilon^{(i)}$ is the energy eigenvalue and $\nabla_{i,l}$, $\nabla_{i,t}$ are the components of the ∇ operator projected along the longitudinal and transverse direction of valley i respectively. The choice of $U(\mathbf{r})$ is the critical part of effective mass theory. For long ranges the potential assumes a screened coulomb potential $U(\mathbf{r}) \approx -e^2/(4\pi\epsilon r)$, but it is the deviations from this potential, i.e. the central cell correction that is critical for the correct binding energies of the donor. $U(\mathbf{r})$ leads to off-diagonal interaction terms that couple the wavefunctions of different valleys, which is known as valley-orbit scattering [129, 130].

For the purposes of this thesis a phenomenological treatment of the resulting Hamiltonian for the conduction valley energies in the valley basis $+x, -x, +y, -y, +z, -z$ is sufficient. Following Wilson *et al.* the Hamiltonian (3.10) reduces to the following form [118]:

$$H_{\mathrm{D}^0,\,\mathrm{EMT}} = \begin{pmatrix} E_0 & \Delta_1 & \Delta_2 & \Delta_2 & \Delta_2 & \Delta_2 \\ \Delta_1 & E_0 & \Delta_1 & \Delta_2 & \Delta_2 & \Delta_2 \\ \Delta_2 & \Delta_1 & E_0 & \Delta_1 & \Delta_2 & \Delta_2 \\ \Delta_2 & \Delta_2 & \Delta_1 & E_0 & \Delta_1 & \Delta_2 \\ \Delta_2 & \Delta_2 & \Delta_2 & \Delta_1 & E_0 & \Delta_1 \\ \Delta_2 & \Delta_2 & \Delta_2 & \Delta_2 & \Delta_1 & E_0 \end{pmatrix} \tag{3.11}$$

where E_0 is the unperturbed energy of the conduction band valleys and Δ_2 and Δ_1 represent the valley-orbit terms between the orthogonal and non-orthogonal valleys, respectively. Pursuing a phenomenological approach, E_0, Δ_1 & Δ_2 are fitted to the experimental donor binding energies of reference [131] and receive the fitted parameters of Table 3.1. Figure 3.3 summarizes the binding energies of various shallow donors in silicon.

The corresponding donor ground and excited state wavefunctions can be deduced from symmetry arguments [118]: The presence of the impurity in the silicon lat-

	$E(A_1)$	$E(E)$	$E(T_2)$	E_0	Δ_1	Δ_2
^{31}P	−45.31 meV	−32.36 meV	−33.69 meV	−35.4 meV	−1.51 meV	−2.17 meV

Table 3.1: Experimentally obtained binding energy and excited levels of phosphorus in silicon [131] and the fitted valley-orbit Hamiltonian parameters for Eq. (3.11).

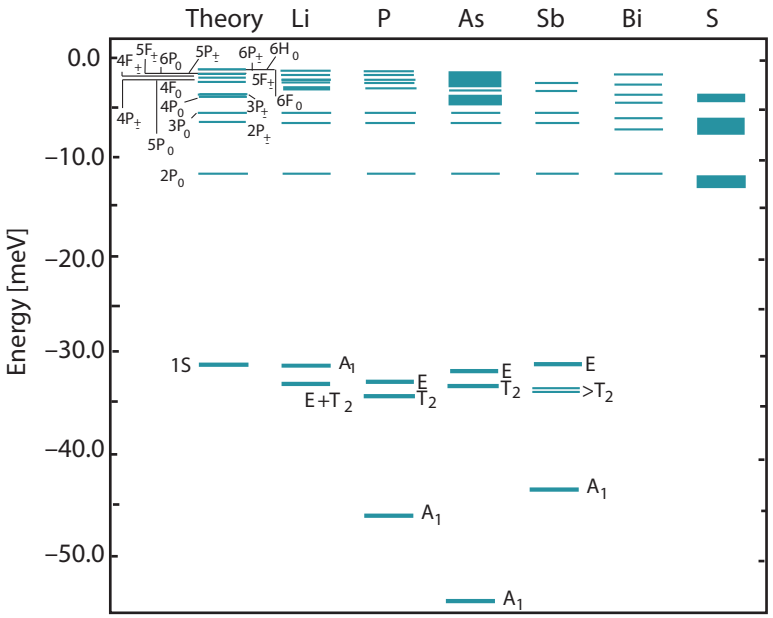

Figure 3.3: The ground and excited state energies of various shallow donors in silicon. Energies are with respect to the conduction band minimum. The ground state of Bismuth is located below the y-axis scale at −70.98 meV [132]. Figure reproduced from reference [112].

tice changes the system symmetry from a qubic symetry to a tetrahedal symetry. Therefore, the six-fold conduction band degeneracy is expected to split into new states, explicitly a singlet state A_1, a doublet E and a triplet T_2. Of these, only the singlet state wavefunction has a finite amplitude at the impurity nucleus, which leads to a depression of the singlet in energy with respect to the doublet and triplet [129]. The donor wavefunctions of the ground and excites states in the valley basis

are given by:

$$\begin{aligned}
&\text{Singlet } (1\text{sA}_1)\left\{\ \alpha_1 = \tfrac{1}{\sqrt{6}}(1,1,1,1,1,1)\right.\\
&\text{Doublet } (1\text{sE})\left\{\begin{array}{l}\alpha_2 = \tfrac{1}{2}(1,1,-1,-1,0,0)\\ \alpha_3 = \tfrac{1}{2}(1,1,0,0,-1,-1)\end{array}\right.\\
&\text{Triplet } (1\text{sT}_2)\left\{\begin{array}{l}\alpha_4 = \tfrac{1}{\sqrt{2}}(1,-1,0,0,0,0)\\ \alpha_5 = \tfrac{1}{\sqrt{2}}(0,0,-1,-1,0,0)\\ \alpha_6 = \tfrac{1}{\sqrt{2}}(0,0,0,0,-1,-1)\end{array}\right.
\end{aligned}$$

As discussed in Section 3.2.1, external stress can lift the degeneracy of the six conduction band minima. In this case, the valley energies E_0 of (3.11) have to be replaced with the respective strained energy levels $E^{(i)} = E_0 + \Delta E^{(i)}$ (cf. Eq. (3.4) & (3.5)). The donor Hamiltonian in the presence of strain is thus:

$$H_{\text{D}^0}(\epsilon) = H_{\text{D}^0,\,\text{EMT}} + H_{\epsilon\text{CB}}(\epsilon) \tag{3.12}$$

The general solution of the strained donor Hamiltonian is a mixing of the ground state with the excited donor states, with a redistribution of valley population towards lower energy valleys and a shift of the donor energies $E(1\text{sA}_1)$, $E(1\text{sE})$ and $E(1\text{sT}_2)$.

3.3.2 Zeeman and hyperfine interaction

As discussed above, the unpaired donor electron is loosely bound to its positive nucleus and its wavefunction overlaps in the donor ground state with the nucleus. In an external magnetic field, this donor electron is thus subject to the Zeeman interaction. Furthermore, all group-V elements carry nuclear spin, resulting in further terms in the Hamiltonian due to the nuclear Zeeman and hyperfine interaction. The nuclear quadrupole interaction has an additional (but small) contribution in nuclear spin resonance [133], but is chosen to be neglected here. Both the g-factors and the hyperfine interaction are isotropic for donors in silicon and can be expressed by a scalar quantity and thus it is possible to write the spin Hamiltonian of a donor as:

$$H/h = \gamma_{\text{e}}\mathbf{SB} - \gamma_{\text{n}}\mathbf{IB} + A\mathbf{SI} \tag{3.13}$$

It is often more intuitive to discuss spin resonance phenomena in frequency units (Hz), hence the Hamiltonian has been divided by the Planck constant h. The first

	^{31}P	^{75}As	^{121}Sb	^{123}Sb	^{209}Bi
Electron spin number S	1/2	1/2	1/2	1/2	1/2
Nuclear spin number I	1/2	3/2	5/2	7/2	9/2
Electron gyromagnetic ratio γ_e (GHz/T)	27.972	27.970	27.973	27.973	27.997
Nuclear gyromagnetic ratio γ_n (MHz/T)	17.23	7.3	10.26	5.6	6.9
Hyperfine interaction A (MHz)	117.53	198.3	186.8	101.5	1475.2

Table 3.2: The spin parameters of group-V donors in silicon [17, 134, 135].

term on the right hand side is the electron Zeeman interaction between a spin-1/2 with Pauli matrices vector **S** and an external magnetic field **B**. The prefactor is the gyromagnetic ratio, which determines the rotation frequency of the spin in an external magnetic field $f_\mathrm{L} = \gamma_\mathrm{e}|\mathbf{B}|$. It is related to the electron g-factor g_e via the Bohr magneton μ_B as $\gamma_\mathrm{e} = g_e\mu_\mathrm{B}$. Similarly, the second term is the nuclear Zeeman interaction with the nuclear gyromagnetic ratio $\gamma_\mathrm{n} = g_n\mu_\mathrm{n}$ defined by the nuclear g-factor and the nuclear magneton. **I** is the vector of the Pauli matrices of the nuclear spin, whose dimension depends on the nuclear spin number I.

The last term is the hyperfine interaction between the electron and nuclear spin whose strength is given by hyperfine constant A. A is proportional to the overlap of the electron and nuclear wavefunctions, and since the nuclear spin wavefunction is essentially a δ-function, A depends on the electron wavefunction at the nuclear core. Electric fields are able to distort the electron wavefunctions, leading to a reduction of the hyperfine constant, which is visible as shifts in the transition frequency [35, 37, 136].

Table 3.2 summarizes the various spin Hamiltonian parameters for the group-V donors. Section 3.4 discusses the details of the solutions to the spin-Hamiltonian, the allowed transitions and the use of donor states as qubits.

3.3.3 Summary

Figure 3.4 summarizes the various influences on the energy of the donor and valence band discussed over the last two sections. The valence band consists of the split-off ($J = 1/2$) and the heavy-hole and light-hole bands ($J = 3/2$, $m_{j,\mathrm{hh}} = \pm 3/2$, $m_{j,\mathrm{lh}} = \pm 1/2$). The conduction band minima are sixfold degenerate at finite k. The donor ground state $1\mathrm{sA}_1$ is composed of equal contributions from all six minima and its electron is weakly bound. Under stress, the strain ϵ splits the degenerate heavy- and light-hole band and also causes repopulation and mixing of the donor ground and excited states. The hyperfine interaction A splits the donor ground state due

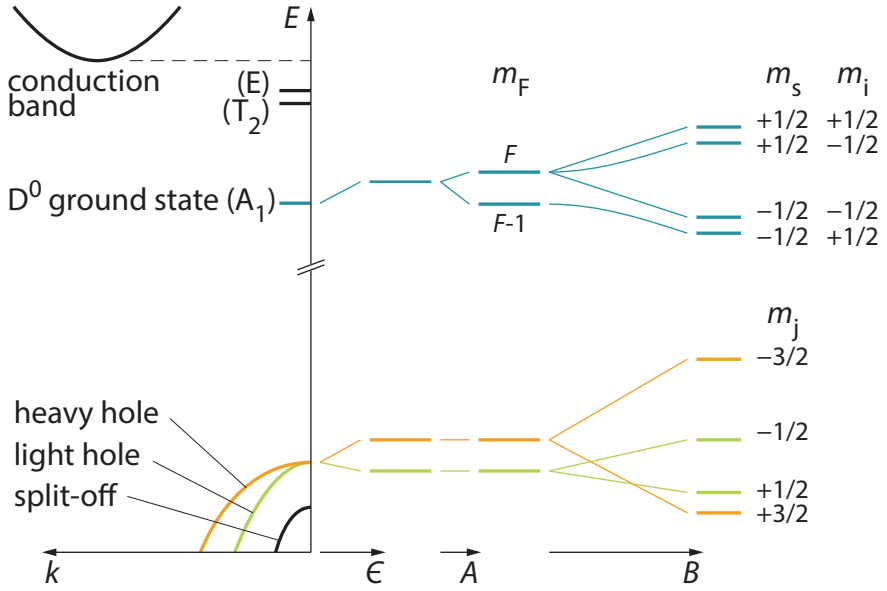

Figure 3.4: A summary of the observed shifts of the donor and valence band with strain ϵ, hyperfine constant A and magnetic field B. A phosphorus donor ($I = 1/2$) is used in this example.

to a finite nuclear spin I and an external magnetic field B furthermore lifts donor and valence band spin-degeneracies via the Zeeman interaction.

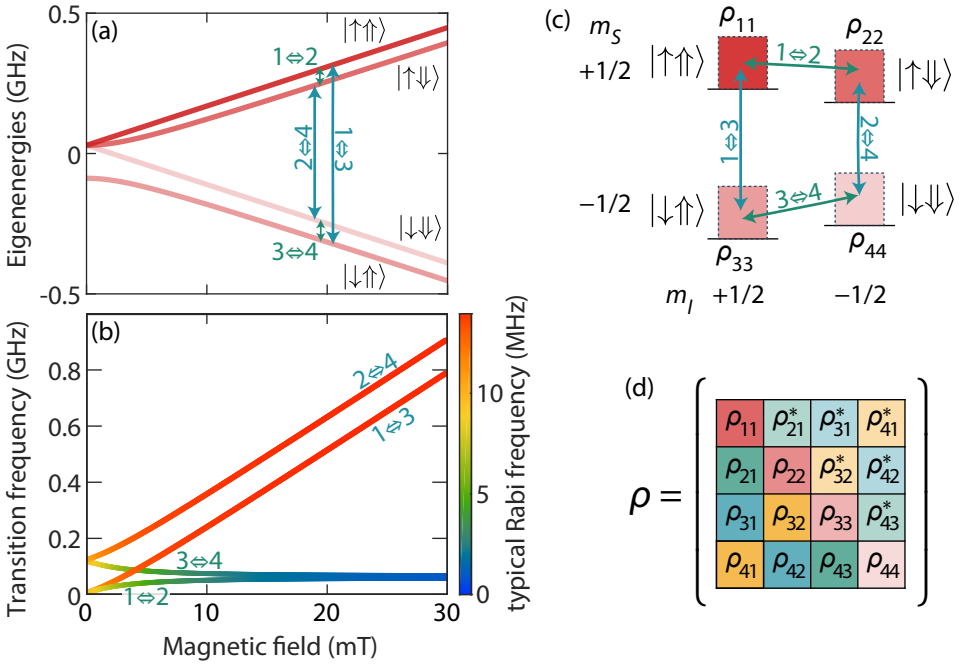

Figure 3.5: The ESR and NMR transitions of phosphorus in silicon as a function of magnetic field. (a) The low-, intermediate- and high-field region of the phosphorus spin-Hamiltonian and the energy and labelling of the four eigenstates. (b) The frequencies of the four dipole-allowed transitions and their respective typical Rabi frequency following Eq. (3.19) with $|\mathbf{B}_{\mathrm{mw}}| = 1\,\mathrm{mT}$. (c) The energy level diagram in the high-field limit where m_s and m_i are good qunatum numbers. The dipole-allowed ESR- (blue) and NMR-transitions (green) are labelled. (d) A diagram of the density matrix of the phosphorus spin system with the populations on the diagonal (red) and, off-diagonally, the indications for electron spin- (blue), nuclear spin- (green) and zero- and double-quantum coherences, i.e. Bell states (yellow).

3.4 Spin resonance of neutral donors in silicon

This section introduces the theoretical description and the pulse sequences of common electron spin resonance experiments. First, the quantum mechanical description using the density matrix is introduced, followed by a discussion of the allowed transitions between spin-states. At the end, common electron spin resonance experiments are listed and the relevant decoherence and relaxation mechanisms for donor spins in silicon are reviewed.

3.4.1 Density matrix representation

The solution of the donor spin-Hamiltonian (Eq. (3.13)) features $2I+1$ eigenstates. In the following, the discussion is restricted to phosphorus as a donor with $I = 1/2$, but can readily be extended to the other silicon donors with larger I.

Figure 3.5(a) shows the eigenenergies of the four phosphorus spin eigenstates as a function of magnetic field. In the low field limit, the total spin $F = S + I$ is a good quantum number, featuring a triplet for the $F = 1$ states and a singlet for $F = 0$. In the high field limit, the electrons spin and nuclear spin state m_s and m_i are good quantum numbers and an energy level diagram with the states nomenclature of Fig. 3.5(c) can be drawn. Due to the selection rules for magnetic transitions, $\Delta m = \pm 1$, four different transitions are possible. The vertical, higher frequency transitions ($1 \Leftrightarrow 3$ & $2 \Leftrightarrow 4$) are labelled ESR (electron spin resonance) transitions since they involve electron spin rotations. The lower-frequency, horizontal transitions are the NMR (nuclear magnetic resonance) transitions involving nuclear spin flips ($1 \Leftrightarrow 2$ & $3 \Leftrightarrow 4$) .

In general, state vectors $|\psi\rangle$ are not suitable for the quantum mechanical description of ESR experiments on spin ensembles since state vectors may only represent pure quantum mechanical states. ESR experiments are, however, predominantly conducted on the thermal state of spin ensembles which is a probabilistic ensemble of individual pure states, i.e. a mixed quantum state [71]. In contrast to pure quantum states, mixed states can only be treated using the density matrix representation. A density matrix is defined as the sum of the outer product of the individual spin states $|\psi_i\rangle$ found in the ensemble with respective probability p_i [71, 137]:

$$\rho = \sum_i p_i \left|\psi_i\right\rangle \left\langle\psi\right| = \begin{pmatrix} \rho_{11} & \rho_{12}^* & \rho_{13}^* & \rho_{14}^* \\ \rho_{21} & \rho_{22} & \rho_{23}^* & \rho_{24}^* \\ \rho_{31} & \rho_{32} & \rho_{33} & \rho_{34}^* \\ \rho_{41} & \rho_{42} & \rho_{43} & \rho_{44} \end{pmatrix} \tag{3.14}$$

The off-diagonal terms of the density matrix describe the relative populations of the four eigenstates and hence the trace of the density matrix equals to one ($\mathrm{Tr}\,(\rho) = 1$). The diagonal terms indicate coherences between states, i.e. signalize that a (sub-) set of donors is in a superposition of two or more states. In a way, the density matrix representation is also a more intuitive representation of the quantum state, since the eigenstates are more closely related to their operators. Take for example the eigenstate of a single spin to the S_y operator. In the usual S_z basis, the state vector has the form $|i\rangle = 1/\sqrt{2}\,(|\uparrow\rangle + i\,|\downarrow\rangle)$. The corresponding density matrix of $|i\rangle$ is simply $\mathbb{1}/2 + S_y$, with the non-identity component of the matrix directly indicating the operator corresponding to the its spin state. Analogously, $|-i\rangle$ is simply $\mathbb{1}/2 - S_y$ and the same is true for the eigenstates of S_z and S_x, as well as for multi-spin systems. In fact, any pure state of a single spin may be represented by a

linear combination of the Pauli matrices as $\rho = \mathbb{1}/2 + \mathbf{rS}$, where $\mathbf{S}$ is the vector of Pauli matrices and $\mathbf{r}$ is the well-known Bloch vector in Cartesian coordinates [71].

The time evolution of the density matrix (i.e. the equivalent of the time-dependent Schrödinger equation) is the Liouville-von Neumann equation:

$$i\hbar\frac{\partial\rho}{\partial t} = [\mathcal{H}(t), \rho(t)] \tag{3.15}$$

If the Hamiltonian $\mathcal{H}$ is time-independent ($\mathcal{H}_0$) then this equation has the formal solution

$$\rho(t) = e^{-i\mathcal{H}_0 t/\hbar}\rho(0)e^{i\mathcal{H}_0 t/\hbar} = U(t)\rho(0)U^\dagger(t) \tag{3.16}$$

where the propagation operator $U(t)$ has been introduced.

Rotation of the Hilbert space such that the Hamiltonian $\mathcal{H}_0$ is diagonal reveals that the off-diagonal components of the density matrix evolve as [137]:

$$\rho_{kl} = \exp(-i(\mathcal{H}_{0,kk} - \mathcal{H}_{0,ll})t)\rho_{kl}(0) = \exp(-i\omega_{kl}t)\rho_{kl}(0) \tag{3.17}$$

The off-diagonal components thus acquire phase at the rate of the energy separation between the two involved states. This means that e.g. an initial S_x state rotates to S_y, $-S_x$, $-S_y$ and back to the initial S_x state, which can be visualized by a precessing spin on the Bloch sphere with an angular velocity equal to the energy separation.

The resulting time dependence of the density matrix evolution in a static Hamiltonian can be mathematically simplified by a change of reference frame to a rotating coordinate system (for the single spin case) or by using the interaction picture of quantum mechanics for more complicated static Hamiltonians, which both eliminate the time dependence of the off-diagonal components.

3.4.2 Spin state transitions

Transitions between spin states can be driven by a small oscillating magnetic field[3] $\mathbf{B}_1(t) = \cos(\omega_{\mathrm{mw}}t)\mathbf{B}_{\mathrm{mw}}$ perpendicular to the stronger eigenstate-defining static magnetic field B_0. In the lab frame $\mathbf{B}_1$ is oscillating with linear polarisation. In the rotating frame of a single spin, however, $\mathbf{B}_1$ may be decomposed into a static part and a fast ($2\omega_{\mathrm{mw}}$) oscillating part. Neglecting the latter due to its minor influence ("rotating wave approximation"), it can be seen that in the rotating frame again a

[3] A second source of transitions could be oscillating electric fields. These modulate the hyperfine constant periodically enabling electrically driven as e.g. shown in [49].

constant magnetic field exists. Consequently, in the rotating frame the spin starts rotating around the microwave magnetic field vector and hence a transition from e.g., S_z over S_x to $-S_z$ is occurring for a microwave field with phase along $\hat{x}$ of the rotating frame.

The exact solution of the density matrix evolution of an arbitrary spin-system to an oscillating magnetic field is quite complicated [137]. Given that the initial and final state are sufficiently separated in energy from other transitions (i.e. under the assumption that no other transitions are excited by the bandwidth of the pulse), the problem may effectively be reduced to the dynamics of an effective two-level, single spin system and the simple rotating frame picture for the spin transition discussed above is valid [138, 139]. The strength of the transition, i.e. the Rabi frequency with which the system oscillates between the two involved levels (assuming resonant driving) is given by [138]:

$$\Omega_{\mathrm{R}} = \langle \psi_2 | \hat{W} | \psi_1 \rangle / \hbar \tag{3.18}$$

$$\hat{W} = (\gamma_{\mathrm{e}} \mathbf{S} - \gamma_{\mathrm{n}} \mathbf{I}) \mathbf{B}_{\mathrm{mw}} \tag{3.19}$$

Here, $\hat{W}$ is the amplitude of the time-dependent part of the Hamiltonian (3.13) subject to $\mathbf{B}_1(t)$. It is evident that $\hat{W}$ must contain off-diagonal elements in order to allow for transitions between different initial and final eigenstates ψ_1 & ψ_2, requiring $\mathbf{B}_{\mathrm{mw}}$ to be perpendicular to the eigenstate-defining, static magnetic field $\mathbf{B}_0$.

Figure 3.5(b) plots the transition frequencies and respective Rabi frequencies following Eq. (3.19) for all four transitions of phosphorus as a function of magnetic field. In the high field limit, two different sets of transition exists. The ESR transitions with larger transition frequency feature relatively fast Rabi oscillations due to the stronger electron gyromagnetic ratio γ_{e}. In contrast, the NMR transitions can only be driven much more slowly and have typical π-pulse durations of $\sim$5 µs.

3.4.3 Spin echo and common ESR sequences

Due to the imperfect solid-state host lattice, with impurities (being in a charged/neutral state and possibly carrying a magnetic moment) and local strain variations, (modifying the hyperfine constant), each donor of the spin ensemble is exposed to a slightly different electric and magnetic field environment. Furthermore, the external magnetic field may be inhomogeneous, which, together with the aforementioned local field variations, leads to a distribution of spin precession frequencies, i.e. an

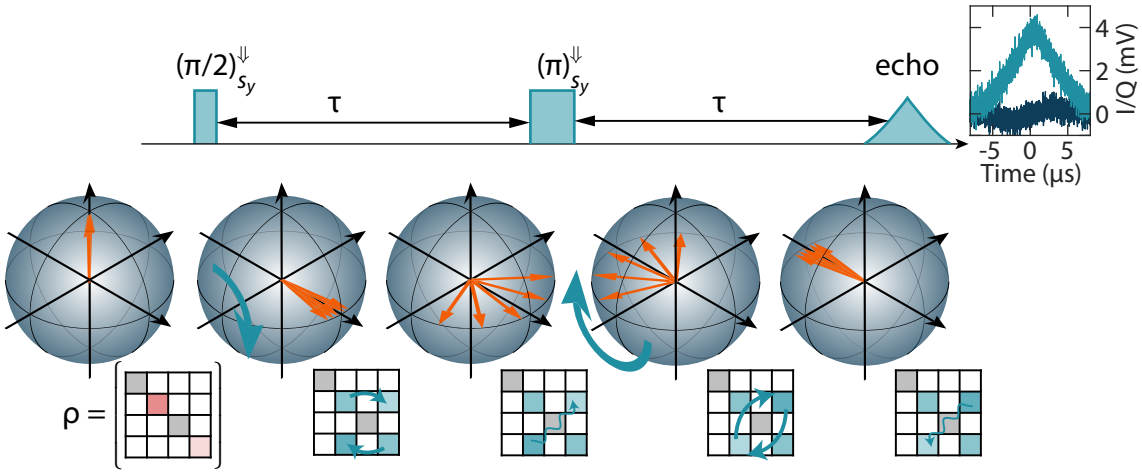

Figure 3.6: A sketch of a Hahn echo sequence, performed on the $m_I = -1/2$ ESR transition of the phosphorus donor. The microwave pulse sequence is depicted on top with an experimentally obtained echo signal in the I-channel of the IQ mixer. The diagrams below show the Bloch sphere dynamics and the involved density matrix components of the spin ensemble.

inhomogeneously broadened linewidth[4]. The associated time constant describing the decay of the macroscopic magnetisation of a precessing spin ensemble is called dephasing time T_2^* and is, for silicon donors, usually in the range of ∼100 ns up to several µs.

Since the distribution of frequencies is static, a pulse sequence may be used to negate its effect and hence the time-scale on which information may be stored in donor electron spins can be prolonged by several orders of magnitude. These sequences consist of a series of microwave (π)-pulses and are called refocussing sequences or dynamical decoupling sequences. The simplest dynamical decoupling sequence, with just a single (π)-pulse, is the Hahn spin echo and its pulse sequence and influence on the spin-state of the spin-ensemble, as well as the density matrix is depicted in Fig. 3.6.

The sequence starts with a single $(\pi/2)^{\Downarrow}_{S_y}$ microwave pulse, here acting as an example on the phosphorus $m_I = -1/2$ transition and with phase to rotate around the $+y$-axis of the Bloch sphere. With the spins projected into the equatorial plane of the Bloch sphere, the ensemble precesses at slightly different rotation frequencies, which, in the rotating frame of the mean ensemble precession, manifests itself as a dephasing and spread of the donor spins. The refocussing $(\pi)^{\Downarrow}_{y}$ pulse can be interpreted as a reflection of the spin system at the $y - z$ plane, and hence those

[4]Even for a single donor qubit, imperfections of the silicon host lattice such as nuclear spin-flips or trap charging may modulate the single spin precession frequency within a certain time frame, leading to a temporal instead of spatial inhomogeneous broadening [26].

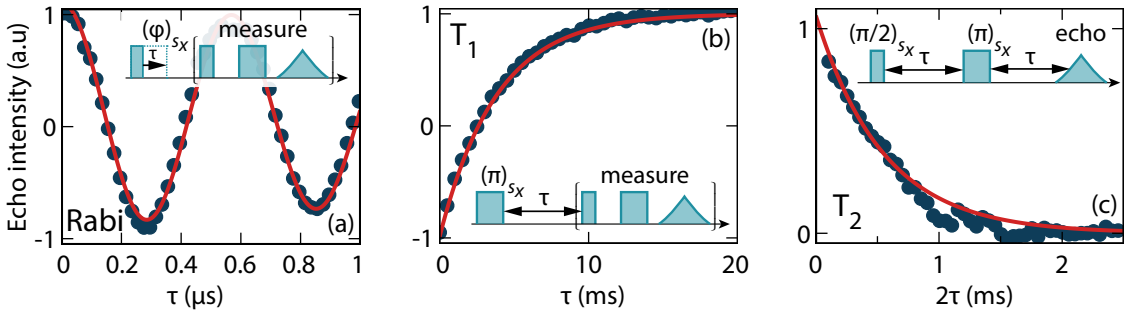

Figure 3.7: Sketch of common ESR sequences and the obtained data. (a) Rabi oscillations are signatures of coherent oscillations between the two eigenstates, which decay over time due to a finite T_2^* and can be fitted by a combination of cosine and exponential decay. (b) T_1 inversion recovery experiment with an exponential relaxation back to thermal equilibrium. (c) Hahn echo coherence time measurement, with a decoherence process-dependent lineshape. The data here is affected at ∼1 ms due to phase noise by an unstable magnet (cf. Ch. 6.3).

spins that showed a positive phase accumulation compared with the rotating frame in the first part of the sequence are now lagging exactly that phase compared to the mean phase of the spin-ensemble. In the free evolution of the second part of the pulse sequence, the accumulated phase of the first part is neutralized and at a certain point in time, all ensemble spins refocus and give rise to a finite magnetisation. This finite in-plane, precessing magnetisation emits microwave photons which are picked up by the resonator, amplified and IQ-mixed (cf. Ch. 4.2.3) and thus give rise to the depicted spin echo. The echo intensity depends on the difference between $|\uparrow\rangle$ and $|\downarrow\rangle$, i.e. the spin polarization and is hence extensively used in ESR experiments, simply as a final "measure-S_z" block of the pulse sequence.

In the following three different typical ESR pulse sequences are introduced and the role of their measured quantities is discussed:

Rabi oscillations Rabi oscillations are the signature of coherent driving of a spin system. The pulse sequence (Fig. 3.7(a)) consists of a microwave pulse whose duration is swept. A certain time later, the polarization after the pulse driving is measured using a short echo sequence. Multiple oscillations are observed as the spin is coherently driven between the two eigenstates. Furthermore, an exponential decay of the amplitude is found since the bandwidth of the pulse becomes gradually smaller and is not able to excite the whole inhomogeneously broadened line anymore.

T_1 relaxation Two different types of relaxation/decoherence mechanisms are distinguished for spin qubits. The first, described by the T_1 time-scale, is a

relaxation towards the equilibrium polarization, i.e. a relaxation along the quantization axis which requires the environment to absorb or supply energy to the spin system. A variety of possible processes for donors in silicon are discussed in the next section. One possible sequence to measure T_1 is the so-called 'inversion recovery' experiment: It consists of a (π)-pulse inverting the thermal polarization and a subsequent S_z measurement with varying delay time τ. An exponential relaxation back to thermal equilibrium is observed as evident from Fig. 3.7(b).

T_2 decoherence The second decoherence process concerns the loss of phase coherence of the spin ensemble during a Hahn echo sequence. As mentioned, the Hahn echo sequence neutralizes dephasing due to static inhomogeneous electric and magnetic fields. It is not possible, however, for the Hahn sequence to refocus the effects of inhomogeneous fields that feature a time dependence. If. e.g. due to defect spins in the environment, a positive phase shift is acquired during the first part of the echo sequence and, due to a flip of the defect spin, a negative phase is acquired during the second part, then the echo sequence is not able to neutralize such dephasing. The corresponding time scale on which the Hahn echo sequence decays is called T_2, and the pulse sequence used to measure this simply consists of a Hahn sequence with varying free evolution time τ (cf. Fig. 3.7(c)). As the number of refocussing pulses (and hence the decoupling frequency) is increased an increasingly narrower part of the magnetic (electric) noise spectrum is able to cause decoherence. Thus, typically dynamical decoupling with a high number of pulses provides T_2s that may be a few orders of magnitude larger than the T_2 measured by a Hahn sequence [140].

3.4.4 Sources of decoherence and relaxation

A variety of physical phenomena limit T_1 and T_2 of the donor electron and nuclear spin in silicon. These processes depend on temperature, doping concentration, magnetic field and the (isotopic) purity of the host lattice. In the following, the common sources of relaxation and decoherence for the electron spin of a donor are introduced. Although not discussed here, similar arguments may be made for the nuclear spin relaxation and decoherence, although their time scales are typically a few orders of magnitude longer due to the three orders of magnitude smaller gyromagnetic ratio γ_n. A discussion of nuclear decohrence mechanisms may be found

in [140], while an useful overview chart for T_1 and T_2 of phosphorus electron spin ensembles in isotopically-purified ^{28}Si lattices can be found in reference [16].

3.4.4.1 Electron spin relaxation T_1

All T_1 processes above 1 K require the absorption and/or emission of phonons[5], which is why this type of relaxation is also known as 'spin-lattice relaxation'. The energy transfer between phonon and spin is provided by the fluctuating local magnetic fields of the lattice vibration.

Three different processes are generally found as a function of temperature and transition frequency ω. First, the direct process simply involves the emission/absorption of a lattice phonon. This process depends on the number of phonons with frequency ω and thus T_1 varies as $\omega^4 T^{-1}$. This process is dominant at temperatures below 4 K, where $T_1 \approx 10\,\mathrm{s}$ to 1000 s for phosphorus donors.

The second process is the Raman process. At temperatures for which the thermal energy is larger than ω, the peak density of phonons is at a frequency much larger than ω. As the number of phonons increases with temperature it becomes more and more efficient to absorb an high energy phonon with energy $\omega_{\mathrm{ph,abs}}$ and emit a slightly less energetic phonon with energy $\omega_{\mathrm{ph,em}} = \omega_{\mathrm{ph,abs}} - \omega$. This process involves a virtual higher energy level of the donor and the process scales with T^{-7} for spin systems with non-integer spin quantum number S [137]. This process is usually limiting between 4 K and 10 K for phosphorus donors [140].

The third process is called the Orbach process, which also involves two phonons whose energy is, however, resonant with a real, excited state of the donor, which increases the probability of this process. It follows an exponential temperature dependence $\exp(\Delta_{\mathrm{exc}}/k_{\mathrm{B}}T)$, where Δ_{exc} is the energy separation of ground and excited state involved [137]. The Orbach process is dominant at temperatures in excess of 10 K for phosphorus donors [140].

3.4.4.2 Electron spin decoherence T_2

In general, the time scale of T_2 can not exceed T_1 for donor spins in silicon and the two are roughly equal at higher temperatures [16, 137]. As T_1 increases significantly towards lower temperatures other decoherence mechanisms become relevant:

[5] The spontaneous emission process is on the order of 10^3 s and thus irrevelevant under normal circumstances [137]. In the presence of enhanced vacuum field fluctuations due to a resonant high-Q cavity, the spontaneous emission rate may be significantly higher, which is known as Purcell effect [141].

The most prominent decoherence mechanism in ^{nat}Si is due to flip-flops of neighbouring nuclear spins of the ^{29}Si isotope. Due to the large extent of the donor wavefunction, typically several nuclear spins couple to the donor via the hyperfine interaction. Each nuclear spin experiences a different coupling strength, due to the individual wavefunction overlap. The presence of nearest-neighbour ^{29}Si permits nuclear spin flip-flops via their individual dipolar coupling on a 10 kHz time scale, which, in turn, modulates the hyperfine constant with the central donor electron spin and leads to decoherence. This effect is called spectral diffusion and features a distinct Gaussian T_2 decay in place of the usual exponential decay. The spectral diffusion limited T_2 depends on crystal orientation and is for ^{nat}Si typically between 0.1 ms to 1 ms [140, 142]. Isotopic purification of the ^{28}Si host lattice from the ^{29}Si isotope allows to reduce the impact of spectral diffusion. The purest lattices with ^{29}Si concentrations $\lesssim$ 50 ppm [20] extend the spectral diffusion T_2 limit to $\sim$1 s (cf. Ch. 6.3 and [16, 142]).

The second decoherence mechanism encountered in this thesis is instantaneous diffusion. A high concentration of donor electron spins results in a significant dipolar coupling between neighbouring spins. In contrast to usual, static local magnetic field variations, the dipolar coupling to the nearest neighbour reverses at the moment of the refocussing (π)-pulse of the echo sequence, because the nearest neighbour spin is flipped, too. Therefore, dipolar coupling between spins of the same species can not be refocused. Instantaneous diffusion is strongly concentration dependent since it scales with the distance to the nearest neighbour of the same spin species. Its effect may, however, be discriminated from other decoherence sources by artificially reducing the number of spins that contribute to the formed echo. By shortening or weakening the refocussing pulse to produce a tip angle $\theta < \pi$, only a subset of spins is flipped and contributes to the echo formation. The influence of the other, unflipped and static spin is therefore refocussed and a longer coherence time is measured, albeit at the cost of a smaller signal intensity. Using such measurements with increasingly smaller tip-angles of the refocussing pulse, a coherence time in the limit of infinitely small donor concentration may be extrapolated, which should be a realistic estimate for the isolated spin coherence time limit [16, 143]. Following reference [137], the instantaneous diffusion-limited coherence time $T_{2,\mathrm{id}}$ is given by:

$$\frac{1}{T_{2,\mathrm{id}}} = C\frac{\pi}{9\sqrt{3}}\frac{\mu_0(g\mu_B)^2}{\hbar}\sin^2\frac{\theta}{2} \tag{3.20}$$

Here, μ_0 is the vacuum permeability, g is the electron g-factor, μ_B the Bohr magneton and C is the effective density of on-resonant spins, i.e. the donor concentration divided by the number of nuclear spin-split ESR transitions.

In the limit of intermediate temperatures or both low donor and ^{29}Si concentration three other decoherence mechanisms become important. These are first the indirect electron T_1 process, where a T_1 process on a neighbouring donor spin causes a varying magnetic field for the central spin. Secondly indirect flip-flops, where flip-flops of two neighbouring electron spins due to dipolar coupling results in a fluctuating magnetic field at the central spin and thirdly direct flip-flops between donor and nearest neighbour donor spins. These mechanisms are not directly relevant to the experiments discussed within this thesis and have been discussed in detail in references. [16, 140].

3.5 Electric transport in silicon

Most of the experiments conducted in this thesis aim to measure spin-related phenomena using changes of the sample conductivity. The conductivity can be derived by a variety of theories, ranging from classical treatments such as the Drude-Lorentz model over semi-classical versions (Drude-Sommerfeld equation) up to the fully quantum mechanical treatment such as the Boltzmann equation. The intention of this section is not to derive the relevant transport equations from first principle[6] but merely to introduce the key parameters and main equations. Sec. 3.5.1 does this for single carrier-type transport in a magnetic field. Thereafter the Hall effect (Sec. 3.5.2) and the magnetoresistance are discussed (Sec. 3.5.3), including measured data for sample natSi-Hall, which is also used for the measurement of carrier density under D^0X excitation in Ch. 5.2. Finally, using the same sample, carrier freeze out and the temperature dependence of the mobility are discussed in Sec. 3.5.4.

3.5.1 Single carrier transport in a magnetic field.

The current density $\mathbf{j}$ due to electrons in an external electric field $\mathbf{E}$ is related to the drift velocity $\mathbf{v}_\mathrm{d}$ by:

$$\mathbf{j} = -ne\mathbf{v}_\mathrm{d}(\mathbf{E})$$

where e is the elementary charge and n is the carrier density.

In the Drude model the electrons are subject to different scattering events with a mean scattering time or momentum relaxation time[7] τ_m. The equation of motion of a classical electron then includes two terms, the electric field acceleration $e\mathbf{E}$ and the relaxation term $m^*\frac{\mathbf{v}_\mathrm{d}}{\tau_\mathrm{m}}$:

$$m^*\frac{\mathrm{d}\mathbf{v}_\mathrm{d}}{\mathrm{d}t} = -e\mathbf{E} - m^*\frac{\mathbf{v}_\mathrm{d}}{\tau_\mathrm{m}} \tag{3.21}$$

where m^* is the effective mass of the carrier. The steady state solution for the drift velocity is then

$$\mathbf{v}_\mathrm{d} = -\frac{e\tau_\mathrm{m}}{m^*}\mathbf{E} \equiv -\mu\mathbf{E} \tag{3.22}$$

[6] These first principle calculations can be found e.g. in [109, 120]

[7] τ_m is also the $1/e$ - time scale for which the current approaches zero if the bias is instantaneously removed.

where the carrier mobility is defined as $\mu = \frac{e\tau_\mathrm{m}}{m^*}$. It is convenient to define a conductivity σ as $\mathbf{j} = \sigma\mathbf{E}$. In general σ is a tensor, but for an isotropic material σ can be deduced from the equations above to

$$\sigma = ne\mu = \frac{ne^2\tau_\mathrm{m}}{m^*} \tag{3.23}$$

Hence, a higher mobility, i.e. a longer scattering time τ_m or smaller mass m^* lead to a higher conductivity. To understand the tensorial components of σ in more complex materials a thorough treatment of the Boltzman transport equation is necessary [120].

In a magnetic field, transport is affected by the Lorentz force, which deflects drifting charge carriers. Under the assumption of a weak[8] magnetic field $\mathbf{B} = (0, 0, B_z)$ the Lorentz force modifies the scalar conductivity of an isotropic crystal and results in a tensorial quantitiy given by ([120], Eq. 4.2.34):

$$\sigma_{\mathrm{weak}\,B} = \begin{pmatrix} \sigma_0 + \beta_0 B_z^2 & \gamma_0 B_z & 0 \\ -\gamma_0 B_z & \sigma_0 + \beta_0 B_z^2 & 0 \\ 0 & 0 & \sigma_0 \end{pmatrix} \tag{3.24}$$

with $\sigma_0 = (ne^2/m^*)\langle\tau_\mathrm{m}\rangle = ne\mu$ as the conductivity in zero magnetic field, $\beta_0 = -(ne^4/(m^*)^3)\langle\tau_\mathrm{m}^3\rangle$ and $\gamma_0 = (ne^3/(m^*)^2)\langle\tau_\mathrm{m}^2\rangle$.

3.5.2 Hall effect

As evident from the conductivity tensor of (3.24), the in-plane electric field components E_x and E_y are coupled by the external magnetic field. Defining the current to be directed along x ($j_y = 0$) a voltage arises perpendicular to both magnetic field and current direction. The Hall coefficient R_H is defined as the ratio between perpendicular electric field E_y and current density j_x normalized by the magnetic field strength B_z. From Eq. (3.24) R_H in a small magnetic field can be deduced to:

$$R_\mathrm{H} = \frac{E_y}{j_x B_z} = \frac{V_y t}{I_x B_z} = -\frac{r_\mathrm{H}}{ne} \tag{3.25}$$

t is the thickness of the sample and $r_\mathrm{H} = \langle\tau_\mathrm{m}^2\rangle / \langle\tau_\mathrm{m}\rangle^2$ is known as the Hall factor. Its value is usually between 1 and 2 depending on the type of scattering mechanism that limits the mobility[9] [120]. Following the definition in (3.23), the Hall mobility

[8] Weak compared to the inverse of the carrier mobility, $B \ll 1/\mu$.

[9] For phonon scattering $r_\mathrm{H} = 1.18$, while for ionized impurity scattering $r_\mathrm{H} = 1.93$ [120].

$\mu_\mathrm{H} = \mu / r_\mathrm{H}$ can be deduced from a combination of the measured sample conductivity and the Hall coefficient as:

$$\mu_\mathrm{H} = \frac{\sigma_0}{R_\mathrm{H}} \tag{3.26}$$

The above derived equations are valid for electron transport, for which R_H is negative. R_H reverses sign for hole (p) transport. In semiconductors, often both electrons in the conduction band and holes in the valence band contribute to the current density j_x. In this case the conductivity is given by

$$\sigma_0 = e(p\mu_p + n\mu_n). \tag{3.27}$$

This leads to the Hall coefficient for a semiconductor [112, 120]:

$$R_\mathrm{H} = \frac{r_\mathrm{H}}{e} \frac{p\mu_p^2 - n\mu_n^2}{(p\mu_p + n\mu_n)^2} \tag{3.28}$$

If the carrier density of one carrier type heavily outweighs the other type then the sign of R_H signals the majority carrier type. Similarly, the mobility, deduced from a combination of Hall and conductivity measurement is the mobility of this majority carrier. However, if the two carrier densities are similar, or if the difference in mobility is large, then conclusions from a single Hall measurement regarding carrier type and carrier mobility are difficult to draw. For silicon at low temperatures, the hole and electron mobility are fairly similar [114, 144, 145], so the sign of R_H should directly relate to the majority carrier type. Somewhat counter-intuitively, if the single carrier transport model of (3.25) is applied to a case, where, in fact, two-carrier types with $n = p$ (and $\mu_n = \mu_p$) contribute to the transport, the wrongful conclusion is drawn that n is close to infinity and μ_H is ~ 0.

So far, the expressions were derived for the low magnetic field case, characterized by $(\mu_\mathrm{H} B_z)^2 \ll 1$. For high magnetic fields, it can be shown that the small uncertainty due to r_H can be avoided and that the single carrier Hall coefficient is directly given by $R_\mathrm{H} = -1/(ne)$ [120]. For silicon, with silicon mobilities on the range of 10^4 – $10^5\,\mathrm{cm}^2/(\mathrm{Vs})$, the magnetic field separating low and high field limit is about 0.1 T to 1 T.

3.5.3 Ordinary magnetoresistance

Since a perpendicular magnetic field deflects the charge carriers due to the Lorentz force, it is intuitive that the mobility and thus conductivity of a crystal depend on the magnetic field strength. Starting from the weak field conductivity tensor (3.24)

and using the same definition of $j_y = 0$, it can be shown that j_x is a function B_z^2 and reduces with increasing magnetic field. The relative change in resisitivity $\rho = 1/\sigma$ in the low magnetic field limit can then be calculated as [120]:

$$\frac{\rho(B) - \rho_0}{\rho(B)} = \frac{\Delta\rho(B)}{\rho(B)} = T_{\mathrm{M}}(e \langle\tau_{\mathrm{m}}\rangle B_z/m^*)^2 = T_{\mathrm{M}}(\mu_{B=0} B_z/m^*)^2 \tag{3.29}$$

As with r_{H}, T_{M} depends on the type of carrier scattering and ranges typically from 0.38 (for acoustic phonon scattering) to 2.15 (for ionized impurity scattering) [120]. The magnetoresistance in low magnetic fields is parabolic with proportionality constant dominated by the mobility $\mu_{B=0}$ at vanishing magnetic field.

For high magnetic field strength (such that $\Delta\rho \approx \rho(B)$ or equivalently $(\mu_{\mathrm{H}} B_z)^2 \gg 1$), the magnetoresistance is given by

$$\frac{\Delta\rho(B)}{\rho(B)} = 1 - \frac{1}{\langle\tau_{\mathrm{m}}\rangle \langle\tau_{\mathrm{m}}^{-1}\rangle} \tag{3.30}$$

This is a constant that again depends on the type of scattering mechanism and assumes a value of 0.12 for acoustic phonon scattering and 0.71 for ionised impurity scattering.

Figure 3.8 shows two examples of magnetoresistance in silicon at $T = 4.5\,\mathrm{K}$, with photocarriers created by continuous lasers with photon energies of 1.150 eV and 1.182 eV. The measurements are conducted on sample natSi-Hall, a square cut from a bulk-doped, phosphorous doped wafer with room temperature resistivity of $\sim 3.4\,\Omega\mathrm{cm}$ (cf. Ch. 4.1.2). The square is contacted at the four corners with evaporated aluminium contacts on arsenic doped Ohmic contacts. At each magnetic field point, the data are acquired using the van der Pauw Hall measurements, as outlined in Ch. 5.2.1. For both laser wavelengths, the same qualitative behaviour is observed. The carrier concentration does not depend on the magnetic field, as expected, and the change of resistance is solely due to a change of carrier mobility. Figure 3.8(d) plots the normalized, relative magnetoresistance change as defined by the left-hand side of (3.29). For low magnetic fields, assuming $T_{\mathrm{M}} = 0.55$, the data points are fitted by the parabolic dependence of Eq. 3.29. For magnetic fields higher than $1/\mu_{B=0} \approx 160\,\mathrm{mT}$, the magnetoresistance assumes a constant value, again as expected. The dashed-dotted line shows the expected asymptotic value for ionised impurity scattering. The mobility for silicon at liquid helium temperatures is, however, expected to be limited by neutral impurity scattering, as seen in the next section. The asymptotic value for this scattering mechanism is not known, hence it is impossible to fit the high magnetic field data satisfyingly.

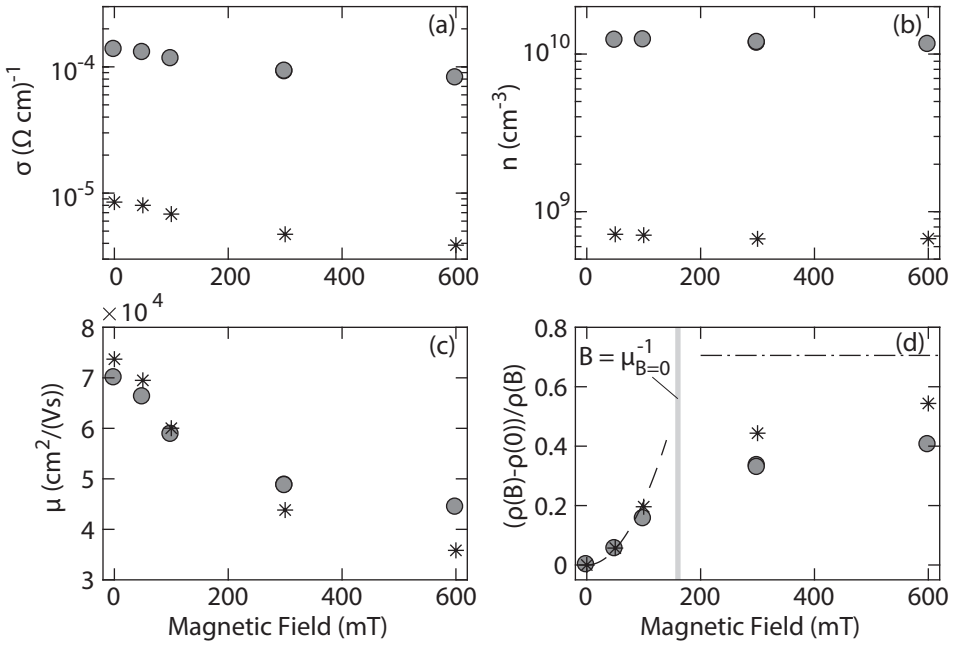

Figure 3.8: The magnetoresistance of photocarriers of sample natSi-Hall at 4.5 K upon illumination with 1.150 eV (grey dots) and 1.182 eV (stars). The sample conductivity (a), carrier density (both n-type) (b), and Hall mobility (c) have been deduced from van der Pauw Hall measurements. (d) plots the magnetoresistance as $\Delta\rho(B)/\rho(B)$. The laser intensities were $I_{\mathrm{L}}(1.150\,\mathrm{eV}) \approx 1 \times 10^4\,\mathrm{W/m^2}$ and $I_{\mathrm{L}}(1.182\,\mathrm{eV}) \approx 50\,\mathrm{W/m^2}$ due to the difference in absorption coefficient.

In summary, a magnetoresistance of silicon is both experimentally observed and theoretically expected. The resistance increases roughly two-fold and saturates at fields above ∼160 mT, which is the expected order of magnitude, but further conclusions can not be drawn due to the unknown value of the asymptotic magnetoresistance for neutral impurity scattering. Both the weak field magnetoresistance and the transition from weak to high field limit are in good agreement with the theoretical prediction.

3.5.4 Carrier freeze out and mobility temperature dependence

This section investigates the temperature dependence of the conduction band electron density and mobility. At room temperature electrons are not localised to the donor due to the small donor binding energy compared to the thermal energy. As the energy is reduced, an increasing number of electrons are bound to the donor and the conduction band electron density decreases sharply, an effect known as carrier freeze out.

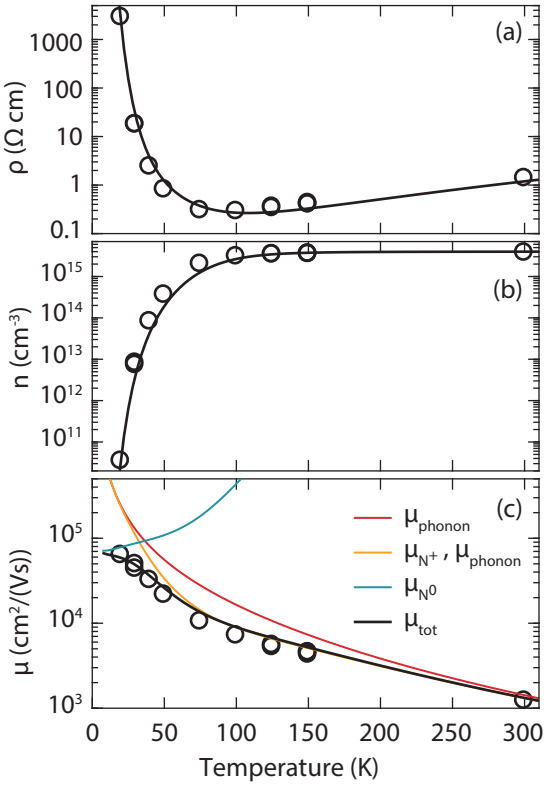

Figure 3.9: Temperature dependence of (a) the resistivity, (b) the carrier density and (c) the mobility of the bulk phosphorus-doped sample natSi-Hall. The lines represent theoretical expressions as developed in the main text.

Figure 3.9 shows this effect with data from the same sample natSi-Hall and setup used in the previous section. Starting from room temperature, at each temperature set point the van-der-Pauw Hall measurements are carried out after a thermalization time of ∼5 min. All mesurements are performed in the dark.

The carrier density n, shown in Fig. 3.9 (b), features the expected constant carrier density towards room temperature, which is equal to the phosphorus concentration of $\sim 3.5 \times 10^{15}\,\mathrm{cm}^{-3}$, and towards smaller temperatures a freeze out of carriers is observed. The data are well explained by the expression for the extrinsic carrier concentration $n(T)$ due to ionisation of a donor with binding energy E_{D^0} ([114] [10], Eqs. (1.36) & (1.56)):

[10] Often a typical assumption used for the development of expressions of $n(T)$ is $N_{\mathrm{D}} \ll \frac{1}{2}U_{\mathrm{c}} \exp\left(-\frac{E_{\mathrm{C}}-E_{\mathrm{D}^0}}{k_{\mathrm{B}}T}\right)$, which is no longer valid for low temperatures. The expressions used in this thesis do not rely on this assumption and are valid for the complete temperature regime [114].

$$n(T) = U_{\mathrm{c}}(T)\ \exp\left(-\frac{E_{\mathrm{C}} - E_{\mathrm{F}}(T)}{k_{\mathrm{B}}T}\right) \tag{3.31}$$

$$U_{\mathrm{c}}(T) = 2\left(\frac{\pi m_{\mathrm{n}}^{*} k_{\mathrm{B}} T}{h^2}\right)^{3/2} \tag{3.32}$$

$$E_{\mathrm{F}}(T) = \frac{E_{\mathrm{C}} + E_{\mathrm{D}^0}}{2} + \frac{k_{\mathrm{B}}T}{2}\ln\left(\frac{N_{\mathrm{D}}}{2U_{\mathrm{c}}(T)}\right) - \tag{3.33}$$

$$- k_{\mathrm{B}}T \sinh^{-1}\left(\sqrt{\frac{U_{\mathrm{c}}(T)}{8N_{\mathrm{D}}}}\ \exp\left(-\frac{E_{\mathrm{C}} - E_{\mathrm{D}^0}}{2k_{\mathrm{B}}T}\right)\right),$$

where E_{F} is the Fermi energy and U_{c} is the effective density of states in the conduction band. The black line of Fig. 3.9 (b) represents the theoretical expression for $n(T)$ from Eq. (3.32) for phosphorus with $E_{\mathrm{D}^0} = -45\,\mathrm{meV}$ and doping level of $N_{\mathrm{D}} = 3.5 \times 10^{15}\,\mathrm{cm}^{-3}$.

The mobility μ of the conduction band electrons in silicon (Fig. 3.9 (c)) exhibits a complex temperature dependence with different regimes as a function of temperature and an asymptotic behaviour for $T < 30\,\mathrm{K}$. For bulk devices away from interfaces, three scattering mechanisms are significant: Electron-phonon scattering (μ_{phonon}), ionised donor scattering (μ_{N^+}) and neutral donor scattering (μ_{N^0}). The individual mobility contributions are plotted in Fig. 3.9(c), following closely the expressions and fitted values for silicon given in references [114, 146, 147]. It should be stressed that the only input to these expression is the above deduced donor concentration $N_{\mathrm{D}} = 3.5 \times 10^{15}\,\mathrm{cm}^{-3}$ and that all other parameters are literature values. The individual mobility contributions are combined by Matthiessen's rule and plotted in black, which results in an excellent agreement between theory and data. Phonon-scattering dominates at room-temperature with ionised impurity scattering being particularly important around 100 K. Below ∼30 K neutral impurity scattering is the major scattering mechanism for the given donor concentration. Although it was impossible to obtain data points at lower temperatures, it is known that the majority carrier mobility of crystalline silicon doesn't change much below 20 K [148] and so from the good agreement between theory and data an electron mobility at 4.5 K of approximately $6 \times 10^4\,\mathrm{cm}^2/(\mathrm{V\ s})$ to $8 \times 10^4\,\mathrm{cm}^2/(\mathrm{V\ s})$ is expected, limited by neutral impurity scattering. This is in good agreement with the mobility of photo-excited carriers in this sample at vanishing magnetic field (cf. Fig. 3.8).

Figure 3.9 (a) plots the measured sample resistivity as circles and the resistivity deduced from the derived theoretical expressions for μ and n, given by $\rho = (e\mu n)^{-1}$. Again, a very good agreement between theory and data is observed.

Chapter 4

Samples, device fabrication and experimental apparatus

This chapter summarizes the 'ingredients' of the experiments of this thesis. The first section features an overview of the used samples and summarizes the fabrication steps of the silicon MOS-devices. The second section introduces the main instrumentation employed for the presented measurements.

4.1 Samples

Two different types of samples have been used throughout this thesis: The first are bulk crystalline samples to study the intrinsic material-related limitations of donors in silicon regarding their spin-coherence and optical D^0X properties. The second set of devices features metal contacts to the sample to perform (photo-) conductivity measurements with direct electrical contacts to the sample. Table 4.1 gives an overview over the samples used throughout this thesis, while Section 4.1.1 and 4.1.2 discuss the origin/fabrication of the bulk crystalline samples and the electrical D0XDEV devices, respectively.

4.1.1 ^{28}Si samples

The bulk-crystalline ^{28}Si samples have been grown from isotopically purified silane gas, as part of the Avogadro project for a redefinition of the kilogram via purified silicon spheres [20]. Sample 28Si-Avo is one of the purest pieces of the resulting ^{28}Si crystal, while samples 28Si-331 and 28Si-321 have intentionally been doped with phosphene gas during growth to achieve n-type silicon with higher donor concentration. All ^{28}Si samples are fabricated using the floating zone (FZ) melting process to achieve a high crystal purity with low concentrations of oxygen and carbon. This

Sample	Type	[P] (cm^{-3})	Chapters	Comments
28Si-Avo	bulk	$\sim 5 \times 10^{11}$	6.3	^{28}Si: 99.995 %, [B] $= 1 \times 10^{13}\,cm^{-3}$
28Si-331	bulk	$\sim 2 \times 10^{14}$	5.4 & 6.2	^{28}Si: 99.991 %(*), [B] $= 1 \times 10^{14}\,cm^{-3}$
28Si-321	bulk	3×10^{15}	6.2 & 6.4	^{28}Si: 99.991 %(*), [B] $= 1 \times 10^{14}\,cm^{-3}$
28Si-Buf	bulk	[P] 2×10^{14}, [As] 5×10^{14}, [Sb] 1×10^{14}	5.4	^{28}Si
28Si-epi	^{28}Si device	10^{15}	5.3 & 7.1	25 µm thick ^{28}Si (99.9 %) layer on ^{nat}Si substrate
natSi-Hall	^{nat}Si device (D0XDEV)	3×10^{15}	3.5 & 5.2	Hall square ($3.5 \times 3.5, mm^2$) of bulk doped wafer
natSi-ResBars	^{nat}Si device (D0XDEV)	5×10^{15}	7.2 & 7.4	Multiple, parallel n^+ contacts on P implant
natSi-parElec10	^{nat}Si device (D0XDEV)	3×10^{15}	7.2 & 7.4	Parallel n^+ contacts (10 µm sep., 50 µm len.) on bulk doped wafer
natSi-parElec20	^{nat}Si device (D0XDEV)	3×10^{15}	7.4	Parallel n^+ contacts (20 µm sep., 800 µm len.) on bulk doped wafer
natSi-smallHall	^{nat}Si device (D0XDEV)	5×10^{15}	7.4	Implanted square ($50 \times 50\,\mu m^2$) with n^+ contacts on the corners
natSi-Scan	^{nat}Si device (D0XDEV)	5×10^{15}	7.3	Parallel n^+ contacts (400 µm sep., 2600 µm len.) with patterned P implant areas

Table 4.1: Overview of samples used throughout this thesis, their donor and acceptor concentration and isotopical purity. The asterisk (*) denotes that the isotopic purity of these samples may be lower than the value listed due to possible unintentional reduction of isotopic enrichment during the growth process.

is desirable for D^0X measurements, since O_2 and C broaden the D^0X linewidth in the same way as a ^{29}Si [29, 149]. The samples are cut into crystals of roughly 2 mm × 2 mm × 10 mm and an image of sample 28Si-331 can be found in Fig. 6.1.

The 28Si-epi sample used for D^0X-assisted ESR measurements of Ch. 7.1 consists of a ^{28}Si layer of 25 µm thickness with purity of 99.9 % that is grown epitaxially under under phosphene gas introduction on top of a nominally undoped ^{nat}Si substrate (FZ). The resulting phosphorous concentration within the ^{28}Si layer is $10^{15}\,cm^{-3}$.

4.1.2 Fabrication of D0XDEV samples

Electrical devices are required to investigate various aspects of the D^0X transition that could not be inferred from the capacitive measurement carried out for the bulk ^{28}Si samples. Due to the high value and scarcity of ^{28}Si wafers and the poor optical properties of Czochralski-grown silicon, it was chosen to use float-zone grown ^{nat}Si wafers for the initial device studies. The fabrication of these devices (labelled 'D0XDEV') was mainly carried out in the cleanroom of the London Centre for Nanotechnology, with the ion-implantation steps performed at the Surrey Ion Beam Centre and the dry oxide grown at the Southampton Nanofabrication Centre. The following describes the fabrication steps, while a more detailed explanation of the specific device designs are presented within each respective experimental chapter.

An overview of the fabrication steps is presented in Fig. 4.1, while the full cleanroom process steps and comments to each step can be found in Appendix A.

I: Alignment marker: To align all subsequent photolithography steps, alignment markers with a depth of 400 nm were etched in a reactive ion-etch.

II: Ohmic contact implantation: Contacts with low contact resistance are achieved using a degenerate arsenic n^+ implantation. A 1.8 µm thick photo resist is used to define the contact area photo-lithographically. The expected implantation profile directly after implantation and after the annealing of step IV is depicted in Fig. 4.2(b), with an expected degenerate As concentration of $10^{20}\,cm^{-3}$ at the interface. Arsenic has been chosen for the n^+ contacts, since its D^0X line does not overlap with the phosphorus D^0X spectrum. Measured sheet resistances for these implantation parameters are 65 Ω/□.

III: Phosphorus implantation: The active area of each device is the phosphorus implantation, which is patterned by the same photo-lithography process. The resulting donor distribution (cf. Fig. 4.2(c)) has a peak concentration of $5 \times 10^{15}\,cm^{-3}$ at a depth of 130 nm, relatively far from the silicon surface.

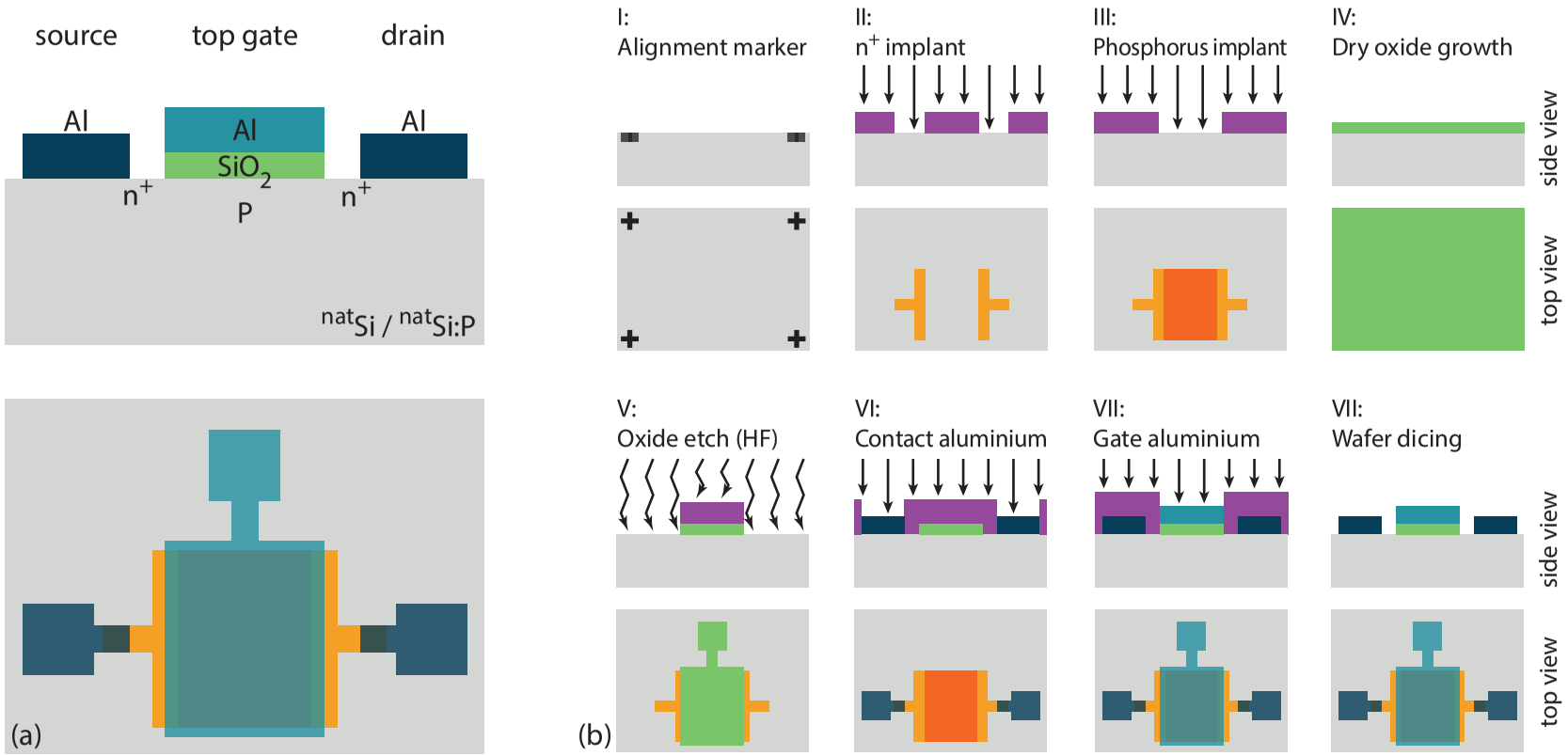

Figure 4.1: (a) A sketch of a MOSFET device realized during the fabrication of the D0XDEV devices. The MOSFET has been chosen as an example here because it utilizes all fabrication steps. However, a majority of the D0XDEV devices do not feature a top gate. (b) A cartoon of the fabrication process.

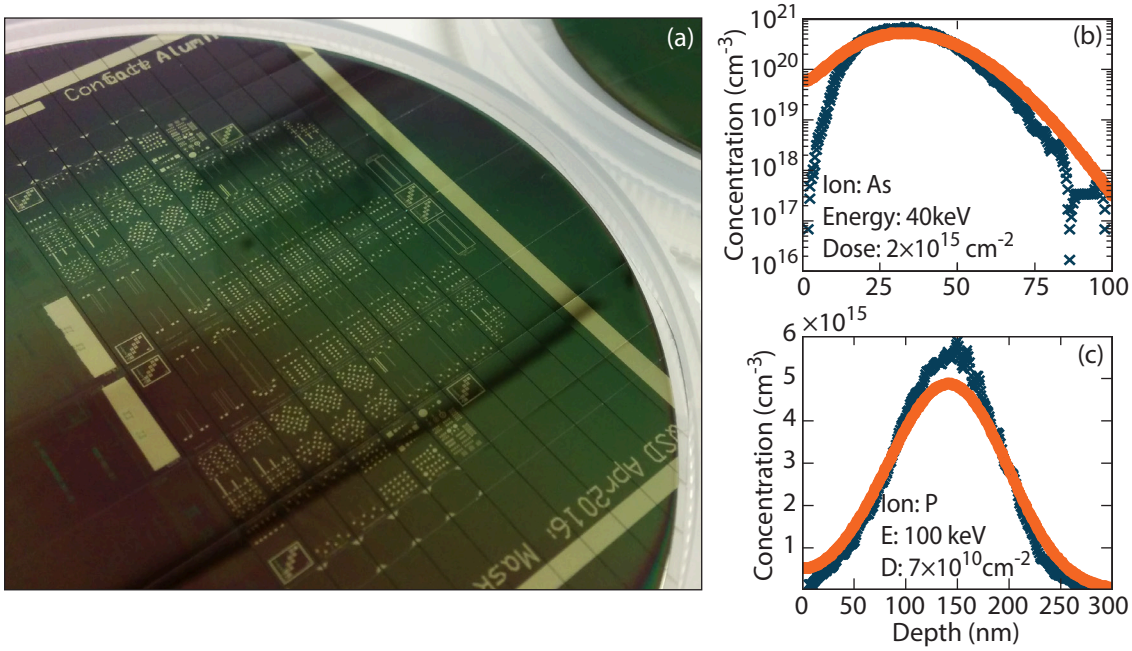

Figure 4.2: (a) An image of the D0XDEV devices of the 4" bulk-doped wafer after the final dicing fabrication step. The width of the diced chips is 3.5 mm. The expected implantation profile immediately after implantation (blue) and after the anneal of the oxide growth step (orange) are shown for (b) the ohmic contact arsenic implant and (c) the low dose phosphorus implant.

The measured room temperature sheet resistance of $\sim$10 k$\Omega/\square$ supports the estimated peak concentration and concentration profile and confirms a high donor activation rate.

IV: Dry oxide growth: Some devices feature gate electrodes, which require a field oxide. An established dry oxide growth process at the University of Southampton has been employed (O_2 atmosphere, 5 min, 950 °C), resulting in a measured oxide thickness of 11 nm to 12 nm. The MOSFET test structures were not affected by gate leakage, showed good transistor behaviour and featured an oxide break-down voltage of $\sim$4 V at room temperature.

V: Oxide etch: To avoid additional straining of the phosphorus implanted areas, the oxide has been removed everywhere except for the vicinity of the gate aluminium using a photolithography mask and a buffered oxide etch for 30 s (NH_4F/HF = 6:1).

VI: Contact aluminium: The aluminium to contact the silicon has been deposited using an optical lithography mask and a thermal evaporator. The targeted final thickness is 30 nm. In the device design it was attempted where possible to maximize the distance between the aluminium deposition and the phosphorus

implantation, to avoid straining of the latter. Measured contact resistances for $20 \times 20\,\mu m^2$ contacts are on the order of $10\,\Omega$ at room temperature.

VII: Gate aluminium: The gate aluminium has been fabricated analogously to the contact aluminium, again with a film thickness of 30 nm.

VIII: Wafer dicing: As the last step of the fabrication, the wafer is diced into chips with a width of 3.5 mm, small enough to fit into the dieelectric ring resonators of the microwave spectrometer.

A processed and diced wafer with D0XDEV devices is shown in Fig. 4.2(a). Devices were fabricated on four different FZ wafer substrates: (1) on a nominally instrinsic FZ silicon wafer, (2) on a bulk doped phosphorus wafer with $[P] = 3 \times 10^{15}\,cm^{-3}$ for which the phosphorus implantation step was omitted, and (3 & 4) for two silicon-on-insulator (SOI) wafers with a FZ grown device layer and two different handle wafer doping concentration. Unfortunately the SOI wafer did not show a D^0X signal (likely due to strain in the device layer), so only results on the first two substrates are shown here.

4.2 Experimental instrumentation

The instruments used for the experiments of this thesis can roughly be divided into four categories: The laser with its optical components, the cryostat and magnet, the microwave-pulse source and echo detection, and the sample-condcutivity measurement. The sample conductivity measurement is either performed capacitively (Ch. 6) or via direct electrical contacts to the sample (Ch. 7) and the details of the respective conductivity measurements are discussed in these chapters. This section introduces the shared components of all measurements, i.e. the employed lasers (Sec. 4.2.1), cryostats (Sec. 4.2.2) and microwave spectrometers (Sec. 4.2.3).

4.2.1 Laser

The main laser used in the experiments is an ytterbium doped fibre laser (Koheras Boostik) from NKT Photonics, labeled throughout this thesis as D^0X-laser or 1.15 eV-laser. The photon energy is tunable from 1.149 60 eV to 1.150 35 eV (1077.8 nm – 1078.5 nm). The output power ranges from 25 mW up to nominally 1 W, but, due to reflections in the setup, was limited to a maximum of ∼200 mW. The nominal linewidth is 0.3 neV (70 kHz). The laser can be set and stabilized at any wavelength within the range using the built-in piezo-tuning. The desired wavelength is set via a computer-controlled voltage source (e.g. Keithley 2400) using the reading from a HighFinesse WS7 wavelength meter. The laser power range is extended towards the low power range via Thorlabs absorptive ND filters and the laser spot diameter is ∼3 mm. In most experiments, higher harmonics or unwanted laser modes are filtered out using a Thorlabs FB1100-10 bandpass filter.

The second laser is a CNI MLL-III-1047 diode-pumped solid state laser, with photon energy of 1.184 eV (1047 nm) slighlty above the silicon bandgap. The laser power is fixed, with a measured value of 590 mW. This laser is labelled as the above-bandgap laser or 1.18 eV-laser. The beam diameter at its output is ∼1.5 mm and the beam divergence is 1.5 mrad.

Both lasers are continuous and can, if required, be modulated using mechanical shutters (Stanford Research SR475), with a shutter open/close time of 5 ms.

4.2.2 Cryostat & magnet

The experiments are carried out in two different types of continuous flow helium cryostats. The first one is an Oxford Instruments CF935 cryostat (Fig. 4.3(a)), which is cooled via an external liquid helium dewar. The dewar is pressurized to

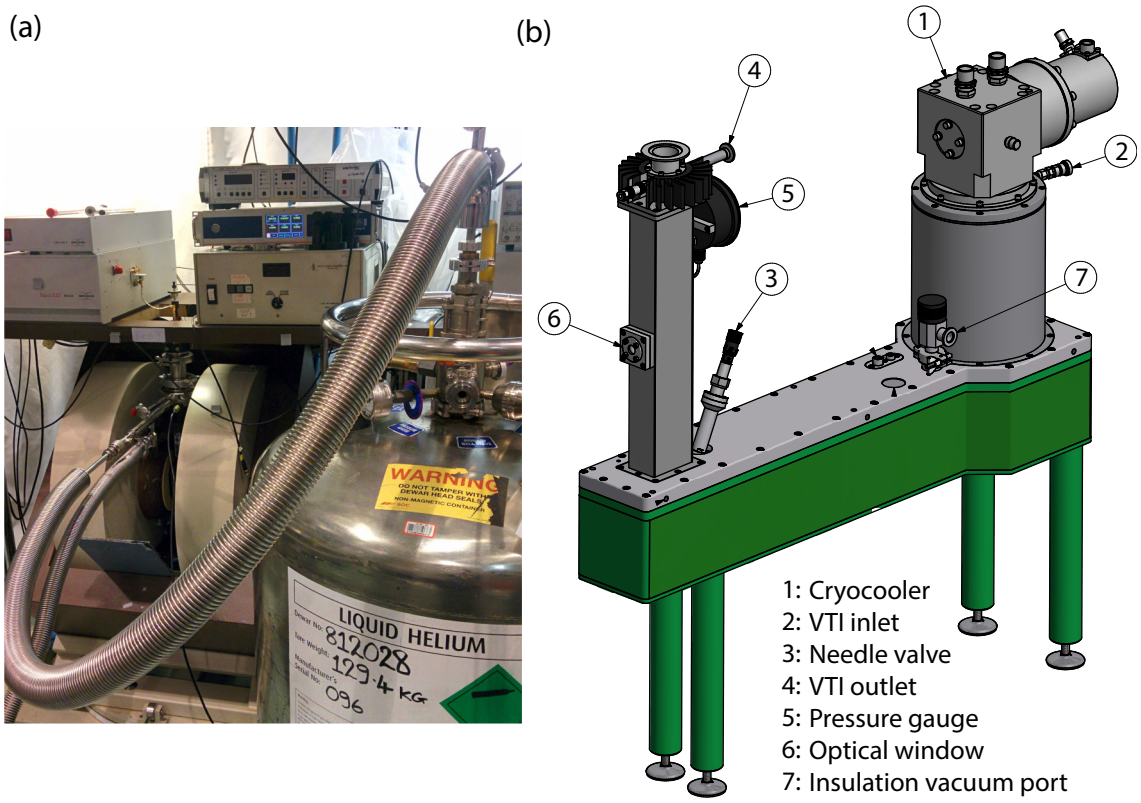

Figure 4.3: The two continuous flow helium cryostats used in this thesis. The Oxford instrument cryostat (a) requires an external, pressurized liquid helium dewar. The Cryogenic closed cycle system (b) features a sample space very similar to the Oxford cryostat including an optical window (6). The primary helium circulation is pushed via a pump into port (2), where it passes a cold trap and the second stage of the cryocooler (1), which is usually at around 2 K. The helium passes a heater and needle valve (3) to control flow and temperature. The sample space is usually at a pressure of ∼10 mbar, although operation close to atmospheric pressure is also possible. The helium exits the cryostat via port (4) and returns to the reservoir. The closed cycle system has a temperature range in continuous operation of 1.5 K to 200 K, while the Oxford cryostat is limited in continuous operation to temperatures $\gtrsim$ 4.2 K.

$\sim$0.5 bar overpressure and the helium is thus pushed through the cryostat without any pump. The temperature is controlled via a heater and temperature sensor close to the inlet to the sample space at bottom of the cryostat. The sample space is roughly at atmospheric pressure.

The second cryostat is a Cryogenic Ltd. CF-VTI, which has been acquired and installed during the course of this thesis via the PhD student equipment fund of UCL's Centre for Doctoral Training in Delivering Quantum Technologies. It is also a continuous flow cryostat with a variable temperature inset, intended to make the sample space very similar to the Oxford Instruments cryostat (cf. Fig. 4.3(b)). The difference however is that the primary helium circulation is closed loop, meaning that no helium is lost during operation. The primary helium circulation is driven by a Oerlikon scroll pump, pushing the helium from the reservoir via charcoal traps past a cold head into the cryostat from which it returns to the reservoir. The primary circuit thus mereley acts as a heat exchanger for the cooling power of the pulse tube cryocooler mounted at the back of the cryostat. Both cryostats feature quartz windows for optical access.

The magnets are water-cooled Bruker electro-magnets, capable of up to 1.5 T, and its poles are depicted in Fig. 4.3(a). One of the magnets is operated by a bipolar power supply and enables a reversal of the magnetic field[1] while the two other magnets are only uni-directional.

4.2.3 Microwave instrumentation

Two types of pulsed ESR spectrometer are used throughout this thesis. The first spectrometer is a commercial Bruker E500/E580 spectrometer, in conjunction with a 1 kW tranveling wave tube (TWT) amplifier. This spectrometer allows for strong and fast microwave pulses with π-pulses down to $\sim$10 ns. However, the software and hardware are not optimal for more complex pulse sequences. Furthermore, it proved not to be suitable for very long coherence time measurements, due to spurious destructive phase noise on the echo signal (E500), which is likely related to the mains frequency as it had a 50 Hz signature.

Hence, the main spectrometer employed within this work is an in-house built ESR spectrometer. The spectrometer was lead-developed by Gary Wolfowicz, a former member of the group, and then further noise-optimized and made compatible with the TWT amplifier during the course of this thesis. The schematic of the pulsed ESR spectrometer is shown in Fig. 4.4. Two different modes of operation occur

[1] Which increases the accuracy of the Hall measurements of Sec. 5.2.

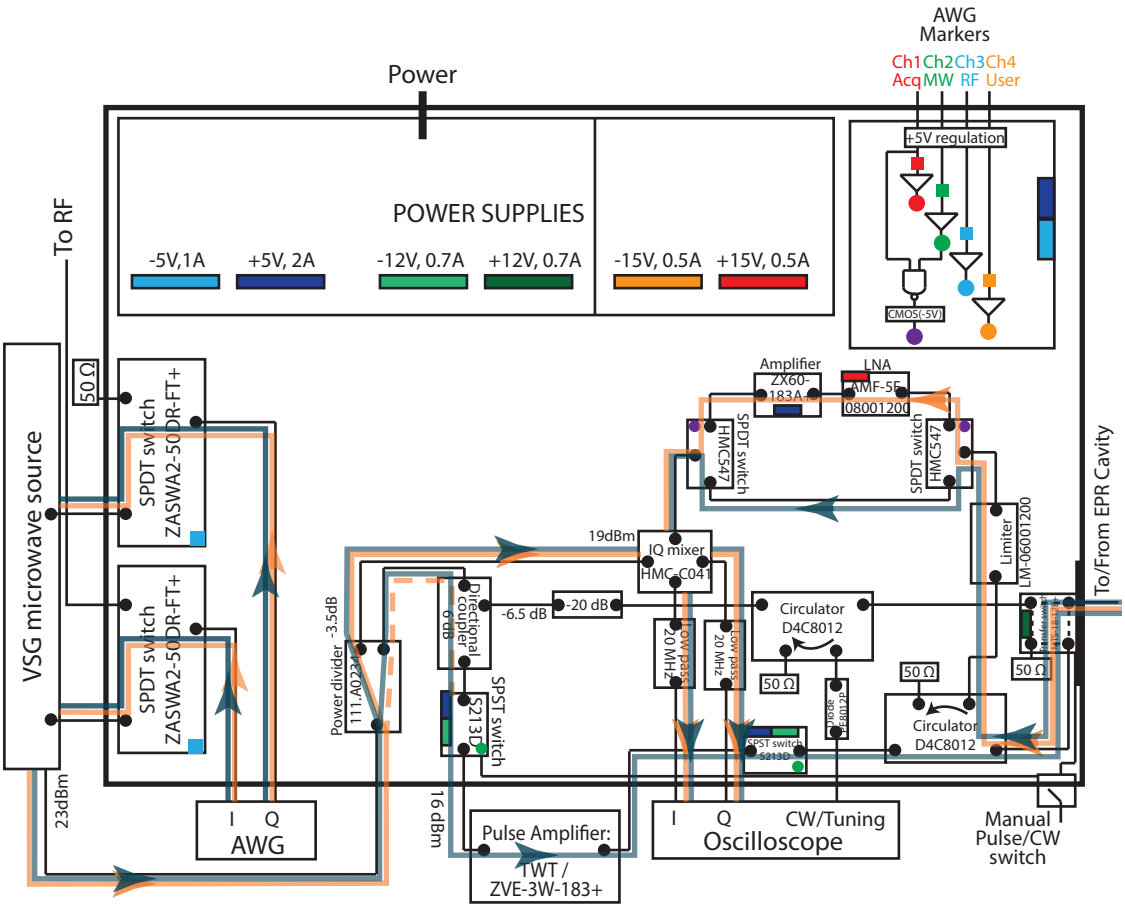

Figure 4.4: The home-built pulsed ESR spectrometer. Its main components consist of the power board (top left), the logic board (top right) to control the microwave switches and the microwave circuitry. The operation of the spectrometer is described in the main text. The spectrometer requires a number of external instruments, namely an AWG (Agilent 81180b), a microwave pulse source with IQ modulation input (Agilent E8267D), an external microwave amplifier (here either a TWT amplifier with subsequent high power attenuator, Weinschel AE117A-69-33 or a less powerful 3 W solid state amplifier (MiniCircuit ZVE-3W-183+) and an oscilloscope (Keysight MSO-X 3104A). The spectrometer furthermore has a microwave cavity tuning path that measures the microwave reflection of the resonator via a microwave diode and is enabled by the bottom right switch.

during a conventional microwave pulse sequence—first, the delivery of microwave pulses and, secondly, the period of echo detection. The microwave paths within the spectrometer are different for each of these periods, which is described below.

Microwave pulses: A microwave sequence first sends microwave pulses of specific power and phase to the sample, which is illustrated as the blue signal path in the spectrometer schematics of Fig. 4.4. In this case, the arbitrary waveform generator (AWG) defines the pulse length and shape and modulates the I and Q input of the microwave source. The upmixed microwave pulses enter the ESR spectrometer where at a power divider, a part of the pulse power is split off to drive the LO port of the main IQ mixer. The other part of the pulse enters the pulse amplifier and is then routed towards the microwave cavity where it drives the spin resonance. The reflected part of the pulse is directed via a circulator and power limiter to the RF port of the IQ mixer. The down-mixed I and Q signals are captured on the oscilloscope and reveal position and phase of the pulses.

Echo detection: During echo detection (orange path of Fig. 4.4), the AWG still sends out a pulse to drive the LO port of the IQ mixer. This time however, the AWG marker pulses shut the switches around the pulse amplifier, ensuring that neither the pulse nor the amplifier noise are sent to the cavity. Instead, the (typically small) echo signal originating from the sample is routed via the circulator and limiter to a low-noise amplifier (LNA) and a second amplifier stage. The amplified echo signal is then downmixed at the IQ mixer and captured by the oscilloscope (as seen in Fig. 3.6).

Further to these modes of operation, the spectrometer is also capable of sending RF pulses for nuclear spin manipulation. The selection of the different spectrometer operation modes is done via marker pulses from the AWG, which enter the spectrometer at the logic board (top right of Fig. 4.4), that in turn power and control the MW switches.

Typical achievable microwave pulse lengths are on the order of 150 ns, due to power limitations of certain components. While this spectrometer is thus more flexible in its usage, it also means that the longer pulse durations require samples with smaller spin linewidths.

Chapter 5

Fundamentals of the bound exciton transition

This chapter focuses on the principles of neutral donor bound excitons in silicon and the phenomena surrounding them. It starts in Sec. 5.1 with a description of the bound exciton and its energy, before discussing the bound exciton Auger decay, the capture time scale of the Auger electron by an ionized donor, and the competing photocarrier generation methods of intrinsic silicon absorption and direct photo-ionisation of donors. From the strength of these transitions, a fidelity estimate for spin-readout via the D^0X transition is deduced.

After this theoretical description of the phenomena, the subsequent sections deal with the experimental validation of three key aspects of the D^0X transition. Firstly, Sec. 5.2 investigates the photo carrier density and carrier type under D^0X laser excitation, both on- and off resonance, using photo-Hall measurements. Secondly, Sec. 5.3 investigates the changes of the D^0X transition energy as a function of crystal strain and magnetic field and the accurate theoretical description of the observed shifts. Finally, Sec. 5.4 concerns the hyperpolarization of the spin system via the D^0X transition and investigates the achievable polarisation degree and the time scale of the polarisation build-up.

5.1 The donor bound exciton

Excitons, i.e. electrostatically coupled electron-hole pairs, occur in semiconductors both as free particles and bound to defects. The free exciton is typically formed by photons with above-bandgap energy, exciting an electron from the valence band to the conduction band, which then binds to the generated hole via a Coulomb interaction. In semiconductors, due to the dielectric screening, the exciton binding energy is reduced, resulting in a Bohr radius ($a_X = 4.9\,\mathrm{nm}$ [150]) much larger than the lattice spacing, which is typical for Wannier-Mott excitons [112].

The energy of the free exciton is given by:

$$E_{\mathrm{X}} = E_{\mathrm{g}} + E_{\mathrm{kin}} - E_{\mathrm{BX}} \tag{5.1}$$

where E_{g} is the semiconductor bandgap, E_{kin} the kinetic energy of the free exciton and E_{BX} the free exciton binding energy, which is 15.0 meV at cryogenic temperatures [151]. Due to the range of possible E_{kin} the photoluminescence linewidths are in general relatively broad.

In contrast, excitons bound to impurities in semiconductors are defined by $E_{\mathrm{kin}} = 0$, resulting in much sharper transitions. Bound excitons can be formed both on acceptors and donors, in their neutral and under the right circumstances also in their charged configuration. The stability of the ionised donor/acceptor bound exciton ($\mathrm{D^+X}$ or $\mathrm{A^-X}$) depends on the ratio of the effective masses of hole and electron. For the case of silicon, this ratio $m_e^*/m_h^* \approx 0.61$ does not allow the formation of ionised donor/acceptor bound excitons [150].

Two different pictures for the neutral bound exciton formation can be found in the literature. The first one understands the bound exciton as the result of a capture process of a free exciton by a neutral donor with a certain capture cross section. This picture has its origin in photoluminesence (PL) measurements, where the $\mathrm{D^0X}$ spectrum is investigated under a constant above-bandgap illumination generating free excitons. In this picture, the bound exciton energy is given by the free exciton energy E_{X} with zero kinetic energy, modified additionally by a localisation energy of the exciton to the donor E_{loc}:

$$E_{\mathrm{D^0X}} = E_{\mathrm{g}} - E_{\mathrm{BX}} - E_{\mathrm{loc}} \tag{5.2}$$

E_{loc} in turn is known to scale with the binding energy of the donor/acceptor E_{D^0}, which is known as Haynes rule and given for the case of donors in silicon as [150]:

$$E_{\mathrm{loc}} = a + bE_{\mathrm{D}^0} \tag{5.3}$$

with $a \approx 0$ and $b \approx 0.1$ [150]. This results in $E_{\mathrm{loc}}(^{31}\mathrm{P}) \approx 5\,\mathrm{meV}$ and the total donor bound exciton energy is $E_{\mathrm{g}} - (E_{\mathrm{BX}} + E_{\mathrm{loc}}) \approx E_{\mathrm{g}} - 20\,\mathrm{meV}$.

A more accurate and quantitative description of the bound exciton ground state energy requires the solution of the Hamiltonian of three charged particles in a screened Coulomb potential plus the Hamiltonian of their mutual interactions [121]:

$$H_{\mathrm{D}^0\mathrm{X}} = H_{0,e_1} + H_{0,e_2} + H_{0,h} + H_{e_1,e_2} + H_{e_1,h} + H_{e_2,h} \tag{5.4}$$

The first three terms represent the single particle Hamiltonians of the two electrons and the hole without interactions and the last three terms represent the electron-electron and electron-hole interactions. Rahman *et al.* have solved this equation in an iterative, self-consistent manner [152] and, among other findings reconfirmed a central statement of the shell model for bound excitons introduced in the 1960's [153]:

Under small perturbations, the bound exciton energy is given by the energy of the three single particle wavefunctions of the electron and hole plus a phenomenological energy term for the particle interactions E_{pi} accounting for the neglected electron-electron and electron-hole interactions:

$$E_{\mathrm{D}^0\mathrm{X}} = E_{0,e_1} + E_{0,e_2} + E_{0,h} + E_{\mathrm{pi}} \tag{5.5}$$

The wavefunctions of the $\mathrm{D}^0\mathrm{X}$ ground state are hence well described by two electrons with opposing spin occupying the donor ground state $1\mathrm{sA}_1(m_s = \pm 1/2)$ and a hole that occupies one of the four-fold degenerate $J = 3/2$ valence band states. Since the electrons form a singlet, the spin of the $\mathrm{D}^0\mathrm{X}$ is entirely given by the hole spin with $m_j = \{-3/2, \ldots, 3/2\}$. Excited states of the bound exciton and multi-exciton complexes exist, in which multiple electron-hole pairs are localized at the donor [154]. Both of these are found at much higher transitions energies and do not play a role in the scope of this thesis.

A schematic of the $\mathrm{D}^0\mathrm{X}$ excitation and relaxation process under illumnation is given in Figure 5.1. Without external magnetic field, the laser excites the donor to its bound exciton state from which it decays non-radiatively via an Auger decay process. The ejected electron thermalizes and recombines with the ionised donor,

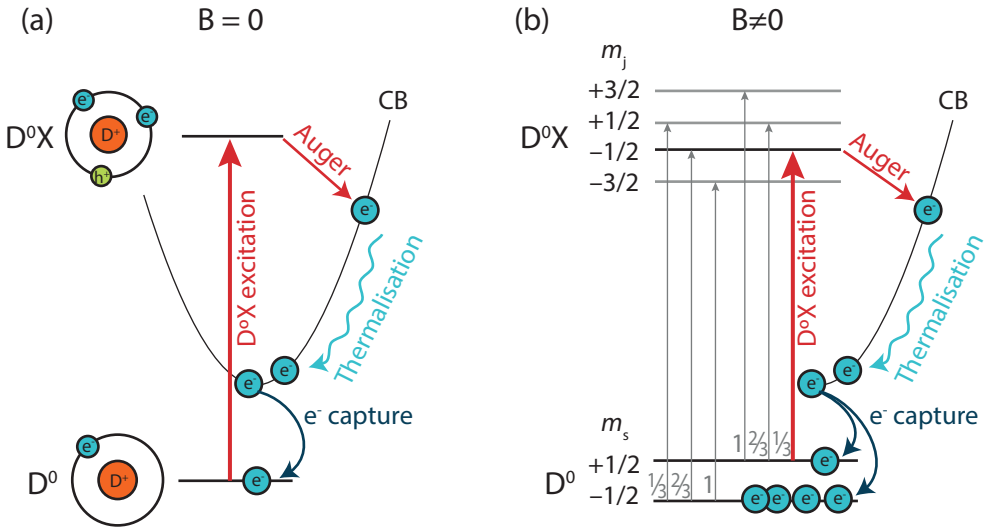

Figure 5.1: Schematic of the D^0X excitation, decay, thermalization and recombination processes of neutral donors in silicon under continuous laser excitation. (a) The situation in vanishing magnetic field, leading to a continuous cycling of the D^0X transition, while (b) in an external magnetic field, pumping on one of the six allowed D^0X transition leads to a depletion of the pumped donor state and a polarisation of the donor spin. The grey numbers in (b) indicate the relative strength of the transition matrix element according to the Clebsch-Gordon coefficients (c.f. Sec. 5.3.1).

forming the neutral donor from which the cycle can start again. Each of these processes is worth a detailed discussion which is done in the subsequent three subsections.

Figure 5.1(b) depicts the situation with finite magnetic field. The D^0X splits into four levels, while the D^0 splits into two[1]. The selection rules permit six allowed transitions. Pumping one of these transitions allows a build-up of polarisation of the neutral donor, which is investigated in Sec. 5.4.

5.1.1 D^0X excitation and oscillator strength

The D^0X excitation and radiative recombination are both single photon processes obeying the selection rule $\Delta m = 0, \pm 1$. Usually in indirect semiconductors either an optical or acoustic phonon has to take part in the process to ensure momentum conservation. However, since the donor impurity breaks the lattice periodicity, the short range potential may scatter the electron within the Brillouin zone, allowing the D^0X creation to be a no phonon process [150]. The equivalent, qualitative picture of this process is as follows: The localisation of the bound exciton leads

[1]Neglecting the nuclear spin terms, including hyperfine interaction, here for simplicity.

	oscillator strength $f_{\mathrm{D^0X}}$	τ_{rad} (µs)	$\tau_{\mathrm{D^0X,Auger}}$ (ns)	$\tau_{\mathrm{rad}}/\tau_{\mathrm{D^0X,Auger}}$
^{31}P	7.1×10^{-6}	2000	272	7353
^{75}As	10×10^{-6}	1420	183	7760
^{121}Sb	$\sim 7 \times 10^{-6}$	–	–	–
^{209}Bi	22×10^{-6}	–	–	–
^{11}B	29×10^{-6}	490	1055	464

Table 5.1: The oscillator strength of the D^0X transition for various donors and acceptors in silicon at $T < 2.1\,\mathrm{K}$ as given by Dean *et al.* [156], the estimated radiative lifetimes τ_{rad} due to these oscillator strengths and the experimentally observed lifetime $\tau_{\mathrm{D^0X,Auger}}$ due to Auger recombination as measured by Schmid *et al.* [28]

to a broadening in k-space due to Heisenberg's uncertainty principle and thus a finite wave function amplitude at $k = 0$. This in turn results in a finite no-phonon transition probability [150].

Both this k-space broadening and the "*giant oscillator*" effect in which all silicon atoms within the D^0X radius act as "antennas" for the transition result in a relatively large oscillator strength for the no phonon D^0X transition compared to their phonon–involved replicas and to the free exciton oscillator strength [150, 155]. Dean *et al.* extracted the D^0X oscillator strength of various donors and acceptors from absorption measurements with heavily doped samples [156]. The extracted values are summarized in Table 5.1.

As a figure of merit for the strength of this transition, the following calculates the Rabi frequency for oscillations between the D^0X state and the donor ground state of a single phosphorus donor in a typical laser intensity. The optical Rabi frequency is given by [157]

$$f_R = 2\pi \frac{2\mu_{21} E_0}{\hbar} \tag{5.6}$$

where $\mu_{21} = 1.3 \times 10^{-31}\,\mathrm{Cm}$ is the transition dipole moment for phosphorus calculated from its oscillator strength $f_{\mathrm{D^0X}} = 7.1 \times 10^{-6}$ following reference [157] and $E_0 = \sqrt{\frac{2I_{\mathrm{L}}}{cn_{\mathrm{Si}}\epsilon_0}}$ is the electric field strength due to the laser intensity I_{L} ($[\mathrm{W/m^2}]$) in a material with diffractive index n_{Si} (here silicon with $n_{\mathrm{Si}} \approx 3.7$). A power of 1 mW focussed on a spot size of 1 µm radius results in $f_R \approx 100\,\mathrm{MHz}$, allowing for coherent driving of a single donor between the bound exciton and neutral donor state. For $P = 100\,\mathrm{mW}$ and a typical beam diameter of the unfocussed laser of 3 mm, $f_R \approx 700\,\mathrm{kHz}$, which is significantly slower than the D^0X decay rate of $\Gamma_{\mathrm{Auger}} \approx 4\,\mathrm{MHz}$ (discussed in the next section), and hence within the scope of this thesis no coherent driving of the D^0X transition is reached.

Finally, an expression for the D^0X excitation rate Γ_{D^0X} of an ensemble of neutral donors with linewidth Δf in vanishing magnetic field is developed: The rate of photon absorption and equivalently neutral donor excitation depends on the Einstein coefficient for photon absorption B_{12}^f and the spectral overlap of the laser spectral power density $\rho(f)$ and the lineshape function of the donor ensemble $g(f, f_0)$. The rate equation for the neutral donor density N^0 is given by [139, 157, 158]:

$$\frac{\mathrm{d}N^0}{\mathrm{d}t} = -N^0 B_{12}^f \int_0^\infty g(f, f_0)\rho(f)df \equiv -\Gamma_{D^0X} N^0 \tag{5.7}$$

B_{12}^f is related to the oscillator strength by $B_{12}^f = e^2/(4\epsilon_0 m_0 \hbar\omega) f_{D^0X}$ [157], which gives for phosphorus $B_{12}^f = 3.1 \times 10^{16}\,\mathrm{J^{-1}m^3s^{-2}}$. $\rho(f)$ describes the laser power per unit volume and per laser frequency interval. In most cases, the D^0X laser is much sharper than the transition linewidth and can be approximated as a delta function:

$$\rho(f) = I_L/(c/n_{Si})\delta(f_0) \tag{5.8}$$

where I_L is the laser intensity $[(\mathrm{W/m^2})]$ and c is the speed of light. $g(f, f_0)$ represents the frequency dependence of B_{12}^f, i.e. it usually is a Lorentzian (for homogeneous broadening) or Gaussian function (for inhomogeneous broadening) with center frequency f_0 and linewidth Δf, whose integral is normalized to unity. The integral returns, for a δ-like laser spectral lineshape, the peak value of the Lorentzian or Gaussian function, which is to a good approximation given by $2/(\pi\Delta f)$.

In summary, the bound exciton transition rate, for a narrow laser linewidth compared to the ensemble linewidth, and when I_L is small enough to neglect coherent driving, is given by:

$$\Gamma_{D^0X} = B_{12}^f \int_0^\infty g(f, f_0)\rho(f)df \approx B_{12}^f \frac{I_L}{c/n_{Si}} \frac{2}{\pi\Delta f} \tag{5.9}$$

In an external magnetic field the D^0X transition strengths of the various transitions are not equal. Leaving a discussion of this effect to Sec. 5.3.1, it should simply be stated here that, for the case of the transitions from the $J = 1/2$ donor to $J = 3/2$ D^0X level, the relative intensities f_r are $f_r = 1$ for $m_s \pm 1/2 \rightarrow m_j = \pm 3/2$ transitions, $f_r = 2/3$ for $m_s \pm 1/2 \rightarrow m_j = \pm 1/2$ transitions, and $f_r = 1/3$ for $m_s \pm 1/2 \rightarrow m_j = \mp 1/2$ transitions. Figure 5.1 labels each transition with its corresponding relative intensity.

5.1.2 Radiative and Auger decay

Since silicon is an indirect semiconductor, the D^0X decays primarily via an Auger process in which one electron and a hole recombine and transfer the remaining energy to the residual electron, thereby ejecting it as a hot electron into the conduction band and leaving behind an ionised donor. The D^0X lifetime has been measured as $\tau_{D^0X,\mathrm{Auger}} = 272\,\mathrm{ns}$ for phosphorus [28] (cf. Table 5.1), which immediately gives a lower bound for the D^0X linewidth of $\Delta f_{D^0X} = 1/(2\pi\tau_{D^0X,\mathrm{Auger}}) = 585\,\mathrm{kHz}$. This is much smaller than the Zeeman splitting of the electron spin or the hyperfine interaction of donors in silicon and allows for spin-dependent D^0X ionisation.

The radiative lifetime is about 10^4 times longer (cf. Table 5.1), thus significantly affecting the luminescence quantum efficiency and rendering optical spin read-out for donors in the bulk of silicon impossible. Photon band structure engineering and Purcell enhancement may, however, be tools to increase the radiative decay rate [159, 160].

5.1.3 Electron capture by the ionized donor

In order to return to thermal equilibrium, the ionized donor left behind by the D^0X Auger decay eventuallys capture an electron from the conduction band. The capture process comprises an initial capture into an excited donor state, with subsequent phonon-assisted relaxation to the donor ground state [148]. The rate of the capture process, from the viewpoint of the ionized donor, should depend on the abundance of conduction band electrons (n). From the viewpoint of an electron in the conduction band the capture rate should depend on the concentration of ionised donors (N^+). The capture rate is thus described by a recombination coefficient $B_{n\to N^0}$ times nN^+ [161, 162]:

$$\frac{dn}{\mathrm{d}t} = \frac{dN^+}{\mathrm{d}t} = -B_{n\to N^0} N^+ n \tag{5.10}$$

The recombination coefficient $B_{n\to N^0}$ can, in principle, be understood as the donor having a certain capture cross section σ_R with which it captures an electron of thermal velocity $v_\mathrm{th} = \sqrt{8k_\mathrm{B}T/(\pi m^*)}$. This gives $B_{n\to N^0} = \sigma_\mathrm{R} v_\mathrm{th}$. However, it is favorable to discuss the capture rate in terms of $B_{n\to N^0}$ instead of σ_R because v_th is often modified due to drift currents and σ_R may furthermore have a dependence on v_th [161]. For silicon at temperatures between 1 K to 4 K $B_{n\to N^0}$ is roughly constant at $B_{n\to N^0} = 6.9\times10^{-6}\,\mathrm{cm^3/s}$ for phosphorus [163] and similar values are found for other shallow donors, as shown in Table 5.2. As a figure of merit, for a typical

	$B_{n\to N^0}$ (cm^3/s)	$\sigma_{\mathrm{direct,\,peak}}$ (cm^2)
^{31}P	6.9×10^{-6}	17×10^{-16}
^{75}As	7.2×10^{-6}	22×10^{-16}
^{121}Sb	1.6×10^{-6}	62×10^{-16}
^{209}Bi	34×10^{-6}	7.2×10^{-16}

Table 5.2: The recombination coefficient $B_{n\to N^0}$ for the conduction band electron capture process by the ionised donor as given by [163] and the peak value of the direct photo-ionisation $\sigma_{\mathrm{direct,\,peak}}$ of selected donors [162].

ionised phosphorus concentration of $N^+ \lesssim 1 \times 10^{13}\,\mathrm{cm}^{-3}$, the capture time scale of a conduction band electron is $1/(B_{n\to N^0} N^+) \gtrsim 15\,\mathrm{ns}$.

It should be noted that there is a competing electron capture process by a neutral acceptor A^0 to form A^-. The capture cross section for this process is about two orders of magnitude smaller [163]. Furthermore, the thermalization of the high energy Auger electron with energy loss via phonon emission is relatively quick, on the order of $\lesssim 1\,\mathrm{ns}$ at $4\,\mathrm{K}$ [148, 164] and is hence treated as an instantaneous process within the scope of this thesis.

If the spin measurement is designed to detect the charge state of the ionized donor instead of the change of sample conductivity due to Auger electrons, then it would be possible to control the recombination time by controlling the conduction electron density in the vicinity of the donor. This may be e.g. realized by using a single electron transistor (SET) to measure the charge state of a single donor. The gate voltages of the SET may then control the occupation of the 2DEG and therefore the reneutralisation time scale of the donor.

5.1.4 Competing carrier generation mechanism

As expected for wavelengths close to the band edge of silicon, there are also other mechanisms that absorb photons and are able to change the conductivity. Figure 5.2 shows a schematic of the processes involved and their photon energy dependence. In the vicinity of the bound exciton line, there are also other excitonic transitions, namely free exciton transitions and bound multi-exciton complexes, along with phonon replicas of all of these lines. Fortunately, in pure crystalline silicon, these lines are sufficiently narrow and spread, and do not overlap with the no-phonon bound exciton line [150]. The two mechanisms that could overlap with the bound exciton line are the intrinsic and extrinsic absorption. The extrinsic absorption describes a direct photo-ionisation of donors and acceptors that promotes a high energetic electron to the conduction band. The intrinsic absorption describes the

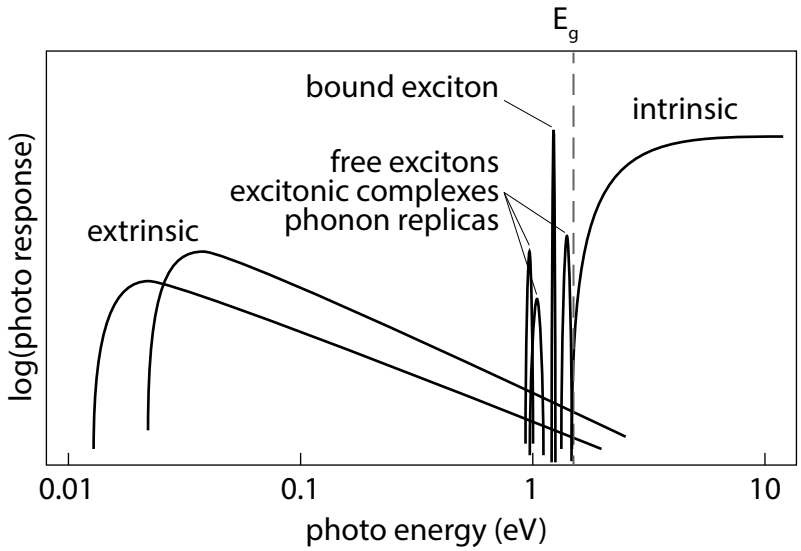

Figure 5.2: A schematic of the photo processes involved close to band edge of doped indirect semiconductors. The intensity ratio between bound exciton and free exciton transitions are arbitrary here, since they depend among other things on the doping concentration [150].

promotion of a valence band electron to the conduction band to form either a free exciton or free electrons and holes. The following sections investigate these two mechanisms in detail. In this section and throughout the thesis heating effects of the sample are largely omitted. This is based on the results of reference [165], which found by studying free exciton photoluminescence lineshapes, that, even for above bandgap radiation ($\hbar\omega \approx 2.5\,\mathrm{eV}$), laser intensities $I_\mathrm{L} > 2 \times 10^6\,\mathrm{W/m^2}$ are required to raise the sample temperature by more than 1 K, with the sample immersed in a liquid helium bath. The laser intensities used throughout this thesis are at least two orders of magnitude smaller, typically four orders of magnitude smaller.

5.1.4.1 Intrinsic absorption of silicon

The intrinsic absorption of a photon in a semiconductor excites an electron from the valence band to the conduction band. For indirect semiconductor absorption, due to momentum conservation, the process must involve the emission or absorption of a phonon with wave vector $\mathbf{k}_\mathrm{phonon}$ that matches the separation in k-space of valence band and conduction band (cf. Sec. 3.2 & Fig. 3.2). In general, all four branches of the silicon phonon spectrum (cf. Sec. 3.1 & Fig. 3.1) can contribute to the absorption, but for silicon, the transitions involving LA and LO phonons are weak. Thus, it is sufficient to only invoke the TA- and TO-assisted transitions with $E_\mathrm{TA} = 18\,\mathrm{meV}$ and $E_\mathrm{TO} = 58\,\mathrm{meV}$. In general, at low temperatures and close

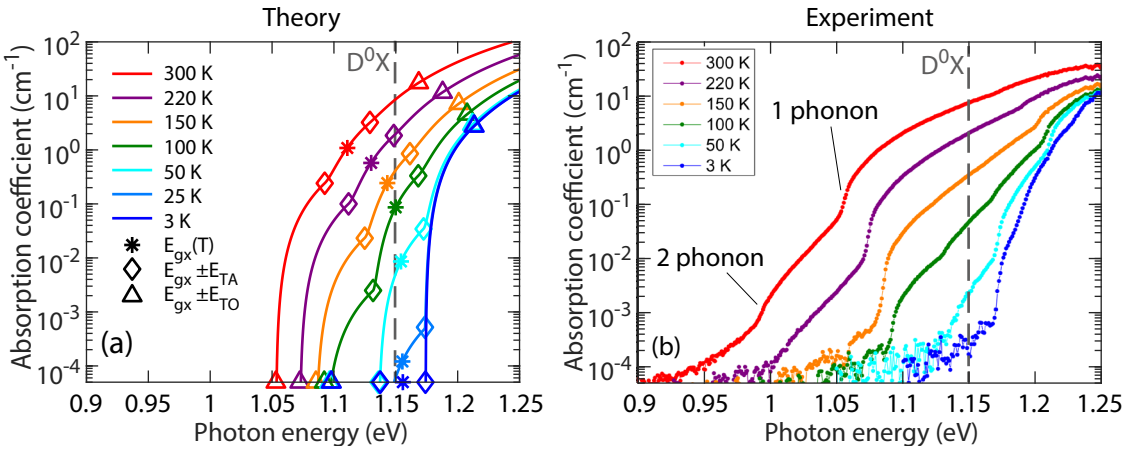

Figure 5.3: The intrinsic photon absorption in silicon. The theoretical analysis (a) features multiple phonon edges corresponding to the emission and annihilation of *TA* and *TO* phonons. A freeze out of the phonon bath towards lower temperatures suppresses the phonon-annihilation assisted absorption. The theoretical description matches well experimental data (b) obtained by J. Komma in the group of R. Nawrodt at the Friedrich Schiller University, Jena. except for 2-phonon annihilation processes at higher temperatures.

to the band edge, the absorption does involve the formation of free excitons with binding energy $E_\mathrm{X} = 15.0\,\mathrm{meV}$ [116, 151]. It is difficult to describe the functional dependence of the absorption edge in a closed analytical form [166], but for photon energies several factors of E_X above the bandgap the dependence can be approximated as $(\hbar\omega - (E_\mathrm{g} - E_\mathrm{X} \pm E_\mathrm{phonon}))^2$, where the $\pm$ sign refers to phonon emission or annihilation.

The phonon-annihilation assisted process also depends on the phonon density at the particular temperature. Hence, the absorption coefficient over the complete temperature range can be approximated as [166, 167]:

$$\alpha_\mathrm{annihilation} \propto \mathcal{N}(E_\mathrm{phonon})\,(\hbar\omega - (E_\mathrm{g} - E_\mathrm{X} - E_\mathrm{phonon}))^2 \tag{5.11}$$

for the case of phonon annihilation, where $\mathcal{N}(E_\mathrm{phonon}) = \left[\exp\left(\frac{E_\mathrm{phonon}}{k_\mathrm{B}T}\right) - 1\right]^{-1}$ is the temperature-dependent phonon occupation number. For processes with phonon creation, the absorption coefficient is correspondingly:

$$\alpha_\mathrm{creation} \propto (1 + \mathcal{N}(E_\mathrm{phonon}))\,(\hbar\omega - (E_\mathrm{g} - E_\mathrm{X} + E_\mathrm{phonon}))^2 \tag{5.12}$$

Figure 5.3(a) plots the thus derived theoretical intrinisic absorption as a function of photon energy and temperature, following closesly the derivation[2]. and fit values of Rajkanan *et al.* [110]. For temperatures close to room temperature, absorption with phonon annihilation gives rise to a distinct increase in absorption at $\hbar\omega = E_g - E_X - E_{TO}$ (red triangle at 1.05 eV in Fig. 5.3(a)), with a further absorption edge at energies where *TA*-annihilation assisted absorption becomes allowed (red diamond at 1.09 eV). With decreasing temperature, the phonon bath freezes out (higher energy *TO* phonons first) and absorption with phonon annihilation is suppressed. For $T = 3\,\mathrm{K}$, phonon-annihilation assisted absorption vanishes completely and the absorption edge is located at the lowest energy phonon-creation process with $\hbar\omega = E_g - E_X + E_{TA}$.

Experimental data at liquid helium temperatures and $\hbar\omega \approx 1.15\,\mathrm{eV}$ is scarce due to the low absorption coefficient value, with instrument sensitivity limits on the order of $1 \times 10^{-2}\,\mathrm{cm}^{-1}$ [169]. Private communication with R. Nawrodt[3] enabled us to access (as yet) unpublished data on the intrinsic absorption of silicon with unprecedented precision. The results are depicted in Figure 5.3(b) and the qualitative and quantitative agreement between data and theory is remarkable, especially since the data for the original theory fit had a sensitivity limit of $10\,\mathrm{cm}^{-1}$ [110]. Still, there are two main differences compared with the theory traces. Firstly, two phonon processes occur at higher temperatures which are not captured by the theory. However, for temperatures with phonon bath freeze out, i.e. $T < 50\,\mathrm{K}$, these processes are not of significance.

Secondly, there is a deviation from the theoretical lineshape for the $T = 50\,\mathrm{K}$ and especially the $T = 3\,\mathrm{K}$ trace at the lower energy side of the absorption edge. While the theoretical treatment predicts a sharp drop at the edge, the data shows a more gentle decrease of the absorption coefficient below the absorption edge. The reason for this discrepancy remains unknown so far and could be due to measurement errors, heating (see i.e. the $T = 25\,\mathrm{K}$ trace in Fig. 5.3(a)) or extrinsic photoconductivity. A systematic study of the absorption coefficient as a function of doping concentration should be able to resolve the origin of this absorption below the excitonic bandgap.

[2]The bandgap used in this publication is in fact the excitonic bandgap $E_{gx} = E_g - E_X$, as evident from the low temperature bandgap value of ∼1.155 eV, about 15 meV lower than the actual low temperature bandgap value of silicon[115, 151, 168]

[3]Ronny Nawrodt, Friedrich Schiller University Jena, with data taken by his PhD student Julius Komma.

Nevertheless, an upper bound for the absorption coefficient at 4.5 K and 1.15 eV can be deduced from the data to:

$$\alpha_{\mathrm{Si}}(3\,\mathrm{K},\ 1.15\,\mathrm{eV}) \lesssim 3 \times 10^{-4}\,\mathrm{cm}^{-1} \tag{5.13}$$

How does the intrinsic absorption contribute to the charge transport? For photon energies much larger than the bandgap it is expected that due to the high energy the exciton dissociates, leading to an increased density of free electron n and free holes p. This is the typical, intuitive photoconductive response to above bandgap light. However, for all lasers used throughout this thesis the photon energy is $\hbar\omega < E_{\mathrm{g}} + E_{\mathrm{phonon}}$ and thus the kinetic energy of the exciton is smaller than its binding energy E_{X}. The formed free excitons do not dissociate thermally at low temperatures, but instead can decay via three possible recombination pathways:

The first path is dissociation in an electric field, i.e. that the electric field is strong enough to overcome its binding energy and rip the exciton apart. The order of magnitude required for this is given by $2E_{\mathrm{X}}/ea_{\mathrm{X}}$ [170], with $a_{\mathrm{X}} \approx 4.9\,\mathrm{nm}$ as the free exciton Bohr radius [150]. This gives an electric field dissociation threshold of $\mathcal{E} \approx 6.7 \times 10^6\,\mathrm{V/m}$. Typical biases used within this thesis are on the order of 1 V over $\sim$1 mm ($\mathcal{E} \approx 10^3\,\mathrm{V/m}$), hence it is unlikely that electric field ionisation plays a role.

The second mechanism is radiative recombination with phonon emission, with a time scale of $\tau_{\mathrm{X,rad}} \approx 50\,\mu\mathrm{s}$ [171, 172]. This pathway does not alter n or p.

The third pathway is the trapping of the free exciton by a neutral donor or acceptor, creating a donor bound exciton. The bound exciton decays via the Auger process and hence leads to an exclusive increase of n for donors or p for acceptors. The trapping process is described by the following equation for the free excition density N_{X}:

$$\frac{\mathrm{d}N_{\mathrm{X}}}{\mathrm{d}t} = \frac{\mathrm{d}N^0}{\mathrm{d}t} = -B_{\mathrm{X}\to\mathrm{D^0X}} N^0 N_{\mathrm{X}} \tag{5.14}$$

with $B_{\mathrm{X}\to\mathrm{D^0X}} \approx 2.3 \times 10^{-7}\,\mathrm{cm}^3/\mathrm{s}$, [172, 173]. The free exciton lifetime can be calculated as $\tau_{\mathrm{X}} = (B_{\mathrm{X}\to\mathrm{D^0X}} N^0)^{-1} = 4\,\mathrm{ns}$ for $N^0 = 1 \times 10^{15}\,\mathrm{cm}^{-3}$. This is much shorter than the radiative lifetime meaning that free excitons are almost instantaneously bound to neutral donors and, via the Auger process, lead to an increase of n.

The free exciton generation rate for the case where the absorption length $1/\alpha_{\mathrm{Si}}$ is much larger than the sample thickness (which is the case for $\hbar\omega \approx 1.15\,\mathrm{eV}$ and

$T < 10\,\mathrm{K}$) is given by [174]:

$$G_{\mathrm{X,intrinsic}} = \frac{I_{\mathrm{L}}}{\hbar\omega}\alpha_{\mathrm{Si}} \tag{5.15}$$

5.1.4.2 Direct photo-ionisation of donors and acceptors

An incoming photon can also directly ionize a donor (acceptor) and send the electron (hole) to the conduction band continuum if the photon energy is larger than the binding energy of the donor E_{D^0}. The direct photo-ionisation absorption cross section σ_{direct} thus has a long-wavelength cut-off at the wavelength corresponding to E_{D^0}, as shown in Fig. 5.4(a) for a variety of donors and acceptors in silicon at liquid helium temperatures [161]. The peak cross section magnitude and the functional dependence of the cross section on wavelength depends strongly on E_{D^0} and there is no unified theoretical description [161]. The cross section is calculated by Fermi's golden rule, but depending on the assumed donor potential (hydrogen-like, effective mass or δ-function) and output states (continuum Hydrogen, Bloch functions) the theoretical predicted cross sections peak between E_{D^0} and $2E_{\mathrm{D}^0}$ and have a functional dependence towards higher photon energies between $(\hbar\omega)^{-7/2}$ and $(\hbar\omega)^{-3/2}$ [175–177].

Figure 5.4(b) depicts the ionisation cross section of arsenic as a function of wavelength. It is found that the cross section for shorter wavelengths follows $(\hbar\omega)^{-1.34} \approx (\hbar\omega)^{-3/2}$. The cross section at the $\mathrm{D^0X}$ transition energy (1.15 eV or 1078 nm) can be extrapolated to $1-2\times10^{-16}\mathrm{cm}^2$, which is approximately 1/10 th to 1/20 th of the peak photo ionisation cross section $\sigma_{\mathrm{direct,\,peak}}$. The values of $\sigma_{\mathrm{direct,\,peak}}$ for various donors are given in Table 5.2. Due to the similar peak cross section value and similar donor binding energies for phosphorus and arsenic, it should be reasonable to assume that the wavelength dependence of the ionisation cross section of phosphorus is similar to that of arsenic.

The off-resonant, direct donor ionisation rate can then be described as [157, 174]:

$$\frac{\mathrm{d}N^0}{\mathrm{d}t} = -N^0\frac{I_{\mathrm{L}}}{\hbar\omega}\sigma_{\mathrm{direct}} \equiv -\Gamma_{\mathrm{direct}}N^0 \tag{5.16}$$

where $I_{\mathrm{L}}/(\hbar\omega)$ is the photon flux, i.e. the number of photons passing the sample per area and time. At 1.15 eV and 4 K, $G_{\mathrm{direct}} = \Gamma_{\mathrm{direct}}N^0 > G_{\mathrm{X,intrinsic}}$ for donor densities $N^0 > 1\times10^{13}\,\mathrm{cm}^{-3}$.

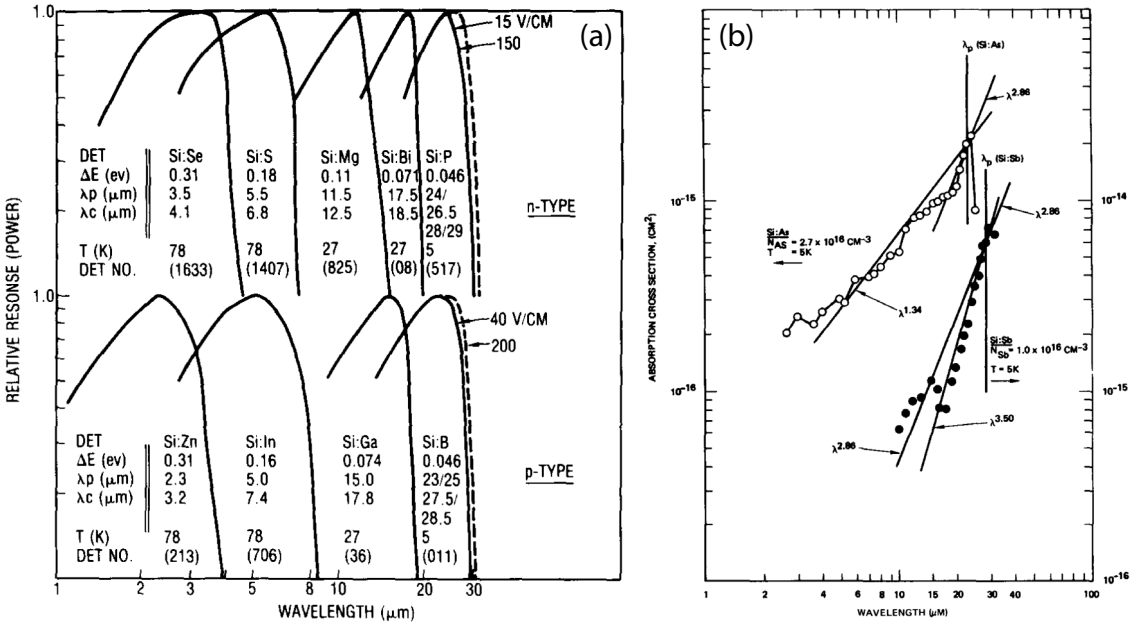

Figure 5.4: The donor ionisation cross section as a function of laser energy. (a) The ionisation cross section peaks at a laser wavelength close to the corresponding ionisation energy of the donor (reproduced from [162]). (b) The dependence towards shorter wavelength for arsenic and antimony at 5 K (reproduced from [161]). The established theory (solid lines) is not able to fit the data (circles) over the entire energy range.

5.1.5 Fidelity estimate for D^0X single spin readout

With known values for the D^0X oscillator strength and the direct donor ionisation cross section, it is possible to estimate an upper limit for the single donor spin readout fidelity via the D^0X-assisted spin to charge conversion. Following this scheme, without loss of generality, the D^0X laser is chosen to pump on the $|\uparrow\rangle$ state for some duration t_p. The $|\uparrow\rangle$ state error $e_\uparrow$ is given by the probability $P_\uparrow$ that the $|\uparrow\rangle$ state remained neutral during illumination, $e_\uparrow = P_\uparrow$. For the $|\downarrow\rangle$ state, an unintentional ionisation constitutes an error, i.e. $e_\downarrow = 1 - P_\downarrow$. The measurement fidelity is defined as the average of these two errors, given by [24]:

$$F_M = 1 - \frac{e_\downarrow + e_\uparrow}{2} \tag{5.17}$$

Two different modes of operation, which depend on the laser power used, must be distinguished: i) weak excitation with laser pulses much longer than the Auger decay, and ii) coherent driving of the $D^0 \rightleftharpoons D^0X$ system, where a short strong laser pulse acts as a π-pulse. This section only discusses the former process, because the derivations for the latter do not show a significant fidelity increase and are discussed in Appendix B.

In the weak excitation limit, the optical Bloch equations for the $D^0 \rightleftharpoons D^0X$ transition reduce to the Einstein rate equations [139]. It is assumed that the Auger decay of the excited D^0X is much faster than the drive and, furthermore, that no reneutralisation is happening. Using the Einstein absorption equation, the evolution for the probability of a $|\uparrow\rangle$ donor to be neutral is given by Eq. (5.7):

$$\frac{dP_\uparrow}{\mathrm{d}t} = -P_\uparrow \Gamma_{D^0X} \tag{5.18}$$

where Γ_{D^0X} depends on the homogeneous linewidth Δf of a single donor. A lower bound[4] for Δf due to the Auger decay rate gives $\Delta f = 585\,\mathrm{kHz}$. The solution of Eq. (5.18) with $P_\uparrow(t=0) = 1$ is:

$$P_\uparrow(t) = \exp(-\Gamma_{D^0X} t) = e_\uparrow \tag{5.19}$$

The direct ionisation process has been omitted above due to its lower excitation rate; it is, however, the driving factor for the ionisation of the $|\downarrow\rangle$ state. Following Eq. (5.16) the rate equation for the probability $P_\downarrow$ of $|\downarrow\rangle$ to stay neutral is given by:

$$\frac{dP_\downarrow}{\mathrm{d}t} = -P_\downarrow \Gamma_{\mathrm{direct}} \tag{5.20}$$

For the calculation of Γ_{direct} a lower estimate for the ionisation cross section is used with $\sigma_{\mathrm{direct}} = \sigma_{\mathrm{direct,\,peak}}/20$. The solution for $P_\downarrow(t)$ with $P_\downarrow(t=0) = 1$ is:

$$P_\downarrow(t) = \exp(-\Gamma_{\mathrm{direct}}\, t) = 1 - e_\downarrow \tag{5.21}$$

Combining these two results gives the measurement fidelity as a function of laser pulse duration:

$$F_{\mathrm{M}}(t) = \frac{1}{2}\left[1 + \exp\left(-\Gamma_{\mathrm{direct}}\, t\right) - \exp\left(-\Gamma_{D^0X}\, t\right)\right] \tag{5.22}$$

Figure 5.5 plots $e_\uparrow$ and $e_\downarrow$ as a function of time and also the combined, average measurement error $1 - F_{\mathrm{M}}(t)$. Clearly, there is an optimum laser pulse duration that allows for optimum D^0X ionisation of $|\uparrow\rangle$, while keeping the direct ionisation

[4] The only reported homogeneous linewidth value for phosphorus has been stated in A. Yang's thesis as $\Delta f \approx 2.4\,\mathrm{MHz}$, approximately four times larger than the lifetime limited value [178].

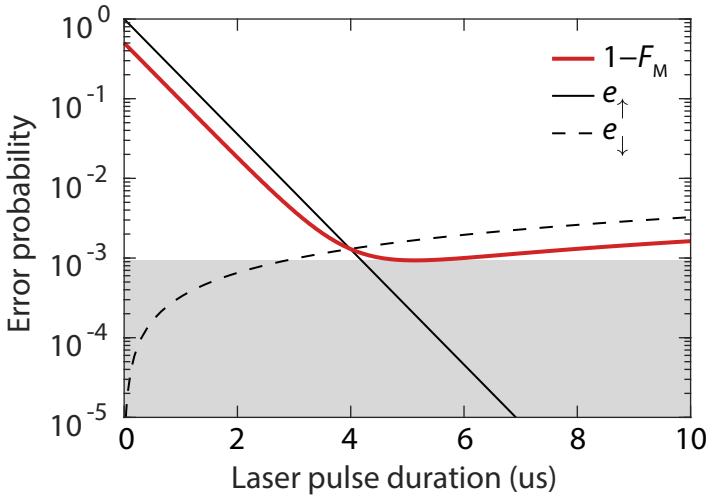

Figure 5.5: Error rate for the $|\uparrow\rangle$- and $|\downarrow\rangle$-state and the average measurement error $1 - F_{\mathrm{M}}$ of the $\mathrm{D^0X}$ spin to charge conversion as a function of laser pulse duration. The $\mathrm{D^0X}$ laser is assumed to be tuned to $|\uparrow\rangle$. The optimum pulse duration (here $t_{\mathrm{p,\,opt}} \approx 5\,\mu\mathrm{s}$) is a function of laser power (here shown for a typical power of $I_{\mathrm{L}} \approx 7 \times 10^3\,\mathrm{W/m^2}$), while the achievable fidelity only depends on the ratio $\Gamma_{\mathrm{D^0X}}/\Gamma_{\mathrm{direct}} \approx 5 \times 10^3$ for phosphorus.

of $|\downarrow\rangle$ as low as possible. This optimum pulse duration is given by:

$$t_{\mathrm{p,\,opt}} = \frac{\ln\left(\frac{\Gamma_{\mathrm{D^0X}}}{\Gamma_{\mathrm{direct}}}\right)}{\Gamma_{\mathrm{D^0X}} - \Gamma_{\mathrm{direct}}} \tag{5.23}$$

and results in a best-achievable measurement fidelity of:

$$F_{\mathrm{M}}(t_{\mathrm{p,\,opt}}) = \frac{1}{2}\left[1 + \left(\frac{\Gamma_{\mathrm{D^0X}}}{\Gamma_{\mathrm{direct}}}\right)^{\frac{1}{1+\left(\frac{\Gamma_{\mathrm{D^0X}}}{\Gamma_{\mathrm{direct}}}\right)}} - \left(\frac{\Gamma_{\mathrm{D^0X}}}{\Gamma_{\mathrm{direct}}}\right)^{\frac{1}{\left(\frac{\Gamma_{\mathrm{direct}}}{\Gamma_{\mathrm{D^0X}}}\right)-1}}\right] \tag{5.24}$$

$$\approx \frac{1}{2}\left[1 + \left(\frac{\Gamma_{\mathrm{D^0X}}}{\Gamma_{\mathrm{direct}}}\right)^{-\frac{\Gamma_{\mathrm{direct}}}{\Gamma_{\mathrm{D^0X}}}} - \frac{\Gamma_{\mathrm{direct}}}{\Gamma_{\mathrm{D^0X}}}\right] \tag{5.25}$$

where the last approximation holds for $\Gamma_{\mathrm{D^0X}} \gg \Gamma_{\mathrm{direct}}$. The achievable fidelity thus only depends on the ratio $\Gamma_{\mathrm{D^0X}}/\Gamma_{\mathrm{direct}}$. Both $\Gamma_{\mathrm{D^0X}}$ and Γ_{direct} depend linearly on I_{L}, meaning that the $F_{\mathrm{M}}(t_{\mathrm{p,\,opt}})$ is independent of laser power. For phosphorus in silicon $\Gamma_{\mathrm{D^0X}}/\Gamma_{\mathrm{direct}} \approx 5 \times 10^3$ and the achievable single spin measurement fidelity is thus $F_{\mathrm{M}}(t_{\mathrm{p,\,opt}}) \approx 99.91\,\%$. It should be noted that this single-shot electron spin measurement fidelity is an estimate, based on relatively old data for the $\mathrm{D^0X}$ oscillator strength and an extrapolated value for direct photo-ionisation cross section σ_{direct}. It could thus be possible that the reported value is inaccurate.

An error rate of 1×10^{-3} is about one order of magnitude above the commonly cited error threshold for surface code quantum computation of 1 % (cf. Ch. 2). Furthermore this value is more than an order of magnitude better than the best experimental donor electron spin-readout with an error rate of 3 % [26].

It should be noted that both of these electron measurement fidelities were derived for the single shot measurement of the electron spin. If the measurement fidelity is of critical importance and if the donor nuclear spin is not used in the quantum circuit, then it should be possible to trade read-out time for fidelity. Since the nuclear spin projection stays constant during D^0X ionisation of the donor [18], it is possible to first perform a SWAP operation, transfering the electron spin coherence to the nuclear spin [18, 19]. Subsequent donor electron spin initilisation and nuclear spin state dependent electron spin flips constitute a quantum non-demoliton (QND) measurement of the nuclear spin. This QND measurement can be repetitively performed, restricted only by the long T_1 time of the nuclear donor spin and thus enables significantly improved measurement fidelities at the expense of measurement time and resource overhead [25].

5.1.6 Coupled rate equations for the donor, exciton and conduction band densities

The final part of this section deals with the coupled rate equations of the processes discussed in this chapter. Restricting the discussion to close-to-bandgap excitation and low temperature the coupled rate equations for the conduction band electron density n, the neutral donor $|\uparrow\rangle$- and $|\downarrow\rangle$- densities $N_\uparrow$ & $N_\downarrow$, the bound exciton density $N_{\mathrm{D^0X}}$ and the free exciton density N_{X} are (cf. Sections 5.1.2 to 5.1.4.2):

$$\frac{\mathrm{d}N_\uparrow}{\mathrm{d}t} = -\Gamma^{\uparrow}_{\mathrm{D^0X}} N_\uparrow - \Gamma_{\mathrm{direct}} N_\uparrow - B_{\mathrm{X}\to\mathrm{D^0X}} N_\uparrow N_{\mathrm{X}} + \frac{1-P_{\mathrm{th}}}{2} B_{n\to N^0} N^+ n - \mathrm{d}N^{\uparrow\downarrow}_{T_1} \tag{5.26}$$

$$\frac{\mathrm{d}N_\downarrow}{\mathrm{d}t} = -\Gamma^{\downarrow}_{\mathrm{D^0X}} N_\downarrow - \Gamma_{\mathrm{direct}} N_\downarrow - B_{\mathrm{X}\to\mathrm{D^0X}} N_\downarrow N_{\mathrm{X}} + \frac{1+P_{\mathrm{th}}}{2} B_{n\to N^0} N^+ n + \mathrm{d}N^{\uparrow\downarrow}_{T_1} \tag{5.27}$$

$$\frac{\mathrm{d}n}{\mathrm{d}t} = N_{\mathrm{D^0X}}/\tau_{\mathrm{D^0X,Auger}} + \Gamma_{\mathrm{direct}}(N_\uparrow + N_\downarrow) - B_{n\to N^0} N^+ n \tag{5.28}$$

$$\frac{\mathrm{d}N_{\mathrm{D^0X}}}{\mathrm{d}t} = \Gamma^{\uparrow}_{\mathrm{D^0X}} N_\uparrow + \Gamma^{\downarrow}_{\mathrm{D^0X}} N_\downarrow + B_{\mathrm{X}\to\mathrm{D^0X}}(N_\uparrow + N_\downarrow) N_{\mathrm{X}} - N_{\mathrm{D^0X}}/\tau_{\mathrm{D^0X,Auger}} \tag{5.29}$$

$$\frac{\mathrm{d}N_{\mathrm{X}}}{\mathrm{d}t} = G_{\mathrm{X,intrinsic}} - N_{\mathrm{X}}/\tau_{\mathrm{X,rad}} B_{\mathrm{X}\to\mathrm{D^0X}}(N_\uparrow + N_\downarrow) N_{\mathrm{X}} \tag{5.30}$$

For the neutral donor density a T_1 term has been included as $\mathrm{d}N_{T_1}^{\uparrow\downarrow} = ((N_\uparrow - N_\downarrow) - P_{\mathrm{th}}(N_\uparrow + N_\downarrow))/T_1$. As discussed in Sec. 5.1.4.2, close to and below the bandgap the direct photo ionisation rate $\Gamma_{\mathrm{direct}}(N_\uparrow + N_\downarrow)$ outweighs the free exciton generation rate $G_{\mathrm{X,intrinsic}}$. In this case the assumption $G_{\mathrm{X,intrinsic}} \approx 0$ and $N_{\mathrm{X}} \approx 0$ is valid. The choice of the ionised donor concentration N^+ is quite critical, as will be seen in Sec. 5.2.2. A common assumption used throughout this thesis is $N^+ = N_{\mathrm{A}} + (N^0 - N_\uparrow - N_\downarrow)$. The basis for this assumption is that a residual acceptor concentration N_{A} leads to donor-acceptor recombination [179], ionising an equal density of donors. It should be noted that under strong photo-illumination a reversal of the donor-acceptor recombination has been observed, with an increase of neutral donors for a fully compensated sample as a function of laser power [179]. At the wavelengths and powers used within this thesis, no such effects seem to occur and the ionised donor concentration seems to be constant as indicated by the linear dependence of n on I_{L} in Secs. 5.2 & 6.2.2).

5.2 D^0X photo-Hall Measurements

This section aims to understand the changes of conductivity, carrier concentration and mobility under illumination with the laser on- and off resonance with the D^0X transition. So far, the D^0X photoconductivity has not been investigated in a quantitative matter, nor has it been known, whether mobility changes, e.g. due to increased ionized donor scattering, play a significant role. Therefore photo-Hall measurements of precisely these quantities as a function of laser power and photon energy are presented in the following section.

Section 5.2.1 introduces the principle of the van-der-Pauw Hall measurement, while Sec. 5.2.2 shows the laser power dependence of carrier concentration and mobility, both on resonance with the D^0X transition and off resonance.

The sample used is the same for which the magnetoresistance and carrier freeze-out were investigated in Sec. 3.5.3 and Sec. 3.5.4, which drew the conclusion that the electron mobility at $\sim$4 K and $B = 0$ T should be 6–8 $\times 10^4\,\mathrm{cm}^2/(\mathrm{V\,s})$.

5.2.1 Van-der-Pauw photo-Hall measurement

Section 3.5.2 described the emergence of a Hall voltage in a magnetic field, perpendicular to both the current and magnetic field direction. The Hall voltage allows one to deduce the carrier density and (in combination with a conductivity measurement) a value for the Hall mobility. These two measurements are ideally carried out using a Hall bar geometry, where the Hall bar arms enable an accurate four-point resistivity measurement and a Hall measurement that is performed with the Hall voltage leads perfectly perpendicular to the current direction. A draw back of this arrangement is that it requires significantly more fabrication steps. An alternative is the method of van-der-Pauw, which allows for conductivity and Hall measurements of arbitrarily shaped samples. Its requirements can be easily met and are:

- The contacts must be made at the edges of the sample.
- The contact separation must be much larger than the thickness of the sample.
- The sample thickness must be uniform and the conductivity must be isotropic and homogeneous.
- The sample must not have have holes or non-conducting islands.

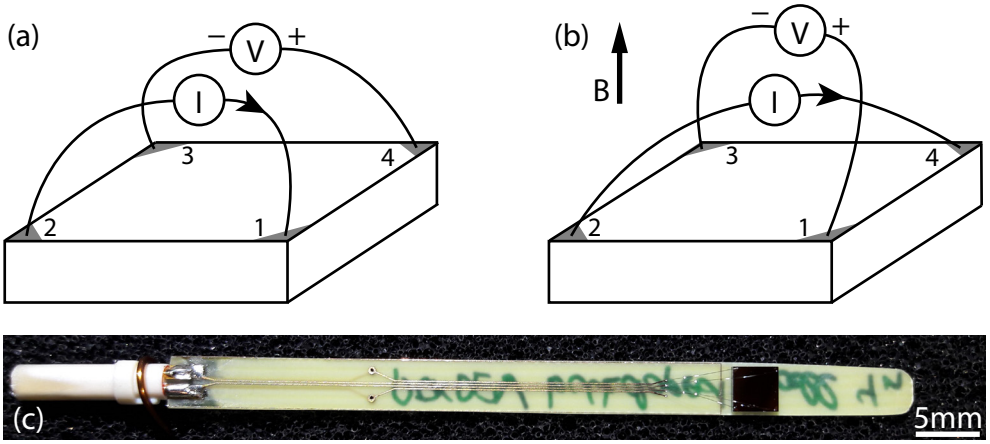

Figure 5.6: The van-der-Pauw conductivity and Hall measurement. Connection schematic of the current source (I) (with the technical current direction indicated by the arrow) and voltmeter (V) for (a) the conductivity measurement and (b) the Hall measurement with positive magnetic field direction indicated. (c) An image of sample natSi-Hall mounted on a PCB that fits into a regular 5 mm ESR tube. It is connected via copper PCB tracks and aluminium bond wires.

The following measurements follow the excellent guide by the National Institute of Standards and Technology[5]. Sample natSi-Hall is a square cut from a bulk doped wafer with 3.5 mm long edges. Four ohmic contacts (arsenic implant and aluminium bond pads) in the four corners are connected via aluminium wire bonds, as depicted in Fig. 5.6(c).

For the conductivity measurements, the sample is connected as depicted in Fig. 5.6(a). The current is sourced along one edge of the sample and the voltage measured on the opposite side. From a linear sweep of the source bias, the resistance value $R_{12,43} = \Delta V_{43}/\Delta I_{12}$ is fitted. Similarly, $R_{23,14}$ is measured along the perpendicular edge of the sample, with current sourced from contact 2 to 3 and voltage measured from contact 1 to 4. Van-der-Pauw showed that the sheet resistivity of the sample R_S links these two perpendicular four-point resistivity measurements according to [180]:

$$\exp(-\pi R_{12,43}/R_S) + \exp(-\pi R_{23,14}/R_S) = 1 \tag{5.31}$$

[5] `https://www.nist.gov/pml/engineering-physics-division/popular-links/hall-effect`, written by W. Robert Thurber at NIST Gaithersburg, Maryland.

This equation is solved numerically[6] to determine the value of R_S. The sample conductivity is given by $\sigma_0 = 1/(R_S d)$ with d as sample thickness. Two further measurements are carried out with current sourced along the other two sides of the sample to deduce another sheet resistance value to improve accuracy and check consistency.

The configuration of the Hall measurement is depicted in Fig. 5.6(b). The current is sourced diagonally from contacts 2 to 4, with voltage being measured on the other diagonal from contacts 3 to 1. As above, a resistance value $R_{24,31} = \Delta V_{31}/\Delta I_{24}$ is determined from a voltage sweep. If the current direction and voltage measurement leads are not perfectly perpendicular, then $R_{24,31}$ will include a component proportional to the voltage drop from contact 2 to 4. By performing the measurement both in positive magnetic field $R_{24,31\mathrm{p}}$ and under field reversal with negative magnetic field ($R_{24,31\mathrm{n}}$) the pure Hall voltage contribution can be extracted as $R_{24,31} = (R_{24,31\mathrm{p}} - R_{24,31\mathrm{n}})/2$. The sign of $R_{24,31}$ determines the carrier type[7], with $R_{24,31} > 0$ identifying electron majority charge carriers and $R_{24,31} < 0$ for hole majority carriers (cf. Eq. (3.28)). The carrier density can be determined according to Eq. (3.25):

$$n = \frac{B_z}{e|R_{24,31}|d} \tag{5.32}$$

Again, to increase accuracy and judge measurement consistency, the measurement and analysis is also carried out with current sourced from contacts 1 to 3 and voltage measured from contact 2 to 4.

The Hall mobility is then calculated by Eq. (3.26) as $\mu_H = \sigma_0/(en)$.

5.2.2 D^0X laser power influence on carrier density and mobility

The photo-Hall measurements are conducted at 4.5 K and in a magnetic field of 300 mT for both the Hall and resistivity measurement. Different photon energies are investigated, with the laser tuned both on- and off resonance with the D^0X transition and an additional measurement at a slightly above bandgap energy of 1.18 eV.

Figure 5.7 plots the photocurrent as a function of photon energy. Compared to typical ^{nat}Si spectra, this sample shows a large D^0X linewidth of 200 µeV, which is likely due to strain caused by the mounting (cf. Sec. 5.3): For various samples an

[6] If the sample is a perfect square, both resistivity measurements should give the same result and Eq. (5.31) can be solved numerically with $R_S = \pi R_{12,43}/\ln 2$, thus requiring only a single measurement. The perfect square assumption has not been taken in the presented measurements.

[7] Bearing the difficulties for similar carrier concentrations $n \approx p$ or vastly different mobilities of holes and electrons, discussed in Section 3.5.2.

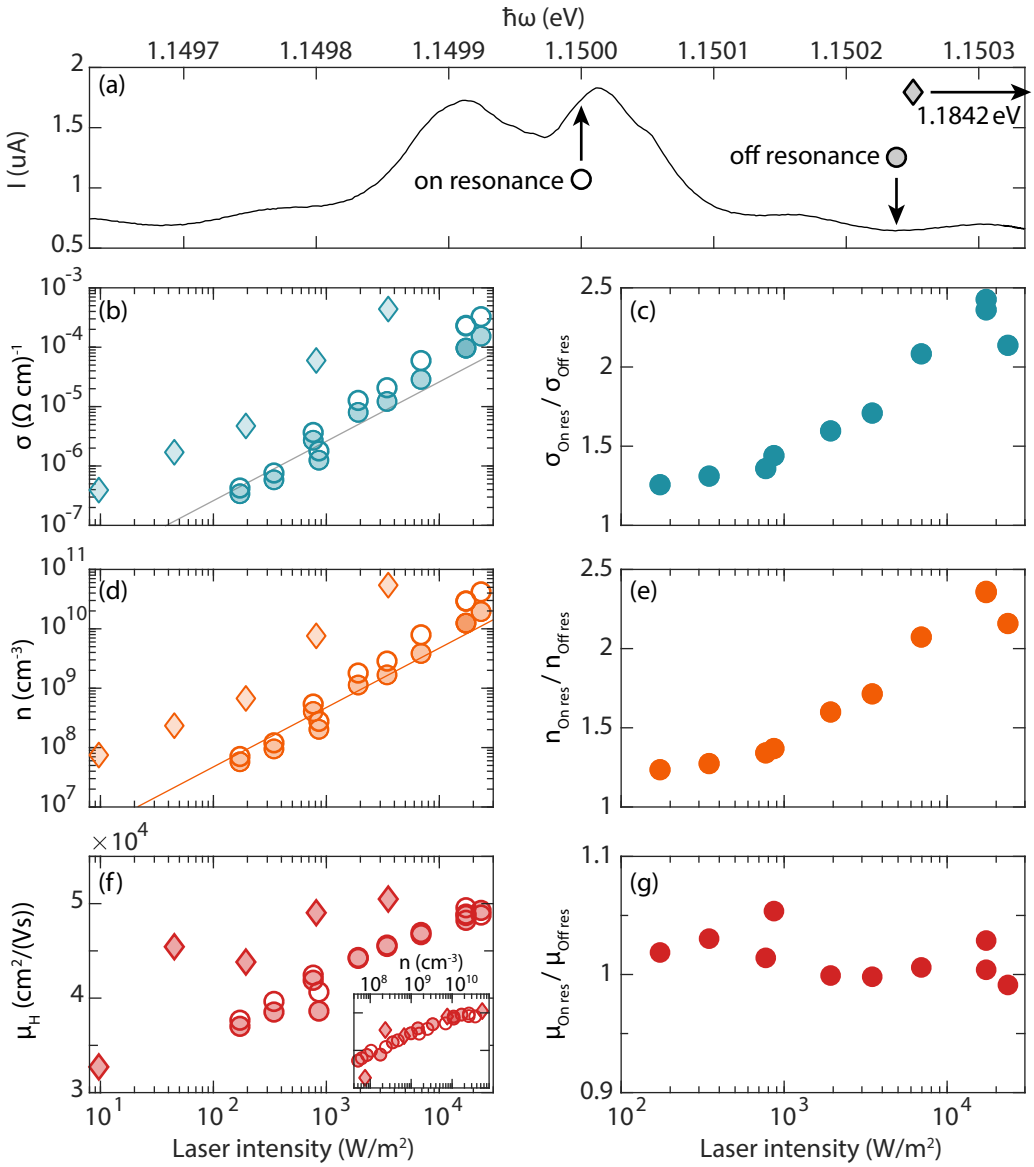

Figure 5.7: (a) The D^0X spectrum, taken for a laser intensity of $I_L = 1.8 \times 10^4\,W/m^2$ and $V_{13} = 1\,V$ voltage bias exhibits a relatively broad linewidth, but clearly shows an on-resonant (clear circles) and off-resonant (shaded circles) behaviour. The oscillations, visible on both sides of the resonance, are likely due to interferences caused by reflections of the two cryostat windows. (b) The carrier density, (d) conductivity and (f) Hall mobility as a function of incident laser power. Data points for 1.18 eV illumination are indicated as diamonds. (c),(e) & (g) The ratio of the respective physical quantities on and off resonance.

increase in linewidth has been observed if the position at which it is glued via GE Varnish to the PCB is close to the measured donors of the device. With this square sample geometry it is impossible to move the glue-location away from the active area of the device, so a large, strain-induced line broadening can not be avoided. Still, a clear increase in conductivity is observed on resonance with the D^0X transition.

A laser energy of 1.150 008 eV (clear circles) is chosen for the on-resonant photon energy and 1.150 238 eV (shaded circles) for the off-resonant data and the Hall measurements are performed for different laser powers under continuous illumination. The results are shown in Figs. 5.7(b,d,f) along with measurements slightly above bandgap at 1.1842 eV indicated as diamonds. Figures 5.7(c,e,g) plot the corresponding ratio between the measured quantity on resonance divided by its value off resonance. In the following, first the D^0X data are discussed, followed by the above bandgap data.

Conductivity on/off resonance with the D^0X transition With the laser energy in the vicinity of 1.15 eV both the conductivity and carrier density increase with increasing laser intensity for all laser conditions. The carrier type is n-type and a linear dependence is observed between n and I_L (cf. orange line). The steady state photocarrier density depends on the balance of the laser intensity-dependent carrier generation rate $G(I_\mathrm{L})$ and photocarrier recombination rate $\tau_n(I_\mathrm{L})$ as [174]:

$$n = G(I_\mathrm{L})\tau_n(I_\mathrm{L}) \tag{5.33}$$

From the discussion of Sec. 5.1.4.2, it can be can assumed that at 1.15 eV the intrinsic charge generation is much weaker than the D^0X- and off-resonant direct ionisation rate and hence $\alpha_\mathrm{Si} \approx 0$. Furthermore, both the D^0X excitation rate $\Gamma_{\mathrm{D^0X}}$ and the direct photo ionisation rate Γ_direct scale linearly with I_L. The main recombination process for the electrons is the trapping by an ionised donor impurity (cf. Sec. 5.1.3) with an recombination time of $\tau_n = 1/(B_{n\rightarrow N^0} N^+)$. In order to ensure a linear dependence of n with I_L, N^+ must be independent of I_L. If only the ionised donors that promoted electrons to the conduction band were partaking in the recombination, τ_n would, however, depend on I_L. Hence, additionally, a mechanism seems to exist that ensures a (to first order) constant N^+ density. A likely mechanism that enables a subset of donors to be permanently ionised is the so-called 'donor-acceptor recombination' [179]: If a donor has an acceptor in its immediate vicinity, the electron of the donor recombines with the hole of the acceptor, thus ionising both the acceptor and donor. The charge transfer time

scale depends exponentially on the donor-acceptor separation, and sufficiently close donors might be ionised independent of conduction band electron density. The acceptor concentration of the wafer is unknown, but a value of $N_A = 10^{12-14}\,\mathrm{cm}^{-3}$ does not seem unreasonable, when compared e.g. with the acceptor concentrations of the ^{28}Si samples.

A further uncertainty in the results is the actual laser power within the sample. Beam reflections on the silicon surface are on the order of 40 % and may additionally be affected by the laser delivery direction, which is in-plane with the sample due to the requirement of perpendicular mounting of the sample in the magnetic field. Furthermore, absorptions/reflections due the metallic grid of the resonator cavity and the various optical windows are present. In the following, the laser power within the sample was estimated to be about 10 % of I_L. Defining an error range for this estimate is difficult but the actual laser intensity could easily be another factor 2–5 off.

The solution of Eq. (5.33) for the off-resonant case is plotted as the orange line in Fig. 5.7(d). Literature values($\sigma_{\mathrm{direct}} = 0.05\sigma_{\mathrm{direct,\,peak}}$) were used for Γ_{direct} and the recombination time was used as a fit parameter, giving $\tau_n \approx 29\,\mathrm{ns}$. This corresponds to a reasonable value of $N^+ \approx 5 \times 10^{12}\,\mathrm{cm}^{-3}$.

The Hall mobility μ_H, both on and off resonance also increases with I_L, but only by around 20 % over two orders of magnitude variation in I_L. It is thus mainly the change of Δn that influences the photoconductivity, which also scales roughly linearly (grey line in Fig. 5.7(b)). The mobility value at $I_L = 1.8 \times 10^4\,\mathrm{W/m^2}$ ($5 \times 10^4\,\mathrm{cm^2/(Vs)}$) is the same as that extracted from the magnetoresistance data at 300 mT (Fig. 3.8). The magnetoresistance study showed that the photocarrier mobility at 4.5 K and 0 mT matched very well the extrapolated electron mobility of the temperature study of Fig. 3.9 and thus it seems very likely that it is purely n-type photoconductivity with only a negligible hole contribution to the photo transport. An even stronger argument for this conclusion can be found from the mobility ratio $\mu_{\mathrm{On\,res}}/\mu_{\mathrm{Off\,res}}$. For all laser powers this ratio is very close to one, while the carrier density change about a factor of 2. This points to the conclusion that in both cases the same photo-carrier type is responsible for the conductivity and since the on-resonant carrier density rise is known to be caused by the D^0X Auger electrons, it is reasonable to assume that the off-resonant photocarriers are also electrons.

Photoconductivity for slightly above bandgap excitation The discussion for photon energies above bandgap, i.e. the diamond data points of Figs. 5.7 (b, d & f) with $\hbar\omega \approx 1.1842\,\mathrm{eV}$, is not as conclusive. The photo carrier density for a given I_L

is about one to two orders of magnitude higher than that for $\hbar\omega \approx 1.15\,\mathrm{eV}$. At first glance, the carrier mobility at $\hbar\omega \approx 1.18\,\mathrm{eV}$ also seems larger for each laser intenstiy. However, when plotting mobility against carrier density (cf. inset of Fig. 5.7), then all three laser conditions show roughly the same behaviour – a slight increase in carrier mobility towards higher carrier densities.

This may lead to the conclusion that also at $\hbar\omega \approx 1.184\,\mathrm{eV}$, electrons are the main charge carrier, which would fit the arguments presented in Sec. 5.1.4.1. For 1.1842 eV the exciton energy after a transition from the valence band to the conduction band via emission of the lowest energy *TA*-phonon is 4 meV below the conduction band. Thus the formed free exciton should localize at a donor to form a bound exciton, which then decays via the Auger process and emission of an electron. Hence, pure electron conduction seems reasonable at 1.1842 eV for this sample ($N_\mathrm{D} \gg N_\mathrm{A}$).

However, when considering the measured absorption coefficient, an inconsistency emerges. From the 3 K graph of Fig. 5.3(b) an absorption coefficient of $\alpha_n(1.1842\,\mathrm{eV}) \approx 0.033\,\mathrm{cm}^{-1}$ is deduced. Using this to calculate the exciton generation rate[8] $G_{\mathrm{X,intrinsic}}$ results in a value that is on the same order of magnitude as the direct ionisation rate $\Gamma_{\mathrm{direct}} N^0$. This would result in a similar conduction band concentration to the one measured under (off-resonant) 1.15 eV excitation. In order to be consistent with free exciton capture and Auger recombination, either the electron lifetime τ_n must be dramatically longer at 1.18 eV compared to 1.15 eV or the experimental absorption coefficient is erroneous. Both of these theories can not be verified with the available data.

Still, the data suggest that indeed, at 1.18 eV the photoconduction is primarily due to a conduction band electron majority. Further investigations are, however, needed to clarify the origin and electron lifetime limiting process behind the photoconductivity at 1.18 eV.

[8] Which by the principle of detailed balance is also the exciton decay rate and therefore electron generation rate.

5.3 Influence of magnetic field and strain on the D^0X transition

This section investigates the D^0X transition energy in greater detail. As both the donor energy and the D^0X state are functions of the local strain and magnetic field, it is expected that the transition energy is also subject to these influences. Theoretical expressions for the transition energy are developed in Sec. 5.3.1 and subsequently used in Sec. 5.3.2 to explain the observed spectrum of Sample 28Si-epi—a strained layer of phosphorus doped ^{28}Si, grown epitaxially on top of a $^{\mathrm{nat}}$Si substrate.

5.3.1 D^0X transition energy

As discussed in Sec. 5.1, under weak perturbations of the wavefunctions, the bound exciton energy can be calculated as the single particle energies of the electrons and hole, which both depend on magnetic field and strain and a (to a first order constant) term for the inter-particle interactions E_{pi}, accounting for the electron-electron and electron-hole interaction. The electron single particle energies are the donor ground state energies in an external magnetic field[9] $E_{0,e} = E_{\mathrm{D}^0,\,m_s}$. The hole occupies one of the Zeeman-split valence bands characterised by m_j with energy $E_{0,h} = -E_{\mathrm{VB},\,m_j}$.

The photon energy required for the transition from the D^0 m_s state to the D^0X m_j state is given by the difference in energy of the D^0X and D^0 levels, given by Eq. (5.5) as:

$$\begin{aligned}\hbar\omega &= E_{\mathrm{D^0X}} - E_{\mathrm{D^0}} && (5.34)\\ &= \left(E_{\mathrm{D^0},+1/2} + E_{\mathrm{D^0},-1/2} - E_{\mathrm{VB},\,m_j} + E_{\mathrm{pi}}\right) - E_{\mathrm{D^0},m_s} && (5.35)\\ &= E_{\mathrm{D^0},\,-m_s} - E_{\mathrm{VB},\,m_j} + E_{\mathrm{pi}} && (5.36)\end{aligned}$$

$E_{\mathrm{D^0},\,m_s}$ and its strain and magnetic field dependence can be calculated from Eqs. (3.12) & (3.13), while the valence band energy $E_{\mathrm{VB},\,m_j}$ follows Eq. (3.8).

The result can also be interpreted in a more intuitive picture of the D^0X-formation: Besides the particle interaction term E_{pi} the transition energy only depends on the difference between the unoccupied donor level and the valence band in which the hole is created. Hence, in a qualitative manner, the D^0X creation

[9] As in Sec. 5.1 the nuclear spin contribution to the Hamiltonian including the hyperfine interaction are neglected here for simplicity.

can be interpreted as the excitation of a valence band electron to the unoccupied donor level. This and the corresponding allowed transitions are illustrated in Figure 5.8(a), along with the conventional labeling of the bound exciton transition. The forbidden transitions are labelled f1 and f2.

As mentioned previously, not all of the D^0X transitions in an external magnetic field are equally strong. The transition strength depends on the transition matrix element between initial state $|J, m_j\rangle$ and final state $|J', m_j'\rangle$ with the dipole moment $e\mathbf{r}$, given by $\langle J, m_j|e\mathbf{r}|J', m_j'\rangle$. Following the Wigner-Eckardt rule the entire angular momentum dependence can be factored out, leading to a decomposition into a reduced matrix element and the Clebsch-Gordon coefficient [139]:

$$\langle J, m_j|e\mathbf{r}|J', m_j'\rangle = \langle J, m_j||e\mathbf{r}||J', m_j'\rangle \, \langle J, m_j|J', 1, m_j', q\rangle \tag{5.37}$$

$$= \langle J, m_j||e\mathbf{r}||J', m_j'\rangle \, (-1)^{J'-1+m_j} \sqrt{2J+1} \begin{pmatrix} J' & 1 & J \\ m_j' & q & -m_j \end{pmatrix} \tag{5.38}$$

The term in the final decomposition is the Wigner *3-j symbol*. As stated, the square of the right-hand side entirely describes the relative transition probability and calculation of these coefficients for the transitions from the $J = 1/2$ donor state to the $J' = 3/2$ D^0X level ($|J, m_j\rangle \rightarrow |J', m_j'\rangle$) result in the following relative intensities:

$$\begin{aligned} |1/2, \pm 1/2\rangle \rightarrow |3/2, \pm 3/2\rangle &\;\widehat{=}\; 1 \\ |1/2, \pm 1/2\rangle \rightarrow |3/2, \pm 1/2\rangle &\;\widehat{=}\; 2/3 \\ |1/2, \pm 1/2\rangle \rightarrow |3/2, \mp 1/2\rangle &\;\widehat{=}\; 1/3 \end{aligned}$$

Figure 5.1 labels each D^0X transition with its corresponding relative intensity.

5.3.2 Phosphorus D^0X transitions measured in a ^{28}Si epilayer

In the following, an experiment is discussed that highlights the strain and magnetic field induced shifts of the D^0X transition. The sample used is sample 28Si-epi for which the donor spin coherence time is measured in Sec. 7.1. A sketch of the sample with its electrical connection is given in Fig. 5.8(c). The sample consists of a 25 µm thick epitaxially grown layer of ^{28}Si:P with a phosphorus concentration of $1 \times 10^{15}\,\mathrm{cm}^{-3}$. The substrate for the ^{28}Si:P layer is undoped natural silicon. Parallel aluminium contacts (thickness: 30 nm, length: 700 µm, separation: 100 µm)

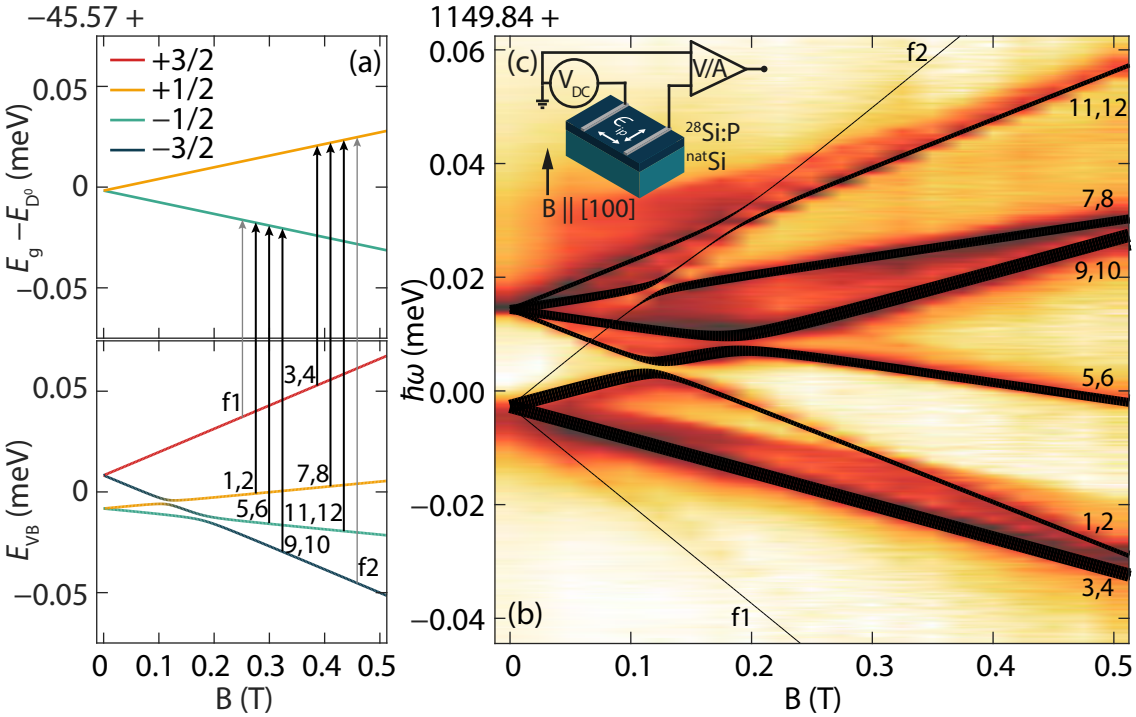

Figure 5.8: The strain and magnetic field dependence of the D^0X transition. (a) The shifts of the donor energy E_{D^0} and valence band E_{VB} as a function of magnetic field. Intrinsic in-plane compressive strain is assumed, leading to a zero-field splitting between heavy-hole and light-hole states. (b) The current through the device (sketched in (c)) as a function of laser energy and magnetic field. Each magnetic field slice is normalized to erase the superimposed effect of magnetoresistance and darker areas correspond to higher photocurrents. Superimposed on top of the color plot is a calculation of the shifts of the D^0X transition energy, where the linewidth corresponds to the transition probability. The transition labelling follow the convention of [31], which takes into account the donor hyperfine splitting.

are lithographically patterned on top of the ^{28}Si:P layer. A bias voltage of $V = 100\,\text{mV}$ is applied and the photocurrent is measured via a Femto DLPCA low noise amplifier. The sample is mounted with its [100] axis roughly parallel to the external magnetic field. The donors are excited with the D^0X laser oriented in-plane and the temperature is 4.5 K.

Figure 5.8(b) plots the colour-coded current through the device as a function of laser wavelength and magnetic field. For each magnetic field step, the photocurrent data is normalized to erase the effect of magnetoresistance. When the laser is on resonance with a D^0X transition, the photocurrent increases as discussed in the previous section. At high magnetic field, the six characteristic D^0X lines are observable. At vanishing magnetic field, however, these lines do not reduce to a single degenerate transition. Instead, a zero-field splitting of $\Delta_{zfs} \approx 20\,\mu\text{eV}$ is observed.

The observed splitting can be explained by a lifting of the valence band degeneracy between the heavy-hole and light-hole bands. This is shown in Fig. 5.8(a) for biaxial tensile strain, following Eq. (3.8). The cause of the strain is a mismatch between lattice parameters of the ^{nat}Si substrate and the ^{28}Si epitaxial layer. Following the derivation detailed in references [122, 181], the zero field splitting caused by a lattice parameter mismatch $\Delta a/a$ between film and substrate is given by:

$$\Delta_{\mathrm{zfs}} = 4b\frac{C_{11}}{C_{11}+2C_{12}}\frac{\Delta a}{a} \tag{5.39}$$

where $b = -1.72\,\mathrm{eV}$ [121] is the deformation potential introduced in Sec. 3.2.1 and $C_{11} = 1.6772 \times 10^{11}\,\mathrm{Pa}$ and $C_{12} = 0.6498 \times 10^{11}\,\mathrm{Pa}$ are the elastic constants of silicon towards 0 K [122]. For the measured $\Delta_{\mathrm{zfs}} \approx 20\,\mu\mathrm{eV}$ a relative difference between the ^{28}Si and ^{nat}Si lattice constant of $\frac{\Delta a}{a} \approx -3.2 \times 10^{-6}$ can be inferred, with the ^{nat}Si lattice constant being larger. These findings are in very good agreement with the result of Yang *et al.* of $\frac{\Delta a}{a} = 3.0 \times 10^{-6}$, acquired for a 5 µm thick ^{28}Si epitaxial layer with lower doping concentration [122].

In order to understand the magnetic field dependence of the spectrum, Fig. 5.8(b) overlays the predicted D^0X transition energy as calculated by Eq. (5.34) over the measured data. The transition probability, determined by the Clebsch-Gordon coefficients, is encoded in the width of the plotted lines. Since the strain and the magnetic field cause a mixing of heavy-hole and light hole states, even the forbidden transitions f1 & f2 become semi-allowed at lower magnetic field.

Excellent agreement between experiment and theory can be observed with very reasonable simulation inputs: The strength of the avoided crossing of line 5,6 and 9,10 at ∼0.2 T is due to the misalignment of crystallographic [100] axis and the axis of the magnetic field and the simulation uses a reasonable misalignment of 8°. The avoided crossing of line 1,2 and 9,10 at ∼0.15 T, can only be explained by an asymmetry of the two in-plane strain components $\epsilon_{y,\mathrm{ip}} = 0.8\epsilon_{x,\mathrm{ip}}$. The reason of this asymmetry is unknown, but could derive from the sample mounting or sample dicing.

The intensities of the measured spectrum follow the respective transition probability very well. Furthermore, there is clear evidence in the data of avoided crossings caused between the allowed transistions 7,8 & 11,12 and the forbidden transition f2. There is also a faint signal in the vicinity of the theoretically predicted forbidden transition f1. Its field dependence, however, deviates from the prediction by the fit to the rest of the observed spectrum.

In summary, excellent agreement between the measured data and the predicted transition energy and transition probability has been reached. The observed shifts of the D^0X transitions due to strain and magnetic field were related to shifts of the single particle energy levels and all observed avoided crossings are explained by the theory. The line intensities followed the expected Clebsch-Gordon transtion probabilities.

5.4 D^0X hyperpolarisation of the electron spin

All ensemble measurements of spin-related phenomena require a population difference between the the $|\uparrow\rangle$ and $|\downarrow\rangle$ states, i.e. a net polarisation of the spin ensemble. In thermal equilibrium, the spin polarisation P is given by a Boltzmann distribution, resulting in $P_{\mathrm{th}} = \tanh(\hbar\omega/2k_{\mathrm{B}}T)$ for a two-level system with energy separation $\hbar\omega$. At liquid helium temperatures $T = 4.2\,\mathrm{K}$ and X-band frequencies $\omega/2\pi = 10\,\mathrm{GHz}$, this results in an electron spin polarisation of 5.7 % and negligible nuclear spin polarisation.

Optical pumping of the D^0X transition provides a mechanism to exceed the thermal equilibrium polarisation. Pioneering work regarding D^0X spin hyperpolarisation has been performed in Prof. Thewalt's group at Simon Fraser University. First, using n-type ^{28}Si samples in which the hyperfine splitting could be resolved, Albion Yang demonstrated an electron spin polarisation of $P_{\mathrm{e}} = 90\,\%$ and a nuclear spin polarisation of $P_{\mathrm{n}} = 76\,\%$ [33]. Here, the laser was tuned to depopulate the $|\uparrow\Downarrow\rangle$ state and a strong nuclear spin polarisation was achieved due to the cross relaxation process ($|\downarrow\Uparrow\rangle \leftrightharpoons |\uparrow\Downarrow\rangle$). In later work by Steger and Saeedi, a more complex hyperpolarisation scheme was used, involving simultaneous pumping of two D^0X transitions and RF pulses to manipulate the nuclear spin. With these improvements $P_{\mathrm{n}} \approx 90\,\%$ could be reached on a time scale of 100 ms [18, 31].

In both cases, the polarisation degree was deduced from the photoluminescence spectrum obtained by a weak probe laser. In this Section, a complementary and more direct measurement of the achieved polarisation is employed—the intensity of an ESR echo. Section 5.4.1 explains the mechanism of hyperpolarisation, Sec. 5.4.2 discusses the resulting ESR and photoconductivity spectra under cw illumination and Sec. 5.4.3 investigates the time scale and efficiency of the process.

5.4.1 Polarisation process

A schematic of the (hyper-) polarisation process is given in Fig. 5.9(a). The laser is tuned to pump selectively on one spin orientation (here the $|\uparrow\rangle$ state). This leads to a spin-selective ionisation of donors with electrons in the $|\uparrow\rangle$ state. The created D^0X decays via the Auger process and the Auger electron thermalizes quickly to the bottom of the conduction band, adopts a thermal spin polarisation and is captured by a donor[10].

[10] From the initial Auger decay to the capture process the electron looses 1.15 eV of energy through multiple scattering processes. When compared to the Zeeman splitting of ∼40 µeV at 340 mT

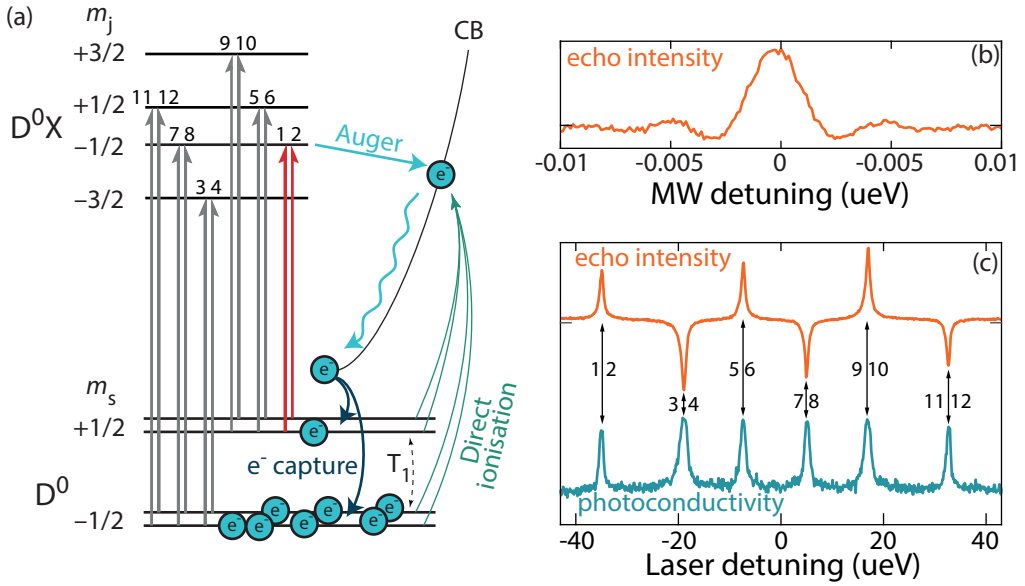

Figure 5.9: (a) Principle of donor hyperpolarisation by a continuous D^0X drive. (b) The ESR echo intensity in the dark, used for the calibration of the ensemble polarisation axis. (c) The echo intensity and capacitively measured photoconductivity of sample 28Si-Buf as a function of photon energy around $\hbar\omega = 1.149\,85\,\text{eV}$.

Continuous pumping on one state thus leads to an increased population in the opposite spin state (not addressed by the laser). Counteracting this polarisation process are two effects:

The first is spin-lattice relaxation, i.e. T_1 processes. At liquid helium temperatures and $\omega/2\pi = 10\,\text{GHz}$ these are on the order $\sim$10 s [16, 182], hence should not have a strong influence on the achievable polarisation. However, at elevated temperatures T_1 becomes comparable to the D^0X generation rate. As an example, for ^{28}Si with a D^0X linewidth of $\sim$1 µeV ($\sim$250 MHz) and for a typical laser intensity of $I_\text{L} = 2 \times 10^3\,\text{W/m}^2$, the D^0X excitation rate according to Eq. (5.9) is $\Gamma_{D^0X} \approx 2.5 \times 10^3\,\text{s}^{-1}$, which is larger than $1/T_1$ only for temperatures $T \lesssim 9\,\text{K}$ [16]. Furthermore, interaction of donor electron spins with photo carriers in the conduction band may lead to enhanced T_1 relaxation processes under illumination, which, however, could not be quantified within this thesis.

The second effect reducing the achievable ensemble polarisation is the direct ionisation of neutral donors, as discussed in Sec. 5.1.4.2. This process is independent of spin-orientation and thus serves to reduce population imbalances. The achievable donor polarisation in the limit of negligible T_1 processess hence depends only on the ratio between the D^0X generation rate and the direct donor ionisation rate [33].

it is not surprising that the orginal spin orientation of the electron is lost and the electron recombines with the thermal polarisation.

5.4.2 ESR measurement of the donor polarisation

As a measurement of the electron spin polarisation, the ESR echo following a standard Hahn sequence with duration $2\tau = 30\,\mu s$ is used. The echo intensity in the dark (cf Fig. 5.9(b)) is used to calibrate the polarisation magnitude, assuming thermal polarisation.

Two different samples were used within this section: The first one is sample 28Si-331, which is a bulk ^{28}Si sample with a phosphorus concentration of $[P] = 2 \times 10^{14}\,cm^{-3}$. The second sample is sample 28Si-Buf, which also has $[P] \approx 2 \times 10^{14}\,cm^{-3}$, but has also been coimplanted with arsenic ($[As] \approx 5 \times 10^{14}\,cm^{-3}$) and antimony ($[Sb] \approx 1 \times 10^{14}\,cm^{-3}$). Both samples have a similar phosphorus D^0X linewidth of $\sim$250 MHz.

Fig. 5.9(c) depicts a laser wavelength sweep and the simultaneous recording of the echo amplitude and the photoconductivity[11] of sample 28Si-Buf. The six D^0X transitions are clearly visible, but are too broad ($\sim$250 MHz) to resolve the hyperfine splitting (117.5 MHz) of the donor levels. On resonance, the sample conductivity increases and simultaneously the echo intensity increases in absolute magnitude. Three of the D^0X resonances, when excited, lead to an increase of the thermal polarisation direction (lines 1-2, 5-6 & 9-10), while three of the transitions invert the polarisation (lines 3-4, 7-8 & 11-12). The relative strength of the six ESR lines, and therefore the achievable polarisation degree follows the strength of the D^0X transition. Those lines with higher Clebsch-Gordon coefficients (3-4 & 9-10) and therefore stronger D^0X excitation rate exhibit a higher polarisation compared to the weak lines (1-2 & 11-12). This will be explained in the following section.

5.4.3 Polarisation dynamics and polarisation degree

The time dynamics of the hyperpolarisation process are depicted in Fig. 5.10(a) in which the ensemble spin polarisation (measured by ESR) is plotted against time with the D^0X laser active for $t > 0.1\,s$. Thermal equilibrium is achieved by a long above-bandgap illumination prior to the captured time window. Upon illumination with the D^0X laser on resonance (light blue) the polarisation increases with a $1/e$-time scale of 30 ms and assumes a steady state value of about 85 %. In contrast, with the laser off resonance (dark blue), the steady state polarisation does not significantly differ from the thermal equilibrium polarisation of a trace in the dark (black dots).

[11] Measured capacitively with the technique discussed in Ch. 6.

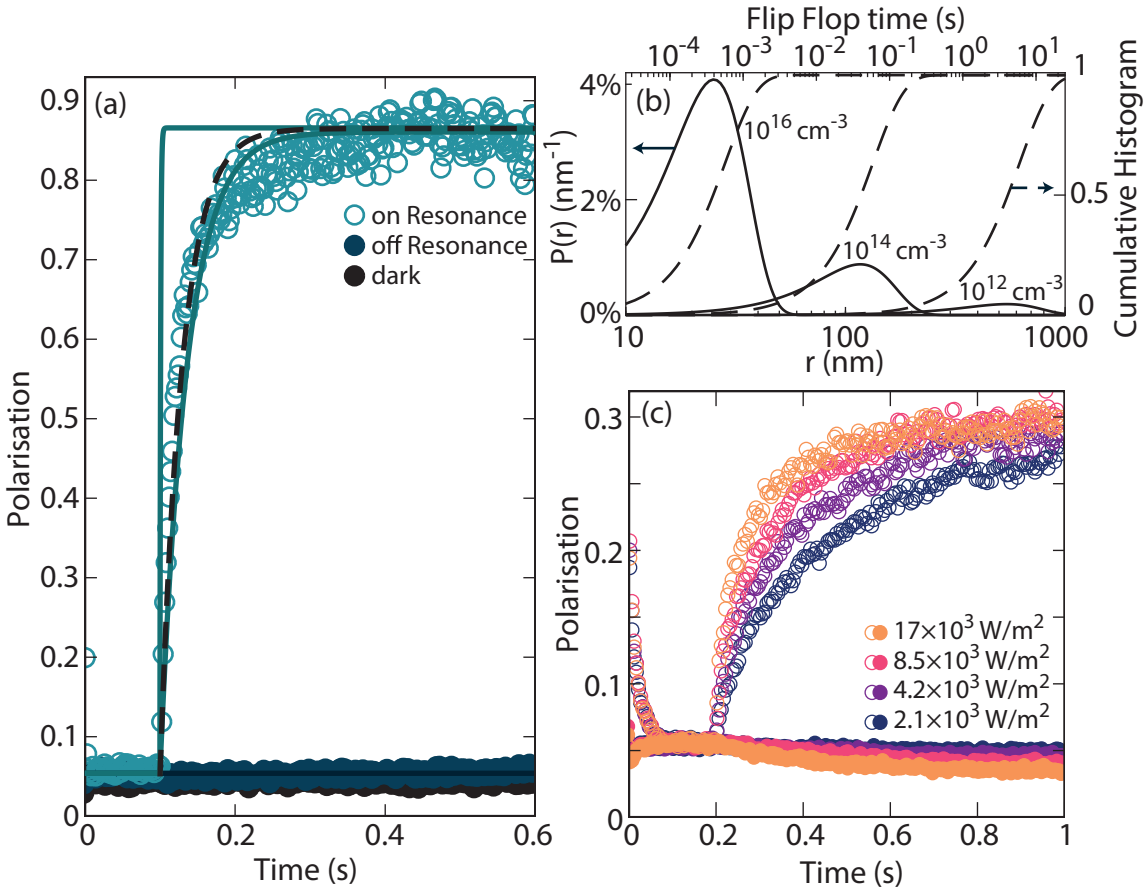

Figure 5.10: The time-resolved spin polarisation process of ^{28}Si donor ensembles upon resonant D^0X excitation. (a) The donor electron spin polarisation of sample 28Si-331 increases with the laser tuned to the D^0X transition, while off-resonant laser excitation does not alter the polarisation or number of neutral donors significantly compared to the thermal equilibrium value in the dark. (b) The distribution and cumulative histogram for the nearest neighbour donor distances (bottom axis) and the time scale of nearest-neighbour flip-flops due to dipolar interactions (top axis). (c) The phosphorus polarisation of sample 28Si-Buf upon excitation on- and off resonance and as a function of laser power. The initial drop, observed for the on-resonant traces of (c) is due to an above-bandgap, 1.18 eV laser pulse, which is used to reset the spin system to its thermal equilibrium value. The legend denotes the incident laser intensity I_L.

In the following, the origins of the observed behaviours are investigated. First, it should be noted that the laser linewidth (70 kHz) and the homogeneous D^0X linewidth due to Auger decay (585 kHz, cf. Ch. 5.1.5) are orders of magnitude smaller than the inhomogeneously broadened linewidth of the D^0X transition with a measured FWHM of ∼250 MHz. Hence, the D^0X laser only pumps on a tiny fraction of the whole spin ensemble. The spread of the polarisation of the pumped subensemble to the rest of the spin-ensemble thus plays a major role for the dynamics. If this polarisation exchange is quick, the pumping rate of the D^0X determines the hyperpolarisation time scale. If the polarisation exchange time scale is slower than the D^0X excitation rate Γ_{D^0X}, then the exchange process limits the polarisation time scale.

The rate equation for the first case in which the polarisation exchange within the ensemble is quicker than the excitation rate have been developed in Sec. 5.1.6. The two solid blue lines in 5.10(a) represent a numerical solution of these coupled equations for two different laser intensities. The simulation uses the measured D^0X linewidth of 250 MHz and literature values for D^0X oscillator strength. The direct donor ionisation cross section is set to a reasonable $\sigma_{\text{direct}} \approx 0.12\sigma_{\text{direct, peak}}$ and the literature value for T_1 in the dark is used with $T_1 = 10\,\text{s}$ [16]. The only difference between the two simulations is the laser intensity. The fast rising line represents the expected laser intensity within the sample ($\sim 0.1 I_L$), accounting for losses due to the optical window and metallic grid of the resonator as well as reflections at the silicon-air interface. The second solid line shows an increase with a longer time constant and assumes a laser intensity that is 40 times lower than that estimated within the sample.

Both calculations are able to reproduce the steady-state polarisation value very well. Solving the steady state solution of the coupled differential equations predicts a polarisation of

$$P = 1 - \frac{2\Gamma_{\text{direct}}}{\Gamma_{D^0X} + 2\Gamma_{\text{direct}}} \tag{5.40}$$

This is indeed independent of laser intensity since both Γ_{D^0X} and Γ_{direct} are proportional to I_L. Hence it is reasurring that the calculation, only dependent on literature values and the measured D^0X linewidth, is able to reproduce the measured steady state electron polarisation.

In contrast to the steady state polarisation, the dynamic behaviour is less well reproduced by the simulation. The realistic laser intensity gives a transient response that is much too quick. Only a laser intensity 40x smaller than the realisitc estimate fits the observed rise time reasonably—a value that seems experimentally

unjustified. Hence, the assumption that the spread of spin polarisation across the ensemble is faster than $\Gamma_{\mathrm{D^0X}}$ should likely be rejected.

Instead, it seems likely that the spread of polarisation via spin-spin interactions between neighbouring donors determines the polarisation time scale. Figure 5.10(b) plots the distribution of nearest neighbour distances for three different donor concentrations. The upper x-axis shows the corresponding time scale for a flip-flop of the two spins. The curve for the cumulative histogram (i.e. the percentage of donors that could have undergone a flip-flop during some time period) is also shown in Fig. 5.10(b). For the trace with $N = 1 \times 10^{14}\,\mathrm{cm}^{-3}$ it is observed that most of the donors interact with their neighbours on a time scale of 10 ms to 100 ms. Fig 5.10(a) also plots a trace whose time scale is determined by the calculation of a cumulative histogram for the flip-flop time scales of $N = 2 \times 10^{14}\,\mathrm{cm}^{-3}$. A good agreement with the data is observed

In the following, the limitations of the calculations used above are examined. First, only the nearest neighbour couplings of the donor spins have been considered, and longer-range couplings with its environment have been neglected. Hence, the true spread of polarisation within a sample could be quicker than the estimate shown here. Furthermore, the illumination of the sample is likely inhomogeneous due to the microwave resonator grid, which has not been accounted for. Finally, other mechanisms than dipolar coupling, possibly mediated by the conduction band electrons, could be the root of the observed polarisation spread within the sample, and these have not been ruled out categorically.

The laser-power dependence of the polarisation process is investigated in Fig. 5.10(c), which plots the echo intensity of the phosphorus ESR transition of sample 28Si-Buf as a function of laser pulse duration and laser intensity. The polarisation transient is indeed laser power dependent, while the steady state value is, to a first approximation, laser power independent—both observations consistent with the 'polarisation transfer' model described above. A strong reduction in steady state polarisation compared to sample 28Si-331 is observed, although the phosphorus $\mathrm{D^0X}$ linewidth is only 25 % to 50 % larger than the 28Si-331 linewidth. This is inconsistent with the steady-state polarisation result of Eq. (5.40).

A possible explanation for the polarisation reduction is the presence of a As and Sb spin ensemble within the sample. These donors are subject to direct donor ionisation, but no $\mathrm{D^0X}$ pumping (as their $\mathrm{D^0X}$ transitions are off-resonance with the phosphorus $\mathrm{D^0X}$ transition being pumped here). Still, the polarisation of the (unpumped) As and Sb donors is coupled to the P spin polarisation, since it has been observed that also the echo intensity of the As and Sb increases during P $\mathrm{D^0X}$

illumination (not shown here for brevity). The off-resonant, direct ionisation causes the polarisation of As and Sb to decrease, which due to the inter-ensemble spin coupling could reduce the phosphorus polarisation degree below the value if only P was present in the sample. It should be noted that the exact cross-species interaction mechanism is unknown, with an RKKY interaction one possible candidate, due to the presence of photo carrier. Direct dipolar coupling can be excluded since the difference in transition frequency of P, As and Sb avoids inter-species flip-flops.

In summary, the spin polarisation degree and polarisation time scale for phosphorus electron spins in ^{28}Si has been measured. A good agreement of the steady state polarisation value with a model based on spin-selective D^0X ionisation and spin-independent, direct ionisation has been found for an ensemble with a single donor species. The time scale of the polarisation process is on the order of 30 ms to 200 ms and depends on the laser power used. From the developed model, it seems likely that, for higher laser powers, the time scale of the ensemble polarisation enhancement is limited by the time scale of spin-exchange between nearest-neighbour donors.

Chapter 6

Capacitive donor bound exciton measurements

The following chapter discusses experiments that combine the spin dependent conductivity change of the bound exciton transition with capacitive conductivity measurements of bulk ^{28}Si samples. Since the D^0X transition is very sensitive to strain, a contactless method to measure the sample photoconductivity has been employed, based on the capacitance of a parallel plate capacitor with the sample inserted inbetween. The properties of this photoconductivity measurement are characterized in Sec. 6.2. With the origin of the D^0X signal explained, Sec. 6.3 shows how laser and microwave pulses can be combined to enable the photoconductive measurement of typical pulsed electron spin resonance (ESR) sequences. The D^0X based method has the benefit of higher sensitivity to smaller spin ensembles compared with the echo-based conventional ESR measurement and it is used to measure the coherence time of the purest available ^{28}Si crystal, sample 28Si-Avo. Finally, Sec. 6.4 explores a D^0X-based spin measurement that goes beyond the capabilities of conventional echo-based ESR: A D^0X-tomography sequence is developed that is based on absolute state population measurements to determine the (mixed) density matrix of the spin ensemble.

Firstly though, Sec. 6.1 discusses the key elements of the experimental setup.

6.1 Experimental setup

The setup of all experiments discussed in this chapter is similar and depicted in Fig. 6.1(a). The setup can roughly be divided into four main categories: i) The laser with its optical components, ii) the continuous flow cryostat and magnet, iii) the microwave pulse-source, which is stripped of its echo-detection arm, and iv) the capacitive photoconductivity measurement. All experiments have been carried out using an Oxford Instrument CF935 cryostat and the custom-built microwave spectrometer, which have been discussed in Ch. 4.2. The discussion of this section focusses on the details of the capacitive photoconductivity measurement.

To measure the photoconductivity capacitively, the silicon crystal is placed between two PCB boards, taking care to minimise any applied strain. The electrodes are separated by two teflon spacers within a quartz tube of 4 mm diameter (Fig. 6.1(b)). The copper electrodes of the PCB face outward to avoid direct electrical contact with the sample and are contacted via two cryogenic stainless steel coaxial cables (LakeShore Type SS) to avoid thermal load. The probe stick is inserted into a Bruker Flexline dielectric ring microwave resonator and cooled to 4.5 K.

Figure 6.1(d) shows the electric readout circuitry employed. A Stanford Research SR830 lock-in amplifier biases one side of the electrode with an AC voltage, typically on the order of $V_{\mathrm{bias}} = 1\,\mathrm{V}$ and a frequency on the order of 10 kHz. The current input of the lock-in is connected to the second coaxial cable and measures the current through the PCB capacitor via its internal current-to-voltage converter. For the time resolved measurements of Sec. 6.3 and 6.4 the time constant of the lock-in is on the order of $\sim$1 ms and its X and Y outputs are captured with an oscilloscope.

First, the experiments of Sec. 6.2 are discussed, which investigate the origin of the photoconductive signal in the capacitive measurement. For this, the restricted bandwidth of the lock-in current-to-voltage converter, with a maximum input frequency of 60 kHz, proves too small. Instead, the probe stick electronics are connected to a dedicated instrument for time-averaged capacitance measurements, an Agilent E4980A Precision LCR Meter, able to perform impedance measurements up to 2 MHz. The electrical connections are displayed in Fig. 6.1(c). Instead of moving the four-point connection point to the PCB electrodes, it was chosen to leave the four point connection at the connectors at the end of the stainless cable, which allows comparison of the capacitance meter results with the lock-in measurement. The use of grounded coax cables minimizes the stray capacitances C_{p} between the

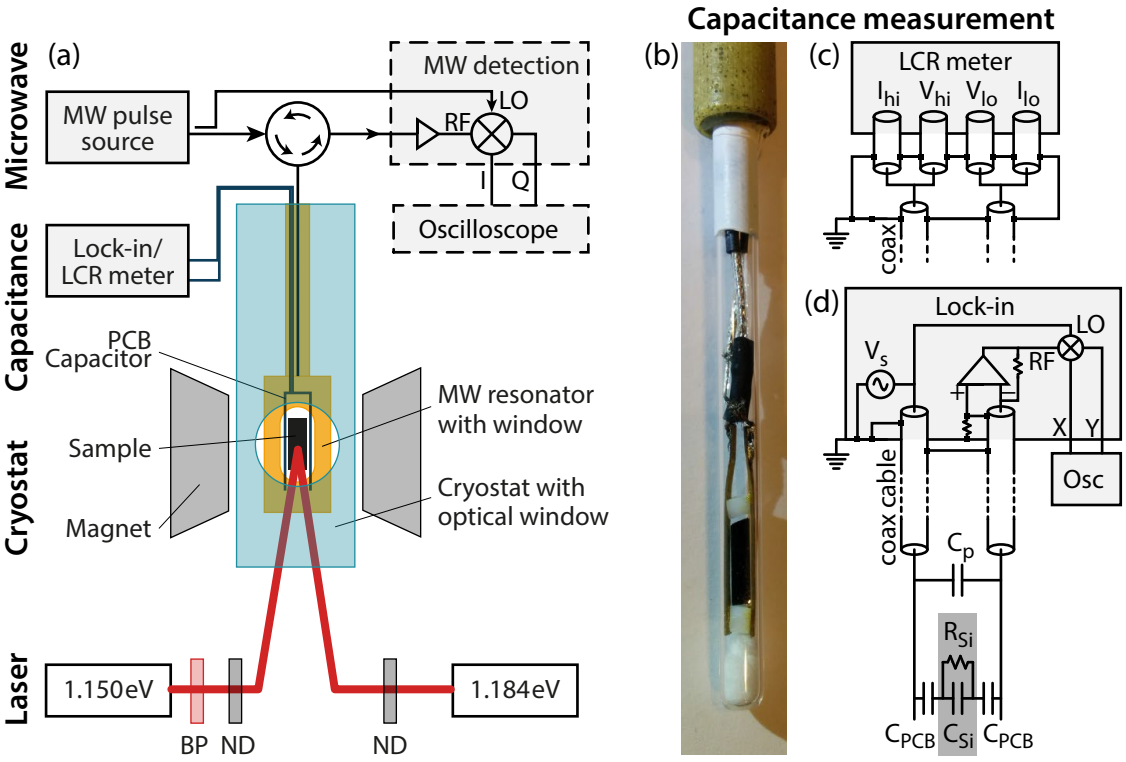

Figure 6.1: The shared setup of the capacitively measured D^0X experiments. (a) The instrumentation can be divided into four categories: i) The microwave spectrometer of which only the pulse source is used, ii) the capacitance measurement, iii) the cryostat & magnet and iv) the lasers and their filters. The capacitance measurement is performed on a parallel plate electrodes (b) with the silicon sample placed strain-freely in between two PCB-electrodes, connected by two stainless steel coaxial cables. The capacitance is either measured using (c) a dedicated LCR meter or (d) a lock-in amplifier in current detection mode.

two center conductors. The outer conductors of the coaxial cables are not connected at the PCB side to avoid ground loops[1]. Hence, to a good approximation the only stray capacitance measured is the parallel capacitance from the unshielded parts of the wire, close to the PCB capacitor (cf. Fig. 6.1(b)).

[1]For details refer to Keysight's Impedance Measurement Handbook, 6th Edition.

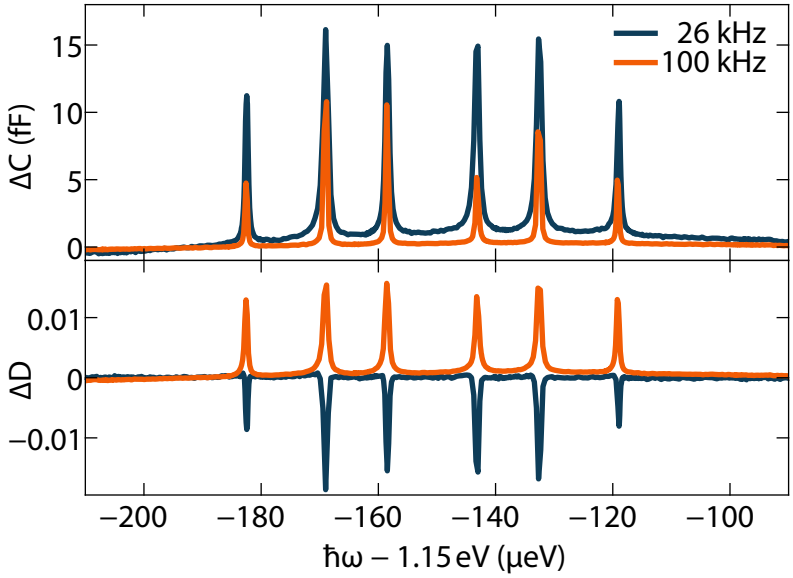

Figure 6.2: Changes of the capacitance and loss of the PCB capacitor with inserted sample as a function of photon energy for two different bias frequencies. The spectrum is measured for sample 28Si-331 with incident laser power of $\sim$40 W/m^2 in a magnetic field of 340 mT.

6.2 Capacitive measurement of the sample conductivity

As an example of why a detailed understanding of the origin of the capacitive, contactless D^0X signal is necessary, consider Fig. 6.2: Both the change of the capacitance C and the change of the loss tangent $D = \mathrm{Re}(Z)/|\mathrm{Im}(Z)|$ measured by the capacitance meter are plotted as a function of laser energy. Due to the finite magnetic field, the D^0X transition splits into six lines. For the capacitance, the D^0X transitions consistently show an increase of capacitance on resonance. The loss tangent, however, features either a negative or positive response on resonance, depending on the frequency of the AC voltage. For frequencies far away from 50 kHz, i.e for $f = 2$ MHz, a very weak, almost non-existing, signal is detected at this particular laser power. The capacitance and loss directly transfer to the out-of-phase and in-phase component of the current detected by the lock-in. Depending on the frequency of the bias voltage and on the laser power, very different signal magnitudes and phases are thus observed.

To understand the origin of this behaviour, both the capacitance and loss are measured over a range of frequency and laser powers, both on and off resonance with the D^0X transition. In order to achieve a large signal contrast between on- and off-resonant conductivity, a vanishing magnetic field ($B = 0$ T) is chosen, where no polarisation build-up occurs. Two different samples are investigated, sample 28Si-331 and 28Si-321, with similar results.

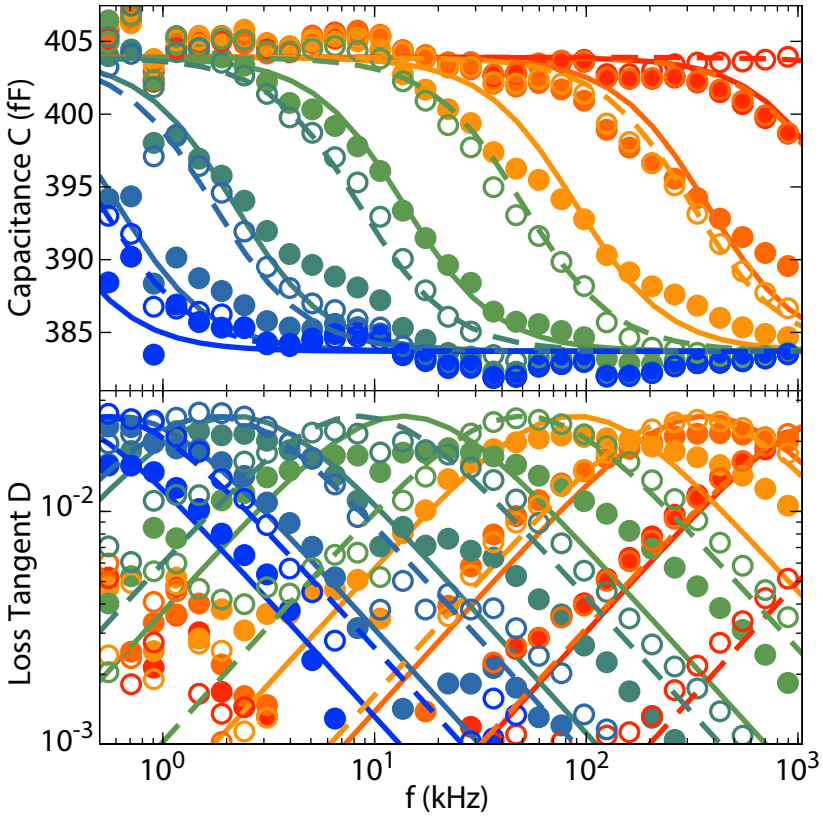

Figure 6.3: The capacitance and loss tangent of the probe stick with sample 28Si-321 as a function of bias frequency. Traces are taken for different laser powers from $1.4 \times 10^{-1}\,\mathrm{W/m^2}$ (blue) to $3.5 \times 10^{3}\,\mathrm{W/m^2}$, both on resonance (empty circle) and off resonance (full circles). Fits of the electric circuit model sketched in Fig. 6.1(d) are drawn as dashed lines (off resonance data) and solid lines (on resonance data). $B = 0\,\mathrm{T}$.

6.2.1 Interpretation of the capacitively measured photoconductivity signal

Figure 6.3 shows the results of sample 28Si-321. The plotted laser intensity ranges from $1.4 \times 10^{-1}\,\mathrm{W/m^2}$ (blue) to $3.5 \times 10^{3}\,\mathrm{W/m^2}$ (red). Data points with the laser on resonance with the D^0X transitions are clear circles, while the off resonance data are depicted as solid circles. The loss tangent data have had a linear phase shift observed at higher frequencies removed, as well as a small resonant behaviour at 10 kHz, since these could be traced back to a finite length of the coaxial cables, and a resonance of the empty probe stick respectively.

For all laser traces, a transition from a higher to a lower capacitance value is observed with increasing frequency. At the center of this transition, a peak in the loss can be detected: a clear indication of a resonant behaviour. The center

frequency of the resonance changes with applied laser power, with higher laser powers resulting in higher transition frequencies.

The transition frequency for the data on resonance is consistently higher than the off resonance transition of the same laser power. The observed behaviour explains the consistently positive changes of C and the sign change of D, seen in the D^0X spectrum of Fig. 6.2. Tuning the laser from off resonance to on resonance solely leads to a positive shift of the capacitance value, as seen e.g. for the green trace of Fig. 6.3. Furthermore, only a bias frequency close to the transition frequency allows for an observable D^0X signal. For the loss, the sign of the D^0X signal depends on the choice of frequency, again as observed for e.g. the green trace. High frequencies ($f \gtrsim 70\,\mathrm{kHz}$) exhibit an increase of D on resonance, i.e. a positive D^0X signal. In contrast, low frequencies ($f \lesssim 10\,\mathrm{kHz}$) feature a reduction of the loss, i.e. a negative D^0X signal on resonance.

The observed resonant behaviour and its change with laser conditions can be traced back to a change of sample conductivity. This becomes evident from a model for the electric circuit of the PCB capacitor with the inserted sample. The assumed circuit model is depicted in Fig. 6.1(d): The silicon sample is taken to be a lossy capacitor (dielectric constant ε_r), with some resistance connected in parallel. The capacitance between the electrodes and the PCB are modelled as two air-gap capacitors C_PCB and the stray capacitance between the parts of the capacitor that are not filled with the sample is labelled C_p. From this model, at lower frequencies, a larger capacitance value is expected than for higher frequencies: At lower frequencies, the resistance of the silicon sample R_Si shorts the reactance associated with the silicon capacitance C_Si and thus the total capacitance is determined by the series connection of two C_PCB. As the frequency increases, the reactance associated with C_Si becomes smaller, and eventually determines the sample impedance. Thus, for higher frequencies, the total capacitance of the probe stick is lower, since it is given by the series of what are now three capacitances, $2 \times C_\mathrm{PCB}$ & C_Si, instead of just two at lower frequencies. The transition from one regime to the other is given by the equality of the impedances associated with the resistance R_Si and reactance $\mathrm{X_{Si}} = 1/(\omega C_\mathrm{Si})$. The solution of this equation leads to an angular transition frequency condition which is independent of sample geometry:

$$\omega_\mathrm{t} = \frac{\sigma_\mathrm{Si}}{\varepsilon_0 \varepsilon_\mathrm{r}}, \tag{6.1}$$

where σ_{Si} is the laser intensity-dependent sample conductivity and $\varepsilon_{\mathrm{r}} = 11.45$ at 4.5 K [183], which is independent of laser intensity[2]. Using the described electric circuit model, it is possible to fit the whole data set (both $C(\omega)$ and $D(\omega)$) simultaneously with one fit parameter σ_{Si} for each trace and the two remaining fit parameters C_{p} and C_{PCB} shared between the whole data set. The fit of the unwanted parallel capacitance gives $C_{\mathrm{p}} = 290\,\mathrm{fF}$, which is reasonable for the given geometry. The other global fitting parameter, the capacitance between the electrode and the silicon sample on each side, takes a value of $C_{\mathrm{PCB}} = 220\,\mathrm{fF}$. This value coincides well with the given dimensions and also with the probe stick capacitance without sample inserted. The results of the extracted conductivity values for each laser condition are discussed in the next section.

It should be noted here that, in general, due to the resonant feature underlying the $\mathrm{D^0X}$ signal of C and D, no linearity between conductivity changes $\Delta\sigma_{\mathrm{Si}}$ and the changes ΔC and ΔD can be expected. A linear response of C to first and second order can only be ensured with the driving frequencies tuned to the center of the sample self-resonance and for conductivity induced shifts that are small compared to the width of the transition. Therefore great care is required when interpreting capacitively measured photoconductivity signals and assumptions such as $\Delta C \propto \Delta\sigma_{\mathrm{Si}}$ have to be corroborated.

6.2.2 Analysis of the extracted sample conductivity

The sample conductivity σ_{Si} extracted from the fits to the frequency sweeps of Fig. 6.3 are plotted in Fig. 6.4 as a function of laser intensity I_{L}. The data for both samples are included, with the data from sample 28Si-321 plotted in dark blue and the 28Si-331 data in light blue. For all laser powers, the data on resonance (empty circles) show a higher conductivity than the off resonance data (full circles). A linear dependence between σ_{Si} and I_{L} is observed over about five orders of magnitude. At lower intensity, the conductivity rolls off towards a constant value, possibly due to a small amount of above-bandgap light reaching the sample via the sample windows or small above-bandgap modes of the laser.

The measured data, and especially the off-resonant part, should be compared to the data and theory developed for the photo-Hall $\mathrm{D^0X}$ measurements of Sec. 5.2. During that discussion, it was found that the off-resonant conductivity is likely caused by direct photo-ionization of the donor with a carrier generation rate

[2]The polarisibility and concentration of phosphorus is negligible compared to the polarisibility of the silicon host lattice [184].

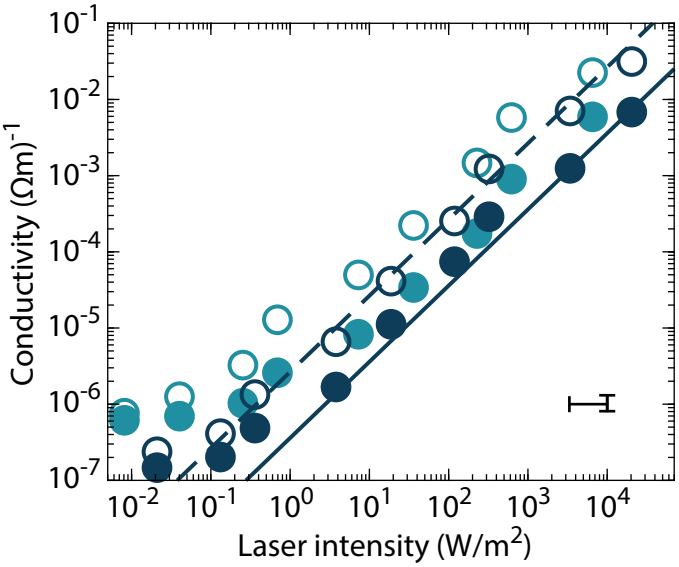

Figure 6.4: The extracted photo-conductivity from the fits of Fig. 6.3 as a function of incident laser intensity. Dark (light) blue data points correspond to sample 28Si-321 (28Si-331). The conductivity on resonance with the D^0X transition (empty circles) is about a factor 4 to 8 higher than that off resonance (full circles). The solid and dashed lines represent theoretical treatment of the on- and off-resonant conductivity discussed in the main text. The indicated error in y is the fit-uncertainty, while the x-error is an estimate for the uncertainty of the laser intensity within the sample due to reflections[3].

$G_{\text{off Res}} = \Gamma_{\text{direct}} N^0$. The on-resonant generation rate is given by $G_{\text{on Res}} = (\Gamma_{D^0X} + \Gamma_{\text{direct}})N^0$, where the first term scales inversely with the D^0X linewidth. The steady state conductivity is given by:

$$\sigma = e\mu\Delta n = e\mu\frac{G}{\tau_n} \tag{6.2}$$

where τ_n is the lifetime of the ejected, thermalized Auger electron in the conduction band, given by the capture coefficient of the ionised donor concentration as $\tau_n = (B_{n\to N^0} N^+)^{-1}$. Unfortunately, the mobility of these particular samples at $T = 4.5\,\text{K}$ is not known. A reasonable estimate can be made for sample 28Si-321: In section 3.5.3 the mobility of photo excited electrons at low temperatures and at $B = 0\,\text{T}$ has been determined for sample natSi-Hall, which gave $\mu \approx 7 \times 10^4\,\text{cm}^2/(\text{V s})$, limited by neutral donor scattering. The donor density of sample natSi-Hall and 28Si-321 is almost the same, so it seems reasonable to assume the same mobility values for the two samples. The mobility for sample 28Si-331, which has a 15× lower donor concentration, should have a higher mobility, but its value remains largely unknown. Thus, only qualitative statements can be made in the remainder for the latter.

The solid line of Fig. 6.4 shows the off-resonant solution of Eq. (6.2) (with $G = G_{\text{off Res}}$), while the dashed line represents the corresponding expression on resonance. Reasonable parameter values, similar to those of Sec. 5.2, are employed. The laser power within the sample is assumed to be $0.4I_{\text{L}}$. The direct photoionisation cross section at 1.15 eV is taken as $\sigma_{\text{direct}} = 0.05\sigma_{\text{direct, peak}}$, while the generation rate $\Gamma_{\text{D}^0\text{X}}$ is calculated from the measured D^0X linewidth of 4 µeV and the known oscillator strength of the D^0X transition. Lastly, the ionised donor concentration is assumed to be constant at $N^+ = 2.5 \times 10^{13}\,\text{cm}^{-3}$, compared to $N^0 = 3 \times 10^{15}\,\text{cm}^{-3}$ & $N_{\text{A}} \approx 1 \times 10^{14}\,\text{cm}^{-3}$ for sample 28Si-321.

These calculations can only be an order-of-magnitude estimate due to the assumptions taken for the ionised donor concentration, the carrier mobility and the actual laser intensity value within the sample. Still, none of the assumed values seem unreasonable and it gives confidence in the model to see that the calculations are able to reproduce the linear dependence and the order of magnitude for the conductivity both on and off resonance.

Interestingly, the conductivity of sample 28Si-331 is quite similar to that of sample 28Si-321, despite its donor concentration being over an order of magnitude smaller. This should have resulted in an order of magnitude lower steady state carrier concentration due to the scaling of the carrier generation rates $G_{\text{off Res}}$ and $G_{\text{on Res}}$ with donor density. A possible, albeit unlikely reason why such a large conductivity is observed could be that the sample mounting/loading is different between the two measurements, giving rise to a systematic change of delivered laser power of about an order of magnitude. Another possibility for the observed higher conductivity could be that an increased carrier lifetime balances a lower carrier generation rate, resulting in the same steady state carrier concentration. The increased carrier lifetime would be due to a smaller N^+ concentration. Although both samples have the same boron concentration ($N_{\text{A}} \approx 1 \times 10^{14}\,\text{cm}^{-3}$), this could indeed be the case, since the average nearest donor distance for a given acceptor is larger in the lower doped sample, leading to a smaller portion of acceptors and donors undergoing donor-acceptor recombination. A final explanation for the similar sample conductivity, and perhaps the most likely one, could be a difference in carrier mobility between sample 28Si-331 and 28Si-321. From the discussion of Sec. 3.5.4, it seems likely that for sample natSi-Hall the mobility at 4 K is limited by neutral donor scattering. For this scattering type, the mobility scales inversely with the donor concentration, suggesting that sample 28Si-331 could have a correspondingly higher mobility than 28Si-321—if no other scattering mechanisms start to become a limiting factor at lower donor densities. Hence, an increased mobility could balance

a reduced steady state carrier density stemming from a reduced carrier generation rate. From the above discussion it is obvious that no definitive explanation for the observed conductivity similarity of the two samples can be made. Furthermore, combinations of the discussed effects are also possible.

6.2.3 Conclusion

In summary, it has been shown that the strain-free, capacitive measurement of the D^0X signal is fundamentally a self-resonance phenomena of a lossy capacitor and therefore only works for specific ranges of bias frequencies for each laser power. From frequency sweeps, the conductivity of two ^{28}Si samples could be extracted both on- and off resonance, showing a linear relationship between conductivity and laser intensity over about five orders of magnitude. This is in accordance with the Hall measurement results discussed in Ch. 5.2.2. Following the results of that chapter, a simple carrier generation-recombination model is employed. Using very reasonable assumptions regarding the laser intensity, the carrier mobility and the density of ionized donors, we find good agreement between this theoretical model and the data for sample 28Si-321. The description of the data for sample 28Si-331 is made difficult by the unknown strength of donor-acceptor recombination and the lack of data for the carrier mobility at $N_\mathrm{D} \approx 1 \times 10^{14}\,\mathrm{cm}^{-3}$.

As a final remark, it should be noted that with the laser off resonance, frequency sweeps have also been conducted as a function of magnetic field. Unsurprisingly, a decrease in conductivity with increasing magnetic field is observed, stressing that magnetoresistive effects (cf. Sec. 3.5.3) do also play a role also for ^{28}Si samples and for the strain-free D^0X photoconductivity measurement.

6.3 Coherence time limits of phosphorus in silicon

This section investigates the electron spin coherence time of phosphorus in sample 28Si-Avo. The sample is to-date the highest purified ^{28}Si sample, with a ^{29}Si concentration of 47 ppm and C, O_2, B and P concentrations smaller than $1 \times 10^{13}\,\mathrm{cm}^{-3}$ (for details see Ch. 4.1.1). The low concentration of the nuclear spin-carrying ^{29}Si isotopes provides an almost spin-free ^{28}Si host crystal, in which both the electron and nuclear spin of phosphorus exhibit extraordinary long coherence times.

Work on the phosphorus nuclear spin coherence times in the 28Si-Avo material has been carried out by Prof. Thewalt's group at the Simon Fraser University: Hahn echo coherence times of 44 s at 1.7 K for the neutral donor [31] and a similar 27 s for the ionized donor at 1.9 K [18] have been achieved. $XY16$-dynamical decoupling improved the nuclear spin coherence time of the neutral donor to 192 s, while the ionized donor spin reaches an even longer 3 h, since its nuclear spin Hamiltonian is not affected by noise from the hyperfine coupling to the donor electron. Due to the sensitivity limit of conventional ESR spectrometers, all of these 28Si-Avo nuclear spin measurements relied on the capacitive photo-conductivity readout in combination with RF pulses in the frequency range of 1 MHz to 50 MHz

For the electron spin coherence time in ^{28}Si, most work has been focussing on phosphorus concentrations on the order of $1 \times 10^{14}\,\mathrm{cm}^{-3}$ or larger to achieve a detectable ESR echo intensity. At these concentrations the donor coherence time is still limited by dipolar coupling between neighbouring donor spins (instantaneous diffusion), limiting the Hahn-echo coherence time with a full-π refocussing pulse to $T_2 = 20\,\mathrm{ms}$ for a concentration of $1.2 \times 10^{14}\,\mathrm{cm}^{-3}$ at 2.1 K [16]. As discussed in Sec. 3.4.4.2, the effect of instantaneous diffusion can be artificially weakened by reducing the tip-angle, e.g. by shortening the duration, of the refocussing pulse. This can be understood as a reduced probability of surrounding donors being flipped during the refocussing pulse, and their—now static—dipolar coupling with the central spin is refocussed in the echo sequence. Using a refocussing pulse with tip-angle of 0.1π, a coherence time of $\sim$450 ms is found, with an extrapolated value of $\sim$1 s for vanishing tip-angle, which is an estimate for T_2 in the limit of negligible donor concentrations [16]. However, new effects may arise at low donor concentrations, such as donor-acceptor recombination and the extrapolated electron spin coherence time values should hence be verified by experiment.

In this chapter, the electron spin coherence time of the residual phosphorus of sample 28Si-Avo, with a concentration of $5 \times 10^{11}\,\mathrm{cm}^{-3}$, is investigated. Due to the low donor concentration, the ESR echo intensity is below the sensitivity limit

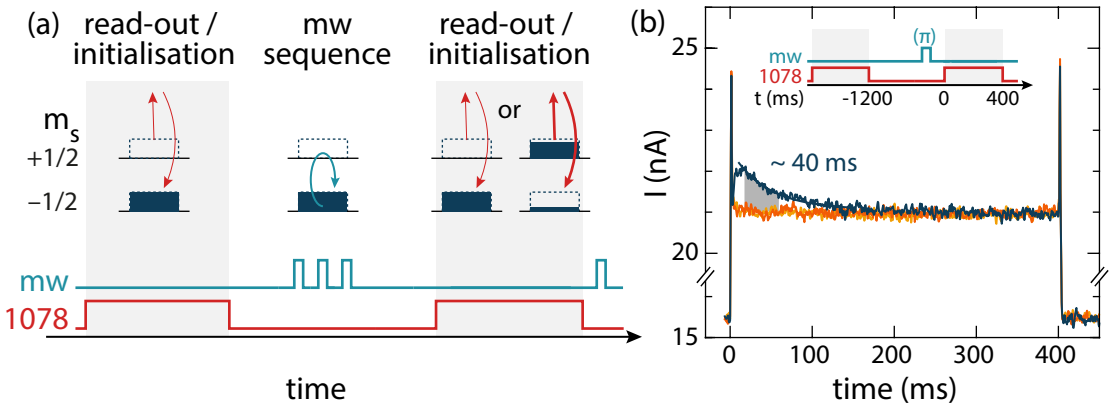

Figure 6.5: D^0X-assisted spin-readout requires the synchronized pulsing of the laser and microwave source. (a) A typical sequence can be divided into an initialisation phase during which the laser hyperpolarises the ensemble, a microwave (mw) manipulation period in the dark, and a readout step, during which the laser-induced photocurrent provides a measurement of the spin ensemble polarisation. (b) The capacitive photoconductivity trace for the case of a single (π)-pulse on resonance with the ESR transition (blue) shows a distinct response, in contrast to traces with an off-resonant microwave pulse (orange) or no microwave pulse (yellow). The timescale of the transient is similar to the hyperpolarisation time discussed in Ch. 5.4.

of our ESR spectrometer. Instead, a measurement using the D^0X assisted-spin readout relying on the spin-sensitive D^0X photoconductivity is carried out. Section 6.3.1 introduces the D^0X spin-measurement technique, which is followed by a brief overview of the preparation experiments in Sec. 6.3.2. Finally, Sec. 6.3.3 analyses the results of the electron spin coherence time measurement of phosphorus in 28Si-Avo.

6.3.1 Measurement technique

Figure 6.5(a) shows the pulse sequence of the laser and microwave source used for D^0X-assisted spin readout. Initially a long laser pulse, tuned to one of the D^0X transitions, is used to hyperpolarise the spin ensemble. After this, a microwave pulse sequence manipulates the donor spin, essentially following a conventional ESR experiment, except that the formed echo is converted into a population difference by a projective $\pi/2$-pulse (with the correct phase) at the point of echo formation. Finally a read-out laser pulse generates a spin polarisation-dependent photoconductivity trajectory: If the microwave sequence left most of the spin population in the original spin state, a flat photoconductivity response is observed. This is shown in Fig. 6.5(b) for the yellow and orange traces, which are measured traces for no microwave pulses and an off-resonant microwave pulse, respectively. In contrast, if

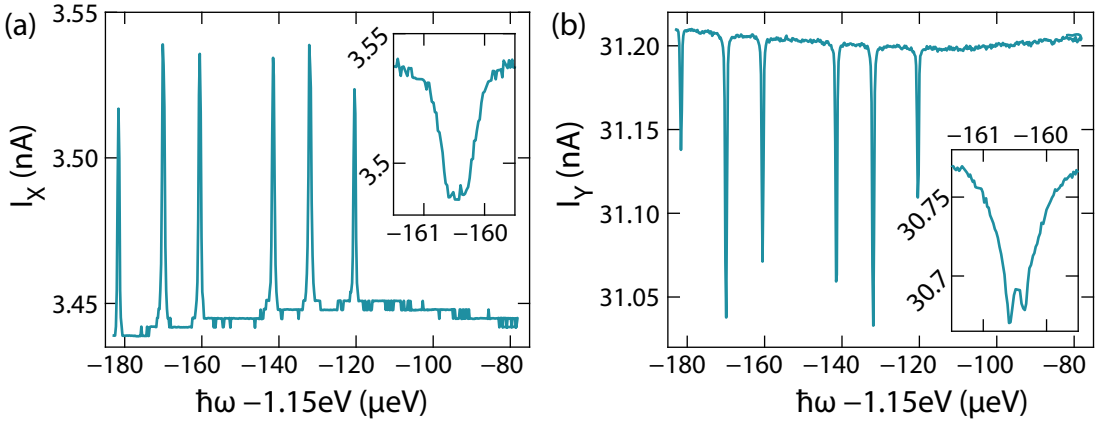

Figure 6.6: The D^0X spectrum of the 28Si-Avo sample, as determined by the in-phase (I_X) and quadrature (I_Y) current components, measured by the lock-in for a bias voltage of 1 V. The overview (main panel) and the detail of line 5-6 (inset) have been measured on consecutive days and a sign-reversal is observed for the spectrum of the channel that is related to the loss D. This is likely due to slightly different laser and/or sample positions on consecutive cool-downs and its related change of the sample self-resonance under illumination, as discussed in Sec. 6.2.

the microwave sequence results in significant population in the spin state that the laser pumps on, an excess photoconductivity $\propto \Gamma_{D^0X} N^{\uparrow}$ is observed, depicted as the blue trace of Fig. 6.5(b) for an on resonance microwave π-pulse. An integration of the grey area indicated in Fig. 6.5(b) thus acts as a measure of the spin-polarisation.

In order to reduce measurement time, the read-out and initilisation laser pulse are often combined into one longer pulse sequence, which is here usually 400 ms. The laser intensity and AC bias frequency are linked as discussed in the previous section, and optimized during experiment setup. Values used for the following experiments are $I_L = 2 \times 10^2\,\mathrm{W/m^2}$ and $f = 20\,\mathrm{kHz}$.

6.3.2 D^0X spectrum, microwave transition and Rabi drive

Figure 6.6 plots the steady state in-phase and out-of-phase current components from the lock-in, which are respectively related to the loss (I_X) and capacitance (I_Y) upon sweeping the laser photon energy $\hbar\omega$. The main figure shows an overview of the six D^0X transitions while the inset shows a close up of line 5-6, that is used in the subsequent measurement. Very sharp D^0X transitions are observed, for which even the hyperfine splitting of 117 MHz (0.48 μeV) is observable.

After tuning the laser energy to line 5-6, the laser pulse sequence is used to optimize the laser, AC frequency and phase of the microwave source to optimize the response in one of the lock-in channels. The resulting current transients are

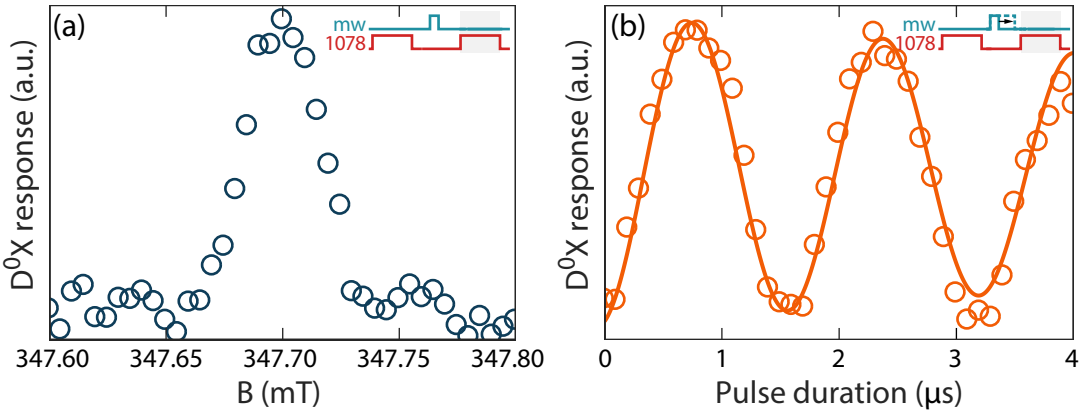

Figure 6.7: (a) The integrated D^0X photo response following a single microwave pulse ($f_{mw} = 9.7496\,GHz$) allows the measurement of the corresponding resonant magnetic field with a power-broadened linewidth of 39 µT. (b) A sweep of pulse duration demonstrates coherent spin-driving over multiple cycles with a Rabi frequency of 0.6 MHz.

shown in Fig. 6.5(b) for a single microwave pulse. A sweep of magnetic field tunes the spin-transition into resonance with the selected microwave frequency and the current trace shows a distinct transient behaviour. Integration of this transient response (grey area) serves as a measurement of the $|\uparrow\rangle$ population. Fig. 6.7(a) shows the integrated D^0X response as a function of magnetic field, revealing a resonance field of 347.70 T. Here, the magnetic field linewidth 39 µT is microwave power limited due to short microwave pulses.

With the magnetic field on resonance, the (π)-pulse duration is determined by a Rabi sequence, as shown in Fig. 6.7(b). Coherent oscillations between the $|\downarrow\rangle$ and $|\uparrow\rangle$ state are observed with only slight dephasing on the measured timescale of 4 µs. The Rabi frequency of 0.6 MHz is relatively slow due to the use of a 3 W pulse amplifier instead of the typical 1 kW TWT amplifier. However, due to the long dephasing time, this is sufficient for a simple Hahn echo measurement.

6.3.3 Coherence time

The results of the D^0X assisted coherence-time measurement of the Avogadro sample 28Si-Avo are shown in Fig. 6.8(a). The microwave sequence comprises $(\pi/2)^{\Downarrow}_{S_x}$—$\tau$—$(\pi)^{\Downarrow}_{S_x}$—$\tau$—$(\pi/2)^{\Downarrow}_{\pm S_x}$ pulses with free evolution time τ. The final $(\pi/2)^{\Downarrow}_{\pm S_x}$ pulse projects the formed echo either into the $|\uparrow\rangle$ state or the $|\downarrow\rangle$ state, depending on its phase. This is very similar to conventional phase-cycling in pulsed ESR sequences, and helps to differentiate spin-dependent signals from instrumentation offsets. The free evolution time τ is plotted logarithmically to highlight three distinct time scales:

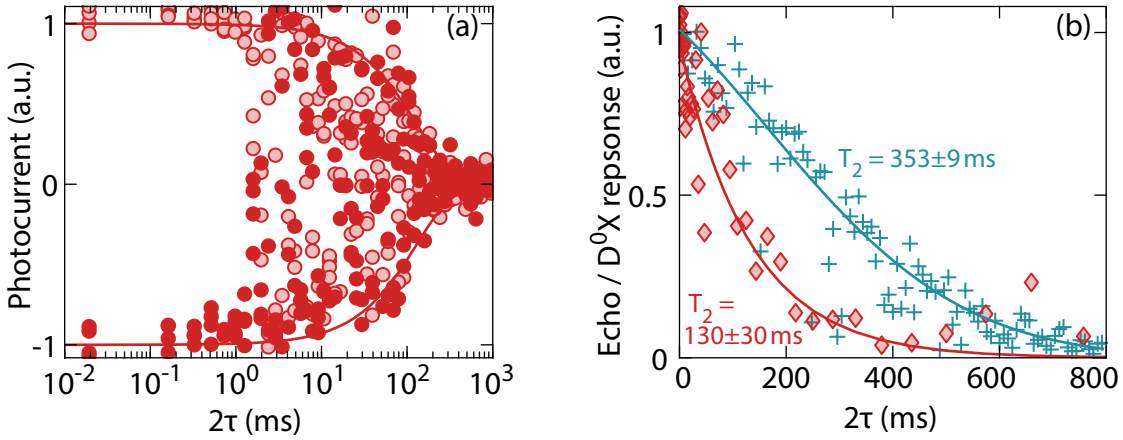

Figure 6.8: (a) The coherence time of the 28Si-Avo sample at 4.5 K with final $(\pi/2)^{\Downarrow}_{\pm S_x}$ pulse projecting the echo either into the $|\uparrow\rangle$ state (light red circles) or $|\downarrow\rangle$ state (full red circles). (b) The maximum data points of (a) and an exponential fit to the data along with the magnitude detected data of a two pulse ESE decay of a ^{28}Si sample with $c(\mathrm{P}) = 4 \times 10^{12}\,\mathrm{cm}^{-3}$, measured at 1.7 K. To enhance the signal intensity a $\mathrm{D}^0\mathrm{X}$ hyperpolarisation pulse has also been employed for the echo-detected data.

For $2\tau < 1$ms, the projective pulses consistently project the echo into the respective spin-population, which is the normal behaviour expected for this sequence. During this phase, no significant decoherence is observed.

For $1\,\mathrm{ms} < 2\tau < 100\,\mathrm{ms}$, the formed echo is randomly projected into both the $|\uparrow\rangle$ and $|\downarrow\rangle$ state. This is not an effect of decoherence, but rather an instrumentation limitation. Fluctuations of the external magnetic field on a time scale of $\sim$1 kHz shift the phase of the echo. In a normal ESR sequence, due to the heterodyne detection, such phase noise can be recovered by magnitude detection of the two channels. In contrast, for the photoconductive method the last $(\pi/2)^{\Downarrow}_{\pm S_x}$ pulse measures the spin-projection along a single channel only, leading to random projections into both $|\uparrow\rangle$ and $|\downarrow\rangle$ states. Still, the maximum amplitude of these projections corresponds to the magnitude of the echo for each τ and with enough statistics a measurement of the echo intensity is possible [18]. During this period $1\,\mathrm{ms} < 2\tau < 100\,\mathrm{ms}$, as evident from the maximum data points, only moderate decoherence is observed. The phase noise instrumentation limitation could be avoided or improved with superconducting magnets in persistent mode or permanent magnets with magnetic shielding [185].

Finally, for $2\tau > 100\,\mathrm{ms}$, the echo intensity collapses due to decoherence. The time scale of this collapse can be extracted from a fit to the maximum data points. This is done in Fig. 6.8(b) with the maximum data points of Fig. 6.8(a) shown as

the red diamonds. The single exponential fit suggests an electron spin coherence time of $T_2 = 130 \pm 30$ms.

What is the limiting process for T_2? Firstly, it can be ruled out that the decoherence time is limited by either a T_1 process or by donor-acceptor recombination, because the result of an inversion recovery measurement gives a lower bound for these processes of $T_1 > 2\,\mathrm{s}$. Furthermore, instantaneous diffusion, i.e. dipolar coupling between neighbouring donor spins should not affect T_2 at the low donor density and a calculation estimates $T_{2,\mathrm{id}}(5 \times 10^{11}\,\mathrm{cm}^{-3}) \approx 5\,\mathrm{s}$, much longer than the observed time scale [16, 143]). Instead, the nuclear spin of the residual ^{29}Si concentration of 47 ppm is expected to be the primary source of decoherence via spectral diffusion. Detailed theoretical calculations suggest a $T_{2,\mathrm{sd}} \approx 0.5\,\mathrm{s}$ [142] and a line shape $\propto \exp(-(t/T_{2,\mathrm{sd}})^2)$, both of which are not observed here.

The apparent discrepancy between the measured and expected value is likely be due to instrument limitations: In particular, vibrations can be a source of instrumentation limited decoherence, as detailed in the following: Inhomogeneous DC magnetic fields, i.e. a static distribution of spin frequencies do not affect the echo of a Hahn sequence since the refocussing pulse leads to a phase synchronization at the time of the echo. Homogeneous AC magnetic fields on the other hand randomly shift the phase of the echo formation, observed as phase noise for the times $1\,\mathrm{ms} < 2\tau < 100\,\mathrm{ms}$, which leads to random projections of the echo, but no collapse of the echo, hence no decoherence. A combination of these two, i.e. an AC magnetic field which is inhomogeneous across the sample dimensions, however, would lead to different parts of the sample forming echos with different phases such that the combined echo vanishes. It is known that the Bruker magnets used in these experiments do exhibit a slightly inhomogeneous magentic field distribution[4]. Hence, one possibility for the occurence of inhomogeneous AC magnetic field could be the vibrations of the sample. Since the sample can not be mounted rigidly to avoid straining of the sample, it is conceivable that simply the flow of helium gas around the sample could affect the experimentally determined coherence time.

One way to validate this assumption is to submerge the sample in liquid helium and to pump the sample space, bringing the boiling point below 2.1 K where the superfluid helium lacks turbulences. Collaborators from Princeton University[5] kindly shared data which demonstrate this effect. Fig. 6.8(b) plots the coherence time of a higher doped ^{28}Si sample with $[\mathrm{P}] = 4 \times 10^{12}\,\mathrm{cm}^{-3}$ measured in super-

[4] An educated guess for the field inhomogeneity is $\sim$2 µT across a sample volume of $0.5 \times \times 0.5 \times 1\,\mathrm{cm}^3$.

[5] Measurements performed by Brendon Rose and Alexei Tyryshkin in the group of Steve Lyon at the Department of Electrical Engineering, Princeton University.

fluid helium at 1.7 K. A coherence time of 350 ms was measured, which could not be achieved above superfluid temperatures. As evident from its shape, the measured echo decay consists of the combination of a fixed instantaneous diffusion term (with $T_{2,\mathrm{id}}([\mathrm{P}] = 4 \times 10^{12}\,\mathrm{cm}^{-3}) = 600\,\mathrm{ms}$), and a fitted ^{29}Si spectral diffusion term $T_{2,\mathrm{sd}} = 530\,\mathrm{ms}$ which is in accordance with the expected spectral diffusion due to ^{29}Si nuclear spins [142]. This means that a sample from the same host material with a higher phosphorus concentration shows a 2.5× longer coherence time when measured in superfluid helium. Hence, it is assumed that the apparent shorter T_2 of sample 28Si-Avo is likely limited by vibrations caused from the helium gas.

Attempts to use the D^0X-photoconductivity method at $T < 2.1\,\mathrm{K}$ were unsuccessful. In order to reach superfluidity, the cryostat needs to be filled with liquid helium and then the sample space must be pumped with the vibrations from the pump carefully isolated from the setup. The limited amount of He liquid within the cryostat allows each experiment a time window of ∼30 min. Unfortunately, 30 min was not enough to tune the laser, the lock-in bias frequency, find the resonant magnetic field and perform the coherence time measurement. In principle, there are however no known reasons preventing the D^0X method from operating at temperatures $< 4.2\,\mathrm{K}$.

Finally, a brief remark regarding the coherence time of the $[\mathrm{P}] = 4 \times 10^{12}\,\mathrm{cm}^{-3}$ sample: To the knowledge of the author, the measured 350 ms $1/e$-decay is the longest measured Hahn coherence time of an electron spin in a semiconductor—away from the magnetic field insensitive clock transitions [17].

6.3.4 Conclusion

In summary, a D^0X-assisted spin measurement has been introduced that relates the observed photoconductivity during a pulsed laser experiment to the polarisation degree of the neutral donor. This measurement method was combined with microwave pulses to enable ESR measurements on spin ensembles that are below the sensitivity limit of conventional ESR spectrometers. A lower bound for the coherence time of phosphorus in the 28Si-Avo sample has been measured as $T_2 = 130 \pm 30\mathrm{ms}$, which is likely to be below the intrinsic spin coherence time and due to vibrations of the sample in the helium gas flow.

An outstanding experiment, and a possible future work, is to characterize if, and to what extend, the laser influences a subsequent coherence time measurement in the dark. It is possible that (de-)charging of defects during the hyperpolarisation laser period is occurring, which leads to charge noise in the subsequent dark period,

as the system relaxes back to thermal equilibrium. No such effects were obvious for phosphorus, neither in experiments carried out in London, nor in Princeton, but a systematic study has yet to be carried out.

6.4 Donor state tomography beyond the pure-state approximation

This section introduces an experiment that goes beyond the capabilities of conventional ESR experiments. ESR quantum state tomography is limited in the respect that it can only measure relative differences of polarisation along the three axis of the Bloch sphere. An absolute state population measurement is required to calibrate the measured echo intensities. Simply put, it is impossible to decide without additional assumptions, whether a measured echo intensity corresponds to a spin polarisation of, say, 1 % or 100 %. In contrast, the photoconductive D^0X spin measurement can, in principle, give an absolute state measurement and this chapter shows how this readout method can be combined with ESR pulse sequences to measure the full, possibly mixed density matrix of a donor ensemble.

Section 6.4.1 reviews the elements of single-spin tomography by ESR and its limitations. Section 6.4.2 introduces the D^0X tomography sequence as an extension towards the coupled electron-nuclear system of phosphorus. The method to calibrate the measured transient intensities is discussed and the pulse sequences for the measurement of the state population and coherences are introduced. Finally, Sec. 6.4.3 discusses the tomography results and methods to improve its efficiency and validity.

6.4.1 Quantum state tomography and echo-based tomography sequence

The goal of quantum state tomography is to measure the full quantum state of a single qubit or a qubit ensemble. From the discussion of quantum error correction (cf. Ch. 2.1) it is known that a quantum state can not be determined from a single measurement, due to the projective character of the measurement process. Instead, multiple measurements are required, for operators that span the Hilbert space of the quantum system. The tomography procedure for a single spin is laid out in this section.

The state ρ of a qubit (mixed or pure) can be expressed in the basis of the Pauli matrices [71]:

$$\rho = \frac{\mathbb{1} + \mathrm{Tr}\left(S_x\rho\right) S_x + \mathrm{Tr}\left(S_y\rho\right) S_y + \mathrm{Tr}\left(S_z\rho\right) S_z}{2} \tag{6.3}$$

$$= \mathbb{1} + \frac{\mathbf{rS}}{2} \tag{6.4}$$

The Pauli matrices are defined within this chapter as $\left\{\mathbb{1} = \begin{pmatrix} 1 & 0 \\ 0 & 1 \end{pmatrix}, S_x = \begin{pmatrix} 0 & 1 \\ 1 & 0 \end{pmatrix}, S_y = \begin{pmatrix} 0 & -i \\ i & 0 \end{pmatrix}, S_z = \begin{pmatrix} 1 & 0 \\ 0 & -1 \end{pmatrix}\right\}$. The expansion coefficients $\mathrm{Tr}\left(S_{\{x,y,z\}}\rho\right)$ can be identified as the expectation value of a measurement of $S_{\{x,y,z\}}$ on ρ. The expectation value in turn is given by as the average of N measurement outcomes of $S_{\{x,y,z\}}$, with $N \to \infty$.

How can $\mathrm{Tr}\left(S_{\{x,y,z\}}\rho\right)$ be extracted from a conventional ESR experiment? First, let A_z be the echo amplitude following a Hahn echo sequence with $(\pi/2)_x$—τ—$(\pi)_x$—τ—*echo*. The echo amplitude is directly proportional to the polarisation of the spin system, $A_z \propto \mathrm{Tr}\left(S_z\rho\right)$. In a similar way, a refocussing sequence τ—$(\pi)_x$—τ—*echo*, i.e. an echo sequence without the initial $(\pi/2)_x$, refocusses any initial coherences of $S_{\{x,y\}}$ into echo amplitudes $A_x \propto \mathrm{Tr}\left(S_x\rho\right)$ for the in-phase channel and $A_y \propto \mathrm{Tr}\left(S_y\rho\right)$ quadruature channel. Due to the weak-measurement property of an ESR echo, all three of these components can be measured in a single microwave sequence, as detailed in [19].

The difficulty in ESR state tomography is to find the constant of proportionality c, relating the echo intensities to the expectation values: $\mathrm{Tr}\left(S_{\{x,y,z\}}\rho\right) = cA_{\{x,y,z\}}$. Two different approaches are usually taken. The first is the pseudo-pure approximation, in which the ESR-inactive, mixed, part of the density matrix is simply disregarded, thus rendering the density matrix pseudo-pure. For a pure state, the Bloch vector $\mathbf{r}$ is on the surface of the Bloch sphere, resulting in $||\mathbf{r}|| = 1$, which allows for the normalization of the echo amplitudes according to $\sqrt{A_x^2 + A_y^2 + A_z^2} = 1$. The second approach typically used is to measure the density matrix of the thermal spin state. The thermal equilibrium density matrix is given by

$$\rho_{\mathrm{thermal}} = \frac{1}{\mathcal{Z}} \exp(-\frac{\mathcal{H}}{k_{\mathrm{B}}T}) \tag{6.5}$$

with Boltzmann constant k and temperature T. $\mathcal{H}$ is the spin Hamiltonian and $\mathcal{Z}$ the grand partition function. The expected spin polarisation of ρ_{thermal} is then used to calibrate c to the measured A_z; the same constant c can then be used for all further tomography experiments.

Both approaches to ESR-echo based state tomography are somewhat dissatisfying. The pseudo-pure approximation clearly does not represent the true physical system, while the thermal calibration relies on assumptions about the sample temperature of the sample and a thermal equilibrium polarisation.

In contrast, D^0X assisted spin-measurement could overcome these difficulties and result in quantitative measurements of the density matrix of a donor spin ensemble. The details of the D^0X state tomography are discussed in the next section.

6.4.2 Principle of D^0X-assisted state tomography of D^0 spins

D^0X-assisted state tomography of D^0 spins relies on the same pulsed-laser principle that was used for the coherence time measurement of sample 28Si-Avo in Sec. 6.3. A laser is tuned to (e.g.) the $|\uparrow\rangle$ state and upon illumination produces a transient photoconductivity that is proportional to the number of donors in the $|\uparrow\rangle$ state. The D^0X measurement constitutes a measurement of $S^\alpha = \begin{pmatrix} 1 & 0 \\ 0 & 0 \end{pmatrix}$ with the laser tuned to $|\uparrow\rangle$, or for the laser tuned to the $|\downarrow\rangle$ a measurement of $S^\beta = \begin{pmatrix} 0 & 0 \\ 0 & 1 \end{pmatrix}$. The donor spin-system is furthermore hyperfine coupled to the nuclear spin and thus the general density matrix has a dimension of $d = (2S+1)(2I+1)$.

In the following, the density matrix for phosphorus with $S = 1/2$ and $I = 1/2$ and dimension $d = 4$ is considered. In principle, the D^0X transition could be sufficiently sharp to enable measurements of the individual hyperfine-split levels, i.e. measure $S^\alpha I^\alpha$, $S^\alpha I^\beta$, etc. Unfortunately, all of the ^{28}Si samples of this thesis have D^0X linewidths that are too broad to enable such individual state measurements. Hence, it is only possible to measure both electron $|\uparrow\rangle$ states simultaneously, regardless of their nuclear spin projection. This constitutes a measurement of $S^\alpha \otimes \mathbb{1}$, which is furthermore enforced experimentally by 'jittering' the laser over the full D^0X linewidth at a rate of 1 kHz.

The state tomography of the two-spin system is analogous to the single-spin case and the density matrix is reconstructed according to [71]:

$$\rho = \sum_{j,k=0..3} \frac{\mathrm{Tr}\left((\sigma_j \otimes \sigma_k)\rho\right)(\sigma_j \otimes \sigma_k)}{4}, \tag{6.6}$$

$$\tag{6.7}$$

where σ_j, σ_k are the chosen basis set for the electron and nuclear spin. For the D^0X state tomography the following basis set was chosen[6]:

$$\{\mathbb{1}, S_x, S_y, S_z\} \otimes \{\mathbb{1}, I_x, I_y, I_z\} = \{\mathbb{1}, S_z, I_z, S_z I_z, \tag{6.8}$$

$$S_x, S_y, I_x, I_y, \tag{6.9}$$

$$S_x I_x, S_x I_y, S_x I_z, \tag{6.10}$$

$$S_y I_x, S_y I_y, S_y I_z, \tag{6.11}$$

$$S_z I_x, S_z I_y\} \tag{6.12}$$

In order to measure the expectation values of these operators, microwave pulse sequences must be derived that map the respective operator into the S^α observable of the D^0X readout. This is done in the next paragraph, which discriminates between operators that measure the state population, i.e. those operators of line (6.8), and those that measure the coherences between the four states, i.e. operators (6.9)-(6.12). During this derivation, ideal pulses are assumed without any dephasing during the pulse duration, or rotation errors.

Reconstruction of state population The four operators given in line (6.8) can be used to reconstruct the diagonal entries of the density operator, i.e. the state populations. However, they are not the most natural set, given a D^0X measurement method capable of measuring state populations directly. Following the definition of the population operators S^α,S^β the diagonal components of the density matrix can also be expressed as:

$$\frac{\mathbb{1} + \mathrm{Tr}\left(S_z\rho\right) S_z + \mathrm{Tr}\left(I_z\rho\right) I_z + \mathrm{Tr}\left(S_z I_z\rho\right) S_z I_z}{4} = \tag{6.13}$$

$$\rho_{11} S^\alpha I^\alpha + \rho_{22} S^\alpha I^\beta + \rho_{33} S^\beta I^\alpha + \rho_{44} S^\beta I^\beta \tag{6.14}$$

Thus, the diagonal entries are chosen to be reconstructed by the measurement of individual state populations. As detailed at the end of the section and also discussed in Sec. 6.3 and Ch. 5.1.6 the transient response of the conductivity upon illumination with a tuned D^0X laser is proportional to the occupation of those levels that the laser is tuned to. With the laser tuned to pump simultaneously on both the $|\uparrow\Uparrow\rangle$ and $|\uparrow\Downarrow\rangle$ level, it can thus be stated that the integrated transient of measurement k is given by

$$A^k = c\mathrm{Tr}\left(S^\alpha \rho^k\right) = c(\rho^k_{11} + \rho^k_{22}) \tag{6.15}$$

[6]Refer to [137] for other choices of matrices basis sets, such as $\{S^\alpha, S^\beta, S^+, S^-\}$.

where c is the constant of proportionality relating the measurement outcome to the physically measured observable, i.e. here the photo-current. ρ_{11}^k and ρ_{22}^k are the $|\uparrow\Uparrow\rangle$ & $|\uparrow\Downarrow\rangle$ level occupations at the end of the microwave pulse sequence k.

By choosing microwave pulse sequences that transfer the different donor levels under investigation into the laser readout states via electron- and nuclear-spin (π)-pulses, different combinations of state occupations can be measured. For the four pulse sequences I to IV depicted in Fig. 6.9, this results in the following linear equation system:

$$\begin{pmatrix} A^{\mathrm{I}} \\ A^{\mathrm{II}} \\ A^{\mathrm{III}} \\ A^{\mathrm{IV}} \end{pmatrix} = c \begin{pmatrix} 1 & 1 & 0 & 0 \\ 0 & 1 & 1 & 0 \\ 1 & 0 & 0 & 1 \\ 0 & 1 & 0 & 1 \end{pmatrix} \begin{pmatrix} \rho_{11} \\ \rho_{22} \\ \rho_{33} \\ \rho_{44} \end{pmatrix} \tag{6.16}$$

Together with the unitary condition $\mathrm{Tr}\,(\rho) = 1$, these five coupled equations can be solved for c and the state populations ρ_{11} to ρ_{44}.

With the above four pulse sequences, four different state combinations have been projected into the $\mathrm{D^0X}$ readout state $|\uparrow\rangle$, while two state combinations have not been measured (namely $\rho_{11}+\rho_{33}$ & $\rho_{33}+\rho_{44}$). It should be noted that, alternatively for better accuracy, it is also possible to measure all six state combinations and determine the ρ_{11} to ρ_{44} entries via a least-squares fit.

Mapping of the coherences into the S^α $\mathrm{D^0X}$ readout With the diagonal components of the density matrix determined and a known value for c, the components remaining are the coherences of the density matrix.

How can operators like $S_x I_y$ be measured using S^α? Firstly, since S^α measures the $|\uparrow\rangle$ population, it is not surprising that S^α is related to S_z, the measurement of population difference between $|\uparrow\rangle$ and $|\downarrow\rangle$. The corresponding mathematical identity is $S^\alpha = (\mathbb{1} + S_z)/2$ and hence

$$\mathrm{Tr}\,(S_z\rho) = \mathrm{Tr}\,((2S^\alpha - \mathbb{1})\rho) = 2\,\mathrm{Tr}\,(S^\alpha\rho) - 1 \tag{6.17}$$

A measurement of S^α is thus equivalent to a measurement of S_z.

In a similar way, S_z can also be determined from a measurement of both S^α and S^β using the identity $S_z = S^\alpha - S^\beta$. A measurement of S^β is performed either by a second laser tuned to the $|\downarrow\rangle$ states or, as is done in this chapter, via a global microwave $(\pi)_{S_x}$ pulse prior to the $\mathrm{D^0X}$ measurement. The advantage of this method is that any baseline errors discussed in Sec. 6.4.4 are eliminated. On the other hand,

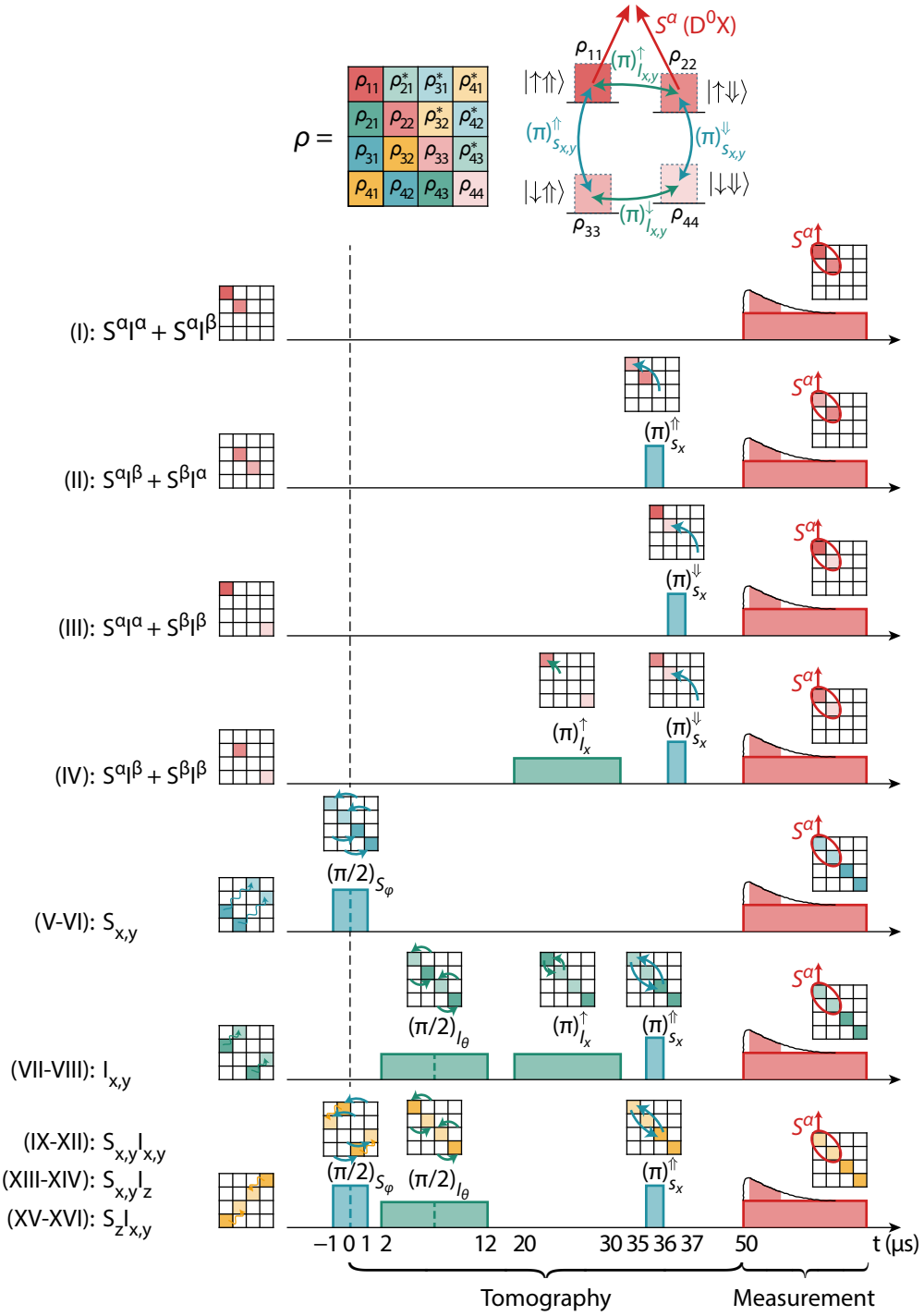

Figure 6.9: The pulse sequences used for the D^0X-assisted D^0 spin tomography. Top shows the components of the 2×2 density matrix, with population entries (red), pure nuclear coherences (green), pure electron coherences (blue) and mixed coherences (yellow). Top right depicts the energy level diagram with the available ESR and NMR transitions and the D^0X laser S^α readout. Below, the 16 pulse sequences required for the tomography are depicted, along with their influence on the density matrix entries. Sequences I to IV target the reconstruction of the diagonal matrix elements, while sequences V to XVI measure the spin coherences. Global ESR or NMR pulses can be implemented either as two subsequent selective pulses (dashed lines within pulses) or by a synthesized global pulse with usually half the amplitude on each transition. θ and φ are chosen according to the operator to be mapped.

it increases the number of pulse sequences required for the reconstruction of the off-diagonal component from 12 to 24.

In the following the pulse sequences that map the coherence operators (6.9)-(6.12) into S_z are discussed.

Global electron spin coherences The electron spin coherence operators S_x & S_y can be measured by projecting their measurement outcome into S_z and then measuring S^α. The required mapping sequence is analogous to the ESR tomography sequence for a determination of S_z via the measurement operator S_x: The S_z operator is mapped into the measurement operator S_x via a $(\pi/2)_{S_y}$ pulse.

The mathematical principle behind the reverse, i.e. the determination of the S_x via a measurement of the S_z operator is the following: A unitary operation U is required such that a measurement of S_x on the original system produces the same measurement result as a measurement of S_z after the unitray operation U:

$$\mathrm{Tr}\left(S_x\rho\right) = \mathrm{Tr}\left(S_z U\rho U^\dagger\right) \tag{6.18}$$

Traces of matrix products are invariant under cyclic permutation and hence the equation can be reduced to:

$$\mathrm{Tr}\left(S_x\rho\right) = \mathrm{Tr}\left(U^\dagger S_z U\rho\right) \tag{6.19}$$

$$S_x = U^\dagger S_z U \tag{6.20}$$

$$U S_x U^\dagger = S_z \tag{6.21}$$

The last line describes a process that rotates an S_x state into an S_z, which means that the required U is simply a $(\pi/2)_{-S_y}$, i.e. $U = \exp(-i(-\pi/2)S_y)$. So in general, an operator can be measured via S_z by the same sequence that rotates an eigenstate of that operator into S_z. It should be noted that this process is independent of the nuclear spin, i.e. this $(\pi/2)_{-S_y}$ pulse must be applied on both ESR transitions.

The resulting pulse sequences, devoted V & VI, for the measurement of S_x and S_y are depicted in Fig. 6.9. A global microwave pulse rotates the operator to be determined into S_z, which is then measured by a D^0X-based readout of S^α.

Global nuclear spin coherences The nuclear spin coherences, I_y & I_x, are measured in a similar way to the electron spin coherences (cf. Fig. 6.9, sequences VII & VIII). First, a global $(\pi/2)_{\pm I_{x(y)}}$ pulse projects the I_y (I_x) coherence into I_z, which

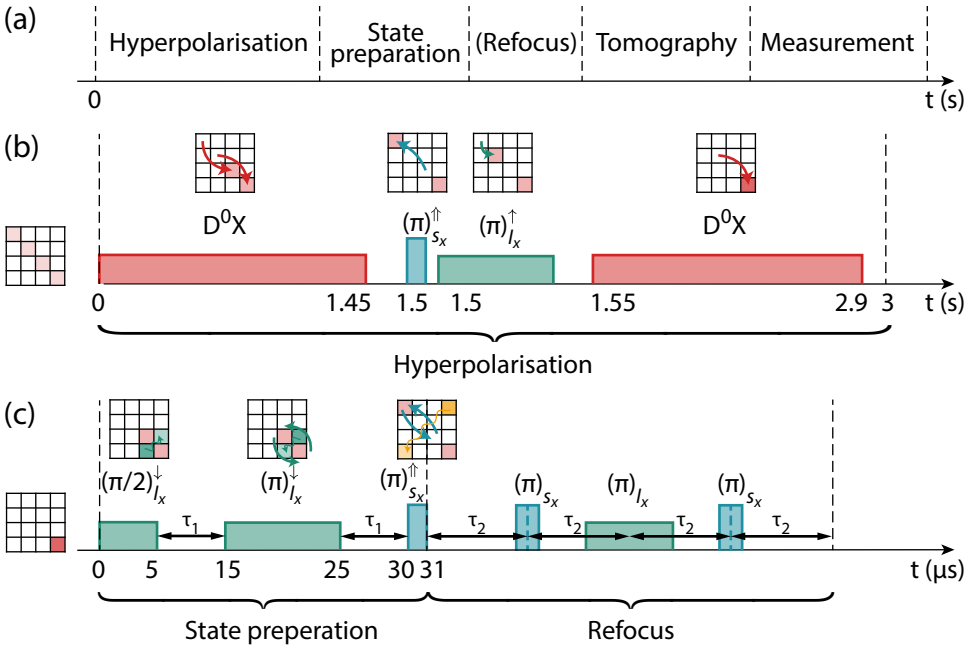

Figure 6.10: The individual parts of the full D^0X tomography sequence is depicted in (a), where most times the measurement D^0X pulse is the same pulse as the first pulse of the hyperpolarisation sequence. The hyperpolarisation sequence (b) intends to produce a pure state for the whole donor spin ensemble, with all population in $|\downarrow\Downarrow\rangle$. The state preparation part (c) is adjusted depending on the desired state, with the example of a Bell state $(|\uparrow\Uparrow\rangle + |\downarrow\Downarrow\rangle)/\sqrt{2}$, while the second part of (c) shows a potential, but unused global refocussing sequence.

is in turn is projected into S_z by a selective $(\pi)^{\uparrow}_{I_x}$ pulse, followed by a selective microwave pulse $(\pi)^{\Uparrow}_{S_x}$. S_z is finally measured via the D^0X S^α readout.

Mixed electron and nuclear coherences The remaining terms of (6.10)-(6.12), such as S_xI_y are first projected into S_zI_z via respective global ESR and NMR $(\pi/2)$-pulses. S_zI_z in turn is projected into S_z via a selective $(\pi)^{\Downarrow}_{S_x}$ pulse. The corresponding sequences IV to XVI are depicted in Fig. 6.9.

6.4.3 Experiment

The experimental realisation of the D^0X tomography is now discussed. First, the full pulse sequence including the hyperpolarisation and state preparation steps is introduced, followed by a review of the necessary preparation experiments. Finally, the achieved degree of hyperpolarisation and the tomography results are presented and discussed. The experiment has been carried out with sample 28Si-321 at 4.5 K.

Full tomography pulse sequence The different elements of the full tomography pulse sequence are depicted in Fig. 6.10(a). First, a hyperpolarisation sequence aims to achieve a high degree of state purity by projecting most of the population into a single state, here state $|\downarrow\Downarrow\rangle$. The subsequent state preparation sequence generate the state that is to be inspected using both NMR and ESR pulses. This is followed by an optional global refocussing sequence to reverse the effects of inhomogeneous broadening. Finally, the tomography pulse sequences discussed above map the operator to be measured into S_z and the D^0X laser pulse measures S^α.

The hyperpolarisation sequence employed here is depicted in Fig. 6.10(b). First, a D^0X laser pulse depletes the $|\uparrow\rangle$ states and transfers their population (spread equally over ρ_{11} & ρ_{22}) to the $|\downarrow\rangle$ states (i.e. to an equal mixture of ρ_{33} & ρ_{44}). A selective microwave pulse $(\pi)^{\Uparrow}_{S_x}$ and NMR pulse $(\pi)^{\uparrow}_{I_x}$, transfers the ρ_{33} population to ρ_{22}. The final D^0X laser pulse then brings ρ_{22} to ρ_{44}. Relatively long laser pulses of $\sim$1.5 s were required, since a relatively low laser power of $I_\mathrm{L} = 8.5 \times 10^2\,\mathrm{W/m^2}$ gave the best transient response for read-out.

The state preparation sequence is shown in Fig. 6.10(c) for the example of a Bell state. Here, a refocussing NMR pulse ensures that the nuclear spin coherence is maximum at the point of the microwave pulse, creating the Bell state. Furthermore, a potential global refocussing sequence is shown, consisting of symmetrically placed global microwave $(\pi)_{S_x}$ pulses and a global NMR $(\pi)_{I_x}$ pulse. To avoid introducing additional errors due to imperfections of the refocussing pulses, the refocussing sequence is omitted in the following. Instead, directly after the state creation, the projective microwave $(\pi/2)_{S_\phi}$ pulses of the tomography sequence were placed and the NMR $(\pi/2)_{I_\theta}$ pulses follow 2 µs later.

Preparation experiments Figure 6.11 summarizes the key preparation measurements of the D^0X tomography. After the determination of the resonant magnetic field $B = 324.324\,\mathrm{mT}$, both nuclear spin transitions $\omega_I^{\uparrow(\downarrow)}/2\pi$ are determined via echo-detected Davies ENDOR measurements (see Fig. 6.11(a) & (b)). Rabi measurements on these nuclear spin transitions determine selective $(\pi)^{\uparrow(\downarrow)}_{I_\theta}$ durations of 10 µs (see Fig. 6.11(c)). Fig. 6.11(e) sketches the approximate position of the two microwave transition frequencies compared to the response of the microwave cavity. The Q factor of the cavity is a trade-off between enabling both transitions to be addressed (which would favor low Q factors) and the stored microwave power in the cavity (which favors higher Q factors). While measuring an echo on the lower frequency $\omega_S^{\Downarrow}/2\pi = 9.65\,\mathrm{GHz}$, the second transition is detected by an ELDOR sequence, consisting of a selective $(\pi)^{\Uparrow}_S$ pulse, followed by a selective $(\pi)^{\Downarrow}_I$ pulse. With

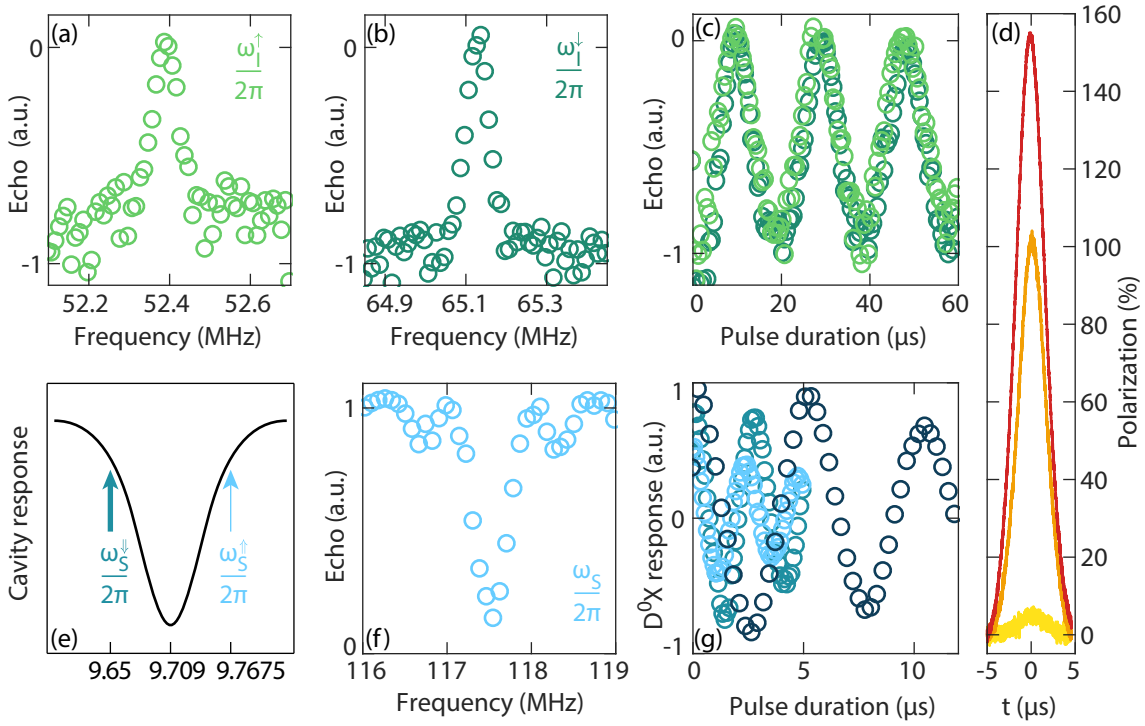

Figure 6.11: Preparation experiments required for the D^0X state tomography on sample 28Si-321. The two NMR transition frequencies (a,b) are identified by a Davies ENDOR sequence. Nuclear spin Rabi oscillations show a (π)-pulse duration of 10 µs. (d) shows the enhancement of electron spin echo intensity on the $\Downarrow$-ESR transition, with the echo obtained without hyperpolarisation (yellow) calibrated to the thermal polarisation of 5.1 % at 4.5 K. From the echo decay an electron dephasing time of $T_{2e}^{*} \approx 2\,\mu s$ is extracted. (e) sketches the position of the microwave transitions in comparison to the microwave resonator with $Q \approx 300$. (f) shows the ELDOR detection of the second, synthesized microwave transition using an ELDOR experiment and (g) shows the D^0X detected Rabi oscillations of the individual ESR transitions (circles in respective colour) and of a global microwave pulse with half the Rabi frequency (dark blue).

all pulses on resonance, the population difference on the echo-transition vanishes. As seen in Fig. 6.11(f), this is the case for $\omega_S^{\Uparrow}/2\pi = \omega_S^{\Downarrow}/2\pi + 117.45\,\mathrm{MHz}$, with the difference being the hyperfine constant of phosphorus. Fig. 6.11(g) shows selective electron Rabi oscillations on the two lines with $(\pi)_S^{\uparrow(\downarrow)}$ durations on the order of 1 µs. These pulses are relatively long, since the microwave frequency are at the edges of the cavity resonance and furthermore because only a 3 W microwave amplifier is used since the 1 kW TWT amplifier was not incorporated into the setup at the time of the experiments. Fig. 6.11(g) furthermore shows the D^0X detection of global ESR Rabi oscillations in dark blue.

Fig. 6.11(d) shows the intensity of a Hahn echo on the I^β ESR transition. The intensity of the thermal polarisation of this transition is shown in yellow and is calibrated to its thermal equilibrium value of 5.1 %. In comparison to this, the intensity after a 1.5 s D^0X laser pulse without any microwave or NMR pulses, i.e. simple D^0X polarisation is shown in orange, while the echo intensity after the full hyperpolarisation sequence of Fig. 6.10(b), including NMR pulses to enable nuclear polarisation, too is shown in red. Both of these traces have been calibrated to the thermal equilibrium polarisation. It is clear that the full hyperpolarisation sequence exceeds a polarisation of 100 %, meaning that population from the $|\Uparrow\rangle$-states has been transferred to the $|\downarrow\Downarrow\rangle$-state. The thermal density matrix population difference of the I^β ESR transition is $\rho_{44}-\rho_{22} = 0.026$ and with an increase of the echo intensity by a factor of ∼30, the population difference for the hyperpolarised state is thus expected to be $\rho_{44} - \rho_{22} \approx 0.76$.

Tomography of hyperpolarised state The tomography sequence is first performed on the hyperpolarised state. Figure 6.12(a) shows the ideal and the recovered density matrix by the full 30 pulse tomography sequence, consisting of 6 pulse sequences for the mapping of the populations and 24 pulse sequences for the coherence mapping into S^α and S^β. This leads to an extracted density matrix of the hyperpolarised state as:

$$\rho_{\mathrm{hyperpolarised}} = \begin{pmatrix} 0.11 & 0.00+0.01i & -0.01+0.02i & -0.00+0.01i \\ 0.00-0.01i & 0.23 & -0.01+0.00i & 0.00+0.01i \\ -0.01-0.02i & -0.01-0.00i & 0.10 & 0.01-0.00i \\ -0.00-0.01i & 0.00-0.01i & 0.01+0.00i & 0.56 \end{pmatrix} \tag{6.22}$$

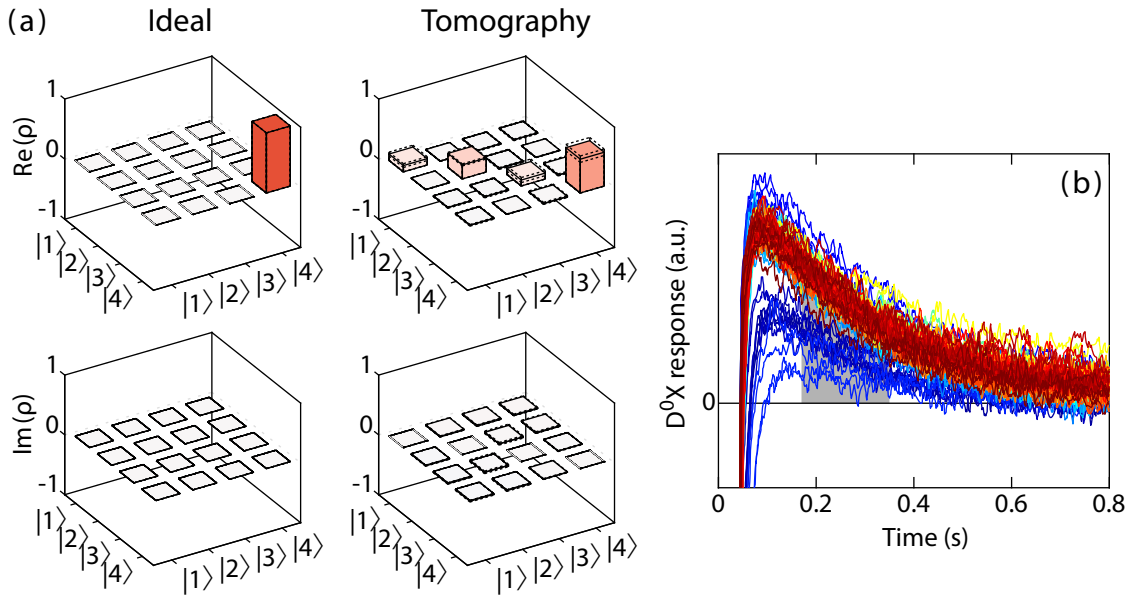

Figure 6.12: (a) The measured D^0X tomography result for the hyperpolarised donor ensemble of sample 28Si-321. The ideal state is compared to the experimentally determined state. (b) The transients of the 30 microwave sequences that enabled this result, with the D^0X transient integration window depicted in grey.

Strikingly, the population difference of the I^β microwave transition is only $\rho_{44}-\rho_{22} \approx 0.33$, less than half of the expected value of 0.76. What could be a reason for the difference between echo-detected hyperpolarisation degree and the polarisation measured by the D^0X state tomography? It is possible that mapping pulse imperfections or noise from inactive pulse, only intended to be active for the coherence mapping sequences have affected the tomography measurement. A drift of the efficiency of the hyperpolarisation degree can be ruled out, since the echo enhancement measurement of the hyperpolarisation sequence has been performed both before and after the tomography experiments with matching results. Furthermore, it should be noted that the choice of the baseline, as discussed in Sec. 6.4.4, does modify the state populations of the recovered matrix. However, no physically viable choice of the baseline allows to match the polarisation values extracted by the D^0X-assisted tomography to the polarisation degree measured by the echo intensity enhancement.

Hence, overall it must be stated that the reason for the difference between the extracted hyperpolarisation degree from the the echo intensity measurement and the D^0X tomography remains unresolved.

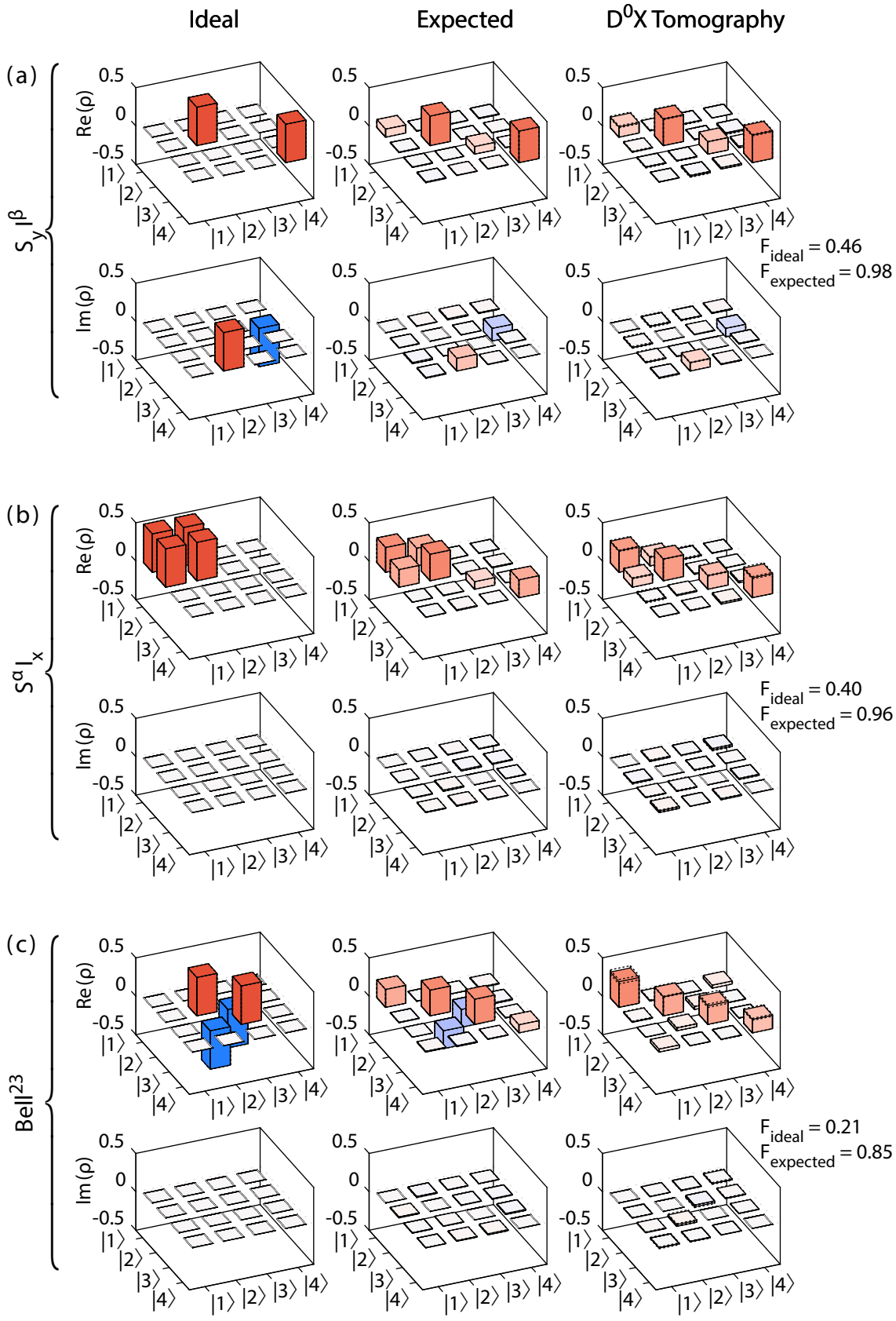

Figure 6.13: The D^0X state tomography results for input states with (a) electron coherence, (b) nuclear coherence and (c) combined electron-nuclear coherences. For each type of coherence, the ideal input state and the expected input state derived from the real hyperpolarised state of Fig. 6.12 are compared against the experimentally determined D^0X tomography density matrix.

Tomography results of input states with coherences The results of the full D^0X tomography for various input states are shown in Fig. 6.13. For each column, the ideal (wanted) state is depicted, along with the expected result for the state preparation pulse sequence applied to the measured hyperpolarisztion density matrix of (6.22). The third column shows the recovered density matrix from the D^0X tomography with 30 pulse sequences. To improve accuracy, the data is the average of 5 runs, with the standard deviation plotted as dotted line. The fidelity of the recovered density matrix compared to the intended, ideal state is given as F_{ideal} and the fidelity of the recovered matrix with the expected state from the hyperpolarisation density matrix is stated as F_{expected}. Both fidelities are calculated according to [71]:

$$F(\rho, \sigma) = \left(\mathrm{Tr} \sqrt{\sqrt{\rho}\sigma\sqrt{\rho}} \right)^2 \tag{6.23}$$

The tomography of the states $S_y I^\beta$ and $S^\alpha I_x$ os plotted in Fig. 6.13(a) & (b). For both, the electron and nuclear spin coherence, the D^0X tomography recovers the expected quantum state quite well with $F_{\text{expected}} > 96\,\%$. This proves that the tomography sequences does work in principle and that the general concept of the D^0X tomography is valid.

Unfortunately, a Bell state could not be recovered with reasonabe fidelity. Fig. 6.13(c) shows the example of a $(|\uparrow\Downarrow\rangle - |\downarrow\Uparrow\rangle)/\sqrt{2}$ state. The reason why these states could not be recovered with reasonable fidelity is unknown.

6.4.4 Baseline problem and possible solution

One problem remains with the D^0X tomography as discussed so far: The derived tomography sequence so far was based on the assumption that the measured transient response is directly proportional to the S^α measurement (cf. Eqs. (6.16) & 6.15). If the resonant D^0X ionisation would be the only source of conductivity change, then this assumption would be valid. However, the direct photoionisation process discussed in Ch. 5.1.4 also results in a change of conductivity, regardless of the polarization of the donors. Hence, more realistically the measurement amplitude introduced in Eq. 6.15 is given by:

$$A^k = b + c\mathrm{Tr}\left(S^\alpha \rho\right) \tag{6.24}$$

with b being the offset due to the off-resonant photoconductivity. In the discussed experiments, the offset b was chosen to be the lowest steady state value of all traces,

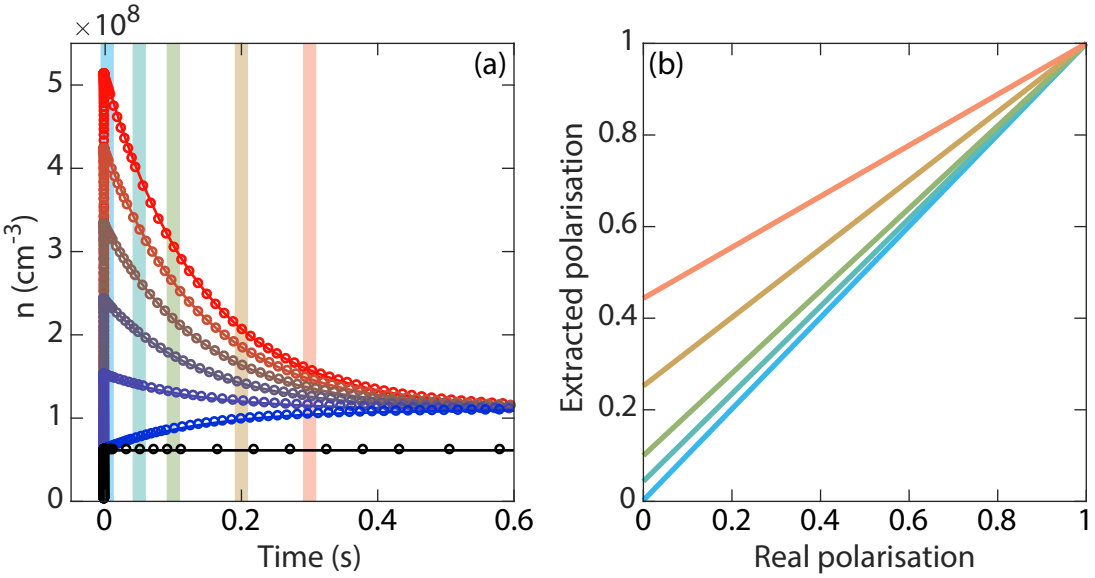

Figure 6.14: The simulated transient response upon D^0X laser illumination tuned to the $|\uparrow\rangle$ state for a sample with a natural silicon linewidth of 4 µeV and initial donor spin polarizations between 100 % (red) and 0 % (blue). A trace with the laser tuned off-resonant (black) reveals the donor-spin insensitive conductivity baseline. The measured, i.e. extracted polarisation following Eq. (6.24) as a function of the real polarisation is plotted in (b) for various integration windows.

as seen by the choice of $y = 0$ of Fig. 6.10(b). The reasoning behind this choice is that as the D^0X laser continues to deplete the $|\uparrow\rangle$ states, the population that it is pumping on approaches zero, leading to $\mathrm{Tr}\,(S^\alpha\rho) \to 0$ and allows for setting b as the steady state value. Certainly for samples with small linewidths, such as the ^{28}Si samples, this is a good approximation, since the ratio of $\Gamma_{D^0X}/\Gamma_{\mathrm{direct}} \gg 1$, leading to a high polarization degree (and hence small steady state population in $|\uparrow\rangle$, cf. Ch. 5.4.2. Still, it is an assumption and for samples with larger linewidths, i.e. comparable rates of Γ_{D^0X} and Γ_{direct} where the steady state polarisation is not close to 100 %, this assumption becomes problematic.

A solution to this problem is to measure a trace with the D^0X laser tuned off resonance, to guarantee $\mathrm{Tr}\,(S^\alpha\rho) = 0$ and directly measure b due to Γ_{direct}. Figure 6.14(a) shows the calculated transient response of an ensemble with spin polarisation P values between $P = 0$ (blue) to $P = 1$ (red), calculated according to the coupled rate equations of Ch. 5.1.6. Furthermore, the response with the laser off resonance is shown in black. Taking the steady state conduction electron concentration of the off resonance laser as the value for b, the polarization degree is reconstructed from the transient response. This is done at five different time traces, leading to the recovered values depicted in Fig. 6.14(b). The reconstruction works best for

integration windows straight after the laser illumination, while later windows lead to deviatons between the real and the D^0X tomography reconstructed polarization[7].

A more technically demanding, but alternative solution for the baseline problem would be a measurement of a trace pumping on the full donor ensemble. By tuning two lasers to pump respectively on the $|\downarrow\rangle$ and $|\uparrow\rangle$ states, a trace could be captured that measures the full ensemble population with $A^k = b + c\mathrm{Tr}\,(\mathbb{1})$. This, in combination with the measurement of the individual state populations would allow for the determination of b, c and the state populations.

Unfortunately, at the time that these experiments were conducted, no such trace, either off resonance, or with two lasers, has been measured. Still, as this was measured on a ^{28}Si sample with small linewidth, the assumption that the $|\uparrow\rangle$ states are empty under continuous pumping should be accurate to a few 10 %.

6.4.5 Conclusion

In summary, a tomography method based on the spin-dependent photoconductivity change of a laser tuned to the D^0X transition has been developed that allows for the determination of the full, potentially mixed donor density matrix, without relying on assumptions such as a thermal equilibrium of the spin ensemble. The theoretical framework has been developed and the required preparation measurements have been reviewed. It has been shown that the tomography sequence works in principle, with high-fidelity recovered matrices for single quantum coherence. The method was still based on a small assumption for the correct scaling of the measurement variable, but a method has been introduced to eliminate the uncertainty associated with the baseline shift due to the off-resonant photoconductivity. Two unresolved issues remain: Firstly, the observed difference of the hyperpolarisation degree between the D^0X state tomography and the ESR Hahn echo enhancement is puzzling. Secondly, the unsuccessful preparation or tomography of the Bell state is not understood.

[7] If, for reasons such as long lock-in timescales, a measurement can only be taken a certain period after the laser curtain, then the conductivity value at the time of the laser-shutter can still be extrapolated by an exponential fit to the transient response.

Chapter 7

Bound exciton measurements in silicon devices

This chapter introduces first steps towards silicon devices that exploit the D^0X transition for donor spin readout. As a proof-of-principle, Sec. 7.1 demonstrates that the same kind of spin-measurement demonstrated in the previous chapter via a capacitive measurement is also possible using conductivity measurements with direct contact to the sample. The intrinsic, donor concentration-limited coherence time is measured using parallel aluminium electrodes. This demonstrates that devices are conceivable for applications such as magnetic field sensing, which are based on phosphorus donor spin coherence, but do not require microwave cavities on chip to perform the donor spin readout.

The transport characteristics of the aluminium-silicon Schottky interface used for the proof-of-principle device are not optimal. Hence, in Sec. 7.2 the transport of purposely fabricated samples with n^+ electrodes is investigated. Models for the underlying processes observed at 4.2 K are developed, both for the high and the low bias regime which find qualitative agreement with the measured IV curves under illumination and in the dark.

Section 7.3 addresses the question of whether the contacts play a specific role in the D^0X signal. A laser spot is scanned across the device and the photocurrent is observed as a function of position. The resulting excitation maps are quite complicated to interpret, with a variety of dependencies on bias, laser power, temperature and magnetic field, but largely validate that the signal is generated within an area up to $\sim$250 µm away from the electrodes.

Finally, Sec. 7.4 deals with the dependence of the D^0X transition energy to electric fields. Two different—and contradicting—theoretical treatments are explored and several experiments show that the electric field induced shifts are indeed relatively small. Hence, electric field induced shifts of the D^0X transition in devices may be

less of a concern than previously thought. Good agreement with an effective mass theory for the D^0X shifts is achieved.

7.1 Spin readout in ^{28}Si devices

This section aims to demonstrate that, in addition to the capactive measurement of the previous chapter, the D^0X transition allows furthermore the spin-measurement of donors in devices via direct electrical contacts. Both the device, its strain-affected D^0X spectrum, and the measurement technique, have already been introduced in chapters 6.3 and 5.3, respectively, so the presentation and discussion of the results in this chapter is kept relatively short.

7.1.1 Setup, D^0X spectrum and pulse sequence

The experiments are conducted on sample 28Si-epi and the inset of Fig. 7.1 (a) features an illustration of the sample and electrical connection. The active layer of the device is a 25 µm thick layer of ^{28}Si:P (with a phosphorus concentration of $1 \times 10^{15}\,\mathrm{cm}^{-3}$) which is epitaxially grown on an intrinsic natural silicon substrate. Two parallel aluminium contacts are evaporated onto the sample (thickness: 30 nm) for electrical connection (length: 700 µm, separation: 100 µm). The photo-current for a bias voltage of $V = 100\,\mathrm{mV}$ is measured via a Femto DLPCA low noise amplifier and captured on an oscilloscope. The sample normal is parallel to the magnetic field and the temperature of the experiments is 4.5 K.

Figure 7.1(a) plots the photo-current as a function of photon energy at $B = 340\,\mathrm{mT}$, i.e. a cross-section of Fig. 5.8(b) at the magnetic field suitable for X-band ESR experiments ($g \approx 2$). The spectrum is asymmetric due to the strain caused by the lattice mismatch between the ^{28}Si layer and the $^{\mathrm{nat}}$Si substrate and hence two pairs of D^0X transitions overlap. Line 5,6 does not feature overlapping transitions in its vicinity and is thus chosen as the transition on which the following experiments are carried out.

A pulsed laser and microwave sequence, essentially equivalent to the sequence introduced in Ch. 6.3.1 is employed for the spin readout: The sequence is shown in Fig. 7.1(b) and starts with the polarisation of the ensemble during the initialisation D^0X pulse. The following microwave sequence performs the desired ESR experiment and a final read-out D^0X laser pulse produces a photo-current whose recorded oscilloscope trace is shown at the bottom of Fig. 7.1(b). The orange trace for a $(\pi)_{S_x}$ microwave pulse features a clear transient response, while the trace without microwave pulse (blue) features a flat response. As discussed previously, the integrated transient is used as a measurement of the $|\uparrow\rangle$ population at the end of the microwave pulse sequence.

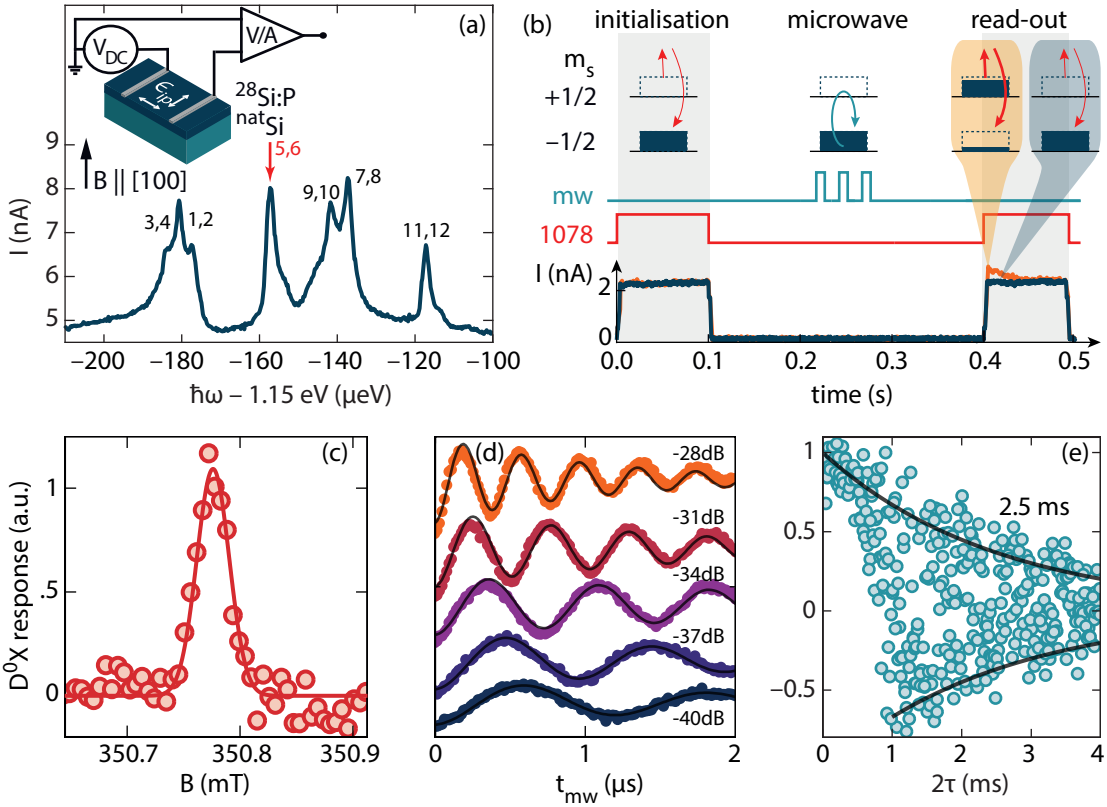

Figure 7.1: The D^0X-assisted donor elecron spin coherence time measurement of sample 28Si-epi. (a) The D^0X spectrum at 340 mT, 4.5 K and 100 mV, which is affected by strain from the ^{nat}Si substrate (cf. Fig. 5.8). The inset is a sketch of the sample and measurement electronics. (b) The pulse sequence used for the D^0X assisted spin-measurement, with the measured photocurrent traces for an off resonance and on resonance microwave (π)-pulse. (c) The integrated photo-response to a microwave (π)-pulse ($f_{mw} = 9.7293$ GHz) as a function of magnetic field. (d) Rabi oscillations at different microwave attenuations of a 1 kW microwave pulse. (e) The coherence time measurement with an approximately exponential envelope of $T_2 = 2.5$ ms, limited by instantaneous diffusion, with phase noise evident for $2\tau \gtrsim 0.5$ ms.

7.1.2 Rabi oscillations and coherence time

Figure 7.1(c) shows that the source of the transient response is clearly the phosphorus donors, since a microwave pulse only results in a D^0X response at the resonant magnetic field of phosphorus. A sweep of the microwave pulse duration, depicted in Fig. 7.1(d), results in coherent driving of the electron spin with multiple Rabi oscillations.

Finally, Figure 7.1(e) plots the results of the coherence time measurement. The experiment is again affected by magnetic field instability resulting in phase noise for free evolution times $2\tau \gtrsim 0.5\,\mathrm{ms}$—analogous to the 28Si-Avo coherence time measurement of the previous chapter. Still, from the envelope of the echo decay a coherence time of $T_2 \approx 2.5\,\mathrm{ms}$ can be extracted for this phosphorus ensemble with concentration of $\sim 10^{15}\,\mathrm{cm}^{-3}$. The measured coherence time is indeed the intrinsic value expected for instantaneous diffusion at this donor concentration, given by Eq. (3.20). For phosphorus, with nuclear spin $I = 1/2$ and two ESR transitions $C = [\mathrm{P}]/2$, the expression gives $T_{2,\mathrm{id}}([P] = 1 \times 10^{15}\,\mathrm{cm}^{-3}) = 1.9\,\mathrm{ms}$ and the difference between measured and expected value may be attributed to the uncertainty in the sample phosphorus concentration and the phase-noise affected fit.

7.1.3 Summary and sensing applications

In summary, it has been demonstrated that spin-readout of donor ensembles is achievable with devices that measure the D^0X photoconductivity using direct contacts. This permits the measurement of spin-related phenomena in devices without the need for echo-detection and allows thus for pathways to the spin-measurement of increasingly smaller spin ensembles. Hereby, it is encouraging that the donor coherence time is not affected by the read-out and/or the surface proximity and remained at its bulk-value.

For the future, this opens the door to CMOS compatible magnetic-field sensitive devices that could be used for sensing applications. A CCD-like array of such devices would allow for spatially resolved magnetic field measurements—a research area known as magnetometry. At the forefront of solid-state spin based magnetometry is the NV center, which has the benefit of optical spin-readout at room temperature [61, 62, 65]. Silicon, however, shows longer coherence times and thus promises superior magnetic-field sensitivity compared to NV centers. Furthermore, CMOS devices fabrication is comparatively cheap to the confocal setups required for NV center measurements and hence silicon-based devices with D^0X spin-readout might

be promising candidates for ultra-sensitive magnetometers with applications ranging from security to medicine [56, 57].

7.2 Transport in n$^+$nn$^+$ structures at 4 K

Due to the low thermal energy of electrons and holes at 4 K, transport characteristics of silicon devices at liquid helium temperatures may significantly differ from their room temperature characteristics. In this chapter the current–voltage characteristics of a basic device is investigated—a resistor with degenerately (n^+)-doped source and drain contacts and a lightly doped n-region of phosphorus in-between, whose photoconductivity shall be measured. At room temperature, the I-V characteristics are perfectly ohmic, with a sheet resistance determined by the doping density of the low dose n implant. At low temperatures, however, the observed I-V curves exhibits multiple plateaus and kinks and significant modelling with a variety of physical phenomena is required to understand the changes of the transport upon illumination.

The section starts with a discussion of the devices used, the expected band structure and the measured current-voltage characteristics. Section 7.2.2 investigates the high-bias transport regime and corresponding literature, suggesting that impact ionization of dopants determines the sample conductivity. A simulation is developed to explain the observed trends as a function of laser illumination and voltage bias. This model is no longer valid in the low-bias regime which is discussed in Sec. 7.2.3. Here, thermionic or laser-induced emission over the built-in potential from the n^+ to the n regime is limiting the current. A second model is developed for this regime, which, taken together with a reasonable guess for certain parameters allows for qualitative agreement between data and simulation over the complete bias regime.

7.2.1 Device, band structure & experimental results

The devices used throughout the remainder of this chapter are all part of the D0XDEV fabrication process outline in Chapter 4.1.2. A cross-section of the resistors used in this section is depicted in Fig. 7.2(a). Two aluminium contacts are placed above the parallel, degenerately-doped n^+ electrodes. The contact resistance between metal and the n^+ region as well as the resistance of the degenerately doped region are negligible, as confirmed[1] by two point sheet-resistance measurements at 4 K with Ohmic characteristics and a sheet resistance of 55 $\Omega/\square$. Between the electrodes a lightly doped region (phosphorus) is implanted with peak concentration of $3 \times 10^{15}\,\mathrm{cm}^{-3}$.

[1] Ludman [186] also reports ohmic characteristics for the metal-n^+ interface at 4 K and no significant changes of the n^+ layer resistance at cryogenic temperatures.

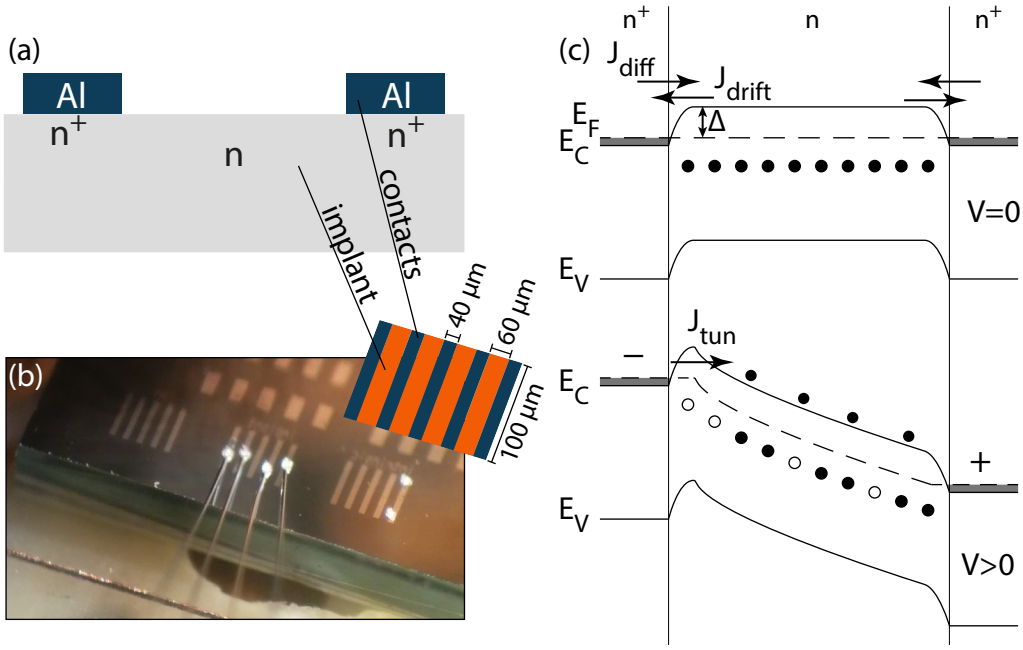

Figure 7.2: (a) Cross-section of the n^+nn^+ resistor used in this section. (b) Image and sketch of sample natSi-ResBars with 5 parallel n^+ electrodes contacted by aluminium bars and bond wires. (c) Sketch of the band structure of the n^+nn^+ resistor with the degenerately doped emitter and collector contacts and the band-bending of $\Delta \approx 20\,\mathrm{meV}$ at emitter and collector. Under a strong voltage ($\mathcal{E} \gtrsim 1 \times 10^5\,\mathrm{V/m}$) a tunnelling current flows through the barrier at the emitter and a certain ionised donor and conduction band electron concentration is established in the bulk due to impact ionization from field accelerated hot electrons.

The expected band structure of the device is displayed in Fig. 7.2(c). At the interface between the degenerately doped and the lightly doped region a potential barrier is formed, which has been determined experimentally to be on the order of 20 meV to 30 meV [187, 188]. The exact band structure at the interface depends on the workfunction of the n^+ region, which is doping level dependent and may become complicated due to the effect of bandgap narrowing with increasing doping density [189, 190]. However, for all doping densities above the Mott transition, the Fermi level in the degenerately doped region (where $E_\mathrm{F} > E_\mathrm{C}$) is higher than that of the lightly-doped region (where $E_\mathrm{F} \approx (E_{\mathrm{D}^0} + E_\mathrm{C})/2$, cf. Eq. (3.33)), leading to a diffusion of electrons from the n^+ to the n region, with the established space charge region giving rise to a barrier of[2] $\Delta \approx 20\,\mathrm{meV}$. At room temperature, this barrier is negligible compared to the thermal energy and hence allows for ohmic transport

[2]Following the argument of reference [189], at the used n^+ doping concentration in excess of $1 \times 10^{20}\,\mathrm{cm}^{-3}$ the Fermi level of the degenerately doped region is even above the conduction band of the lightly doped region, leading to band bending below the steady state Fermi level at the n side of the interface, as indicated in Fig. 7.2(c).

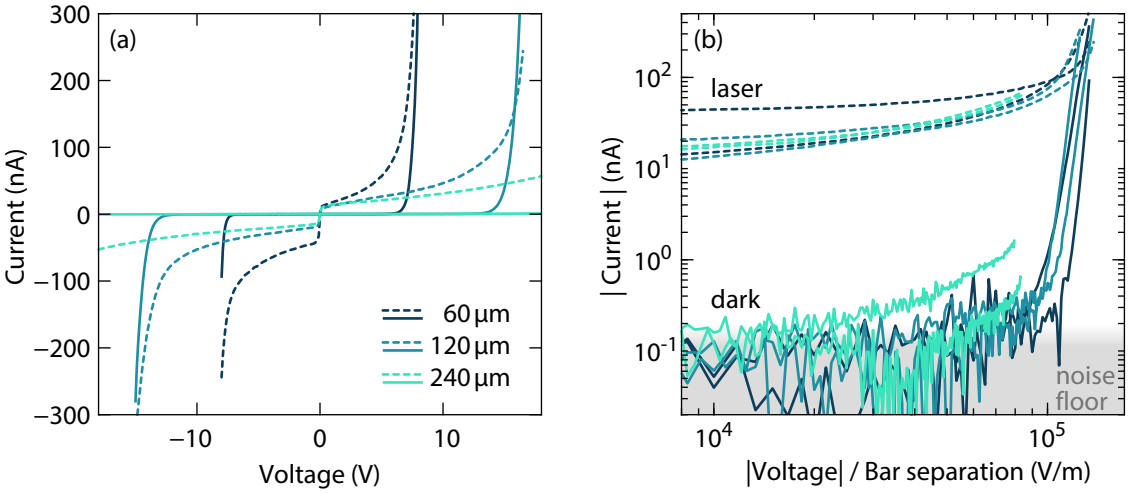

Figure 7.3: The I-V measurement of sample natSi-ResBars (cf. Fig. 7.2(c)) for three different contact separations between 60 µm and 240 µm. (a) IV charachteristics in the dark (solid lines) and under laser excitation (dashed lines) that is off-resonant with the D^{0}X transition ($\hbar\omega \approx 1.15\,\mathrm{eV}$, $I_\mathrm{L} \approx 1.7 \times 10^4\,\mathrm{W/m^2}$). (b) The same data on double log scale with the voltage axis rescaled for the respective contact separation. The current density under illumination and low bias is roughly $J \approx 20\,\mathrm{nA}/(100\,\mu\mathrm{m} \times 100\,\mathrm{nm}) = 2 \times 10^3\,\mathrm{A/m^2}$ The data resolution close to $V = 0\,\mathrm{V}$ is insufficient in this data set, in contrast to the data presented in Fig. 7.4.

characteristics. At 4.2 K, however, with average thermal energy $k_\mathrm{B}T \approx 0.4\,\mathrm{meV}$, the formed contact is blocking. In the contact region, similar to Schottky diodes and *pn*-junctions, due to the space charge region, the diffusion of electrons from the n^+ region towards the low doped region is balanced by the drift current back to the n^+ contact.

How does the current of such a device behave under a voltage bias? To investigate this, device natSi-ResBars has been fabricated with five parallel bars of metal-n^+ contacts, and a low-doped region covering the areas in-between and below the contacts, as sketched in Fig. 7.2(a). Four of these bars are contacted via aluminium wire bonds[3], to be able to compare the transport of devices with different contact separations.

The measured I-V characteristics are depicted in Fig. 7.3. For the traces captured in the dark[4], both in the regular (Fig. 7.3(a)) and the log-log plot (Fig. 7.3(b)) a sudden, drastic increase of current is observed above a certain threshold voltage. This threshold seems to depend linearly on the contact separation, i.e. it seems

[3]Which resulted in broad D^{0}X spectra due to strain, which is why only off-resonant laser illumination is used throughout this section.

[4]No special precautions are taken to block ambient radiation leaking through the cryostat window which is a likely cause of the finite dark current for the 240 µm device. In this context "dark" simply means "without laser illumination".

like that a certain threshold electric field exists above which the current increases dramatically. Below this threshold, the dark current is lower than the detection limit.

Upon illumination, a considerable current is observed even for small biases. The current in the low bias region appears, however, to have almost no voltage dependence. At higher biases, the current starts to increases roughly quadratically and finally shows the same behaviour as the dark current close to the threshold voltage.

In the following, first the high voltage behaviour is discussed while in the subsequent section a model for the low-bias region is developed.

7.2.2 Shallow donor impact ionization regime

There are relatively few publications offering comparable data for the high bias regime in the dark: Gutierrez *et al.* [191] find a turn-on bias of $0.5 \times 10^5\,\mathrm{V/m}$ for a n-well resistor of 30 µm length. Simoen *et al.* [192, 193] found a threshold bias of $1.2 \times 10^5\,\mathrm{V/m}$ above which the current through an 80 µm wide p^+pp^+ resistor increases dramatically at 4.2 K. Both of these thresholds are quite similar to the here observed turn-on bias of $\sim 1 \times 10^5\,\mathrm{V/m}$.

The origin of this sudden increase has been explained with a combination of a tunneling process through the barrier and the onset of current induced impact ionisations of dopants. In the following, the model developed by Simoen *et al.* [192–195] is introduced and extended to include laser-induced ionization of donors.

The model starts with the assumption that at 4 K the diffusion current can be neglected at sufficiently high bias due to the low diffusion coefficient, given by the Einstein relation $D = \mu k_\mathrm{B} T/e$. At low biases, this assumption obviously breaks down, as carrier transport at the emitter (left contact of Fig. 7.2(c)) is due to diffusion through an opposing electric field region. As the bias increases however, the position at which the electric field reverses (i.e. the maximum of the conduction band) moves towards the emitter contact and in the bulk of the sample the current is dominated by drift. The threshold upon which this so called "virtual cathode" approximation is valid is given at thermal equilibrium for $V \gtrsim 10 k_\mathrm{B} T/e = 4\,\mathrm{mV}$ [193, 196]. Under illumination, due to the increased average electron temperature of the hot photo carriers, the lower threshold for the validity of this model might increase, but is expected to still be relatively small (maybe a few hundred mV).

Following Simoen's treatment, the coupled equations that need to be solved within the low-doped region are then given by:

$$-\frac{\mathrm{d}^2\Phi}{\mathrm{d}x^2} = \frac{\mathrm{d}\mathcal{E}}{\mathrm{d}x} = \frac{q}{\epsilon_{\mathrm{Si}}}\left(n - N^+\right) \tag{7.1}$$

$$J = q\mu n\mathcal{E} \tag{7.2}$$

$$\frac{\mathrm{d}N^+}{\mathrm{d}t} = \Gamma_{\mathrm{D^0X}}N^0 + nA_{\mathrm{ii}}N^0 - nB_{n\rightarrow N^0}N^+ \tag{7.3}$$

The first equation is the Poisson equation for the electric field $\mathcal{E}$, assuming only conduction band electrons and ionised donors as charges in the bulk[5]. The second equation is the drift-diffusion equation, with only a drift current contribution here. The third equation is the rate of change of ionized donors, with generation terms due to the laser induced ionization ($\Gamma_{\mathrm{D^0X}}N^0$ which here includes both on and off-resonant terms) and donor impact ionization due to high-energetic charge carriers ($nA_{\mathrm{ii}}N^0$). The recombination term for the ionised donor concentration ($nB_{n\rightarrow N^0}N^+$) is due to electron capture from the conduction band and has been discussed before in Ch. 5.1.3. Both A_{ii} and $B_{n\rightarrow N^0}$ are strong functions of $\mathcal{E}$ whose functional dependence and strength have largely only been derived theoretically [194] as they are difficult to measure experimentally. The calculations follow closely the details laid out in [194] and are shortly summarized here:

Impact ionization of donors may only take place above a certain kinetic energy, i.e. above a certain electron drift velocity. The drift velocity is related to the electric field via the mobility[6] μ as $v_{\mathrm{drift}} = \mu\mathcal{E}$. Hence, A_{ii} is essentially zero up to a threshold electric field of $\mathcal{E} \approx 6 \times 10^4\,\mathrm{V/m}$, above which A_{ii} rises steeply [194]. It should be noted that no other mechanisms of donor ionization, such as Poole-Frenkel ionization or tunneling ionization are taken into account here, since the former requires temperatures larger than 10 K, while the latter requires electric fields in excess of $\sim 1 \times 10^6\,\mathrm{V/m}$ [114, 193].

The electron capture coefficient $B_{n\rightarrow N^0}$ on the other hand is largely constant for low electric fields with a value of $4 \times 10^{-6}\,\mathrm{cm^3/s}$, as derived in Ch. 5.1.3. Above $\sim 1 \times 10^4\,\mathrm{V/m}$, $B_{n\rightarrow N^0}$ drops significantly: The electron capture process is fundamentally an electron capture into an excited state and a subsequent cascade down to the ground state. These excited states are more strongly effected by thermal Poole-Frenkel ionisation (which effectively reduces the barrier height) than the ground

[5] Neglecting the ionized acceptor contribution

[6] The mobility in these calculations is not taken as a constant either, because of the effect of velocity saturation at $v_{\mathrm{drift}} \approx 1 \times 10^5\,\mathrm{m/s}$ [197, 198]. This can in turn be modelled as an electric field dependent mobility [194].

state and hence the capture process becomes less likely with increasing electric field strength [194].

In the steady state, there is no change of the ionised donor concentrations ($\mathrm{d}N^+/\mathrm{d}t = 0$) and Eq. (7.3) can be solved for the ionised donor concentration:

$$N^+ = N^0 \frac{\Gamma_{\mathrm{D^0X}} + nA_{\mathrm{ii}}}{\Gamma_{\mathrm{D^0X}} + nA_{\mathrm{ii}} + nB_{n\to N^0}} \tag{7.4}$$

This value, along with the drift current (7.2) solved for n is then inserted into the Poisson equation (7.1), resulting in a single first order differential equation for the electric field $\mathcal{E}$:

$$\frac{\mathrm{d}\mathcal{E}}{\mathrm{d}x} = \frac{q}{\epsilon_{\mathrm{Si}}} \left(\frac{J}{q\mu\mathcal{E}} - N^+ \right) \tag{7.5}$$

Finally, a boundary condition is required to determine a solution. This boundary condition is given by the tunnelling current at the emitter electrode. Here the tunneling current density is purely determined by the shape of the triangular barrier, i.e. by the height of the barrier and the applied electric field, and has the form [193]:

$$J_{\mathrm{emitter}} = \alpha\mathcal{E}(0) \exp(\mathcal{E}_{\mathrm{crit}}/\mathcal{E}(0)) \tag{7.6}$$

For a barrier height of $\sim$20 meV $\alpha = 2.3 \times 10^{-5}\,\mathrm{A/V^2}$ and $\mathcal{E}_{\mathrm{crit}} = -1.93 \times 10^7\,\mathrm{V/m}$ [193]. Since the current J is constant throughout the device, this equation can be solved numerically for a boundary condition for the electric field at the emitter $\mathcal{E}(0)$.

The simulation is written in `MATLAB` and is solved using the boundary value problem solver `bvp4c` [199]. As mentioned, the current density J is an input parameter and the solver calculates the resulting solution for $\mathcal{E}$, and, in turn, the values of n, N^+ and the potential Φ.

Φ allows for the extraction of the voltage bias across the contacts and the resulting simulated J-V curves are plotted as dashed lines in Fig. 7.4 (b) as $J_{\mathrm{tun,ii}}$ for different laser intensities. The plotted simulation is for a device length of 10 µm, but it has been confirmed that the simulated turn on voltages scale linearly with device length, as has been observed for the measured data of Fig. 7.3.

The exact details of the ionised donor and electron concentration as well as the electric field distribution within the device are plotted in Appendix C, but the simple sketch of the situation at the turn-on voltage is depicted in Fig. 7.2 (c). At the emitter contact, a space charge region with fully ionized donors and a small conduction band electron density establishes the required band-bending for tunneling through the barrier. Further into the bulk, the electron density increases, while the ionised donor density reduces until both are equal to a certain current-dependent

steady state value. The electric field in the bulk is constant and just enough to provide for sufficient conduction band electrons via impact ionization. The electric field in the bulk of the device is indeed simply the voltage drop between the contacts by the length of the device, and this is true up to the carrier injection regime in which more carriers than neutral donors are injected into the device – a regime characterised by a linear I-V curve at much higher biases, which is not reached in the experiments discussed here. The dark current is hence well understood as a combination of tunneling current at the emitter and hot carrier induced impact ionization of shallow donors.

Under illumination, the ionised donor density is higher and, due to the charge neutrality in the bulk of the device, a higher electron density exists in the bulk. The space charge region at the emitter stays unaffected (completely ionized donors, a lower, but finite electron density to allow for strong impact ionization) while in the bulk, due to the higher electron density, a smaller electric field is required to maintain the same current density, thereby decreasing the required voltage bias. From the simulations, the I-V curve shows roughly a square to cubic dependence in this regime, which is similar to the illuminated traces of Fig. 7.4 and Fig. 7.3, close to the threshold voltage, except that these illuminated traces feature an offset current all the way down to very small biases. In order to understand the current behaviour under illumination at low bias a different theoretical description is required, since the approximation to neglect the diffusion currents at the emitter is no longer valid. This is done in the next section.

7.2.3 Photo-emission over the barrier

As mentioned above, a barrier exists at the emitter interface between the degenerately doped region and the lower-doped region with a height of $\Delta \approx 20\,\mathrm{meV}$. While this barrier prevents injection of currents under thermal equilibrium in the dark, one would expect the situation under illumination to be different. Due to optical absorption in the emitter, carriers close to the interface are provided with kinetic energies of 1.15 eV (given the laser energies used here) and are hence able to cross the barrier. This process is similar to Schottky-barrier based infrared detectors, and infrared detectors with tunable cut-off wavelength have been proposed [189, 200] and tested [188, 201] based on this photoemission process across a n^+–n interface at low temperatures.

Similar to the tunnelling current through the interface, the height of the potential barrier alone determines the emission current across the barrier under thermal

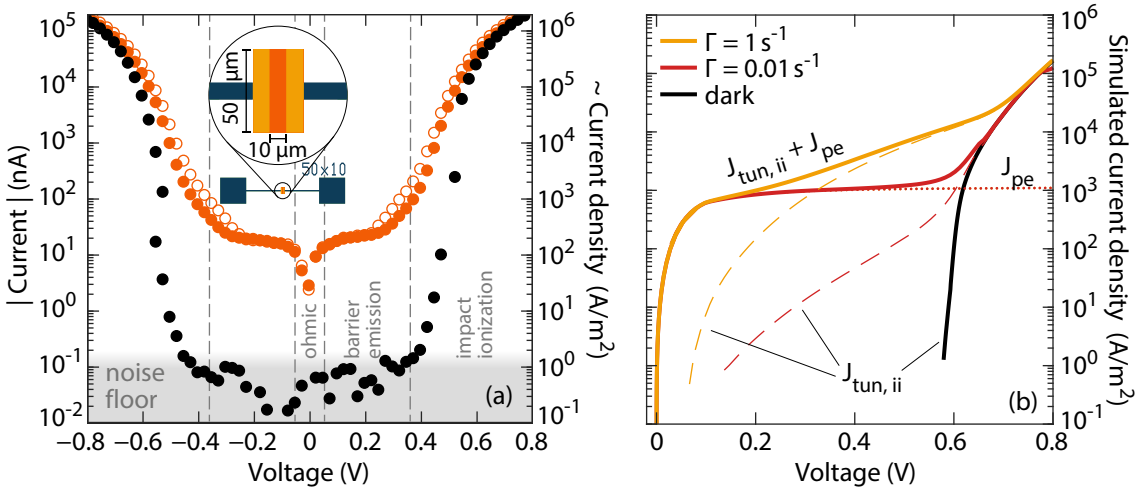

Figure 7.4: The I-V characteristics of a 10 µm wide n^+nn^+ resistor (sample natSi-parElec10) at 4.5 K and 0 T. (a) I-V curve of the device sketched in the inset, in the dark (black) and under laser illumination (I_L = $\sim 3.5 \times 10^3$ W/m^2), both on resonance with the D^0X transition (empty circles) and off resonance (full circles). (b) Summary of the low bias, photo emission current (J_{pe}, dotted) limited by the threshold thermionic emission current $J_{the} \approx 10^3$ A/m^2 and the high bias regime characterized by tunnelling through the barrier and impact ionization of donors $J_{tun,ii}$ (dashed), with the sum of the two depicted as solid lines. The simulations are carried out for no laser-induced ionization, i.e. the situation in the dark (black) and also for ionization rates of $\Gamma = 1 \times 10^{-2}$ s^{-1} and $\Gamma = 1$ s^{-1}, similar to the expected off-resonant ionisation rate.

equilibrium in the dark, which is known as thermionic emitter current J_{the}. Expressions for this current as a function of barrier height Δ and temperature have been developed in the context of Schottky barrier emission, summarized by the so-called Richardson-Dushmann equation [144, 202, 203]:

$$J_{the} = A^* T^2 \exp(-\Delta / k_B T) \tag{7.7}$$

$A^* = 4\pi e m_e^* k_B^2 / h^3 \approx 1.1 \times 10^6$ A m^{-2}K^{-2} is the Richardson constant [202]. J_{the} is the maximal current that a barrier-contact is able to provide, i.e. , there is a certain bias threshold V_{cr} above which the current density saturates at J_{the}. The situation is analogous to the reverse current of a Schottky diode.

In the dark and at 4.2 K, thermal excitation limits the emission current to $J_{the} \approx 5 \times 10^{-13}$ A/m^2, far below the noise limit of our setup, hence no current is observed in the dark up to the tunnelling regime. Under illumination, the carriers are photo-excited over the barrier. As a first approximation, this is treated as a lowering of

the barrier in the following simulations[7], creating a finite photo-emission current across the barrier even at lower temperatures.

Hence, a second model for the low bias region is developed following the treatment developed by Yuan and Perrera [203, 204]. The Poisson equation and ionised donor concentration are unchanged from the previous section, while the diffusion current is added to the drift-diffusion equation:

$$\frac{\mathrm{d}\mathcal{E}}{\mathrm{d}x} = \frac{q}{\epsilon_{\mathrm{Si}}}\left(n - N^+\right) \tag{7.8}$$

$$J = q\mu n\mathcal{E} - qD\frac{\mathrm{d}n}{\mathrm{d}x} \tag{7.9}$$

$$N^+ = N^0\frac{\Gamma_{\mathrm{D^0X}}}{\Gamma_{\mathrm{D^0X}} + nB_{n\to N^0}} \tag{7.10}$$

Impact ionization has been neglected and $B_{n\to N^0}$ is treated as a constant since the theory without tunnelling current is only applicable in the low bias (low electric field) regime. Two coupled differential equations for $\mathrm{d}\mathcal{E}/\mathrm{d}x$ and $\mathrm{d}n/\mathrm{d}x$ have to be solved using two boundary conditions. Following the arguments laid out in [203], the thermionic emission current (7.7), can be used to provide boundary conditions for the electron densities at the emitter n_e and collector n_c. An effective barrier height $\Delta = 6.1\,\mathrm{meV}$ under illumination achieves $J_{\mathrm{the}} \approx 1 \times 10^3\,\mathrm{A/m^2}$, which is the right order of magnitude for the illumination intensities used.

To extend the range of measured contact separations and to investigate the low bias regime more thoroughly, measurements have been conducted on a device with 10 µm electrode separation and a length of 50 µm. The device layout is depicted in the inset of Fig. 7.4 (a). I-V curves have been measured for $I_{\mathrm{L}} \approx 3.5 \times 10^3\,\mathrm{W/m^2}$ without external magnetic field, and under three illumination conditions: in the dark, on resonance with the $\mathrm{D^0X}$ transition and off resonance. The results are depicted in Fig. 7.4 (a), with the corresponding low bias (J_{pe}) and high bias simulation ($J_{\mathrm{tun,ii}}$) shown in Fig. 7.4 (b) for two different laser ionisation rates. No further attempts at fitting or fine tuning the simulation parameters have been attempted as only a qualitative understanding is deemed reasonable due to the number of simulation parameters.

All the features observed in the measurement are reproduced by the simulation. At high bias, the impact ionization regime is found, which becomes almost

[7] It could be argued that the photo-absorption creates hot electron, thereby raising the average electron temperature, which is mathematically roughly equivalent to a reduction of the barrier height in 7.7. A modified barrier height is preferred here, since various other terms of the simulation, such as the diffusion coefficient D also depend on temperature.

illumination-independent above the dark current threshold voltage. At low biases under illumination, starting from 0 V, at first an ohmic regime exists where the drift currents which depends linearly on the applied electric field are the main current source [203]. As the current density reaches values close to the laser power-dependent emission current threshold J_{the}, the rate of carrier injection over the barrier per time saturates and the current becomes independent of applied bias[8]. It has been observed (see Fig. 7.11) that the low-bias emission current J_{the} is indeed laser intensity dependent, however, it does not feature any D^0X characteristic resonance features, as photo-emission from the degenerate contact is not a resonant phenomena. Hence, the current both on- and off resonance is the same for voltages of 0 V to 0.2 V . In contrast, the laser dependence of the high bias, tunnelling regime ($|V| > 0.3\,\mathrm{V}$) does depend on the bulk carrier concentration, which depends on the ionization rates of the donors in the low-dosed phosphorus n region. Here, going on resonance with the D^0X transition increases the ionization rate of the donors and hence the steady state carrier concentration, which is why the strongest D^0X signals are observed at the transition from the flat photoemission current to the tunnelling regime. At high biases, the relative D^0X intensity decreases again because the impact-ionization rate exceeds the laser-induced donor ionisation rate.

7.2.4 Conclusion

In this section, I-V characteristics of an n-type region contacted by degenerately doped n^+ regions have been examined at 4.5 K for varying contact separations with the aim to understand the optimum conditions for D^0X-based donor spin readout in silicon devices. The main feature in the dark is a sudden turn on of the device, which can be modelled by impact ionization of neutral donors by high energetic electrons and a tunnelling process at the emitter. At high biases, the same process is observed under illumination with the laser, but furthermore a finite current is observed even below the impact ionization threshold, explained by photo-ionisation of donors in the bulk. Furthermore, under illumination a bias-independent current is observed for smaller voltages which is over a large extent independent of bias and can not be modelled by the above tunnelling process. The strength of this saturation current is laser power dependent and is likely due to photo emission of carriers from the n^+ region over the barrier to the n region. Simulations have been developed for both bias regimes and a qualitative agreement could be achieved.

[8] The carrier concentration at the emitter and in the bulk of the device reduces in the same way as the electric field increases, leaving the current density constant.

7.3 Scanning photocurrent microscopy

The experiments presented in the following section are motivated by the need to confirm whether the signal originated from the bulk of the sample or the contact area. To this end, an experimental setup with localized laser excitation is devised, and the results are presented in this chapter and in Appendix D. However, the observed dependencies and results are difficult to interpret and a confirmation of the transport model of the previous section proved inconclusive.

In the literature, this kind of experiment is referred to as "scanning photo current microscopy" (SPCM) [205, 206] and is often used to determine diffusion lengths of minority carriers and other transport characteristics [207, 208].

This section is divided into an introduction to setup and sample in Sec. 7.3.1, followed by an excerpt of the derived results presented in Sec. 7.3.2 and finally Section 7.3.3 discusses the (arguably limited) conclusions that can be drawn from the results.

7.3.1 Setup and device

In order to scan the laser spot across the sample, a movable objective or a lens close to the sample is required. A schematic of the solution devised for these experiments is shown in Fig. 7.5(a). The setup comprises a bare termination of the optical fibre, whose light field diverges with the numerical aperture of the fibre (0.14). A bi-convex lens ($f = 25.4\,\mathrm{mm}$) focusses the divergent laser onto the sample inside of the cryostat. The optical components are mounted inside of a tube which can be pushed to be close to the cryostat window. This is necessary since the spot size depends on the numerical aperture of the setup. The higher the numerical aperture, i.e. the smaller the working distance and the larger the diameter of the illuminated objective, the smaller the achievable laser spot. Due to the cryostat diameter and the size of the optical windows, only a relatively small numerical aperture of ~ 0.1 to 0.2 of the optics allows for scan ranges undisturbed by the window diameter. The motion of the tube is achieved by a motorized xyz stage, with the focus (z) adjusted manually and the scan directions (x & y) being controlled by Thorlabs DC servo actuators (MT1-Z8) as shown in Fig. 7.5(c).

The spot size of this setup is determined by a knife edge experiment (cf. Fig. 7.5(c)), where the transmitted power is measured as a function of y and as a function of distance between knife edge and objective. The transmission traces (inset of Fig. 7.5(b)) are fitted using the expected Gaussian beam profile and determine

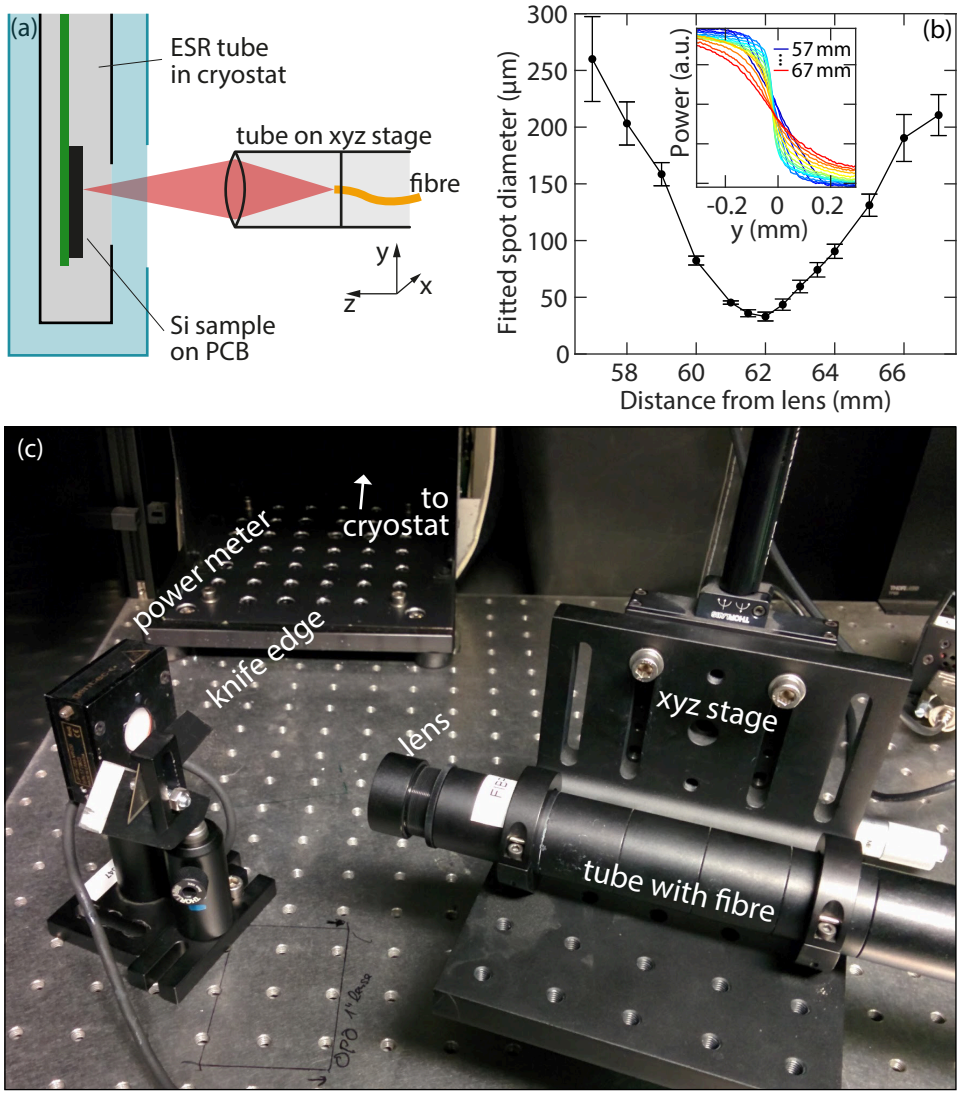

Figure 7.5: The setup of the scanning photocurrent microscopy experiments (SPCM). (a) Sketch of the experimental setup with the laser spot created by a bi-convex lens and uncollimated optical fibre. The silicon sample is fixed on a PCB within an ESR tube with IR absorbive coating. (b) The spot size and focal length of the setup, as deduced from a fit to the traces (inset) of a knife edge experiment, whose setup is depicted in (c). For the SPCM experiments, the tube with the optical components is pushed towards the cryostat, with the motorized stage remaining on the optical bench.

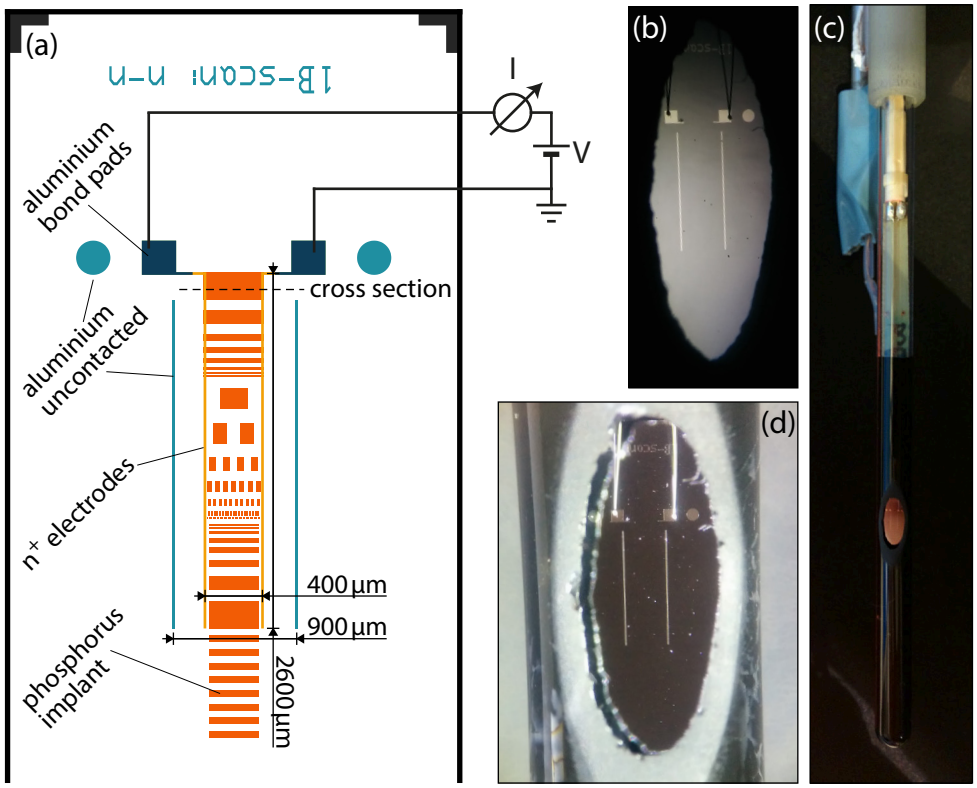

Figure 7.6: Sample natSi-Scan, used for the scanning photocurrent microscopy experiments. (a) The device layout and the electrical circuit measuring the photocurrent for a fixed bias voltage. A cross-section of the device at the dashed line is sketched in Fig. 7.2(a). (b,d) Microscope images of the sample, visible through the hole of the coated ESR tube. (c) Full image of the partly coated ESR tube with sample and PCB.

the spot size as a function of working distance. In focus, at a working distance of 62 mm, a spot size of 30 µm is achieved.

The schematic of sample natSi-Scan, used in this section, is shown in Fig. 7.6 (a), while images of the sample within the ESR tube are depicted in Fig. 7.6 (b-d). Two parallel n^+ electrodes are separated by 400 µm over a length of 2.6 mm. The electrodes are contacted by aluminium tracks and bond wires. In-between the electrodes, patches of low dose phosphorus implants with variable size are fabricated. The implant patches at the top overlap with the electrodes, while for the other structures an intrinsic silicon region exists between implanted areas and electrodes. The electrodes are contacted with a Keithley 2400 Voltmeter (ground connected to the right electrode) and record current as a function of voltage. Furthermore, other metal contacts are placed onto the sample to investigate and discriminate reflection signals. To prevent reflections within the metallic cryostat from hitting the sample, the ESR tube is coated on the inside with blackboard paint, which has been tested to absorb infrared radiation, and a hole is cut to optically access the sample only

from the front (cf. Fig 7.6 (c & d)). All experiments discussed in this section are performed at 4.5 K and 0 T.

7.3.2 Experiment

An overview of the current as a function of laser position for two different bias conditions $V = \pm 1\,\mathrm{V}$ is depicted in Fig. 7.7. The features of the sample are clearly visible, with the bond pads, bond wires and non-contacted metal acting as reflective surfaces on which lower current densities are achieved. Off resonance with the D^0X transition, the highest current densities are achieved in the vicinity of the electron-collecting electrode. No signatures of the phosphorus implant patches are observed off resonance. On resonance, the implanted patches are visible, with the strongest contrast between implanted area and intrinsic area again in the vicinity of the collector electrode. In general, only those doping patches that overlay with the n^+ contacts are visible, which is true for all tested conditions. On top of the signal seen in the vicinity of the collector electrode, a second strong signal located directly at the emitter electrode is observed, only on-resonance. This signal does not feature any signature of the doping patches and is furthermore unique to the bias of $\sim$1 V and laser intensity $P_\mathrm{L} \approx 25\,\mathrm{W}$, as seen later. An interesting observation is that off resonance the bond wires are visible as a single line of low current (as expected), while on resonance both the bond wires and what looks like a "shadow" of the bond wires is observed. The origin of the "shadow" is not understood, may however suggest that reflections between sample surface and optical window still play a role for the generated photocurrent.

Figure 7.8 investigates the strength and location of the signal as a function of voltage bias and laser intensity. For Figs. 7.8 (a-f) the current along a horizontal cross-section at the top of the device ($y \approx -0.25\,\mathrm{mm}$) is plotted against bias voltage. This is done both on and off resonance with the D^0X transition and for cross-sections that cross a phosphorus implant patch ("on implant") and for a cross-section in-between those patches. In general, the strongest signal is observed in the vicinity of the collector, for almost all laser intensities and biases below 2 V. Only for a laser power of $P_\mathrm{L} \approx 24\,\mathrm{mW}$ and biases above 0.5 V, an on-resonant signal is observed right at the emitter contact. The same trend is shown in Figs. 7.8 (g-l) which are the I-V-curves taken at five different positions between emitter and collector electrodes. In general, the largest contrast between on- and off-resonant photocurrent is found for laser powers of $P_\mathrm{L} = 7.3\,\mathrm{mW}$ to 24 mW.

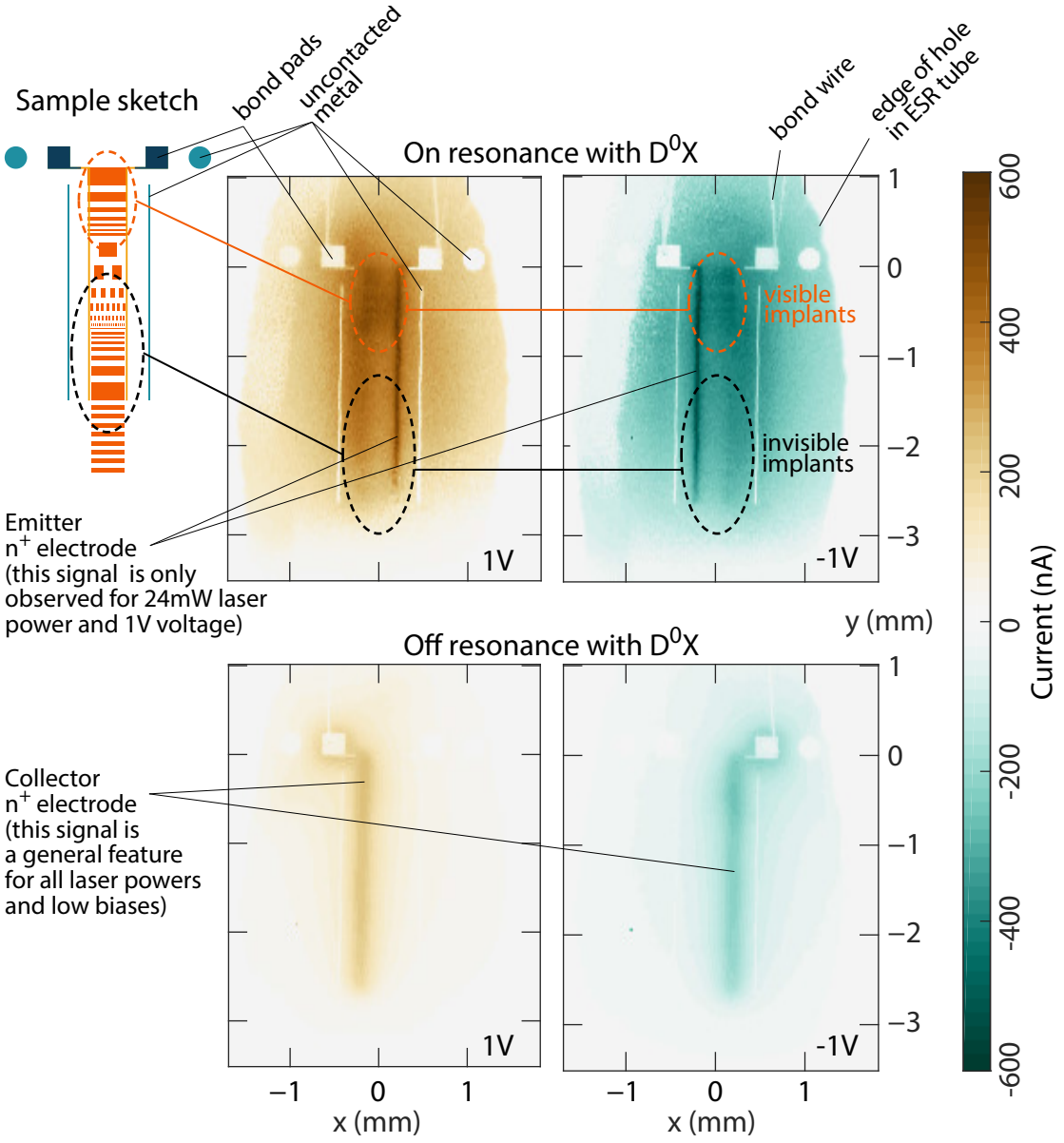

Figure 7.7: Scanning photocurrent microscopy image of sample natSi-Scan for a positive and negative bias of 1 V (right electrode is grounded) and $P_L = 24\,\mathrm{mW}$ at 0 T and 4.5 K. Top left shows the schematic of Fig. 7.6(a) and identifies its features in the obtained data. Top row shows the results on resonance with the D^0X transition, with those implanted areas visible that overlap with the degenerately doped contacts. The strong signal on the emitter electrode is specific to the used voltage bias and laser power combination, as seen from Figs. 7.8 & 7.9. For the off-resonant case (bottom row) a signal is detected only in the vicinity of the collector electrode. The scan range is limited on the sides by the size of the hole in the ESR tube, visible as the ellipse shade (see Fig. 7.6(d)).

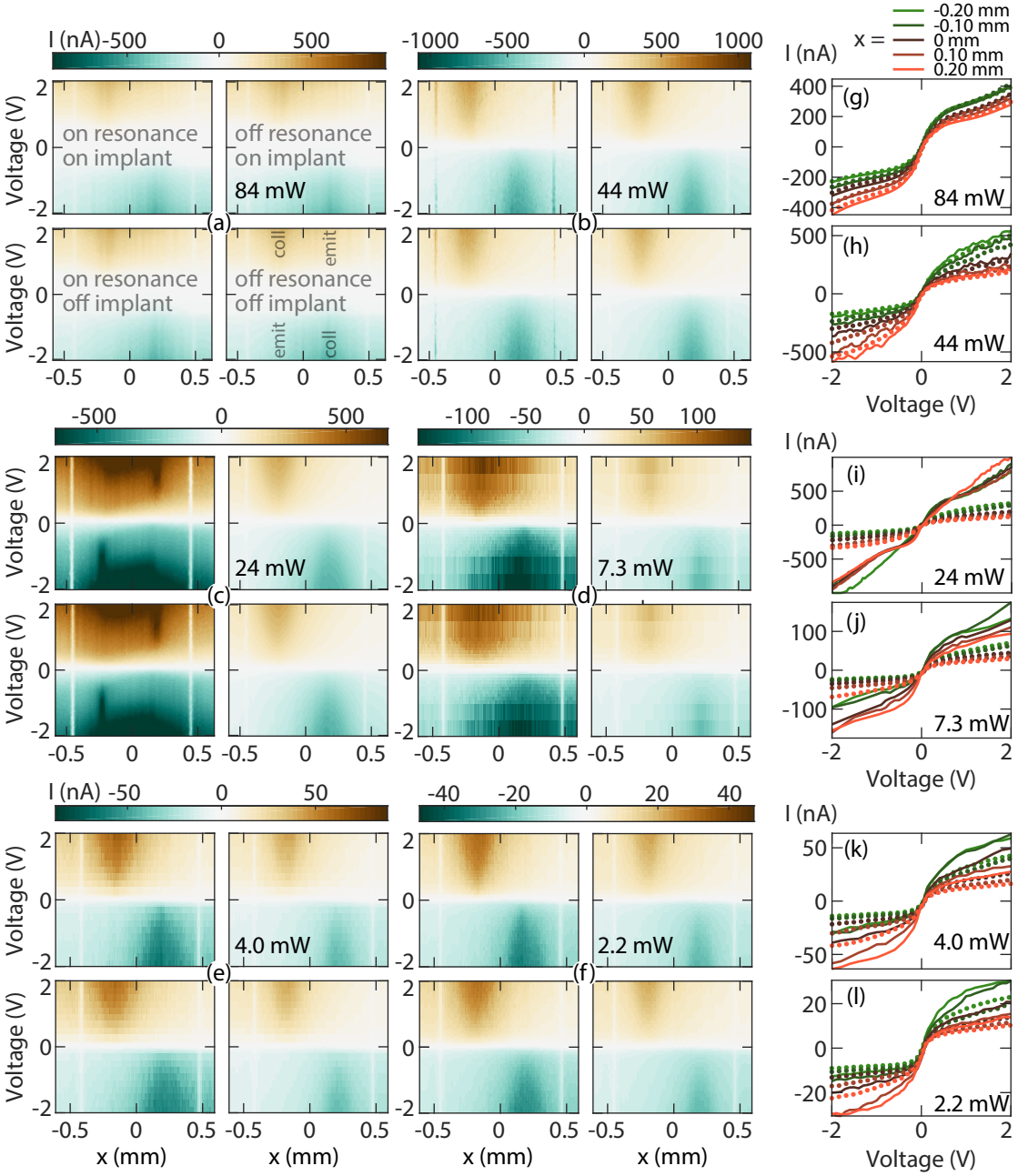

Figure 7.8: The bias and laser power dependence of the SPCM images of sample natSi-Scan (4.5 K, 0 T). (a-f) Cross-sections at constant height through the second implant patch from top (on implant) and between the first and second implant patch from the top (off implant), taken as a function of voltage both on and off resonance with the D^0X transition for a variety of laser powers. The right electrode at $x \approx 0.2$ mm is grounded, thus defining the emitter and collector (indicated in (a)) for positive and negative voltages. The colormap is scaled for each laser power to the off resonance current for $|V| = 2$ V with the laser spot on the implant region. (g-l) are the I-V curves at different x-positions between the two electrodes with the laser spot on the an implant patch, with the laser either on resonance (solid line) or off resonance (dotted line).

For the lower laser powers of $P_L = 7.3\,\mathrm{mW}$ and $2.2\,\mathrm{mW}$, Fig. 7.9 plots detailed SPCM images from the top of the device for a larger range of bias voltages up to $V = 25\,\mathrm{V}$ with the colormap for each bias scaled to the maximum off-resonant current. As mentioned, the difference between on- and off resonance photocurrent is strongest for $P_L = 7.3\,\mathrm{mW}$. Furthermore, a shift of the location of the photocurrent can be observed. At low biases, as discussed before, the photocurrent is highest close to the collector electrode. As the voltage increases, the location shifts towards the emitter electrode and assumes a more or less equally strong level regardless of the excitation location between the two electrodes. The bias voltage at which this cross-over occurs seems to depend on laser power, or absolute current magnitude: Compare, for example, the on resonance image for the lower laser power of $2.2\,\mathrm{mW}$ at $-25\,\mathrm{V}$ with the on resonance image of $7.3\,\mathrm{mW}$ at only $-1\,\mathrm{V}$. Both the current distribution and current magnitude of these two SPCM images are quite similar. As a final remark it can be observed that the greatest visibility of the implantation patches is found for lower biases and that the patch visibility fades towards the higher biases. Off resonance, almost no trace of the implant patches is visible, except for, perhaps, some minor features for the ($7.3\,\mathrm{mW}$,$-1\,\mathrm{V}$) and ($2.2\,\mathrm{mW}$, $-25\,\mathrm{V}$) combinations. It should be noted that with finite external magnetic field, the implantation patches are also visible in the off resonance photocurrent (cf. Appendix D).

7.3.3 Discussion

The discussion of the underlying phenomena is difficult particularly due to the multitude of dependencies observed, which include bias and voltage (shown in this section) but also magnetic field and temperature (shown in Appendix D). Additionally, as mentioned before, reflections between sample surface and optical window may play a role, although likely a minor one.

In a first step it was attempted to use the simulations developed in the previous section to explain the SPCM I-V characteristics, using a Gaussian photo-excitation profile in the simulations. The low-bias simulations do not show a significant variation of photocurrent with position of the laser excitation, when the photo-emission current over the barrier is set to be laser-spot location-independent. It could be argued that the contact-limited photoemission current should vary with location of the laser spot, with a higher emission current when the laser spot is at the emitter contact and a lower emission current when the laser spot is closer to the collector. This is however in stark contrast to the observed low-bias photocurrent, which is stronger on the collector. Hence a different mechanism, not captured by these

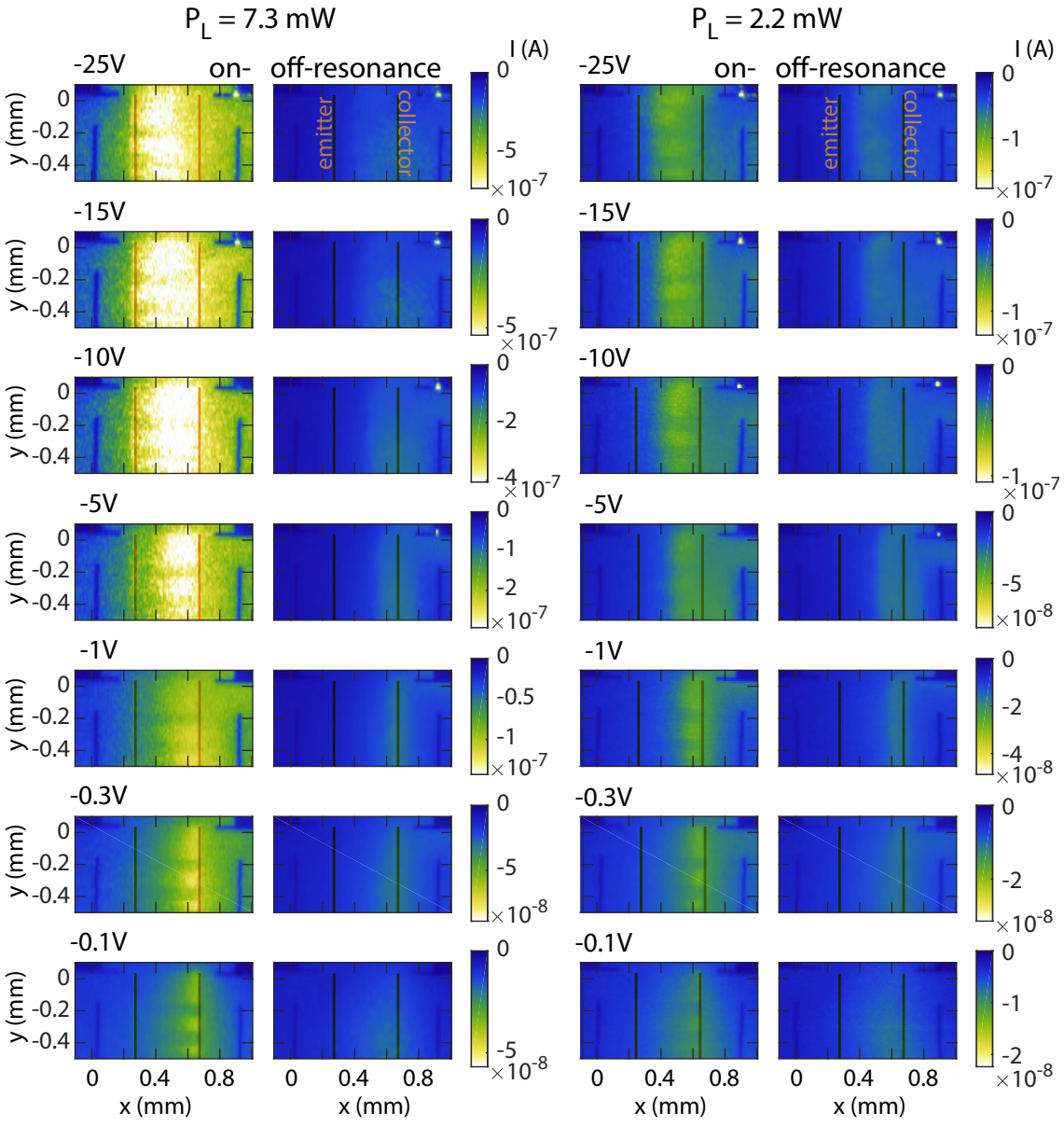

Figure 7.9: Scanning photocurrent microscopy images of the top of device natSi-Scan as a function of bias voltage for two different laser powers (4.5 K, 0 T). The colormap is scaled for the maximum off-resonant current between the electrodes. Emitter and collector location are overlayed as orange bars.

simulations seems to dominate the photocurrent under localized excitation in the low bias regime. For the high-bias simulation, in a similar way a localized laser excitation has been introduced, but these simulations also falsely predict a stronger current with the laser spot at the emitter electrode, as long as the current is not dominated by impact ionization.

In conclusion, both simulations are incapable of explaining the SPCM results and would hence need to be modified/improved, which was not possible in the scope of this thesis. Likely hints to the type of phenomena that may play a role can be taken from literature on SPCM. Here, often currents are observed that exponentially decrease with distance from the electrodes. This is due to the diffusion length of the minority carrier, i.e. due to the number of charge carriers that are able to reach the contact within their carrier lifetime. A similar phenomena might be at work here. Photo-generated hot electrons also have a certain lifetime τ and therefore a certain diffusion length $L_\mathrm{D} = \sqrt{D_n \tau}$ with the diffusion coefficient D_n. If the laser spot is far away from the electrodes, an internal field will build up, leading again to a local electric field that counterbalances the diffusion away from the excitation location and no net contribution to the observed global current. However, if the photo-excited electron reaches the contact it does add to the observed photocurrent, provided the left-behind positive ion gets neutralized by an injected electron from the emitter. This situation could be compared to the photocurrent of a n^+-p solar cell, where the much longer p base acts as the absorption body. As long as the created electron-hole pair is within the minority carrier (i.e. electron) diffusion length of the junction, the created electron and hole add to the current.

For the results presented above, a photocurrent is indeed observed that decreases approximately exponentially with distance from the collector, with a length scale of 200 µm to 250 µm (cf. lower biases of Fig. 7.9), which might be a signature of the electron diffusion length[9]. As the bias voltage is increased, the transport would shift from being diffusion dominated to being drift dominated, resulting in a higher effective carrier velocity towards the collector and hence an extended range up to which electrons can reach the collector before recombination. Hence, an extension/shift of the photocurrent peak towards the middle of the device and towards the emitter electrode would be expected and is indeed observed in the data. Without a proper simulation, this explanation is merely a starting point for discussion and further-

[9]Using a thermal equilibrium diffusion coefficient that is based on the measured $\mu \approx 7 \times 10^4\,\mathrm{cm^2/(V\,s)}$ of Ch. 3.5.3, a diffusion length of $L_\mathrm{D} \approx 200\,\mu\mathrm{m}$ would indicate an electron capture time of $\tau \approx 15\,\mu\mathrm{s}$, corresponding to an ionized donor concentration of $N^+ \approx 10^{10}\,\mathrm{cm^{-3}}$. The diffusion coefficient of photo excited carriers may, however, be significantly higher than that.

more does not explain the observed changes with laser intensity, temperature and magnetic field.

The reason why only those implantation patches that overlap with the n^+ region are visible and not those patches that are isolated is likely due to the much larger built-in potentials at the n-i junction compared to the n-n^+ junction, preventing photoemission across the barrier in the former case.

The low visibility of the implantation patches in the off-resonant data could be an indication that the off-resonant photoconductivity at a photon energy of 1.15 eV is not due to direct photo-ionization of donors, but instead due to band-to-band carrier or exciton generation[10]. However, it might be too early to draw such conclusions for the following reasons: Due to setup limitations, no band-pass filter is included in the setup and hence the laser might potentially have additional above-bandgap modes that reach the sample. The resulting, unintended band-to-band generation might overshadow the weak direct photo-ionization but not the stronger D^0X signal. Also, as particularly evident from Fig. 7.6, even when the laser spot is far away from the device a significant signal is observed both on-and off resonance. Hence likely there are still reflections at work, either within the sample due to internal reflection or between sample and cryostat window that make an interpretation of the results difficult.

7.3.4 Conclusion

In summary, the response of a device with patterned dopant regions to a local photo-excitation has been investigated. Different transport features have been observed, whose origin are difficult to trace. A feature which is present for small biases and all laser powers is a photocurrent when the laser excites in the vicinity ($\sim$200 µm) of the collector electrode. With higher bias, the range that generates a finite photocurrent gradually extents towards the emission electrode and finally assumes a situation where an equally strong signal is observed irrespective of laser location between the electrodes. While currently not fully understood, the origin of this phenomena might be due to the diffusion length of the photo-excited electrons within the sample. Further, in depth analysis are required to understand the observed dependencies on temperature, magnetic field, voltage and laser power.

[10] As discussed in Ch. 5.1.4.1, the free excitons would localize at a neutral donor, form a bound exciton and ionize the donor via an Auger process, thereby ejecting an electron.

7.4 Electric field dependence of the D^0X transition

The final section of this chapter concerns the shifts in transition energy of the bound exciton as a function of electric field. Upon application of an electric field, the two electrons and the hole of the D^0X are deflected into opposing directions and hence give rise to a finite polarization. As the electric field is increased further, at some point the exciton is no longer stable, i.e. it is expected that there is a threshold field above which the electron and hole are ripped off the neutral donor in opposing directions. As a figure of merit, the D^0X ionisation field is roughly reached when the potential drop across the radius of the exciton is equal to the binding energy of the exciton. Below the ionisation field a shift in transition energy is expected as e.g. the D^0X Coulomb energy changes due to a change of spatial overlap of electron and hole.

Both of these phenomena have a significant impact on the suitability of the D^0X transition for single donors in nanoscale devices where quite strong electric fields may occur. Shifts of the transition energy upon changes of gate voltages are undesired, due to the narrow D^0X linewidth of a single donor. Furthermore, if the donor is subject to a field from a gate which is above the ionisation field of the exciton, D^0X-assisted spin-readout is not possible to start with. Hence, a good understanding of the electric field dependence of the D^0X transition is required, which is the subject of this section.

In the first part, the theoretical literature is reviewed and expressions for the expected transition energy shift as a function of electric field are given. Thereafter, in Sec. 7.4.2, the experimentally obtained transition energy shifts of a variety of the devices are presented with a focus on an experiment with two n^+ electrodes separated by 20 µm. The discussion ends with the conclusion remarks in Sec. 7.4.3

7.4.1 Theoretical treatment

Two different theoretical works on the electric field-induced D^0X transition shifts are available, with results that differ quite significantly. In the following the these two publications are summarized and discussed.

The first publication is a recent ArXiV paper by Rajid Rahman [152], which acted as the incentive for the experiments of this section. Rahman and co-workers used an atomic orbital tight-binding method on a 30 nm × 30 nm × 30 nm silicon grid to calculate the energy of a neutral donor and its bound exciton in the center of the grid as a function of electric field. Rahman *et al.* argue that shifts of the

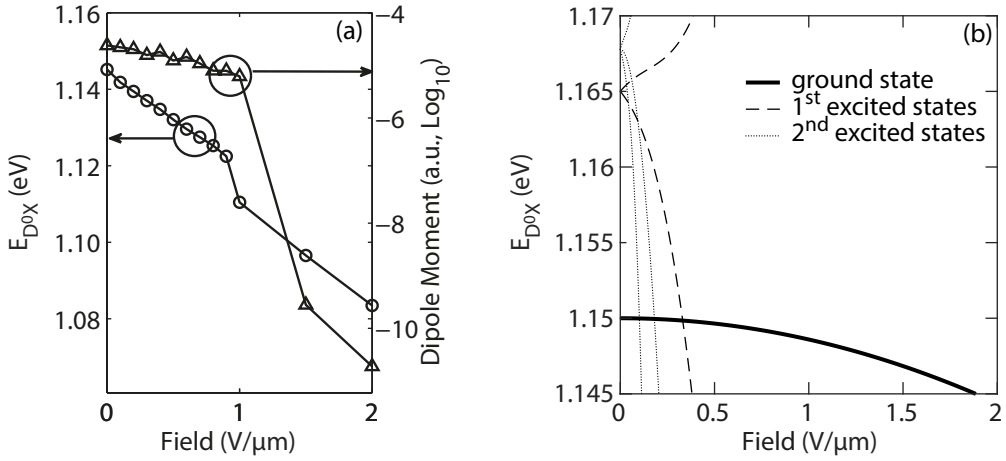

Figure 7.10: The predicted electric field induced D^0X transition energy as a function of electric field. (a) The tight binding calculations of Rahman *et. al.* with predictions for a roughly linear transition energy shift and a reduction in oscillator strength (reproduced from [152]). (b) The shifts of ground and excited state of the D^0X according to Blossey's effective mass theory, with a smaller, quadratic shift of the D^0X ground state transition energy [209].

transition energy are due to changes of the single particle electron and hole energies as well as a reduced Coulomb energy of the two-electron & one-hole system due to the polarization of the exciton and the accompanied reduced spacial overlap. All calculations are performed without additional fitting-parameters and give a D^0X transition energy of 1.145 eV in the absence of electric fields, remarkably close to the experimental value of 1.150 eV. The result of the electric field dependent D^0X transition energy calculation is shown in Fig. 7.10(a). A relatively linear decrease of the transition energy is observed up to the ionisation field of the D^0X which is at $\mathcal{E} \approx 1\,\mathrm{V/\mu m}$. The strength of the transition energy shift is given by $\sim$25 meV/(1 V/µm). The shift of transition energy is accompanied by a reduction in dipole moment, due to the lower spatial overlap of donor and exciton wave function.

In disagreement with the roughly linear shift predicted by the tight-binding theory is the effective mass theory of Daniel Blossey from 1970 [209]. Here, the exciton hole and electrons are treated with the respective Bloch functions of the periodic lattice, while the ionised donor electron and the second electron are merely treated as a neutral localisation center[11]. A theory for the D^0X energy is developed that is supposed to be applicable over a large range of electric field values up to the ionisation field. It is found that for lower fields (up to about half the value of the

[11]This assumption is furthermore corroborated by the spatial distribution found by Rahman *et. al.*, which leaves one electron at the donor location irrespective of electric field strength.

ionisation field) a perturbative approach is sufficient and a formula for the shifts of the hydrogen-like ground and excited states of the exciton is given. For the ground state it reads:

$$\frac{\Delta E_{\mathrm{D^0X}}}{E_\mathrm{g} - E_{\mathrm{D^0X}}} = -\left[1 + \frac{9}{8}\left(\frac{\mathcal{E}}{\mathcal{E}_\mathrm{I}}\right)^2\right] \tag{7.11}$$

where $\mathcal{E}_\mathrm{I} = (E_\mathrm{g} - E_{\mathrm{D^0X}})/(e a_{\mathrm{D^0X}}) \approx 20\,\mathrm{meV}/(e4.9\,\mathrm{nm}) \approx 4\,\mathrm{V/\mu m}$. $\mathcal{E}_\mathrm{I}$ is the aforementioned order of magnitude of the ionisation field, i.e. the field required to create a potential drop across the Bohr radius of the exciton $a_{\mathrm{D^0X}}$ (cf. Sec. 5.1) equal to the binding energy of the exciton.

The predicted shifts calculated by Blossey's perturbative effective mass theory are depicted in Fig. 7.10(b). Similar to the Stark shift of the atomic orbitals of hydrogen, a linear shift is observed for the excited states, while the ground states shows a quadratic shift. Compared to the tight binding theory of Rahman, Blossey's theory predicts a much smaller electric field induced shift, both at lower electric fields (due to the square dependence) but also at fields close to the ionisation field.

7.4.2 Experimental results

Literature on experimental observation of electric field induced D^0X shifts is almost non-existing. The only publication mentioning this process discusses the quenching of the D^0X photo luminescence upon application of an electric field[12] [210]. Within this publication it is remarked that "no spectral shifts were observed with electric field within the spectral resolution used ($\approx 1\,\mathrm{meV}$)" and the largest applied field was $0.015\,\mathrm{V/\mu m}$. Both the spectral resolution and the applied bias are relatively small and are not sufficient to validate or reject one or the other theoretical description.

In the following, improved measurements are presented of a variety of devices fabricated using the D0XDEV process discussed in Sec. 4.1.2. Four different kinds of device (labelled devices I to IV below) have been tested. Only a single device (device IV) featured a consistent, albeit small (compared to the linewidth) shift of D^0X transition energy. First, the tested devices that did not feature a significant spectral shift are summarized and the upper bound for the D^0X Stark shift is estimated:

[12] Such quenching starts at relatively low electric fields of $0.005\,\mathrm{V/\mu m}$ due to impact ionization by field accelerated electrons and holes.

I: Four parallel n$^+$ electrodes on implanted square

This sample (natSi-ResBars) has been used in Sec. 7.2 and is depicted in Fig. 7.2. An implanted square of 400 µm × 400 µm is contacted by five parallel bars of n^+ electrodes with evaporated aluminium on top. For the electric field measurements, a current is sourced between the outermost bars, while the inner bars, separated by 200 µm act as the voltage detection in a four point configuration. Due to the bonding, the spectrum at 0 T is broad and only a significant magnetic field of 600 mT generates lines with the intrinsic $^{\mathrm{nat}}$Si D^{0}X linewidth. Biases up to ∼35 V were applied, resulting in an **electric field ∼0.09 V/µm**, measured by the inner two contacts. No significant shift of any of the six D^{0}X transition energies is detected up to an **accuracy of ∼4 µeV**. The measurement might potentially be flawed due to those donors that are directly beneath the contacts, which are not subject to a strong electric field.

II: Hall square with n$^+$ electrodes on the corners of a 50 µm × 50 µm implanted area

The idea of this device (sample natSi-smallHall) is similar to the Hall measurement discussed in Sec. 5.2.2. The corners of an phosphorus implanted square of 50 µm × 50 µm are contacted by n^+ electrodes which in turn are connected via metallic leads and bond pads. A current is sourced along one side of the implanted area, while the voltage is measured across the opposite side. Both the current through the bias leads and the voltage measured on the opposite side are measured as a function of wavelength for different bias voltages. With an **accuracy ∼4 µeV** no shift of the D^{0}X transition energy either at 0 T nor at 300 mT is observed up to bias voltages of 10 V. This bias resulted in measured voltages on the opposite side of ∼1.5 V and an **electric field bias of the implanted area of $\mathcal{E} > 1.5\,\mathrm{V}/50\,\mu\mathrm{m} = 0.03\,\mathrm{V}/\mu\mathrm{m}$**.

III: Parallel n$^+$ electrodes on bulk-doped wafer, 10 µm × 50 µm

This device (sample natSi-parElec10) has the same layout as device IV, for which a shift is observed, with two parallel n^+ electrodes on top of a bulk-doped wafer, but its dimensions are smaller with an electrode separation of 10 µm and a length of 50 µm. In contrast to device IV, this device shows a pronounced zero-field splitting of ∼8 µeV, which is likely strain induced. A slight shift, smaller than the shift observed for device IV, is also seen in this device for one of the two peaks and is **on the order of 3 µeV for a field of 0.09 V/µm**. This result is somewhat in accordance with the data discussed below, but is certainly not conclusive in itself due

to the observed zero-field splitting, which increased the effective transition linewidth and thus reduced accuracy. Furthermore, the fact that only one of the two peaks features an observable shift is not understood, but could hint that one species of D^0X (either heavy- or light hole D^0X) is stronger influenced by electric fields than the other. However, no theoretical prediction to suggest so is known, and, as stated, the measurements are not conclusive enough to declare such an observation.

IV: Parallel n^+ electrodes on bulkdoped wafer, $20\,\mu m \times 800\,\mu m$

The only device that showed a significant, consistent shift of D^0X transition energy is sample natSi-parElec20 with two parallel n^+ electrodes with a separation of 20 µm and a length of 800 µm, depicted as the inset of Fig. 7.11(b). The device is fabricated on a bulk-doped wafer with a concentration of $3 \times 10^{15}\,cm^{-3}$, which is likely not optimal for the homogeneity of the electric field. However, the relative success of this experiment indicates that donors that are not directly between the two electrodes seem not to contribute significantly to the carrier transport and hence conductivity of the sample.

The experiment is performed by setting a certain voltage bias and monitoring the current as a function of laser wavelength for two different laser intensities $I_L = 3500\,W/m^2$ and $120\,W/m^2$ at 4.5 K and 0 T. The respective current traces– normalized for visiblity– are plotted in Fig. 7.11(a) at their respective average electric field bias. Figure 7.11(b) shows the extracted I-V characteristics both on- and off resonance with the previously observed steep rise of current above a certain threshold voltage, which is expected to be due to the combination of tunneling at the emitter electrode and impact ionization of donors (cf. Sec. 7.2). Figure 7.11(c) depicts the shift in peak position of the bound exciton transition, as deduced from a Gaussian fit to the traces of Fig. 7.11(a). A shift of about 2 µeV is extracted with a high degree of confidence for both laser powers. The observed shift is smaller than the D^0X linewidth (∼6 µeV at lower bias and ∼10 µeV at high bias). It should be noted that, with the developed model for the charge transport in these devices, in the high bias regime the electric field between the contacts is indeed simply the voltage divided by the contact separation (cf. Appendix C).

The extracted shifts for both laser intensities show the same electric field dependence, which is well described by the parabolic behaviour of Blossey's theory. The orange line in Figs. 7.11(a,c) represents the expected quadratic shift according to Eq. (7.11) with reasonable values for $E_g - E_{D^0X} = 20\,meV$ and $\mathcal{E}_I = 5.2\,V/\mu m$. Hence, a good agreement is found between the data and Blossey's theory. In con-

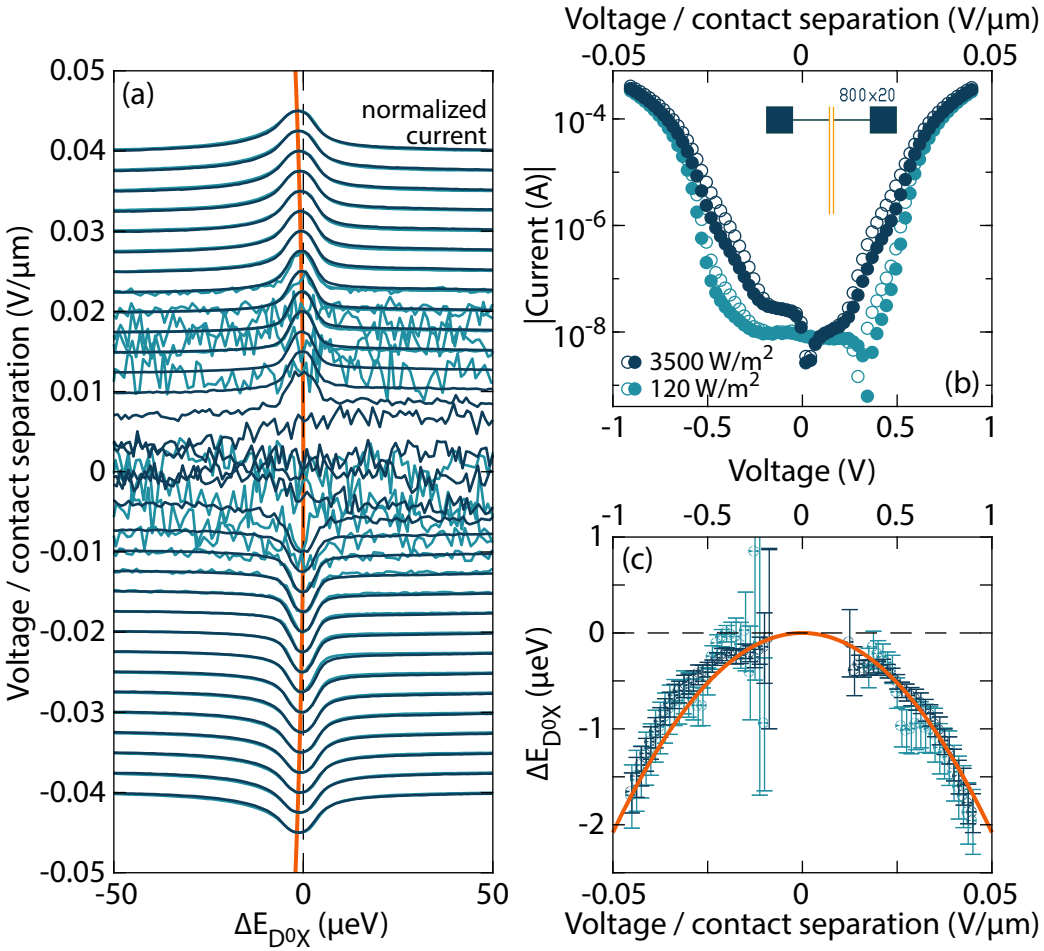

Figure 7.11: The electric field dependence of the D^0X spectrum of sample natSi-parElec20. (a) The current through the device as a function of wavelength and voltage bias. The traces are normalized for visibility and the maximum currents (minimum for negative currents) of each trace is located at the bias voltage. (b) The I-V characteristics for two different laser powers both on resonance (empty circles) and off resonance (full circles). The inset is a schematic of the device. (c) The Gaussian-fitted peak position of (a) as a function of mean electric field. Error bars are the standard deviation of the fit. The orange line is the theoretically predicted shift following Eq. (7.11) with $E_g - E_{D^0X} = 20\,\text{meV}$ and $\mathcal{E}_I = 5.2\,\text{V/μm}$ and is also plotted in (a) for direct comparison of D^0X linewidth in ^{nat}Si and peak shift.

trast, extrapolating Rahman's linear dependence towards lower biases would predict a shift of 1250 µeV for a bias of $\mathcal{E} = 0.05\,\mathrm{V/\mu m}$ — a prediction three orders of magnitude above the experimental result.

7.4.3 Conclusion

From the experimental evidence, it can be concluded that the linear dependence of Rahman's theory is certainly not valid for the low bias regime with electric fields below $\sim$0.1 V/µm. Instead, good agreement is found with a quadratic dependence as predicted by Blossey's theory. There are certainly a number of open questions that must be addressed before a conclusive answer can be drawn. Device I and III did not show a significant shift, although the applied biases are on the same order of magnitude as device IV. Is this simply due to experimental accuracy, or do magnetic fields (device I) or strain (devices I & III) interfere with the small shift due to the electric field? Is it possible to simply add the electric field induced shifts to the shifts due to the magnetic field and strain encountered in Sec. 5.3? Due to the interconnection between strain and electric fields this seems quite unlikely.

Further work could aim to repeat the experiment of device III and IV for a device which is not fabricated on top of a bulk doped wafer, but instead features an implanted area with donors only directly between the electrodes. In such an experiment it is ensured that all of the donors are subject to a homogeneous electric field distribution. These devices have already been fabricated during the D0XDEV process, but have not been measured due to time limitations.

In summary, from the measurements it can be concluded that electric field induced D^0X transition energy shifts seem to be less of a concern than previously feared. This is encouraging for nano-scale devices, for which, however, the severity of electric field D^0X ionisation and the reduction of dipole moments could not be assessed. Certainly for µm-scaled devices that may be of use for magnetometry applications, electric field effects seem not to be of concern.

Chapter 8

Conclusion and future work

8.1 Summary

This thesis provided a broad overview of the relevant physical phenomena for D^0X-assisted optical spin-to-charge conversion. While research on neutral bound excitons in silicon is an established field with the earliest publications in the mid 1960's, their potential application to quantum information processing and quantum sensing has only been realized with the availability of pure ^{28}Si host crystals with sharp linewidths around the year 2010. This might be the reason why so far the competing, off-resonant ionization process under laser illumination at the D^0X wavelength has gained only marginal attention. This thesis brought the off-resonant processes more into focus and finds that in float-zone grown ^{nat}Si the off-resonant photoconductivity is at best an order of magnitude smaller than the photo-conductivity on-resonance with the D^0X transition. The off-resonant effects severely impact the achievable fidelity of D^0X-assisted qubit readout, and the signal quality in sensing applications.

A second point of this thesis is the development of a solid theoretical understanding for the photoconductive charge transport encountered in low temperature devices at the relevant laser energies. The effects of magnetoresistance, shallow-donor impact ionization and the photoemission across the built-in potential at nn^+-interfaces had been observed in the transport measurements before, but within this thesis have now been equipped with a theoretical framework.

Finally, to the knowledge of the author, this thesis represents the first usage of purposely-built silicon devices for D^0X measurements. Previous experiments had been restricted to bulk-doped devices without direct contacts to the silicon. The µm-sized resistive devices introduced here demonstrate that D^0X-assisted spin-to-charge conversion is achievable for small donor ensembles and represents a first step

towards a potential application of donors and the D^0X spin readout in magnetic sensing applications.

In the following a short summary of the achievements of this thesis are given chapter by chapter.

Chapter 2

A novel proposal for surface code quantum computation using solid state spin qubits such as donors in silicon has been developed[1] and simulated against a variety of error sources. The proposed architecture consists of two separated stages which incorporate the probe and data-qubits of the surface code and the two stages are required to perform circular motions with respect to each other. It is found that the device and operation time may be scaled to the available fabrication precision. Surface code threshold calculations showed that the required qubit operation fidelities, implantation accuracy and mechanical requirements for the orbital motion are partly met by current technology and partly expected to be met by the technological process in the field. The most important challenges that need to be faced are uniform qubit placement, the mechanical design of the stages and the multiplexing of qubit-control and -measurement on the probe qubit stage.

Chapter 5

The chapter introduced the fundamental processes of the D^0X transition and the two competing, spin-independent optical ionisation processes (direct donor ionisation and intrinsic absorption in silicon) that may occur in parallel at the D^0X photon energy. Relying on relatively old literature values for the ionisation cross-sections, a measurement fidelity limit for the single electron spin of $\sim$99.9 % has been estimated, which is an error-rate that is about an order of magnitude better than current experimentally obtained values by spin-dependent tunnelling. Photo-Hall measurements confirmed that in agreement with theory, both upon on- and off-resonant laser excitation, the electron density increases, while the electron mobility remains similar to the expected measured dark-current value. In a ^{28}Si device, a combined model for the magnetic field and strain related shifts of the D^0X transition energy has been validated and finally, the polarization degree (up to 90 % electron spin polarization) and time-scale (on the order of 30 ms) of a donor ensemble upon D^0X illumination have been investigated.

[1] In collaboration with Joe O'Gorman, Naomi Nickerson and Simon Benjamin from Oxford University / Imperial College London.

Chapter 6

Chapter 6 represented experiments conducted on bulk-doped devices using a parallel-plate capacitor. A model was developed for the source of the capacitive D^0X signal which is essentially due to a resonant effect by capacitance and resistance of the silicon sample. Using this model, the conductivity of two ^{28}Si samples was measured as a function of laser power. The observed linear dependence and conductivity magnitude confirmed the results and model developed in Sec. 5.2. The capacitive signal was used to measure the coherence time of phosphorus in a dilute ^{28}Si sample with a very low donor concentration. The measured coherence time is likely limited by vibrations of the sample in the magnetic field and hence not representative for the intrinsic coherence time limit of phosphorus in ^{28}Si. Finally, a novel method to perform state tomography on the coupled electron-nuclear spin system of phosphorus donors in silicon was developed and tested. In contrast to conventional, spin-resonance tomography, this method is based on the absolute population measurement of the D^0X-assisted donor ionization. The method is valid, as demonstrated by the tomography of single electron and nuclear spin coherences, but the tomography of a Bell state could not be achieved.

Chapter 7

This chapter comprised measurements on devices purposely fabricated for the direct electrical measurement of the D^0X ionization process. Measurements using a ^{28}Si device with parallel electrodes proved that typical ESR experiments can be conducted using the hybrid optical-electrical spin readout of the D^0X transition, where the coherence time is furthermore not affected by the novel spin readout scheme. The transport characteristics at low temperatures of resistors with degenerately doped contacts were measured and are in qualitative agreement with transport due to photo-excitation over the built-in potentials at the nn^+ interface at low voltage biases, and with a combined tunnelling and impact ionization transport at higher biases. Scanning photocurrent microscopy experiments proved that the D^0X signal is largely created in the bulk, up to $\sim$250 µm away from the contacts, but furthermore showcased many, so far not-understood dependencies of the low-temperature transport. Finally, the electric field dependence of the D^0X transition has been measured and is in accordance with an effective mass theory predicting a small, quadratic reduction of transition energy with increasing electric field. The observed low sensitivity to electric fields further encourages the application of the D^0X transition in nano-devices and/or single donor architectures.

Publications

Chapter 2 has been published in npj Quantum Information [70], while parts of Chapters 5.3, 5.4 & 7.1 have been published in Nature Materials [32]. A manuscript with the results of Chapters 6.2 & 6.3 is in preparation.

8.2 Future research directions

A couple of interesting research questions remain open or have been brought up by the work of this thesis.

The first future direction, mentioned in the conclusions of Ch. 7.4, is a further validation of the observed quadratic D^0X transition energy shift with electric field, using a device that is not fabricated on a bulk-doped wafer, but instead features implanted phosphorus donors only between the electrodes. These devices have been built during the D0XDEV process and are available with a variety of contact separations. If these measurements show the same low electric field dependence as observed in this thesis, then the suitability of the D^0X spin-to-charge conversion with the strong electric fields in the vicinity of single charge detectors (such as SETs) would be confirmed.

Another point of research is the exact origin and strength of the off-resonant ionization process and its strength compared with the D^0X oscillator strength. The latter is especially important since the off-resonant ionisation cross section used throughout this thesis is an extrapolation of data from the 1980's, while D^0X oscillator strength has been measured in 1977. Since then improved wafer purity and smaller D^0X linewidths, together with better spectrometer resolutions should allow the determination of these quantities with higher accuracy. Such high resolution absorption measurements are, e.g., carried out in the group of Ronny Nawrodt at the Friedrich Schiller University Jena, Germany.

A final, continuing research direction is the design of devices with signals that achieve higher spin-sensitivity. Throughout this thesis resistive devices have been measured, which feature a certain optimal bias voltage, at which the contrast between on- and off-resonant D^0X signal is maximal, as seen in Fig. 7.4 & 7.11. Further research may be required to test if the signal quality at these bias points may be increased by a change of device design. Furthermore, enabled by the apparent low electric field sensitivity of the D^0X, new type of devices may be envisioned, which do not rely on a conductivity measurement (whose readout-time scale and sensitivity is ultimately limited by the electron capture time of the ionized donor concentra-

tion). Instead, devices could be envisioned that collect the Auger electrons and gives an output signal that scales linearly with their number. This operation would be similar to a single CCD pixel.

Another path forward is to benefit from the wealth of device designs that have been proposed for extrinsic infrared detectors [161, 211]. These detectors aim to detect the ionisation of shallow donors due to infrared radiation and hence are conceptually very similar. Devices such as modified blocked-impurity-band detectors [212] or other infrared detector designs may inspire donor spin quantum sensing devices that may challenge the best magnetometers of today.

In summary, quantum information processing and quantum sensing has reignited interest in the bound exciton of silicon donors, five decades after the initial papers. The relatively simple spin-to-charge conversion technique promises high-sensitivity magnetometry devices with a µm-spatial resolution. In the realm of quantum information, the D^0X transition may achieve a reliable qubit readout. Albeit an encouraging small electric field sensitivity, its suitability for qubit readout in single donor devices seems to be strongly dependent on whether large, strain-induced transition energy shifts can be avoided in the device design.

Appendices

Appendix A

Fabrication logbook of D0XDEV devices

In the following, the logbook for the fabrication of the D0XDEV devices is presented. The following table details all fabrication steps, while a summary has been given in Sec. 4.1.2.

Table A.1: Fabrication steps of the D0XDEV devices.

Step	Step details
A	**Alignment marker**
A1	Cleaning in 1165 solvent, 5 min, 70 °C.
A2	Fresh 1165 solvent, 5 min, ultrasonics, room temperature.
A3	IPA, 5 min, room temperature.
A4	DI water rinse.
A5	N_2 blow dry.
A6	Dehydration bake in oven, 220 °C, 20 min.
A7	Spin coat photo resist S1818, 1.8 µm thickness (measured), 4000 rpm, 30 s.
A8	Photo resist bake on hot plate, nominal 115 °C, 1 min (*in hindsight maybe a bit short*).
A9	Exposure with Quintel Q4000-6 mask aligner, 7.3 s.
A10	Develop in MF26A, 1 min, DI water rinse, N_2 blow dry.
A11	Reactive ion etching (Oxford Instruments NGP80), Gases: CHF_3 58.3 sccm, SF_6 25 sccm, time: 5 min (*problematic if longer*), pressure: 10 mbar, angle: 65°, strike pressure: 60, DC bias: 20, ramp rate: 6, forward power: 150, lower magnitude: 66 %, lower phase: 47 %.

continued on next page

Table A.1: (Cont.) Fabrication steps of the D0XDEV devices.

Step	Step details
A12	Resist removal: 1165 solvent, 5 min, 70 °C, ultrasonics, DI water rinse, N_2 blow dry.
A13	DektakXT depth check gives alignment marker depths of 370 nm and microscope images show ∼100 nm larger feature sizes than the mask sizes. Measured etch rates of this recipe are 75 nm/min for silicon and 60 nm/min for the S1818 resist.
B	**n^+ Arsenic implantation**
B1	Dehydration bake in oven, 220 °C, 20 min.
B2	Spin coat photo resist S1818, 4000 rpm, 30 s.
B3	Photo resist bake on hot plate, nominal 115 °C, 1 min.
B4	Exposure with Quintel Q4000-6 mask aligner, 7.3 s.
B5	Develop in MF26A, 1 min, DI water rinse, N_2 blow dry.
B6	Descum of resist residue at the bottom of exposed trenches in the Diener plasma asher. gas: O_2, 0.4 mbar, power: 100 %, 2 min.
B7	Ion implantation at the Surrey Ion Beam Centre. Species: ^{75}As, implantation energy 40 keV, implantation angle: 7°, dose: $2 \times 10^{15}\,cm^{-2}$. The expected implantation profile is depicted in Fig. 4.2(b)
C	**Low dose Phosphorus implantation**
C1	Resist removal and cleaning: 15 min 1165 at 70 °C with ultrasonics.
C2	5 min Acetone, 5 min IPA, DI water rinse, N_2 blow dry.
C3	Dehydration bake in oven, 220 °C, 20 min.
C4	Spin coat photo resist S1818, 4000 rpm, 30 s.
C5	Photo resist bake on hot plate, nominal 115 °C, 1 min was too short (wafer stuck to mask), added another 30 s.
C6	Exposure with Quintel Q4000-6 mask aligner, 7.3 s.
C7	Develop in MF26A, 1 min, DI water rinse, N_2 blow dry.
C8	Diener plasma ash descum. gas: O_2, 0.4 mbar, power: 100 %.

continued on next page

Table A.1: (Cont.) Fabrication steps of the D0XDEV devices.

Step	Step details
C9	Ion implantation at the Surrey Ion Beam Centre. Species: ^{31}P, implantation energy 100 keV, implantation angle: 7°, dose: $7 \times 10^{10}\,cm^{-2}$. The expect implantation profile is depicted in Fig. 4.2(c)
D	**Oxide growth and etch**
D1	Resist removal: 5 min 1165 at 70 °C with ultrasonics.
D2	DI water rinse, N_2 blow dry.
D3	Piranha etch for least contamination during field oxide growth. Add 400 ml H_2O_2 slowly to 400 ml H_2SO_4. Add wafers to the fresh, bubbling solution for 10 min (first wafer) to 15 min (last wafers).
D4	DI water rinse, N_2 blow dry.
D5	Dry oxide growth at the University of Southampton. O_2 atmosphere, 5 min, 950 °C (Process developed for the UNDEDD project).
D6	Cleaning: 5 min Acetone, 5 min IPA, DI water rinse, N_2 blow dry.
D7	Dehydration bake in oven, 220 °C, 20 min.
D8	Spin coat photo resist S1818, 4000 rpm, 30 s.
D9	Photo resist bake on hot plate, nominal 115 °C, 1:15 min.
D10	Exposure with Quintel Q4000-6 mask aligner, 7.3 s.
D11	Develop in MF26A, 1 min, DI water rinse, N_2 blow dry.
D12	Diener plasma ash descum. gas: O_2, 0.4 mbar, power: 100 %.
D13	Ellipsometer measurement of the oxide thickness at the exposed structures: 11 nm to 12 nm.
D14	Buffered oxide etch 30 s (NH_4F/HF = 6:1). Di rinse, N_2 blow dry.
D15	Ellipsometer measurement of the oxide thickness at on the etched surface: ∼1 nm.
E	**Contact Aluminium**
E1	Resist removal: 5 min 1165 at 70 °C with ultrasonics.
E2	DI water rinse, N_2 blow dry.

continued on next page

Table A.1: (Cont.) Fabrication steps of the D0XDEV devices.

Step	Step details
E3	5 min Acetone, 5 min IPA, DI water rinse, N_2 blow dry.
E4	Dehydration bake in oven, 220 °C, 20 min.
E5	Spin coat photo resist S1818, 4000 rpm, 30 s.
E6	Photo resist bake on hot plate for 1:15 min.. Probably made a mistake here: Set the hot plate to measure 115 °C, but didn't press down the thermometer. The hot plate was thus nominally at 140 °C and probably to hot. Didn't turn out to be dramatic though, compensate with longer exposure and development time. Only a few devices at the wafer border (Hall squares) were affected.
E7	Exposure with Quintel Q4000-6 mask aligner, 7.3 s to 7.7 s.
E8	Develop in MF26A, 1:00 min – 1:30 min, DI water rinse, N_2 blow dry.
E9	Diener plasma ash descum. gas: O_2, 0.4 mbar, power: 100 %.
E10	Sample transfer to thermal evaporator within 15 min to 20 min. Evaporate Aluminium film of 30 nm, chamber pressure: 3×10^{-7} mbar to 3×10^{-6} mbar, deposition rate: ∼0.5 nm/s.
E11	Lift off in 1165 for a few hours. With ultrasonics for 10 min gives a better result (no collapsing sidewalls).
E12	DI water rinse, N_2 blow dry.
F	**Gate Aluminium**
F1	Wafer clean: 5 min Acetone, 5 min IPA, DI water rinse, N_2 blow dry.
F2	Dehydration bake in oven, 220 °C, 20 min.
F3	Spin coat photo resist S1818, 4000 rpm, 30 s.
F4	Photo resist bake on hot plate for 1:15 min at nominal 115 °C (measured 107 °C).
F5	Exposure with Quintel Q4000-6 mask aligner, 7.5 s.
F6	Develop in MF26A, 1:00 min, DI water rinse, N_2 blow dry.
F7	Aluminium deposition in hermal evaporator with film thickness of 30 nm, deposition rate: ∼0.5 nm/s.
F8	Lift off in 1165 for a few hours. Finish with ultrasonics for ∼10 min.

continued on next page

Table A.1: (Cont.) Fabrication steps of the D0XDEV devices.

Step	Step details
F9	DI water rinse, N_2 blow dry.
F10	Protective cover using S1818 spin coated photo resist.
F11	Dicing of wafers with Disco dicing saw.

Appendix B

D^0X fidelity in the strong excitation limit

Section 5.1.5 calculated the fidelity with which a single phosphorus donor electron spin can be measured by the D^0X-assisted spin-to-charge conversion, assuming a low laser intensity, i.e. no coherent driving. In the following, the corresponding calculations in the strong excitation limit, with coherent driving of the D^0X transition show that the fidelity is not improved over the weak excitation case.

It is assumed that the D^0X transition is tuned to the $|\uparrow\rangle$ state, while the $|\downarrow\rangle$ state is subject to direct, off-resonant ionisation. The error of the $|\uparrow\rangle$ state is set to $e_\uparrow = 0$, assuming perfect optical π-pulses with pulse duration $t_{\pi,\,\text{optical Rabi}}$. The measurement error is thus entirely given by the probability of ionizing a $|\downarrow\rangle$ electron during the laser pulse, which is given by Eq. (5.21). The Rabi frequency for the coherent driving of the D^0X transition depends on the square root of the laser intensity I_L, hence $t_{\pi,\,\text{optical Rabi}} \propto I_\text{L}^{-1/2}$, as given by Eq. (5.6). In contrast, the direct ionisation rate (due to much faster decay rate) increases linearly with I_L. Thus, a shortening of $t_{\pi,\,\text{optical Rabi}}$ by a factor of two, requires an increase in laser power by a factor of four, which, in turn, gives an increase in direct ionisation rate by a factor of four, and, taken together with the two times shorter laser pulse, increases $e_\downarrow$ by a factor of two. Hence, longer pulses and lower laser intensities are beneficial, as shown by the results of the full calculations depicted in Fig. B.1. These are based on the reported oscillator strength of the D^0X transition and a direct photo ionisation cross-section of $\sigma_\text{direct} = \sigma_{\text{direct,\,peak}}/20$ (cf. Tables. 5.1 & 5.2).

The shaded area depicts the limit in which $t_{\pi,\,\text{optical Rabi}} \geq \tau_\text{Auger} = 272\,\text{ns}$, i.e. where the assumption of purely coherent driving with $e_\uparrow = 0$ is not valid any more. At the border of this region, with $t_{\pi,\,\text{optical Rabi}} = 272\,\text{ns}$ (where strictly speaking the assumption is also not really valid), the overall measurement fidelity is $\sim 99.94\,\%$, i.e. it approaches roughly the same fidelity that was calculated for the

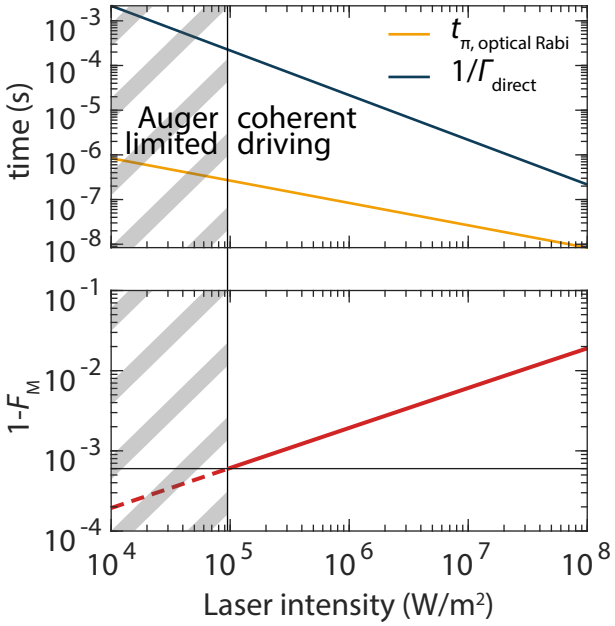

Figure B.1: D^0X-assisted spin-to-charge conversion error of a single donor in the limit of coherent driving of the D^0X transition. (a) The pulse duration $t_{\pi,\,\text{optical Rabi}}$ of a π pulse on the D^0Xtransition and the direct ionisation rate Γ_{direct}, as a function of laser intensity. (b) The measurement error due to a pulse of length $t_{\pi,\,\text{optical Rabi}}$ (assuming $e_\uparrow = 0$) as a function of laser intensity. The error is solely due to the direct ionisation of the $|\downarrow\rangle$ state, as given by Eq. (5.21).

weak laser intensity case in Sec. 5.1.5. Hence, no fidelity improvement are found for laser pulses strong enough to drive the D^0X transition coherently.

Appendix C

Details of the n^+nn^+ resistor simulations

This appendix presents supplementary plots to both the high bias (neglecting diffusion currents, but including tunnelling at the emitter) and low bias (including diffusion currents but neglecting tunnelling) simulations of the n^+nn^+ resistor-type structure at 4 K, as discussed in Ch. 7.2.

High bias simulation

First, the details of the high bias simulations are discussed. The device length is set to 10 µm and the resulting voltage for a certain current density J is plotted logarithmically in Fig. C.1(a). In the dark, the steep rise of current, due to the onset of impact ionization is found at $\mathcal{E} = 6 \times 10^4$ V/m. Figure C.1(b) shows the distribution of potential, electric field (here labelled F), free carrier and ionised donor concentration and current within the device in the dark for various current densities.

For the lower current densities, a space charge region of completely ionized donors forms at the emitter, which maintains the high electric field required for tunneling at the emitter (i.e. satisifies the boundary condition) and brings the electric field to a lower value in the bulk. Here electron and ionised donor concentrations are equal and the electric field is constant with a magnitude just enough to provide enough electrons via impact ionization to sustain the required current J. Above $J = \sim 3 \times 10^7$ A/m^2, the number of injected carriers is greater than the number of donors, which is known as carrier injection regime and is discussed in further detail e.g. in references [193]. It is seen that for the majority of the device, and especially for lower current densities, the electric field in the bulk of the device (solid lines of

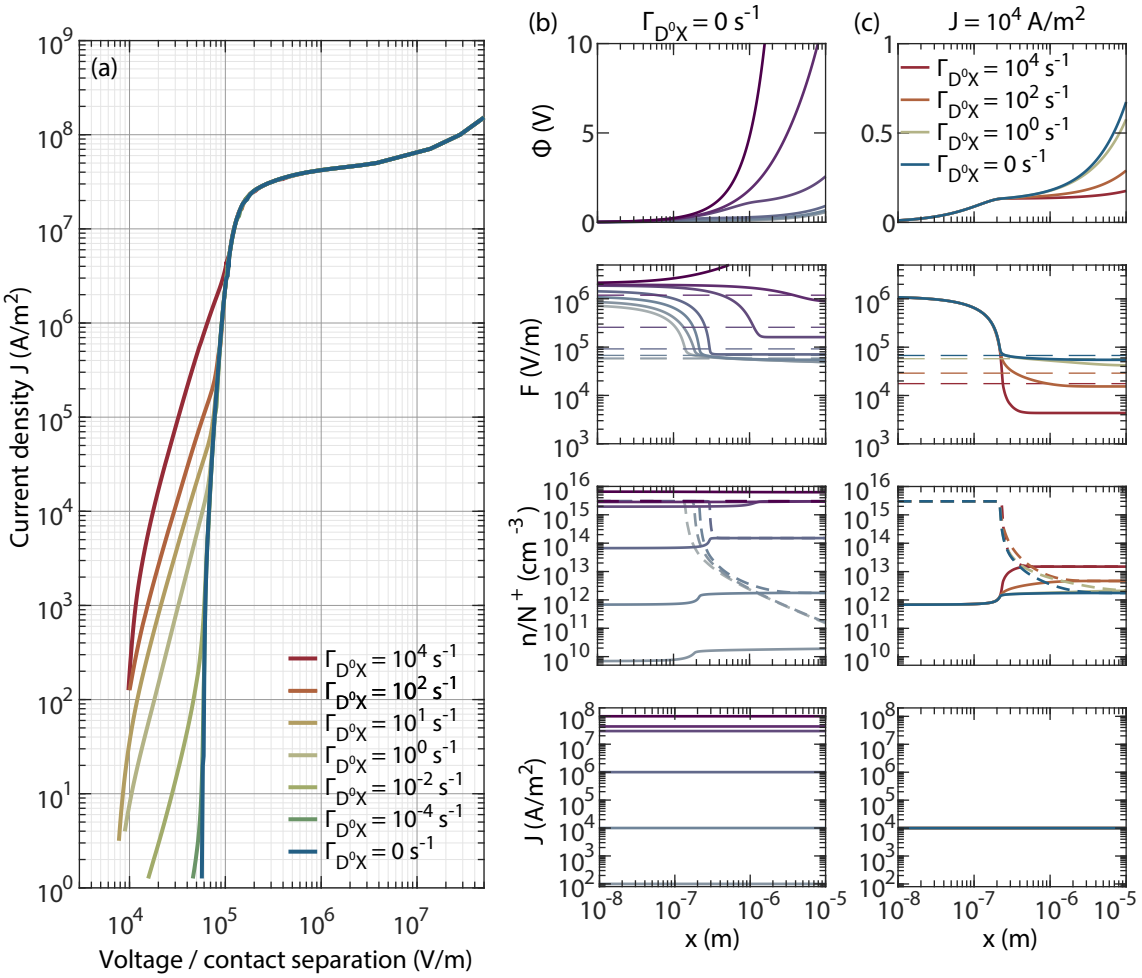

Figure C.1: High bias simulation for a range of laser ionisation rates for a 10 µm device length. For details refer to text.

the electric field plots) is essentially given by the voltage over the contact separation (dashed line).

Figure C.1(c) plots the effect of a laser for a fixed current density of $J = 1 \times 10^4\,\mathrm{A/m^2}$. Here, as the laser ionisation rate $\Gamma_{\mathrm{D^0X}}$ increases, less and less electric field is required to maintain the same electric current, because the number of free carriers increases due to the higher laser ionisation rate. Since the field distribution at the emitter is unchanged, an overall smaller voltage is sufficient to maintain the same current density.

Low bias simulation

In the low bias regime, both drift and diffusion currents are considered and a thermionic emission current $J_{\mathrm{the}} \approx 1 \times 10^3\,\mathrm{A/m^2}$ is used as a boundary condition

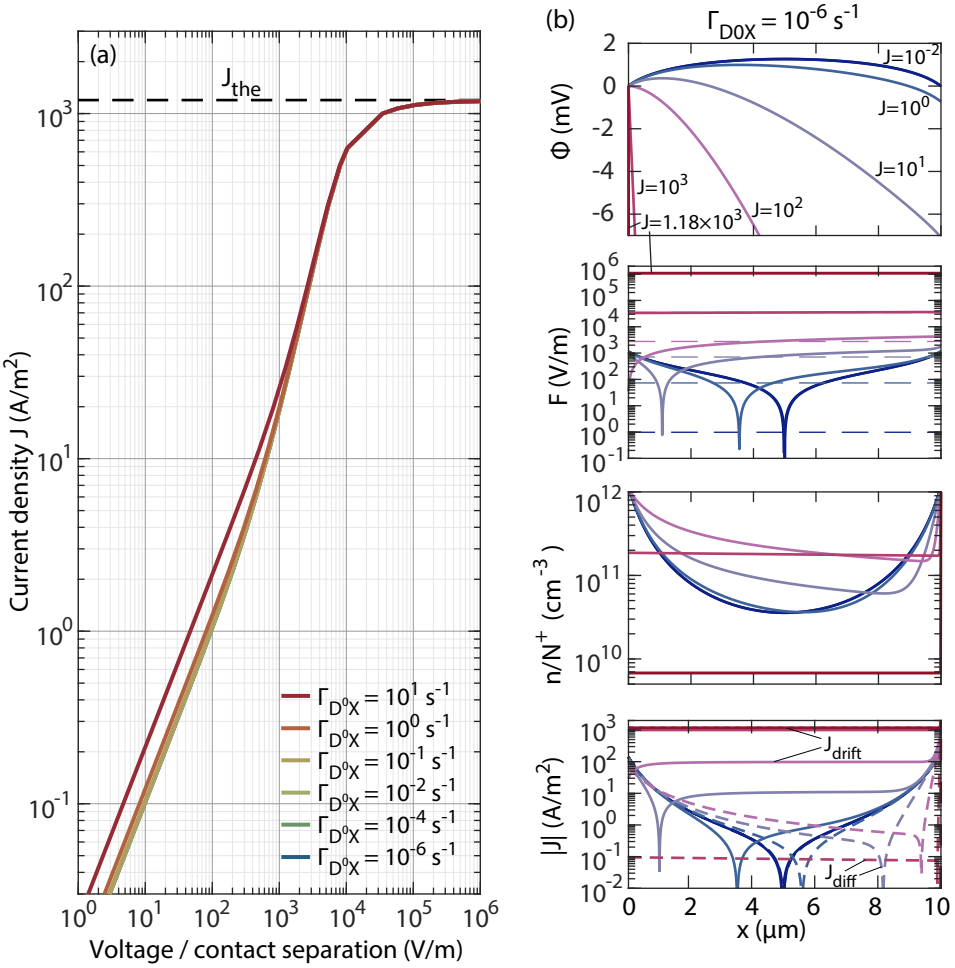

Figure C.2: Low bias simulation, including drift and diffusion currents, for a range of laser ionisation rates for a 10 µm device length. For details refer to text.

for the carrier density at both emitter and collector (following closely [203, 204]). Figure C.2(a) is again the J-V characteristics on log-log plot with the limiting current density due to the finite supply over the barrier of electrons per unit time at the emitter. Figure C.2(b) is again the details for a variety of current densities in the dark. For very low bias (low J) it is seen that drift and diffusion currents oppose each other both at emitter and collector and the potential distribution sketched in Fig. 7.2 for a longer device is found. As the bias (and J) increases, the drift current becomes dominant over the diffusion current and then saturates due to J_{the}. N^+ is low in all cases. Close to J_{the}, the electric field in the bulk of the device (solid lines of the electric field plots) is essentially given by the voltage over the contact separation (dashed line).

Appendix D

Scanning photocurrent microscopy dependencies

This appendix features several supplementary figures to the scanning photocurrent microscopy (SPCM) experiments presented in Ch. 7.3.

Firstly, Fig. D.1 shows the voltage bias dependence for different laser energies, just like Fig. 7.8, but over a larger bias voltage range up to 25 V. Essentially the same dependence is seen, with the $P_{\mathrm{L}} = 7.3\,\mathrm{mW}$ data showing the highest contrast between on- and off-resonance. It is seen that for higher biases, the current signal is relatively strong irrespective of laser spot-location, as long as it is illuminating in-between the electrodes. At lower bias, a stronger signal is observed with the laser spot at the collector, just as previously discussed.

Next Fig. D.2 explores the temperature dependence of the SPCM maps. It is found that at low temperatures of 2 K to 3 K a relatively small $\mathrm{D}^0\mathrm{X}$ signal is generated, while the strongest difference between on- and off-resonance current is measured at 6 K. The signal is again strongest at the collector for low biases and moves then towards the emitter/the whole region in-between the electrodes for higher biases. This transitions seems to depend slightly on temperature, i.e. with higher temperature this transition occurs a little bit earlier.

Finally, Figure D.3, shows the magnetic field dependence of the SPCM images. For each magnetic field, a wavelength scan is conducted to find the corresponding on- and off-resonance wavelengths. The data shows a reduction of current with higher magnetic field which is due to the magneto resistance discussed in Ch. 3.5.3. The 100 mT SPCM images do not significantly differ from the 0 mT images, but interestingly the 600 mT maps look completely different with a strong signal both on- and off-resonance at the emitter electrode. This signal is furthermore only found where both n^+ region and phosphorus implant overlap, which is in contrast to the

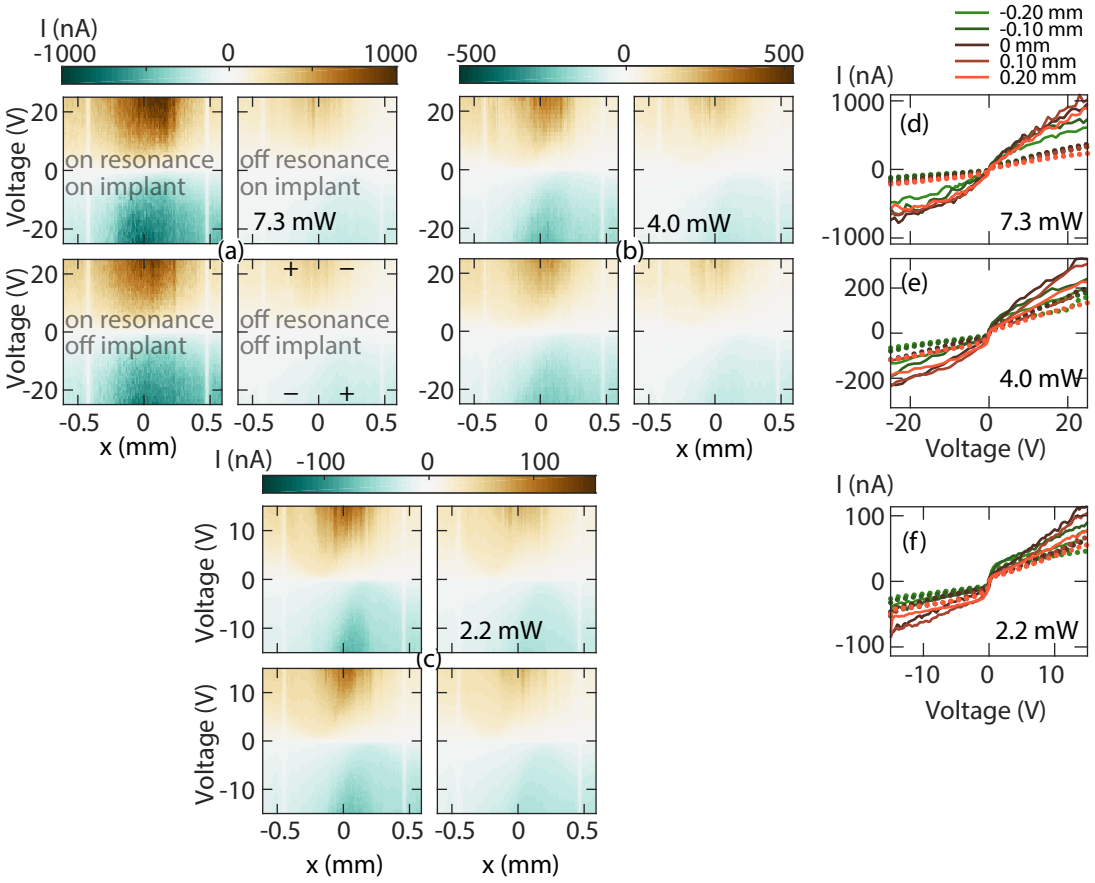

Figure D.1: The same data presented in Fig. 7.8 for the lower laser power but plotted over a larger voltage bias. The x-axis is shifted to have the center of the device at $x = 0\,\mathrm{mm}$.

previously observed emitter signal at certain voltage—laser power combinations (cf. Fig. 7.7).

Both the observed temperature and magnetic field dependence of the SPCM data is not understood.

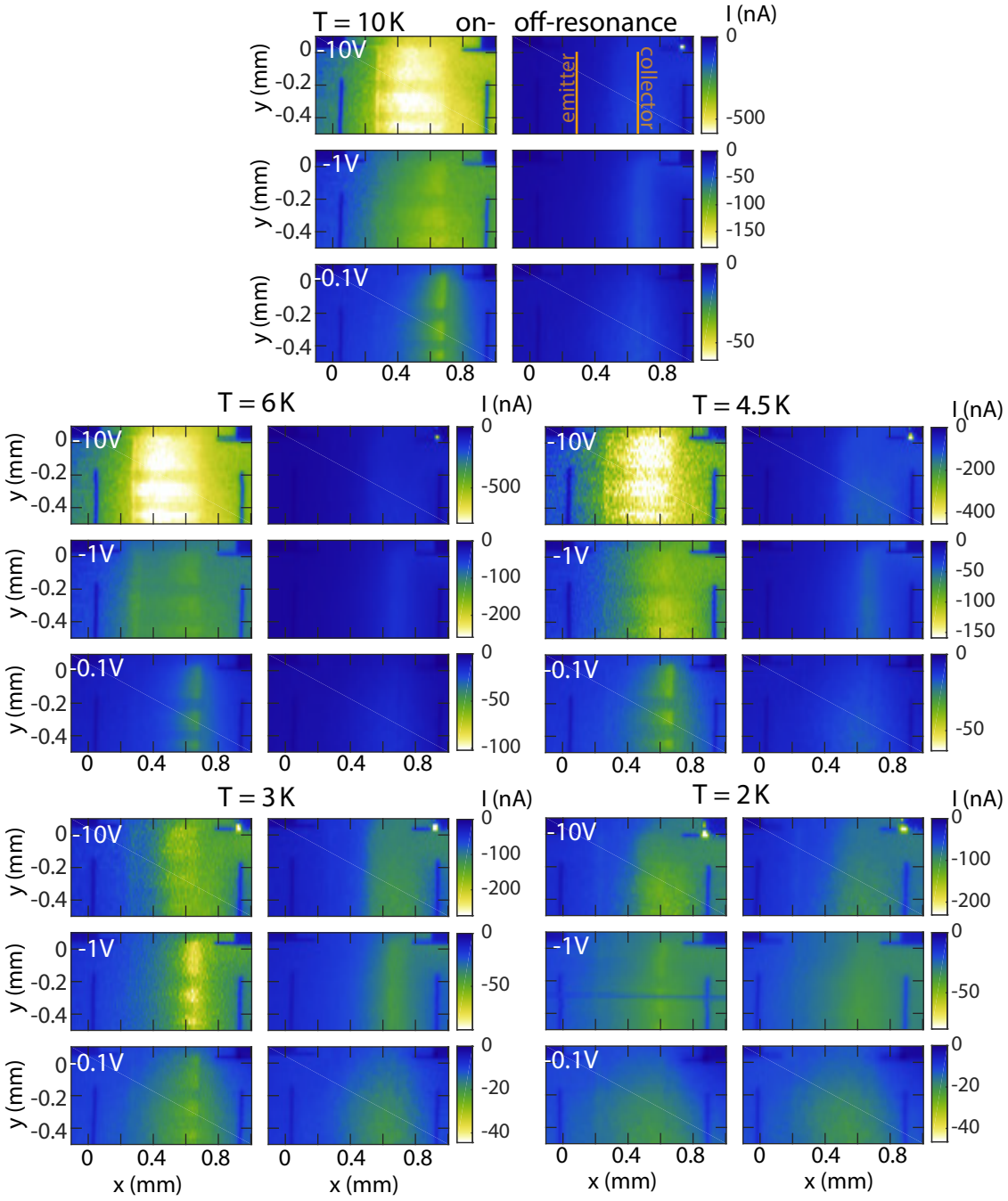

Figure D.2: Temperature dependence of the SPCM images for $P_{\mathrm{L}} = 7.3\,\mathrm{mW}$ and 0 T. The colormap is again scaled for the maximum off-resonant current $I_{\mathrm{off}}^{\mathrm{max}}$, with $I_{\mathrm{off}}^{\mathrm{max}}$ corresponding to 1/3.5 th of the color scale for 10 K, 1/5 th for 6 K, 1/3 rd for 6 K and one half of the color scale for 3 K and 2 K.

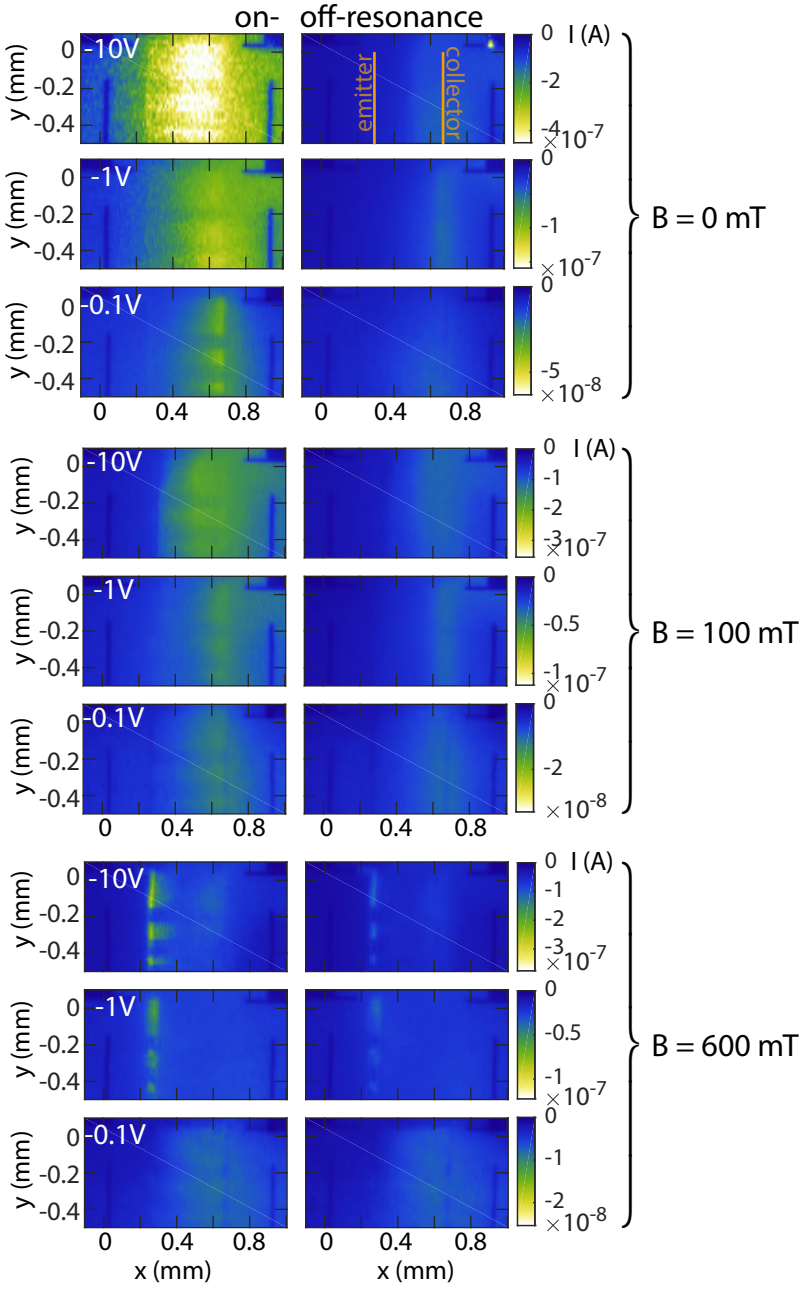

Figure D.3: Magnetic field dependence of the SPCM images for $P_{\mathrm{L}} = 7.3\,\mathrm{mW}$ and 4.5 K. The colormap is scaled for the maximum off-resonant current $I_{\mathrm{off}}^{\mathrm{max}}$ at each bias, with $I_{\mathrm{off}}^{\mathrm{max}}$ corresponding to 1/5 th of the color scale for 0 mT, 1/1.5 th for 100 mT and one half for 600 mT.

Bibliography

[1] K. Dawon. *Electric field controlled semiconductor device*. U.S. Patent No. 3 102 230. 27. Aug. (1963) (cit. on p. 1).

[2] International Roadmap Comittee. *International Technology Roadmap for Semiconductors 2.0; Executive Report*. 2015 (cit. on p. 1).

[3] S. Middelhoek et al. "Silicon sensors". *Measurement Science and Technology* **6** (12), 1641–1658, (1995) (cit. on p. 2).

[4] R. Bogue. "Recent developments in MEMS sensors: a review of applications, markets and technologies". *Sensor Review* **33** (4), 300–304, (2013) (cit. on p. 2).

[5] D. P. DiVincenzo. "The Physical Implementation of Quantum Computation". *Fortschritte der Physik* **48** (9-11), 771–783, (2000) (cit. on p. 2).

[6] T. D. Ladd, F. Jelezko, R. Laflamme, Y. Nakamura, C. Monroe, and J. L. O/'Brien. "Quantum computers". *Nature* **464** (7285), 45–53, (2010) (cit. on p. 2).

[7] A. Steane. "The ion trap quantum information processor". *Applied Physics B* **64** (6), 623–643, (1997) (cit. on p. 2).

[8] D. Kielpinski, C. Monroe, and D. J. Wineland. "Architecture for a large-scale ion-trap quantum computer". *Nature* **417** (6890), 709–711, (2002) (cit. on p. 2).

[9] S. Debnath, N. M. Linke, C. Figgatt, K. A. Landsman, K. Wright, and C. Monroe. "Demonstration of a small programmable quantum computer with atomic qubits". *Nature* **536** (7614), 63–66, (2016) (cit. on p. 2).

[10] J. L. O'Brien, A. Furusawa, and J. Vuckovic. "Photonic quantum technologies". *Nat Photon* **3** (12), 687–695, (2009) (cit. on p. 2).

[11] X. Cai et al. "Integrated Compact Optical Vortex Beam Emitters". *Science* **338** (6105), 363–366, (2012) (cit. on p. 2).

[12] J. Carolan et al. “Universal linear optics”. *Science* **349** (6249), 711–716, (2015) (cit. on p. 2).

[13] R. Barends et al. “Superconducting quantum circuits at the surface code threshold for fault tolerance”. *Nature* **508** (7497), 500–503, (2014) (cit. on p. 2).

[14] R. Barends et al. “Coherent Josephson Qubit Suitable for Scalable Quantum Integrated Circuits”. *Physical Review Letters* **111** (8), 080502, (2013) (cit. on p. 2).

[15] J. Kelly et al. “State preservation by repetitive error detection in a superconducting quantum circuit”. *Nature* **519** (7541), 66–69, (2015) (cit. on p. 2).

[16] A. M. Tyryshkin et al. “Electron spin coherence exceeding seconds in high-purity silicon”. *Nature Materials* **11** (2), 143–147, (2012) (cit. on pp. 3, 26, 31, 35, 58–60, 112, 115, 130, 135).

[17] G. Wolfowicz et al. “Atomic clock transitions in silicon-based spin qubits.” *Nature Nanotechnology* **8** (8), 561–4, (2013) (cit. on pp. 3, 4, 7, 49, 136).

[18] K. Saeedi et al. “Room-Temperature Quantum Bit Storage Exceeding 39 Minutes Using Ionized Donors in Silicon-28”. *Science* **342** (6160), 830–833, (2013) (cit. on pp. 3, 5, 6, 97, 111, 130, 134).

[19] J. J. L. Morton et al. “Solid-state quantum memory using the 31P nuclear spin”. *Nature* **455** (7216), 1085–1088, (2008) (cit. on pp. 3, 35, 97, 139).

[20] P. Becker, H. J. Pohl, H. Riemann, and N. Abrosimov. “Enrichment of silicon for a better kilogram”. *physica status solidi (a)* **207** (1), 49–66, (2010) (cit. on pp. 3, 59, 69).

[21] Y. Kubo et al. “Hybrid Quantum Circuit with a Superconducting Qubit Coupled to a Spin Ensemble”. *Physical Review Letters* **107** (22), 220501, (2011) (cit. on p. 4).

[22] J. M. Elzerman, R. Hanson, L. H. Willems van Beveren, B. Witkamp, L. M. K. Vandersypen, and L. P. Kouwenhoven. “Single-shot read-out of an individual electron spin in a quantum dot”. *Nature* **430** (6998), 431–435, (2004) (cit. on p. 4).

[23] A. Morello et al. “Single-shot readout of an electron spin in silicon”. *Nature* **467** (7316), 687–691, (2010) (cit. on pp. 4, 35).

[24] J. J. Pla et al. “A single-atom electron spin qubit in silicon”. *Nature* **489** (7417), 541–545, (2012) (cit. on pp. 4, 26, 35, 36, 94).

[25] J. J. Pla et al. “High-fidelity readout and control of a nuclear spin qubit in silicon”. *Nature* **496** (7445), 334–338, (2013) (cit. on pp. 4, 97).

[26] J. T. Muhonen et al. “Storing quantum information for 30 seconds in a nanoelectronic device”. *Nature Nanotechnology* **9** (12), 986–991, (2014) (cit. on pp. 4, 5, 26, 35, 36, 55, 97).

[27] J. T. Muhonen et al. “Quantifying the quantum gate fidelity of single-atom spin qubits in silicon by randomized benchmarking”. *Journal of Physics: Condensed Matter* **27** (15), 154205, (2015) (cit. on pp. 5, 26, 35).

[28] W. Schmid. “Auger lifetimes for excitons bound to neutral donors and acceptors in Si”. *physica status solidi (b)* **84** (2), 529–540, (1977) (cit. on pp. 5, 6, 85, 87).

[29] A. Yang et al. “Optical Detection and Ionization of Donors in Specific Electronic and Nuclear Spin States”. *Physical Review Letters* **97** (22), 227401, (2006) (cit. on pp. 5, 71).

[30] M. Steger et al. “Optically-detected NMR of optically-hyperpolarized 31P neutral donors in 28Si”. *Journal of Applied Physics* **109** (10), 102411, (2011) (cit. on p. 5).

[31] M. Steger, K. Saeedi, and M. Thewalt. “Quantum information storage for over 180 s using donor spins in a 28Si “semiconductor vacuum””. *Science* **336** (June), (2012) (cit. on pp. 5, 108, 111, 130).

[32] C. C. Lo et al. “Hybrid optical–electrical detection of donor electron spins with bound excitons in silicon”. *Nature Materials* **14** (5), 490–494, (2015) (cit. on pp. 6, 36, 192).

[33] A. Yang et al. “Simultaneous Subsecond Hyperpolarization of the Nuclear and Electron Spins of Phosphorus in Silicon by Optical Pumping of Exciton Transitions”. *Physical Review Letters* **102** (25), 257401, (2009) (cit. on pp. 6, 111, 112).

[34] B. E. Kane. “A silicon-based nuclear spin quantum computer”. *Nature* **393** (6681), 133–137, (1998) (cit. on p. 6).

[35] G. Wolfowicz et al. “Conditional Control of Donor Nuclear Spins in Silicon Using Stark Shifts”. *Physical Review Letters* **113** (15), 157601, (2014) (cit. on pp. 6, 35, 45, 49).

[36] G. Pica et al. “Hyperfine Stark effect of shallow donors in silicon”. *Physical Review B* **90** (19), 195204, (2014) (cit. on pp. 6, 45).

[37] A. Laucht et al. “Electrically controlling single-spin qubits in a continuous microwave field”. *Science Advances* **1** (3), (2015) (cit. on pp. 6, 35, 49).

[38] C. C. Lo et al. “Stark shift and field ionization of arsenic donors in 28Si-silicon-on-insulator structures”. *Applied Physics Letters* **104** (19), 193502, (2014) (cit. on p. 6).

[39] M. F. Gonzalez-Zalba, A. Saraiva, M. J. Calderón, D. Heiss, B. Koiller, and A. J. Ferguson. “An Exchange-Coupled Donor Molecule in Silicon”. *Nano Letters* **14** (10), 5672–5676, (2014) (cit. on p. 6).

[40] J. P. Dehollain et al. “Single-Shot Readout and Relaxation of Singlet and Triplet States in Exchange-Coupled ^{31}P Electron Spins in Silicon”. *Physical Review Letters* **112** (23), 236801, (2014) (cit. on p. 6).

[41] S. R. Schofield et al. “Atomically Precise Placement of Single Dopants in Si”. *Physical Review Letters* **91** (13), 136104, (2003) (cit. on pp. 7, 27, 36).

[42] M. Fuechsle et al. “A single-atom transistor”. *Nature Nanotechnology* **7** (4), 242–246, (2012) (cit. on pp. 7, 27, 34, 36).

[43] Y. Li and S. C. Benjamin. “One-dimensional quantum computing with a ’segmented chain’ is feasible with today’s gate fidelities”. *ArXiv e-prints*, (2017). arXiv: 1702.05657 [quant-ph] (cit. on p. 7).

[44] A. Fowler, M. Mariantoni, J. Martinis, and A. Cleland. “Surface codes: Towards practical large-scale quantum computation”. *Physical Review A*, (2012) (cit. on pp. 7, 18, 19, 21).

[45] L. C. L. Hollenberg, A. D. Greentree, A. G. Fowler, and C. J. Wellard. “Two-dimensional architectures for donor-based quantum computing”. *Physical Review B* **74** (4), 045311, (2006) (cit. on p. 7).

[46] C. D. Hill et al. “A surface code quantum computer in silicon”. *Science Advances* **1** (9), e1500707, (2015) (cit. on p. 7).

[47] G. Pica, B. W. Lovett, R. N. Bhatt, T. Schenkel, and S. A. Lyon. “Surface code architecture for donors and dots in silicon with imprecise and nonuniform qubit couplings”. *Physical Review B* **93** (3), 1–11, (2016) (cit. on p. 7).

[48] K. J. Morse et al. “A photonic platform for donor spin qubits in silicon”. *ArXiv e-prints*, (2016). arXiv: 1606.03488 [quant-ph] (cit. on p. 7).

[49] G. Tosi et al. “Silicon quantum processor with robust long-distance qubit couplings”. *ArXiv e-prints*, (2015). arXiv: 1509.08538 [cond-mat.mes-hall] (cit. on pp. 7, 53).

[50] C. L. Degen, F. Reinhard, and P. Cappellaro. "Quantum sensing". *ArXiv e-prints*, (2016). arXiv: 1611.02427 [quant-ph] (cit. on pp. 9, 10).

[51] A. Peters, K. Y. Chung, and S. Chu. "Measurement of gravitational acceleration by dropping atoms". *Nature* **400** (6747), 849–852, (1999) (cit. on p. 9).

[52] F. Dolde et al. "Electric-field sensing using single diamond spins". *Nature Physics* **7** (6), 459–463, (2011) (cit. on pp. 9, 35).

[53] M. F. Gonzalez-Zalba, S. Barraud, a. J. Ferguson, and a. C. Betz. "Probing the limits of gate-based charge sensing". *Nature Communications* **6**, 6084, (2015) (cit. on p. 9).

[54] K. Jensen et al. "Non-invasive detection of animal nerve impulses with an atomic magnetometer operating near quantum limited sensitivity". *Scientific Reports* **6**, 29638 EP -, (2016) (cit. on p. 9).

[55] A. Wickenbrock, S. Jurgilas, A. Dow, L. Marmugi, and F. Renzoni. "Magnetic induction tomography using an all-optical 87Rb atomic magnetometer". *Optical Letters* **39** (22), 6367–6370, (2014) (cit. on p. 9).

[56] R. L. Fagaly. "Superconducting quantum interference device instruments and applications". *Review of Scientific Instruments* **77** (10), 101101, (2006) (cit. on pp. 9, 10, 160).

[57] K. Sternickel and A. I. Braginski. "Biomagnetism using SQUIDs: status and perspectives". *Superconductor Science and Technology* **19**, S160–S171, (2006) (cit. on pp. 9, 160).

[58] D. Vasyukov et al. "A scanning superconducting quantum interference device with single electron spin sensitivity." *Nature Nanotechnology* **8** (9), 639–44, (2013) (cit. on p. 9).

[59] C. W. Hicks, L. Luan, K. A. Moler, E. Zeldov, and H. Shtrikman. "Noise characteristics of 100 nm scale GaAs/$Al_xGa_{1-x}As$ scanning Hall probes". *Applied Physics Letters* **90** (13), 133512, (2007) (cit. on p. 9).

[60] C. L. Degen, M. Poggio, H. J. Mamin, C. T. Rettner, and D. Rugar. "Nanoscale magnetic resonance imaging." *Proceedings of the National Academy of Sciences of the United States of America* **106** (5), 1313–7, (2009) (cit. on p. 9).

[61] J. M. Taylor et al. "High-sensitivity diamond magnetometer with nanoscale resolution". *Nature Physics* **4** (10), 810–816, (2008) (cit. on pp. 9, 159).

[62] J. R. Maze et al. “Nanoscale magnetic sensing with an individual electronic spin in diamond.” *Nature* **455** (7213), 644–7, (2008) (cit. on pp. 9, 159).

[63] G. Balasubramanian et al. “Nanoscale imaging magnetometry with diamond spins under ambient conditions.” *Nature* **455** (7213), 648–51, (2008) (cit. on p. 9).

[64] D. Le Sage et al. “Optical magnetic imaging of living cells”. *Nature* **496** (7446), 486–489, (2013) (cit. on p. 9).

[65] S. Steinert et al. “Magnetic spin imaging under ambient conditions with sub-cellular resolution.” *Nature Communications* **4**, 1607, (2013) (cit. on pp. 9, 159).

[66] H. Nowak et al. *Magnetism in medicine: a handbook*. John Wiley & Sons, 2007 (cit. on p. 9).

[67] H. Griffiths. “Magnetic induction tomography”. *Measurement Science and Technology* **12** (8), 1126–1131, (2001) (cit. on p. 9).

[68] H. Malissa, D. I. Schuster, A. M. Tyryshkin, A. A. Houck, and S. A. Lyon. “Superconducting coplanar waveguide resonators for low temperature pulsed electron spin resonance spectroscopy”. *Review of Scientific Instruments* **84** (2), 025116, (2013) (cit. on p. 10).

[69] A. Bienfait et al. “Reaching the quantum limit of sensitivity in electron spin resonance”. *Nature Nanotechnology* **11** (3), 253–257, (2016) (cit. on p. 10).

[70] J. O’Gorman, N. H. Nickerson, P. Ross, J. J. Morton, and S. C. Benjamin. “A silicon-based surface code quantum computer”. *NPJ Quantum Information* **2**, 15019, (2016) (cit. on pp. 13, 24, 30, 31, 192).

[71] M. A. Nielsen and I. L. Chuang. *Quantum Computation and Quantum Information: 10th Anniversary Edition*. 10th. New York, NY, USA: Cambridge University Press, 2011 (cit. on pp. 14, 16, 52, 53, 138, 140, 151).

[72] P. W. Shor. “Scheme for reducing decoherence in quantum computer memory”. *Physical Review A* **52** (4), R2493–R2496, (1995) (cit. on p. 16).

[73] D. A. Lidar and T. A. Brun. *Quantum Error Correction*. Cambridge University Press, 2010 (cit. on p. 16).

[74] A. G. Fowler, A. M. Stephens, and P. Groszkowski. “High-threshold universal quantum computation on the surface code”. *Physical Review A* **80** (5), 052312, (2009) (cit. on p. 18).

[75] D. S. Wang, A. G. Fowler, and L. C. L. Hollenberg. “Quantum computing with nearest neighbor interactions and error rates over 1%”. *Physical Review* **83** (2), (2011) (cit. on p. 18).

[76] A. M. Souza, G. A. Álvarez, and D. Suter. “Robust Dynamical Decoupling for Quantum Computing and Quantum Memory”. *Physical Review Letters* **106** (24), 240501, (2011) (cit. on p. 33).

[77] T. Gullion, D. B. Baker, and M. S. Conradi. “New, compensated Carr-Purcell sequences”. *Journal of Magnetic Resonance* **89** (3), 479–484, (1990) (cit. on p. 33).

[78] U. Boettcher, H. Li, R. A. de Callafon, and F. E. Talke. “Dynamic flying height adjustment in hard disk drives through feedforward control”. *IEEE Transactions on Magnetics* **47** (7), 1823–1829, (2011) (cit. on p. 33).

[79] T. Harness and R. R. A. Syms. “Characteristic modes of electrostatic comb-drive X - Y microactuators”. *Journal of Micromechanics and Microengineering* **10** (1), 7, (2000) (cit. on p. 33).

[80] D. Mukhopadhyay, J. Dong, E. Pengwang, and P. Ferreira. “A SOI-MEMS-based 3-DOF planar parallel-kinematics nanopositioning stage”. *Sensors and Actuators A: Physical* **147** (1), 340–351, (2008) (cit. on p. 33).

[81] J. Dong, D. Mukhopadhyay, and P. M. Ferreira. “Design, fabrication and testing of a silicon-on-insulator (SOI) MEMS parallel kinematics XY stage”. *Journal of Micromechanics and Microengineering* **17** (6), 1154, (2007) (cit. on p. 33).

[82] B. Koo, X. Zhang, J. Dong, S. Salapaka, and P. Ferreira. “A 2 Degree-of-Freedom SOI-MEMS Translation Stage With Closed-Loop Positioning”. *Journal of Microelectromechanical Systems* **21** (1), 13–22, (2012) (cit. on p. 34).

[83] L. L. Chu and Y. B. Gianchandani. “A micromachined 2D positioner with electrothermal actuation and sub-nanometer capacitive sensing”. *Journal of Micromechanics and Microengineering* **13** (2), 279, (2003) (cit. on p. 34).

[84] H.-H. Liao, H.-H. Shen, B.-T. Liao, Y.-J. Yang, Y.-C. Chen, and W.-W. Pai. “A MEMS electrostatic resonator for a fast-scan STM system”. *5th IEEE International Conference on Nano/Micro Engineered and Molecular Systems (NEMS)*, 549–552, (2010) (cit. on p. 34).

[85] S. J. Hile et al. “Radio frequency reflectometry and charge sensing of a precision placed donor in silicon”. *Applied Physics Letters* **107** (9), 093504, -, (2015) (cit. on p. 34).

[86] E. V. Oort and M. Glasbeek. “Electric-field-induced modulation of spin echoes of N-V centers in diamond”. *Chemical Physics Letters* **168** (6), 529–532, (1990) (cit. on p. 35).

[87] A. L. Falk et al. “Electrically and Mechanically Tunable Electron Spins in Silicon Carbide Color Centers”. *Physical Review Letters* **112** (18), 187601, (2014) (cit. on p. 35).

[88] J. J. L. Morton, A. M. Tyryshkin, A. Ardavan, K. Porfyrakis, S. A. Lyon, and G. A. D. Briggs. “High Fidelity Single Qubit Operations Using Pulsed Electron Paramagnetic Resonance”. *Physical Review Letters* **95** (20), 200501, (2005) (cit. on p. 36).

[89] C. Vieu et al. “Electron beam lithography: resolution limits and applications”. *Applied Surface Science* **164** (1–4), 111–117, (2000) (cit. on p. 36).

[90] D. M. Toyli, C. D. Weis, G. D. Fuchs, T. Schenkel, and D. D. Awschalom. “Chip-Scale Nanofabrication of Single Spins and Spin Arrays in Diamond”. *Nano Letters* **10** (8), 3168–3172, (2010) (cit. on p. 36).

[91] C. D. Weis et al. “Single atom doping for quantum device development in diamond and silicon”. *Journal of Vacuum Science & Technology B* **26** (6), 2596–2600, (2008) (cit. on p. 36).

[92] D. N. Jamieson et al. “Controlled shallow single-ion implantation in silicon using an active substrate for sub-20-keV ions”. *Applied Physics Letters* **86** (20), 202101, -, (2005) (cit. on p. 36).

[93] L. Robledo, L. Childress, H. Bernien, B. Hensen, P. F. A. Alkemade, and R. Hanson. “High-fidelity projective read-out of a solid-state spin quantum register”. *Nature* **477** (7366), 574–578, (2011) (cit. on pp. 36, 38).

[94] W. Pfaff et al. “Unconditional quantum teleportation between distant solid-state quantum bits”. *Science* **345** (6196), 532–535, (2014) (cit. on p. 36).

[95] G. Waldherr et al. “Quantum error correction in a solid-state hybrid spin register”. *Nature* **506** (7487), 204–207, (2014) (cit. on p. 36).

[96] N. Bar-Gill, L. M. Pham, A. Jarmola, D. Budker, and R. L. Walsworth. “Solid-state electronic spin coherence time approaching one second”. *Nature Communications* **4**, 1743, (2013) (cit. on p. 36).

[97] P. Ovartchaiyapong, L. M. A. Pascal, B. A. Myers, P. Lauria, and A. C. Bleszynski Jayich. "High quality factor single-crystal diamond mechanical resonators". *Applied Physics Letters* **101** (16), 163505, -, (2012) (cit. on p. 37).

[98] M. Imboden, O. A. Williams, and P. Mohanty. "Observation of Nonlinear Dissipation in Piezoresistive Diamond Nanomechanical Resonators by Heterodyne Down-Mixing". *Nano Letters* **13** (9), 4014–4019, (2013) (cit. on p. 37).

[99] O. A. Williams. "Nanocrystalline diamond". *Diamond and Related Materials* **20** (5), 621–640, (2011) (cit. on p. 37).

[100] S. Pezzagna et al. "Nanoscale Engineering and Optical Addressing of Single Spins in Diamond". *Small* **6** (19), 2117–2121, (2010) (cit. on p. 37).

[101] M. Lesik et al. "Maskless and targeted creation of arrays of colour centres in diamond using focused ion beam technology". *physica status solidi (a)* **210** (10), 2055–2059, (2013) (cit. on p. 37).

[102] B. Naydenov et al. "Enhanced generation of single optically active spins in diamond by ion implantation". *Applied Physics Letters* **96** (16), 163108, -, (2010) (cit. on p. 37).

[103] D. Antonov et al. "Statistical investigations on nitrogen-vacancy center creation". *Applied Physics Letters* **104** (1), 012105, (2014) (cit. on p. 37).

[104] M. S. Grinolds et al. "Nanoscale magnetic imaging of a single electron spin under ambient conditions". *Nature Physics* **9** (4), 215–219, (2013) (cit. on p. 37).

[105] W. F. Koehl, B. B. Buckley, F. J. Heremans, G. Calusine, and D. D. Awschalom. "Room temperature coherent control of defect spin qubits in silicon carbide". *Nature* **479** (7371), 84–87, (2011) (cit. on p. 37).

[106] K. Adachi, N. Watanabe, H. Okamoto, H. Yamaguchi, T. Kimoto, and J. Suda. "Single-crystalline 4H-SiC micro cantilevers with a high quality factor". *Sensors and Actuators A: Physical* **197** (0), 122–125, (2013) (cit. on p. 37).

[107] D. J. Christle et al. "Isolated electron spins in silicon carbide with millisecond coherence times". *Nature Materials* **14** (2), 160–163, (2015) (cit. on p. 37).

[108] B. N. Brockhouse. "Lattice vibrations in silicon and germanium". *Physical Review Letters* **2** (6), 256–258, (1959) (cit. on p. 40).

[109] S. Hunklinger. *Festkörperphysik*. Oldenbourg Verlag, 2009 (cit. on pp. 39, 61).

[110] K. Rajkanan, R. Singh, and J. Shewchun. "Absorption coefficient of silicon for solar cell calculations". *Solid-State Electronics* **22** (9), 793–795, (1979) (cit. on pp. 40, 91).

[111] J. R. Chelikowsky and M. L. Cohen. "Electronic structure of silicon". *Physical Review B* **10** (12), 5095–5107, (1974) (cit. on p. 41).

[112] P. Yu and M. Cardona. *Fundamentals of semiconductors: physics and materials properties*. Springer Science & Business Media, 2010 (cit. on pp. 42, 44–47, 63, 82).

[113] S. Zwerdling, K. J. Button, B. Lax, and L. M. Roth. "Internal Impurity Levels in Semiconductors: Experiments in p-Type Silicon". *Physical Review Letters* **4** (4), 173–176, (1960) (cit. on p. 42).

[114] E. A. Gutierrez-D., M. J. Deen, and C. L. Claeys. *Low Temperature Electronics: Physics, Devices, Circuits, and Applications*. Academic Press, San Diego, 2001 (cit. on pp. 42, 63, 66, 67, 165).

[115] M. Cardona, T. Meyer, and M. Thewalt. "Temperature Dependence of the Energy Gap of Semiconductors in the Low-Temperature Limit". *Physical Review Letters* **92** (19), 196403, (2004) (cit. on pp. 42, 91).

[116] W. Bludau, A. Onton, and W. Heinke. "Temperature dependence of the band gap of silicon". *Journal of Applied Physics* **45** (4), 1846–1848, (1974) (cit. on pp. 42, 90).

[117] C. Herring and E. Vogt. "Transport and Deformation-Potential Theory for Many-Valley Semiconductors with Anisotropic Scattering". *Phys. Rev.* **101** (3), 944–961, (1956) (cit. on p. 43).

[118] D. K. Wilson and G. Feher. "Electron Spin Resonance Experiments on Donors in Silicon. III. Investigation of Excited States by the Application of Uniaxial Stress and Their Importance in Relaxation Processes". *Physical Review* **124** (4), 1068–1083, (1961) (cit. on pp. 43, 46).

[119] I. Balslev. "Influence of Uniaxial Stress on the Indirect Absorption Edge in Silicon and Germanium". *Physical Review* **143** (2), 636–647, (1966) (cit. on pp. 43, 44).

[120] K. Seeger. *Semiconductor Physics: An Introduction*. Advanced Texts in Physics. Springer, 2004 (cit. on pp. 43–45, 61–64).

[121] V. A. Karasyuk, D. M. Brake, and M. L. W. Thewalt. "Ultrahigh-resolution photoluminescence studies of excitons bound to boron in silicon in magnetic fields". *Physical Review B* **47** (15), 9354–9360, (1993) (cit. on pp. 44, 83, 109).

[122] A. Yang et al. "High-resolution photoluminescence measurement of the isotopic-mass dependence of the lattice parameter of silicon". *Physical Review B* **77** (11), 113203, (2008) (cit. on pp. 44, 109).

[123] A. S. Kaminskiĭ, V. A. Karasyuk, and Y. E. Pokrovskiĭ. "Luminescence of excitons bound to phosphorus atoms in silicon subjected to a magnetic field". *Soviet Journal of Experimental and Theoretical Physics* **52**, 211, (1980) (cit. on p. 44).

[124] G. Pikus and G. Bir. *Symmetry and strain-induced effects in semiconductors*. Vol. 624. Wiley New York, 1974 (cit. on p. 44).

[125] P. V. Pavlov, E. I. Zorin, D. I. Tetelbaum, and A. F. Khokhlov. "Nitrogen as dopant in silicon and germanium". *physica status solidi (a)* **35** (1), 11–36, (1976) (cit. on p. 45).

[126] G. Feher, J. C. Hensel, and E. a. Gere. "Paramagnetic resonance absorption from acceptors in silicon". *Physical Review Letters* **5** (7), 309–311, (1960) (cit. on p. 45).

[127] J. K. Gamble et al. "Multivalley effective mass theory simulation of donors in silicon". *Physical Review B* **91** (23), 235318, (2015) (cit. on p. 45).

[128] J. Salfi et al. "Spatially resolving valley quantum interference of a donor in silicon". *Nature Materials* **13** (6), 605–610, (2014) (cit. on p. 45).

[129] W. Kohn and J. M. Luttinger. "Theory of Donor States in Silicon". *Physical Review* **98** (4), 915–922, (1955) (cit. on pp. 45–47).

[130] M. Friesen. "Theory of the Stark Effect for P Donors in Si". *Physical Review Letters* **94** (18), 186403, (2005) (cit. on p. 46).

[131] R. L. Aggarwal and A. K. Ramdas. "Optical Determination of the Symmetry of the Ground States of Group-V Donors in Silicon". *Physical Review* **140**, A1246–A1253, (4A 1965) (cit. on pp. 46, 47).

[132] A. K. Ramdas and S. Rodriguez. "Spectroscopy of the solid-state analogues of the hydrogen atom: donors and acceptors in semiconductors". *Reports on Progress in Physics* **44** (12), 1297, (1981) (cit. on p. 47).

[133] D. P. Franke, M. P. D. Pflüger, P.-A. Mortemousque, K. M. Itoh, and M. S. Brandt. "Quadrupolar effects on nuclear spins of neutral arsenic donors in silicon". *Physical Review B* **93** (16), 161303, (2016) (cit. on p. 48).

[134] G. Feher. "Electron Spin Resonance Experiments on Donors in Silicon. I. Electronic Structure of Donors by the Electron Nuclear Double Resonance Technique". *Physical Review* **114** (5), 1219–1244, (1959) (cit. on p. 49).

[135] N. Stone. "Table of nuclear magnetic dipole and electric quadrupole moments". *Atomic Data and Nuclear Data Tables* **90** (1), 75–176, (2005) (cit. on p. 49).

[136] F. R. Bradbury, A. M. Tyryshkin, G. Sabouret, J. Bokor, T. Schenkel, and S. A. Lyon. "Stark Tuning of Donor Electron Spins in Silicon". *Physical Review Letters* **97** (17), 176404, (2006) (cit. on p. 49).

[137] A. Schweiger and G. Jeschke. *Principles of pulse electron paramagnetic resonance*. Oxford University Press, 2001 (cit. on pp. 52–54, 58, 59, 141).

[138] G. Grynberg, A. Aspect, and C. Fabre. *Introduction to Quantum Optics*. Vol. 1. Cambridge: Cambridge University Press, 2010, 1–697 (cit. on p. 54).

[139] D. A. Steck. *Quantum and Atom Optics*. available online, (revision 0.11.4, 26 October 2016). 2016 (cit. on pp. 54, 86, 95, 107).

[140] G. Wolfowicz. "Quantum Control of Donor Spins in Silicon and their Environment". PhD thesis. University of Oxford, 2015 (cit. on pp. 57–60).

[141] A. Bienfait et al. "Controlling spin relaxation with a cavity". *Nature* **531** (7592), 74–77, (2016) (cit. on p. 58).

[142] E. Abe et al. "Electron spin coherence of phosphorus donors in silicon: Effect of environmental nuclei". *Physical Review B - Condensed Matter and Materials Physics* **82** (12), 9–12, (2010) (cit. on pp. 59, 135, 136).

[143] V. V. Kurshev and T. Ichikawa. "Effect of spin flip-flop on electron-spin-echo decay due to instantaneous diffusion". *Journal of Magnetic Resonance (1969)* **96** (3), 563–573, (1992) (cit. on pp. 59, 135).

[144] S. M. Sze and K. K. Ng. *Physics of semiconductor devices*. John Wiley & Sons, 2006 (cit. on pp. 63, 168).

[145] C. Jacoboni, C. Canali, G. Ottaviani, and A. A. Quaranta. "A review of some charge transport properties of silicon". *Solid-State Electronics* **20** (2), 77–89, (1977) (cit. on p. 63).

[146] C.-T. Sah, P. C. H. Chan, C.-K. Wang, R. L. Y. Sah, K. A. Yamakawa, and R. Lutwack. "Effect of zinc impurity on silicon solar-cell efficiency". *IEEE Transactions on Electron Devices* **28** (3), 304–313, (1981) (cit. on p. 67).

[147] N. Sclar. "Neutral Impurity Scattering in Semiconductors". *Physical Review* **104** (6), 1559–1561, (1956) (cit. on p. 67).

[148] P. Norton, T. Braggins, and H. Levinstein. "Impurity and lattice scattering parameters as determined from Hall and mobility analysis in n-type silicon". *Physical Review B* **8** (12), 5632–5653, (1973) (cit. on pp. 67, 87, 88).

[149] A. N. Safonov, G. Davies, and E. C. Lightowlers. "Line shape of the no-phonon luminescence of excitons bound to phosphorus in carbon-doped silicon". *Physical Review B* **54** (7), 4409–4412, (1996) (cit. on p. 71).

[150] I. Pelant and J. Valenta. *Luminescence spectroscopy of semiconductors*. Oxford University Press, 2012 (cit. on pp. 82–85, 88, 89, 92).

[151] M. A. Green. "Improved value for the silicon free exciton binding energy". *AIP Advances* **3** (11), 112104, (2013) (cit. on pp. 82, 90, 91).

[152] R. Rahman et al. "Bulk and sub-surface donor bound excitons in silicon under electric fields". *ArXiv e-prints*, (2015). arXiv: `1510.00065 [cond-mat.mes-hall]` (cit. on pp. 83, 181, 182).

[153] G. Kirczenow. "A shell model of bound multiexciton complexes in silicon". *Canadian Journal of Physics* **55**, 1787–1801, (1977) (cit. on p. 83).

[154] M. Thewalt. "Excited states of donor bound excitons and bound multiexciton complexes in silicon". *Solid State Communications* **21** (10), 937–939, (1977) (cit. on p. 83).

[155] E. I. Rashba. "Luminescence and spectroscopy". *Journal of Luminescence* **100** (1–4), 57–64, (2002) (cit. on p. 85).

[156] P. J. Dean, W. F. Flood, and G. Kaminsky. "Absorption due to bound excitons in silicon". *Physical Review* **163** (3), 721–725, (1967) (cit. on p. 85).

[157] R. C. Hilborn. "Einstein coefficients, cross sections, f values, dipole moments, and all that". *ArXiv Physics e-prints*, (2002). eprint: `physics/0202029` (cit. on pp. 85, 86, 93).

[158] S. Hooker and C. Webb. *Laser Physics*. Oxford University Press, 2010 (cit. on p. 86).

[159] K.-M. C. Fu, T. D. Ladd, C. Santori, and Y. Yamamoto. "Optical detection of the spin state of a single nucleus in silicon". *Physical Review B* **69** (12), 125306, (2004) (cit. on p. 87).

[160] T. D. Ladd, P. van Loock, K. Nemoto, W. J. Munro, and Y. Yamamoto. "Hybrid quantum repeater based on dispersive CQED interactions between matter qubits and bright coherent light". *New Journal of Physics* **8** (9), 184, (2006) (cit. on p. 87).

[161] N. Sclar. "Properties of doped silicon and Germanium infrared detectors". *Progress in Quantum Electronics* **9** (3), 149–257, (1984) (cit. on pp. 87, 93, 94, 193).

[162] N. Sclar. "Asymmetries in photoconductive properties of donor and acceptor impurities in silicon". *Journal of Applied Physics* **55** (8), 2972–2976, (1984) (cit. on pp. 87, 88, 94).

[163] M. Loewenstein and A. Honig. "Photoexcited electron capture by ionized and neutral shallow impurities in silicon at liquid-helium temperatures". *Physical Review* **144** (2), 781, (1966) (cit. on pp. 87, 88).

[164] P. Norton and H. Levinstein. "Thermalization Time of Hot Photoexcited Holes in *p*-Type Germanium". *Physical Review B* **6** (2), 478–488, (1972) (cit. on p. 88).

[165] I. Pelant et al. "Photoluminescence assessment of B, P, and Al in Si wafers: The problem of sample heating by a laser beam". *Journal of Applied Physics* **73** (7), 3477–3481, (1993) (cit. on p. 89).

[166] R. J. Elliott. "Intensity of Optical Absorption by Excitons". *Physical Review* **108** (6), 1384–1389, (1957) (cit. on p. 90).

[167] B. Pajot. *Optical Absorption of Impurities and Defects in Semiconducting Crystals: Hydrogen-like Centres*. 1st ed. Springer-Verlag Berlin Heidelberg, 2010, 470 (cit. on p. 90).

[168] J. R. Haynes, M. Lax, and W. F. Flood. "Analysis of intrinsic recombination radiation from silicon and germanium". *Journal of Physics and Chemistry of Solids* **8**, 392–396, (1959) (cit. on p. 91).

[169] G. Macfarlane, T. McLean, J. Quarrington, and V. Roberts. "Fine structure in the absorption-edge spectrum of Si". *Physical Review* **111** (5), 1245, (1958) (cit. on p. 91).

[170] M. Fox. *Optical properties of solids*. Vol. 3. Oxford University Press, 2010 (cit. on p. 92).

[171] R. B. Hammond and R. N. Silver. "Temperature dependence of the exciton lifetime in high-purity silicon". *Applied Physics Letters* **36** (1), (1980) (cit. on p. 92).

[172] H. Nakayama, T. Nishino, and Y. Hamakawa. "Analysis of the exciton luminescence of silicon for characterization of the content of impurities". *Japanese Journal of Applied Physics* **19** (3), 501–511, (1980) (cit. on p. 92).

[173] G. Schramm. "Determination of the Free Exciton Capture Gross Sections of Boron and Phosphorus in Silicon by Photolummineseence". *physica status solidi (a)* **125** (2), K113–K116, (1991) (cit. on p. 92).

[174] R. H. Bube. *Photoelectronic properties of semiconductors*. Cambridge University Press, 1992 (cit. on pp. 93, 103).

[175] S. Chaudhuri. "Optical-transition cross sections involving impurities in semiconductors". *Phys. Rev. B* **26** (12), 6593–6602, (1982) (cit. on p. 93).

[176] W. W. Anderson. "Shallow impurity states in semiconductors: Absorption cross-sections, excitation rates, and capture cross-sections". *Solid-State Electronics* **18** (3), 235–245, (1975) (cit. on p. 93).

[177] G. Lucovsky. "On the photoionization of deep impurity centers in semiconductors". *Solid State Communications* **3** (9), 299–302, (1965) (cit. on p. 93).

[178] A. Yang. "Optical Hyperpolarization and Detection of Electron and Nuclear Spin of Phosphorus Donors in Highly Enriched ^{28}Si". PhD thesis. Simon Fraser University, 2010 (cit. on p. 95).

[179] P. Dirksen, A. Henstra, and W. T. Wenckebach. "An electron spin echo study of donor-acceptor recombination". *Journal of Physics: Condensed Matter* **1** (39), 7085, (1989) (cit. on pp. 98, 103).

[180] L. J. van der Pauw. "A Method of Measuring Specific Resistivity and Hall Effect of Discs of Arbitrary Shape". *Philips Research Reports* **13**, 1–9, (1958) (cit. on p. 100).

[181] E. A. Caridi and J. B. Stark. "Strain tensor elements for misfit-strained [hhk]-oriented cubic crystals". *Applied Physics Letters* **60** (12), 1441–1443, (1992) (cit. on p. 109).

[182] G. Feher and E. A. Gere. “Electron Spin Resonance Experiments on Donors in Silicon. II. Electron Spin Relaxation Effects”. *Physical Review* **114** (5), 1245–1256, (1959) (cit. on p. 112).

[183] J. Krupka, J. Breeze, A. Centeno, N. Alford, T. Claussen, and L. Jensen. “Measurements of permittivity, dielectric loss tangent, and resistivity of float-zone silicon at microwave frequencies”. *IEEE transactions on microwave theory and techniques* **54** (11), 3995–4001, (2006) (cit. on p. 126).

[184] S. Dhar and A. H. Marshak. “Static dielectric constant of heavily doped semiconductors”. *Solid-State Electronics* **28** (8), 763–766, (1985) (cit. on p. 126).

[185] T. Ruster, C. T. Schmiegelow, H. Kaufmann, C. Warschburger, F. Schmidt-Kaler, and U. G. Poschinger. “A long-lived Zeeman trapped-ion qubit”. *Applied Physics B: Lasers and Optics* **122**, 254, 254, (2016) (cit. on p. 134).

[186] J. E. Ludman and J. Silverman. “The theory of high-low junction contacts at low temperature with application to extrinsic silicon detectors”. *Infrared Physics* **17** (3), 177–184, (1977) (cit. on p. 161).

[187] Y. N. Yang, D. D. Coon, and P. F. Shepard. “Thermionic emission in silicon at temperatures below 30 K”. *Applied Physics Letters* **45** (7), 752–754, (1984) (cit. on p. 162).

[188] D. D. Coon, R. P. Devaty, A. G. U. Perera, and R. E. Sherriff. “Interfacial work functions and extrinsic silicon infrared photocathodes”. *Applied Physics Letters* **55** (17), 1738–1740, (1989) (cit. on pp. 162, 167).

[189] A. G. U. Perera, H. X. Yuan, and M. H. Francombe. “Homojunction internal photoemission far-infrared detectors: Photoresponse performance analysis”. *Journal of Applied Physics* **77** (2), 915–924, (1995) (cit. on pp. 162, 167).

[190] S. Jain and D. Roulston. “A simple expression for band gap narrowing (BGN) in heavily doped Si, Ge, GaAs and Ge_xSi_{1-x} strained layers”. *Solid-State Electronics* **34** (5), 453–465, (1991) (cit. on p. 162).

[191] E. A. Gutiérrez-D., L. Deferm, S. Decoutere, and G. Declerck. “Experimental determination of selfheating in silicon resistors operated at cryogenic temperatures”. *Microelectronic Engineering* **19** (1), 865–868, (1992) (cit. on p. 164).

[192] E. Simoen, B. Dierickx, L. Deferm, and C. Claeys. “Analytical model for the current-voltage characteristics of a silicon resistor at liquid helium temperatures”. *Cryogenics* **30** (12), 1152–1159, (1990) (cit. on p. 164).

[193] E. Simoen, B. Dierickx, L. Deferm, C. Claeys, and G. Declerck. "The charge transport in a silicon resistor at liquid-helium temperatures". *Journal of Applied Physics* **68** (8), 4091–4099, (1990) (cit. on pp. 164–166, 205).

[194] B. Dierickx, E. Simoen, and G. Declerck. "Transient response of silicon devices at 4.2 K. I. Theory". *Semiconductor Science and Technology* **896**, (1991) (cit. on pp. 164–166).

[195] B. Dierickx, E. Simoen, and G. Declerck. "Small-signal a.c. impedance of an Si resistor at liquid-helium temperatures". *Solid-State Electronics* **34** (11), 1215–1224, (1991) (cit. on p. 164).

[196] A. A. Grinberg, S. Luryi, M. R. Pinto, and N. L. Schryer. "Space-charge-limited current in a film". *IEEE Transactions on Electron Devices* **36** (6), 1162–1170, (1989) (cit. on p. 164).

[197] C. Canali, C. Jacoboni, F. Nava, G. Ottaviani, and A. Alberigi-Quaranta. "Electron drift velocity in silicon". *Physical Review B* **12** (6), 2265–2284, (1975) (cit. on p. 165).

[198] H. De Los Santos and J. Gray. "Field-dependent electron mobility in silicon between 8 and 77 K-a semi-empirical model". *IEEE Transactions on Electron Devices* **35** (11), 1972–1976, (1988) (cit. on p. 165).

[199] L. F. Shampine, J. Kierzenka, and M. W. Reichelt. *Solving boundary value problems for ordinary differential equations in MATLAB with bvp4c*. 2000 (cit. on p. 166).

[200] H. Yuan and A. Perera. "Space charge analysis of Si $n^+ - i$ structures with application to far-infrared detectors". *Solid-State Electronics* **39** (5), 621–628, (1996) (cit. on p. 167).

[201] D. D. Coon and S. D. Gunapala. "New injection mode infrared detector". *Journal of Applied Physics* **57** (12), 5525–5528, (1985) (cit. on p. 167).

[202] H. K. Henisch. *Semiconductor contacts: an approach to ideas and models*. 70. Oxford University Press, USA, 1984 (cit. on p. 168).

[203] H. X. Yuan and A. G. U. Perera. "Space-charge-limited conduction in Si n^+–i–n^+ homojunction far-infrared detectors". *Journal of Applied Physics* **79** (8), 4418, (1996) (cit. on pp. 168–170, 207).

[204] Y. Yuan and A. G. U. Perera. "Effect of i-layer parameters on the performance of Si $n^+ - i - n^+$ homojunction far-infrared detectors". *IEEE Transactions on Electron Devices* **44** (12), 2180–2186, (1997) (cit. on pp. 169, 207).

[205] D. V. Lang and C. H. Henry. “Scanning photocurrent microscopy: A new technique to study inhomogeneously distributed recombination centers in semiconductors”. *Solid State Electronics* **21** (11-12), 1519–1524, (1978) (cit. on p. 171).

[206] R. Graham and D. Yu. “Scanning Photocurrent Microscopy in Semiconductor Nanostructures”. *Modern Physics Letters B* **27** (25), 1330018, (2013) (cit. on p. 171).

[207] H. Yamaguchi et al. “Spatially resolved photoexcited charge-carrier dynamics in phase-engineered monolayer MoS2”. *ACS Nano* **9** (1), 840–849, (2015) (cit. on p. 171).

[208] R. Graham, C. Miller, E. Oh, and D. Yu. “Electric field dependent photocurrent decay length in single lead sulfide nanowire field effect transistors”. *Nano Letters* **11** (2), 717–722, (2011) (cit. on p. 171).

[209] D. F. Blossey. “Wannier Exciton in an Electric Field. I. Optical Absorption by Bound and Continuum States”. *Physical Review B* **2** (10), 3976–3990, (1970) (cit. on p. 182).

[210] H. Weman, Q. X. Zhao, and B. Monemar. “Impact ionization of excitons and electron-hole droplets in silicon”. *Phys. Rev. B* **36** (9), 5054–5057, (1987) (cit. on p. 183).

[211] A. Rogalski. “Infrared detectors: Status and trends”. *Progress in Quantum Electronics* **27** (2-3), 59–210, (2003) (cit. on p. 193).

[212] F. Szmulowicz and F. L. Madarasz. “Blocked impurity band detectors—an analytical model: Figures of merit”. *Journal of Applied Physics* **62** (6), 2533–2540, (1987) (cit. on p. 193).